DEGRADATION MECHANISMS OF ELECTRODE/ELECTROLYTE INTERFACES IN Li-ION BATTERIES

by

Ho Sop Shin

A dissertation submitted in partial fulfillment
of the requirements for the degree of
Doctor of Philosophy
(Mechanical Engineering)
in the University of Michigan
2015

Doctoral Committee:

Professor Wei Lu, Chair
Associate Professor Christian M. Lastoskie
Assistant Professor Jonghyun Park, Missouri University of Science & Technology
Assistant Professor Donald J. Siegel

DEDICATION

To God and my family

ACKNOWLEDGMENTS

First and foremost, I am truly grateful to the Lord God, my shepherd, for providing me the opportunity to study in the excellent academic world, for it is His grace and wisdom that enabled me to achieve excellence in my research during my graduate studies. It was really a blessing to meet my lovely wife, Ayoung, outstanding leaders in the academic and industrial communities, brilliant colleagues, and faithful brothers and sisters in Christ at the Korean Presbyterian Church of Ann Arbor during my time in Ann Arbor.

I express my deep gratitude to my former advisor, Dr. Ann Marie Sastry, and my current advisor, Dr. Wei Lu, for their guidance and support. They gave me great opportunities to gain the knowledge and expertise necessary to explore the fascinating technology associated with Li-ion batteries. With their valuable leadership and intellectual support, both of them trained me to be a true professional with perspectives on science and engineering. They inspired me to keep thinking in practical terms and assessing how I could contribute in ways that would make people's lives and the world better in the future. I also extend my sincere appreciation to Dr. Jonghyun Park, who boosted my confidence and kept me motivated by providing helpful suggestions, opinions, and discussion. Also, I am grateful to the members of my Ph.D. committee, i.e., Dr. Christian Lastoskie and Dr. Donald Siegel, for serving on my dissertation committee and helping me shape this work by sharing their expertise and through valuable discussions.

I also give many thanks to Dr. Kai Sun and Dr. Haiping Sun in the Electron Microbeam Analysis Laboratory (EMAL), Ms. Ying Qi in the X-ray MicroAnalysis Laboratory (XMAL), Mr. James Windak, and Ms. Laura Pfund in the Department of Chemistry who trained and assisted me to perform diverse experiments, including XPS, AFM, XRD, ICP-OES, and Raman spectroscopy.

Many thanks go to former and current members of Drs. Sastry's and Lu's groups, Dr. Myounggu Park, Dr. Jeong Hun Seo, Dr. Greg Less, Dr. Joseph Gallegos, Dr. Sangmin Lee, Dr. Seungjun Lee, Dr. Lin Liu, Dr. Min Zhu, Dr. Sangwoo Han, Dr. Dong Hoon Song, Dr. Yoon Koo Lee, Dr. Xianke Lin, Mr. KC Miller, and Mr. Guangyu Liu for many helpful discussions and their encouragement. I also appreciate former Lab Administrators Ms. Leah Wright, Ms. Nichole Washington, and Ms. Eve Bernos for their support regarding administrative issues. It was a great pleasure to share many wonderful moments with them all over the past years.

Thanks to the many scientists and staff members whom I have met at General Motors, Oak Ridge National Laboratory, and Brookhaven National Laboratory for their helpful discussions and great technical expertise.

Special thanks go to Rev. Sun Myung Ryu and my church members for their prayers, concern, and encouragement that allowed me to endure my long research efforts with a happy and thankful heart.

Most importantly, I express my deepest gratitude to my father, Dongman Shin, and my mother, Sookja Kim, who have supported me with unconditional love, unceasing prayers, and encouragement. Without their endeavors and trust, it would have been impossible for me to undertake and successfully complete my Ph.D. program. I thank my

lovely and precious wife, Ayoung Yoon for being with me during my Ph.D. journey. It was a blessing that we have shared this journey together and built a loving relationship based on mutual trust and respect. I really appreciate your love, care, and encouragement. I love you so much!

Finally, I gratefully acknowledge the financial support provided for this thesis research, which was provided by General Motors (GM/UM Advanced Battery Coalition for Drivetrains), the U.S. Department of Energy (BATT program), and the Ford Motor Company.

PREFACE

All of the work in this dissertation was conducted in the Department of Mechanical Engineering, the Department of Material Science Engineering, and the Department of Chemistry at the University of Michigan over the period from 2010 to 2015. This dissertation is the outcome of my experimental and computational work.

There are seven chapters in this dissertation and they are written in manuscript format, except for Chapters 1 and 7. The first chapter provides an introduction of lithium-ion battery technology and research reviews related to this dissertation. The second chapter is based on the content presented in the poster session at the 16th IMLB conference and in oral presentations at the UM/GM quarterly review meetings. This chapter is currently under revision for a journal submission. The third chapter was developed based on the manuscript submitted to the *Journal of Power Sources*. The fourth chapter extends the article published recently in the *Journal of Power Sources*. The fifth chapter is the manuscript that will be submitted to the *Journal of the Electrochemical Society*. The sixth chapter presents the content of current research that will be submitted to the *Journal of Power Sources*. Chapter 7 summarizes the conclusions and provides suggestions for future research.

TABLE OF CONTENTS

LIST OF TABLES

LIST OF FIGURES

ABSTRACT

Rechargeable lithium-ion batteries have captured the portable electronic market, and, now, they are moving into the markets of large-scale applications, such as electric vehicles and energy storage systems. To facilitate the commercialization of Li-ion batteries in large-scale applications, they must meet more demanding requirements in terms of high energy and power density, long lifetime, low cost, and safety. To achieve these requirements, research is being conducted with the aim of developing new materials for use as anodes and cathodes in the batteries. Many efforts are also focusing on reducing the rate at which the batteries degrade, i.e., the loss of capacity and power over time. Among the many causes of reduced capacity and power, the instability of the interface between the electrode and the electrolyte has emerged as one of the most prominent issues, but, at the same time, it is likely the least understood issue. This instability is mostly associated with degradation processes of electrode/electrolyte interfaces; thereby there is a significant need to shed light on the chemical and mechanical processes that contribute to degradation of the electrode/electrolyte interfaces. Thus, the aim of this dissertation was to elucidate the mechanisms by which degradation occurs at the electrode/electrolyte interface by evaluating the changes in the properties of the interface and correlating these changes with the reduction of the capacity and power of Li-ion batteries over time.

Various types of cells and experimental methodologies have been developed, and the combination of several analytical techniques has been utilized to obtain a conclusive understanding of the changes that occur in the electrode/electrolyte interface. In addition to experimental approaches, atomistic-scale simulations using molecular dynamics (MD) and density functional theory (DFT) have been used to acquire information about these changes that are difficult to measure due to experimental limitations. The simulations have proven to be a useful tool in understanding and explaining what we have observed.

First, this dissertation addresses the chemical degradation of the solid electrolyte interphase (SEI) that can occur during cycling or storage. The results showed that both high temperature and the dissolved manganese ions induced significant deterioration of the SEI layer, which accelerated SEI growth. The main findings of this work were 1) the growth of the SEI at elevated temperatures occurred as a consequence of a competitive mechanism between the precipitation and the dissolution of the SEI layer, and 2) dissolved manganese ions diffused through the porous layer and were deposited mainly in the form of MnF_2 at the inorganic layer and graphite surface regions where the ion-exchange reaction occurred between chemical species of the SEI and the manganese ions, resulting in the deterioration of the SEI layer.

Second, this dissertation addresses the mechanical aspects of the SEI layer, which were investigated by evaluating its elastic properties. Experimental and computational results showed that elastic properties of the SEI layer were strongly dependent on its chemical composition and microstructure (i.e., crystallinity). This result suggested that the importance of having an appropriate chemical composition/structure of the SEI layer in order to prevent its mechanical degradation.

Third, the influence of fluoroethylene carbonate (FEC), which is one of the electrolyte additives, on the performance of Li-ion batteries was evaluated by analyzing the anode's and the cathode's interfaces. While a considerable improvement of performance (such as enhanced capacity and rate capability) was observed at the anode, the degradation of performance at the cathode was severe at elevated temperatures. The adverse effect of FEC was attributed to increases in the amount of dissolved manganese and the thickness of the cathode surface layer, which were caused by an increased concentration of hydrofluoric acid (HF).

Fourth, the influence of the dissolved manganese ions on the structural degradation of graphite was investigated. The DFT calculations predicted that the intercalated Mn ions led to contraction of the interlayer space in graphite, which might cause structural defects or disordering of the graphite. Raman mapping showed that the structural disordering was significant when the dissolved Mn ions were included in the cell. Thus, dissolved Mn ions not only affect the chemical degradation of the SEI layer but also the structural degradation of the graphite.

CHAPTER I.
INTRODUCTION

Li-ION BATTERY RESEARCH: MOTIVATION AND CHALLENGES

Currently, the world faces an increasing demand for renewable and clean energy sources that can substitute for non-renewable fossil fuels. The uneven global distribution of the finite quantities of fossil fuels, the inevitable depletion of fossil fuels in the future, and concerns about environmental issues, such as global climate change, have accelerated the development of sustainable sources of clean energy, such as solar, hydroelectric, thermal, and wind energy sources. Nevertheless, most of these renewable sources are intermittent, which limits their use in many applications. Thus, electrochemical energy storage devices, such as batteries and fuel cells that ensure the efficient conversion of chemical energy into electrical energy as needed, have been referred to as emerging and promising alternative-energy technologies over the last two decades. In particular, batteries are portable and easily can be replaced; they commonly are used in household and industrial applications, and they have attracted considerable interest, perhaps more than fuel cell technology to date [1]. While the technology associated with batteries has made rapid and significant progress over the last decade, there are still issues and technical problems that must be solved in fuel cell technology, such as cost, the size of such systems, durability, air/thermal/water management, and heat recovery [2]. Hence, it

is expected that battery technology will continue to be the primary option in the energy-storage market for many devices and application in the near future.

Among the current battery technologies, Li-ion batteries have become a major component of current research. They are being used to replace lead-acid, Ni-Cd, and Ni-MH batteries because of their high energy density, fairly long life cycle, and fairly good rate-capability [3-5]. Due to these advantages and rapid advances in the technology, Li-ion batteries (LIBs) have captured the portable electronic market, such as cellular phones, laptops, and digital cameras, and they are now being used in the markets of large-scale electric vehicles (xEVs, i.e., all types of electric vehicles, such as hybrid HEV, plug-in hybrid PHEV, and full EV) and energy storage systems (ESSs) [3-5]. According to a recent market forecast of rechargeable batteries conducted by the LG Economic Research Institute (Figure 1.1), the markets for xEVs and ESSs are expected to grow exponentially, and it has been predicted that more than 80% of the LIB market in 2020 will be attributable to these new application sectors [5]. Since the electricity and transportation sectors contribute 60% of the greenhouse gas emission in the U.S., there is no doubt that extensive effort will be devoted to enhancing applications of electric vehicles and energy storage systems [6]. With the emerging markets' demands on large-scale applications, the direction of research and development of LIBs is to pursue higher energy and power densities. Long-term stability, low cost, and safety will be still critical factors for the commercialization of large-scale applications [3].

In the market of electric vehicles, the performance requirements of batteries depend on the types of xEVs. Figure 1.2 shows that the batteries of EVs without gasoline backup require the highest energy density among xEVs, while HEVs and PHEVs are

driven mainly by internal combustion engines with the batteries having a supporting role. Thus, in order to expand the market of EVs, it is critically important to increase the energy density of the batteries further, enabling comfortable, extended-range driving.

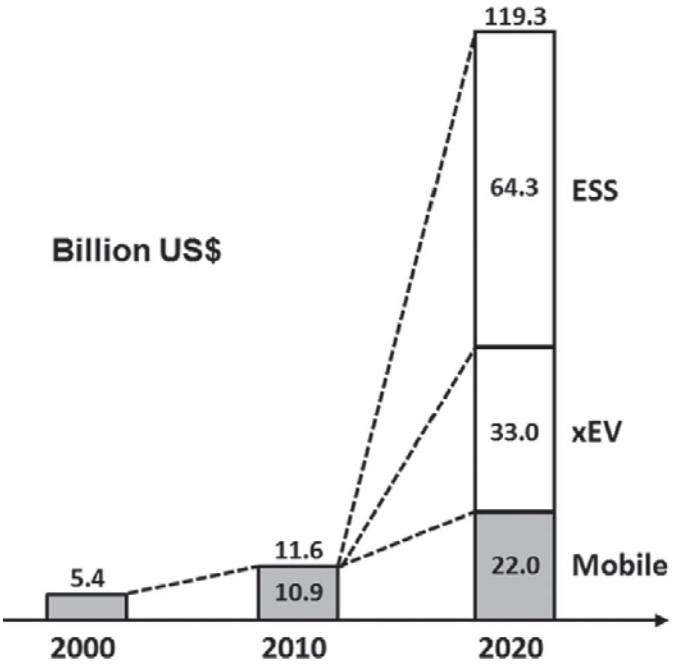

Figure 1-1. A market forecast of rechargeable batteries in the future [5].

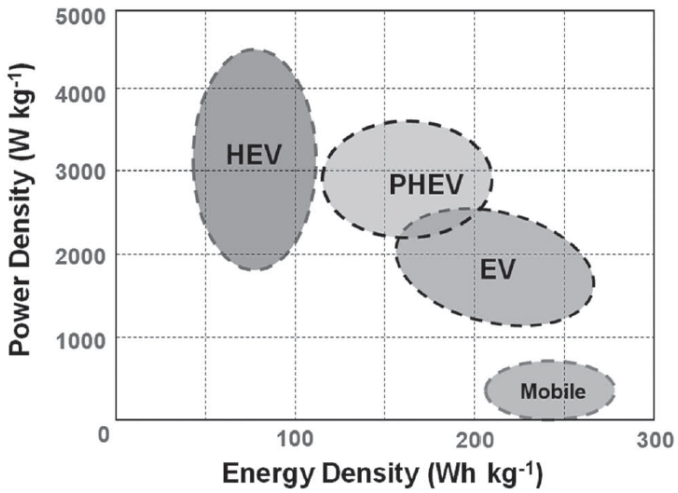

Figure 1-2. Power and energy density requirements of LIBs for xEVs and mobile applications [5].

Although there has been significant progress in Li-ion battery technology, barriers and challenges still remain in many aspects in order to satisfy the requirements of EVs. Table 1.1 shows the typical performance characteristics of various battery systems used in EVs and the United States Advanced Battery Consortium (USABC)'s goals for advanced EV battery systems. There is still a considerable difference between the goals and the current specifications for EVs' battery systems. In particular, significant enhancement of the energy density of the battery system is necessary, and this must be accomplished without compromising other performance characteristics, such as power and lifecycle.

Table 1-1. Comparison between USABC goals of batteries for EVs and current performance characteristics of various battery systems in EVs.

	EV Goals [a]	EV Lead-acid [b]	EV Ni-CD [b]	EV Ni-MH [b]	EV Li-ion [b]	EV Li-polymer [b]
Power density, W/L	1000	400-1000	400	430	429	447
Specific power, W/kg	470	150-400	225	150	350	315
Energy density (C/3), Wh/L	500	90-125	115	165	114	220
Specific energy (C/3), Wh/kg	235	35-50	60	68	93	155
Operating temperature, °C	-30 ~ +52					
Cycle life, cycles	1000	500-1000	2500	600-1200	800 (40 °C)	600
Calendar Life, years	15					
Selling price @ 100K units, $/kWh	125					

[a] USABC goals for advanced batteries for EVs, System level (CY 2020 commercialization).
[b] Typical performance values described in [7]. Values are dependent on the manufacturer.

PRINCIPLES, CURRENT STATUS, AND FUTURE DIRECTION

A battery system is made of an array of electrochemical cells that are connected in series or parallel (or both), depending on the desired output voltage and capacity; the cells are connected in series for higher voltage, and they are connected parallel for higher capacity and current capability [7]. An individual cell consists of a negative electrode and a positive electrode separated by an ionic conducting electrolyte. A thin, porous separator, which is an electronically-insulating material, prevents short-circuiting of the cell by separating the two electrodes, while allowing the flow of ionic charges. Figure 1.3 illustrates the discharge process that takes place in a Li-ion battery to produce electric energy.

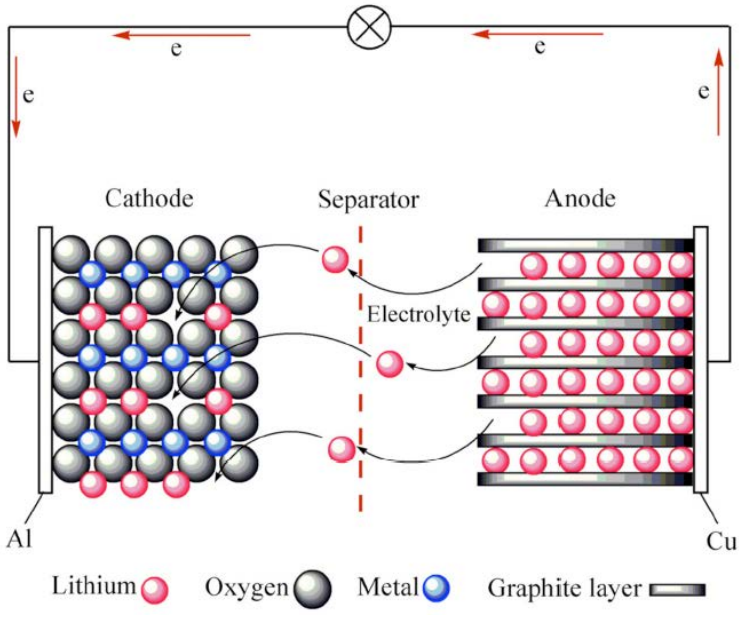

Figure 1-3. A schematic illustration of the discharge process in a lithium ion battery [1].

When the battery is being discharged, i.e., used a source of energy, Li-ions are released from the negative electrode (anodic reaction; oxidation, loss of electrons), and are inserted into the positive electrode (cathodic reaction; reduction, gain of electrons); a

concomitant transfer of electrons take places from the negative to the positive electrode through an external circuit to ensure that charge neutrality is conserved. The electrochemical redox reactions of a C/$LiMO_2$ battery system (M = transition metals such as Mn and Co, C = graphite materials) are described below.

Negative electrode: $Li_xC_6 \rightarrow C_6 + xLi^+ + xe^-$ (anodic reaction; oxidation)

Positive electrode: $Li_{1-x}MO_2 + xLi^+ + xe^- \rightarrow LiMO_2$ (cathodic reaction; reduction)

Overall reaction: $Li_xC_6 + Li_{1-x}MO_2 \rightarrow LiMO_2 + C_6$

When the battery is being charged, the opposite reaction (intercalation of Li-ions into the negative electrode) occurs in the cell. Although an anode is defined as an electrode at which an oxidation reaction occurs (i.e., a negative electrode during when the battery is discharging and a positive electrode when it is being charged), it is common among those in the electrochemistry field to refer to the anode as the negative electrode.

The open-circuit voltage (V_{oc}) of the cell is defined as the difference between the chemical potential of the anode (μ_a) and the chemical potential of the cathode (μ_c):

$$V_{oc} = \frac{(\mu_a - \mu_c)}{e}$$

where *e* represents the charge during the electrochemical reaction. This voltage is limited by either the electrolyte window (E_g) or the top of the anion-p bands of the cathode [8]. As illustrated in Figure 1.4, the electrolyte window refers to the energy gap between a liquid electrolyte's the lowest unoccupied molecular orbital (LUMO) and its highest occupied molecular orbital (HOMO). Reduction of the electrolyte occurs when the electrochemical potential of the anode (μ_a) is located above the LUMO of the electrolyte.

In a similar way, oxidation of the electrolyte occurs when the electrochemical potential of the cathode (μ_c) is below the HOMO of the electrolyte. In typical cathodes, such as layered oxides ($LiMO_2$), the voltage is limited by the top of the O-2p bands because it is located at approximately 4.0 eV below $\mu_{(Li)}$, which is higher than the HOMO of the non-aqueous electrolyte that typically is used in Li-ion batteries (~4.3 eV below $\mu_{(Li)}$) [8]. In the case of anodes, such as graphite and silicon, the electrochemical potential of the anode (μ_a) inevitably is positioned above the LUMO of the electrolyte, resulting in the reduction of the electrolyte. Fortunately, this reduction reaction does not proceed significantly after the 1st cycle, due to the formation of a passivating layer. However, further reduction of the electrolyte is allowed if an intact SEI layer is damaged or broken down during cycling.

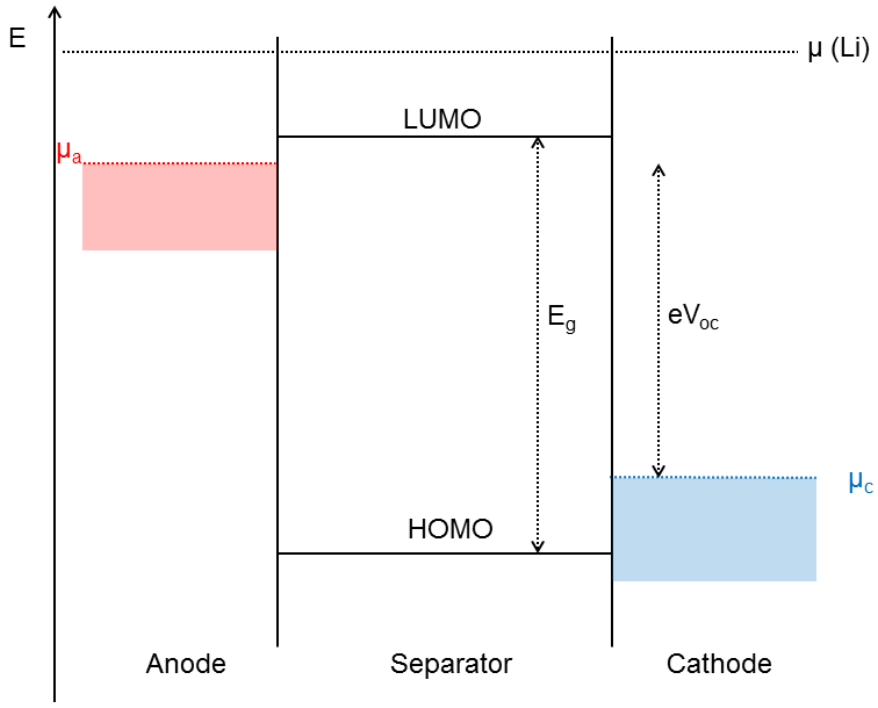

Figure 1-4. A schematic energy diagram of a lithium-ion cell at open circuit condition.

Depending on the capacity of the electrode material and the extent of its operating potential, we can determine the specific energy density (Wh/kg), which is defined as the product of the battery's voltage (V) and the capacity (Ah/Kg) of the electrode. This term is closely related to the driving distance of an electric vehicle. The volumetric energy density (Wh/L) is an important factor considering the limitation of the space available for the battery pack in EVs. Currently, the energy density of a battery is mainly governed by the capacity of the cathode; an increase of 57 per cent in the energy density of a battery can be achieved by simply doubling the capacity of the cathode, while the capacity of the anode needs to be increased by a factor of ten to get a similar increase in energy density (47 per cent) of the battery [3]. Thus, the extensive effort to increase the energy density of the battery system has been focused on the development of cathode materials that exhibit high specific/volumetric capacities as well as high reaction voltage within the electrochemical stability range of the electrolytes [5]. Table 1.2 lists typical cathode materials in Li-ion batteries that are used in many applications, including EVs. Starting with the lithium cobalt oxide ($LiCoO_2$) developed and commercialized by Sony in the 1990s, the first generation of cathode materials, which includes $LiCoO_2$ (LCO) and $LiMn_2O_4$ (LMO), is still used today in Li-ion batteries for various applications. Due to its high structural stability, good rate capability, and excellent cyclability, LCO has been used extensively, and it is still the main cathode material in commercial batteries. However, cobalt (Co) is relatively expensive and toxic, compared with manganese (Mn) and iron (Fe). In addition, the instability of the structure of LCO structure can result in severe degradation of the material and even explosions in the battery system [1]. With the increasing demands for lower cost and better safety, researchers have lost interest in LCO

and have turned to the spinel LMO material. LMO is highly attractive in terms of low cost, good safety, non-toxicity, good stability, and its excellent rate capability. In spite of its relatively low capacity and poor lifecycle at elevated temperatures, this material is considered to be a good candidate for the cathode of batteries in many applications, including xEVs, because of its low cost and good safety. The cost and safety issues are the most important criteria in large-scale applications, since the sizes of the batteries are larger. The problems of dissolution and structural instability associated with LMO have been improved significantly by surface modification and substitution, enabling this compound to be used in commercial xEVs. Another type of cathode is lithium iron phosphate ($LiFePO_4$), which was introduced at the end of the 1990s [4]. Olivine $LiFePO_4$ (LFP) has a crystalline structure with interstitial sites, allowing one-dimensional diffusion pathways for lithium ions. Thus, it exhibits poorer intrinsic ionic conductivity as well as electronic conductivity than layered (LCO) and spinel (LMO) structures. Nevertheless, LFP has attracted the attention of researchers due to its low cost, low toxicity, excellent safety, and good cyclability [11]. With rising concerns about the safety of batteries, it is still considered to be an attractive cathode, since the release of oxygen from the active material is inhibited due to the strong bond of P-O in phosphate in the case of exposure to abnormal conditions, ensuring safe operation [5]. In addition, it is much less thermally active with electrolytes than other cathodes [4]. Currently, LFP is a commercial material with a capacity close to the theoretical value, and it has excellent rate capability; its disadvantages have been overcome by doping with other elements, coating with an electronic/ionic conductive layer, and reducing the sizes of the particles [11].

Table 1-2. Comparison of various cathode materials used in Li-ion batteries [1, 9, 10, 11].

	2D-Layered $LiCoO_2$	3D-Spinel $LiMn_2O_4$	1D-Olivine $LiFePO_4$	2D-Layered NCA	2D-Layered NMC
Theoretical capacity, Ah/Kg	145	148	170		
Practical capacity, Ah/Kg	135-140	100-120	140-170	180-200	160-170
Tap density [a], Kg/L	2.6-3.0	1.8-2.4	0.8-1.4		
Average potential, V vs. Li/Li^+	3.9	4.1	3.45	3.8	3.8
Energy density [b], Wh/kg	546	410-530	518-587	680-760	610-650
Cycle life	500-800	1000-1500	> 3000		
Cost	High	Low	Low	Fair	Fair
Features	High electronic/ionic conductivity Toxic Co Simple process	High electronic/ionic conductivity Moderate safety Several capacity fade at high T Simple process	Low electronic/ionic conductivity Excellent safety Very slow reaction with electrolyte Complex process	High cost of Ni and Co Moderate safety Slow reaction with electrolyte	

[a] The tap density is a measure of the volume fraction of active particles in a cell.
[b] Practical values.

$LiNi_{0.8}Co_{0.15}Al_{0.05}O_2$ (NCA) and $LiMn_{1/3}Ni_{1/3}Co_{1/3}O_2$ (NMC) cathodes have emerged as second generation of cathode materials in Li-ion batteries [4]. As shown in Table 1.2, these layered materials provide relatively higher energy densities than the first-generation materials. The good power density and the high energy density make them for use in electric vehicles. NCA was developed in an attempt to supplement the structural and thermal stability of the $LiNiO_2$ material, and it is commercially available now [5, 9]. However, there are still problems related to safety and cost; the safety concern still exists

due to the release of oxygen at overcharge conditions, and the cost of production cost is still high [5]. The NMC cathode exhibits better rate capability and stability than the NCA cathode. NMC is replacing LCO gradually because of its high specific capacity, enhanced rate capability, and excellent cycleability [5]. Similar to NCA, the safety and cost issues associated with NMC needs to be resolved further before it could be deemed to be suitable for large-scale applications [9].

Nowadays, new cathode materials for future-generation Li-ion batteries are being studied in an attempt to achieve higher energy densities. Promising cathode materials include high-voltage spinel, high-capacity/high-voltage layered oxide, and high-voltage/high-capacity polyanion cathodes [10]. Table 1.3 summarizes the technical challenges that must be overcome before these new materials can be considered to be viable candidates for use as cathodes.

Table 1-3. Various cathode materials with high-voltage and high-capacity [4, 5, 10, 12].

Materials	Voltage (V)	Capacity (mAh/g)	Main issues
Spinel $LiMn_{1.5}Ni_{0.5}O_4$	~ 4.7	~ 147	• Formation of a $Ni_{1-x}Li_xO$ impurity phase and chemical instability of the interface at high voltage
Layered $[Li_2MnO_3]_x[LiMO_2]_y$	~ 4.5	~ 250	• Irreversible capacity loss of 40-100 mAh/g in the first cycle • Poor rate capability
Olivine $LiMnPO_4$ $LiCoPO_4$ $LiNiPO_4$	~ 4.1 ~ 4.8 ~ 5.2	~ 167	• Low electronic and ionic conductivity • Significant side reactions at high voltage
Orthosilicates Li_2FeSiO_4 Li_2MnSiO_4		~ 330	• Difficulty in synthesizing phase-pure material • Low electronic conductivity

Since the capacity of commercial batteries is currently limited by the capacity of the cathode, significant effort has been directed toward improving the cathode to enhance its voltage and capacity. Despite the fact that the cathode has a significantly higher

impact than the anode in increasing the energy density of the cell, alternatives to graphite anodes still need to be identified in order to provide new opportunities for the commercialization of advanced Li-ion batteries that are suitable for large-scale applications. Current and promising anodes for Li-ion batteries can be categorized into three different types according to their energy storage mechanisms, i.e., intercalation-based, alloying reaction-based, and conversion reaction-based materials [5].

The intercalation-based anodes include natural graphite, artificial graphite, and $Li_4Ti_5O_{12}$ (LTO). Among the carbon materials (theoretical capacity 372 mAh/g), natural graphite (NG) is one of the most extensively used. While natural graphite is attractive in terms of its cost, artificial graphites, including hard carbons (HCs) have attracted significant attention because they have higher capacity and rate capability than natural graphite [5]. The graphite materials have an operating voltage close to that of Li/Li^+, resulting in the decomposition of the electrolyte in the first cycle. As a consequence, an irreversible capacity loss (~10%) occurs by forming a passivating layer on the surface of the graphite. Since graphite materials exhibit high irreversible capacity loss, lithium plating/dendrite formation, and safety hazards, LTO (especially, nanostructured LTO) has emerged as a potential candidate for use as an anode material, because it provides excellent safety, rate capability, and cyclability. LTO has a volumetric change of less than 0.2%, which is superior to that of graphite (10% volume expansion/contraction), thereby guaranteeing structural stability during long-term cycling. However, its low capacity (175 mAh/g) and its high operating voltage (1.5 V vs. Li/Li^+) limit its use for large-scale applications.

With the significant progress in research and development on alloying reaction-based anodes, it is believed that this type of material is the most promising alternative to graphite anodes. In particular, considerable research and assessment efforts have been directed at tin-based (Sn-based) and silicon-based (Si-based) materials for high-capacity anodes [12]. A pure Si anode has an extremely high theoretical capacity of 4200 mAh/g, while a pure Sn anode possesses a theoretical capacity of only 960 mAh/g [12]. More importantly, Si is much more abundant than Sn. Some of these materials are favored because they are safer than others, and they have operating voltages above that of Li/Li^+, thereby avoiding lithium plating [10]. The major issue with the alloying reaction-based anodes is the huge volume change that occurs during alloying/de-alloying process, destroying the integrity of the active material. As a result, severe loss of capacity occurs within a few cycles. Several approaches have been considered to overcome the problems induced by very large expansions and contractions of volume, i.e., (1) the synthesis of nano-sized metal particles, (2) the addition of a buffer phase into metals, and (3) the use of an appropriate binder. Various Sn/C, Sn/M/C, (M = Ti, V, Cr, Mn, Fe, or Co), SnO_2, SnO_2/C, and Si/C composite materials are being studied based on the above strategies as an effort to identify materials suitable for use as advanced anodes in Li-ion batteries with high energy density.

Conversion reaction-based materials are usually made of nanoparticles of transition metal oxides (MO, where M is, e.g., Co, Ni, Cu, Fe, or Mn). In spite of the high capacity of these materials (600-1200 mAh/g), severe barriers still prevent them from being a potential candidate for anodes in Li-ion batteries [4, 5, 12].

Diverse efforts are underway in the academic and industrial communities looking beyond Li-ion battery technology, including Li-based batteries (Li-S and Li-air) and non-Li-based batteries (Zn-air, Mg/S, and Ni-ion batteries), which might provide new opportunities for enhancing the future of battery technology.

DEGRADATION MECHANISMS OF Li-ION BATTERIES

The success of the commercialization of large-scale applications, such as electric vehicles (xEVs) and energy storage systems (ESSs), not only depends on increases in energy and power densities but also enhanced lifecycle of a battery. While portable devices require battery cells that can operate well for at least 3-4 years (equivalent to about 500-1000 cycles), the life of Li-ion batteries for xEVs and ESSs should be reach over 3000 cycles and at least 10 years [5]. However, the reliability of Li-ion batteries in terms of long lifetime and safety becomes more problematic, especially in xEVs and ESSs since the battery system can be exposed to diverse environments, e.g., extremely low and high temperatures, voltages, and currents, which could accelerate the degradation of the battery. Extreme conditions can occur over time, resulting in the significant deterioration of the battery's power capability and useful capacity. As systematically described by Vetter *et al.*, the processes of the battery's degradation (i.e., decreasing capacity and power) have several causes, some of which can interact with others, exacerbating the situation. Since these causes and their interactions depend on many factors, it is difficult to predict precisely the degradation of the battery. The complexity and interdependence of the degradation mechanisms of the battery was illustrated nicely by C. Birkl, as shown in Fig. 1.5. [14].

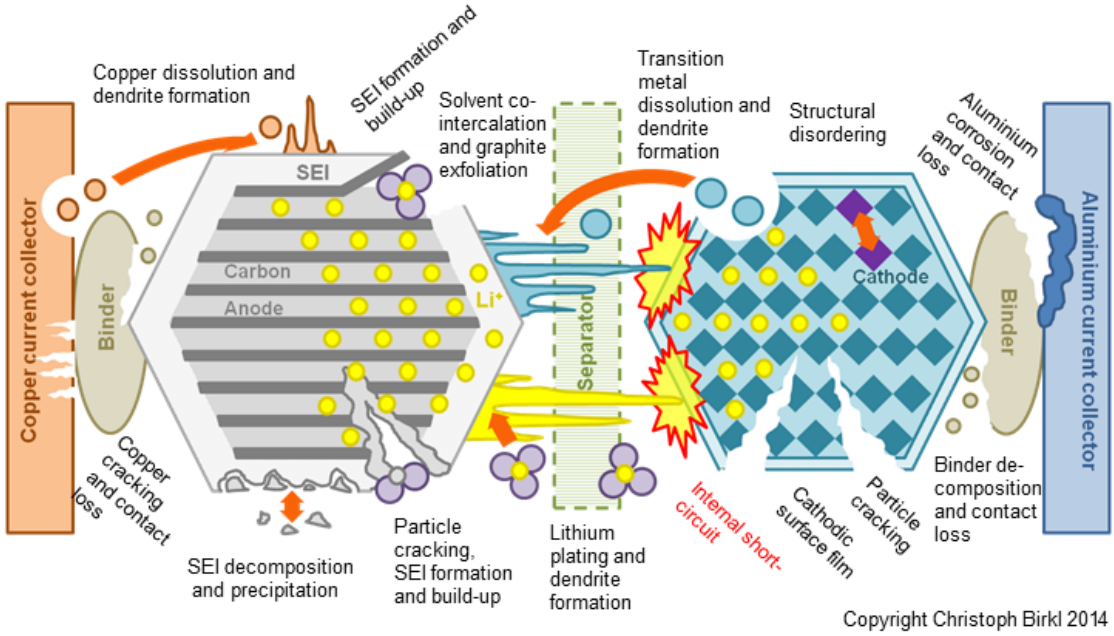

Figure 1-5. A schematic illustration of various degradation mechanisms that occur in a Li-ion battery [14].

Based on the fact that the degradation mechanisms are strongly dependent on the materials for the anode and cathode as well as the electrolytes used, the degradation mechanisms that are introduced in this section are presented with a general perspective in mind. Basically, the origins of degradation mechanisms can be either chemical or mechanical processes, and they can occur in three different regions, i.e., the active material, the composite material, and the electrode/electrolyte interface [13, 15]. Since the electrode/electrolyte is known as the most important component in a Li-ion battery and is the subject of this dissertation, this topic is addressed separately in the section below [13, 15, 16].

The typical problems in active materials are mainly attributed to structural changes, cracking, and loss of active materials. For instance, graphite undergoes ~10% of

expansion/contraction in volume during cycling, which can induce mechanical stress on defects and C-C bonds. In addition, solvent co-intercalation and gas evolution can contribute to mechanical stress on graphite particles, resulting in cracking or related structural damage (such as graphite exfoliation/delamination). The structural damage leads to the exposure of new graphite surfaces so that more decomposition of the electrolyte occurs to form a passivating layer by consuming additional lithium ions. Eventually, these lead to losses in capacity due to the loss of the active material and the loss of lithium.

Similar processes also occur at the cathode. Phase transitions and intercalation-induced structural changes can lead to distortion of the crystal lattice and additional mechanical stress [13]. Also, the dissolution of the transition metal that occurs at the cathode is closely related to the structural instability of the active material. A representative example is the $LiMn_2O_4$ (LMO) material. LMO undergoes structural changes and the dissolution of Mn due to the Jahn-Teller distortion of Mn^{3+} and a disproportionation reaction ($2Mn^{3+} \rightarrow Mn^{4+} + Mn^{2+}$), respectively, at a low state of charge. It is evident that the Jahn-Teller distortion causes severe structural changes; the inhomogeneity of a crystal structure developed by the Jahn-Teller distortion leads to microscopic cracks in the particles as well as the degradation of the crystallinity of LMO [5]. Although the spinel structure of LMO does not change due to the dissolution of Mn, it is known that the vacant manganese sites due to this dissolution are replaced by lithium ions, thereby forming a disordered, lithium-rich spinel or a defective spinel with Mn^{4+} (such as Li_2MnO_3 and $Li_4Mn_5O_{12}$) [11, 13]. At the medium to high charge state (i.e., the delithiated state), thermodynamic instability of the delithiated lithium manganese spinel

takes place, and the dissolution of manganese ions is caused by reaction with hydrofluoric acid (HF) [13]. As a consequence, a considerable loss of capacity and power occurs due to the loss of the active material that originates mainly from the dissolution of the transition metal.

Another reason for the degradation of the battery degradation is the composite electrode. In both the anode and the cathode, the loss of contact in the composite electrode results in an increase in cell impedance. Both volume and structural changes could lead to change in the porosity of the electrode and contact loss (1) between particles of the active material, (2) between current collector and particle, (3) between binder and particle, and (4) between binder and current collector [13]. In addition, the decomposition of the binder and the corrosion of the current collector induced by reactivity with electrolyte, electrochemical potential, and temperature can contribute to the degradation of a battery, leading to loss of electronic/mechanical contact between the current collector and the active material. Finally, gas evolution due to the electrolyte's decomposition can be partially responsible for cracking of the active material during cycling. Figure 1.6 illustrates the degradation mechanisms of cathode materials that are discussed here.

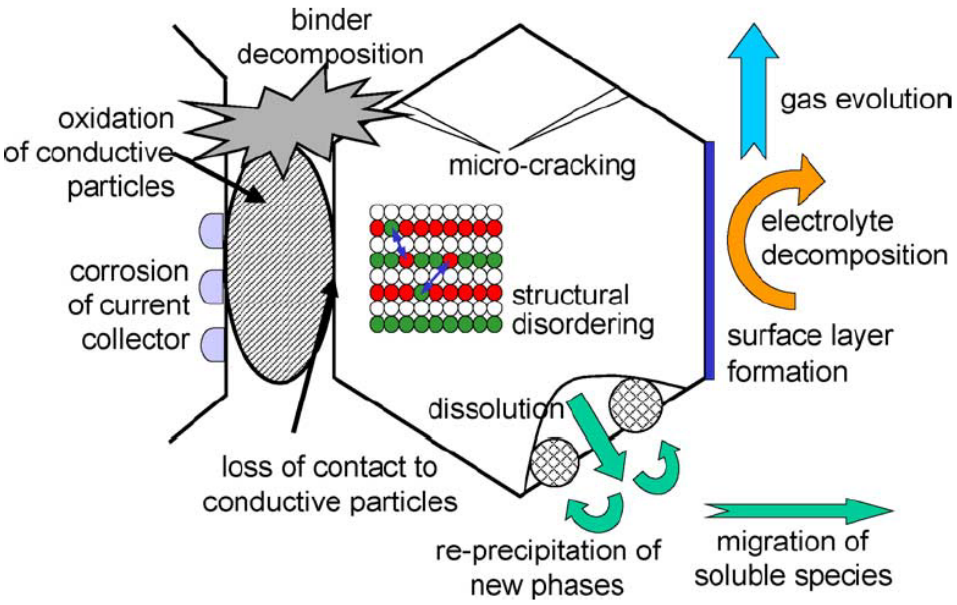

Figure 1-6. Overview of the degradation mechanisms that occurs at a cathode [13].

ELECTRODE/ELECTROLYTE INTERFACE: IMPORTANCE, CHEMISTRY, AND PROPERTIES

Among many degradation mechanisms, electrode/electrolyte interfaces that form at both anode and cathode are primarily responsible for the losses of capacity and power of a battery. It is well known that the electrode/electrolyte interface is associated closely with the reversibility of Li-ion intercalation, which determines the kinetics of the cell's overall reactions [17].

The anode/electrolyte interface, known as the solid electrolyte interphase (SEI), has been a topic of interest during the past decade. In spite of extensive efforts, many issues are still being debated, which makes it difficult to understand the nature of the SEI. That is why Winter *et al*. introduced the SEI as "the most important but least understood component" in a Li-ion battery [18]. This is probably due to the dynamic nature and instability of the SEI layer, which is in contrast to the initial belief that the SEI layer had

static and stable properties. Understanding and dealing with interfacial issues are still complex and challenging due to the characteristics of the SEI layer and the limited number of tools available for *in-situ* characterization.

The cathode/electrolyte interface has generated far less interest among researchers than the anode/electrolyte interface in spite of its significant effect on the battery's performance. Unlike the SEI layer that forms on the anode, it is doubtful that the surface film on the cathode serves as a protective or passivating layer; this is the reason the cathode/electrolyte interface is sometimes called the cathode surface layer or the solid permeable interface (SPI) [19]. It is known that the cathode interface does not effectively protect the cathode from the electrolyte because of the oxidizing environment close to the cathode, allowing for a continuous oxidation process at the surface [19]. As a result, it is common that the interfacial impedance of the cathode tends to increase as the number of cycles increases, and the cathode/electrolyte interface governs the overall impedance of the cell at a certain point [20]. In particular, the interfacial impedance of a cell increases considerably during cycling at high voltage and high temperature. The increased resistance of the cell can reduce the battery's performance in terms of rapid charge and discharge; because of the cell's resistance, polarization is developed in proportion to the current [5]. With the increasing interest in the emergence of 5V-class cathode materials, more emphasis will be placed on the cathode/electrolyte interface, which will have a critical role in the high-voltage battery system.

Anode/electrolyte interface

The SEI layer is formed mainly due to the irreversible reduction and decomposition of the electrolyte during the initial few cycles. It is widely accepted that

the onset potential of SEI formation is around 0.7 V (vs. Li/Li^+). The large irreversible loss in capacity that occurs during the first cycle is attributed to the formation of the SEI layer. This SEI layer consists of various decomposition products that originate from the solvent reduction process, either by one-electron or two-electron transfer, and the salt reduction process initiated by anodic polarization [21]. Despite the fact that the reduction products depend on the electrode materials, salts, and solvents of the electrolyte, the most common species produced from the electrolyte include inorganic, organic, and polymeric species, such as LiF, Li_2CO_3, Li_2O, $ROCO_2Li$, $(CH_2OCO_2Li)_2$, and polyethylene oxide (PEO). Details on the possible reduction mechanisms and pathways have been summarized well in many articles [17, 21, 22, 23]. The decomposition species form the SEI layer, which consists of two distinct layers, i.e., a thin, dense layer of inorganic species close to the electrode side and a thick, porous layer of organic and polymeric compounds close to the electrolyte side, as shown in Figures 1.7c and 1.7d. According to Yan *et al*. the formation and evolution of the two-layer structure of the SEI layer can take place in the following steps: (1) At 1.4 V (vs. Li/Li^+), there is no electron transfer between the electrode and the electrolyte; only the electrophilic reaction of PF_5 with EC and DMC molecules might occur, (2) At 1.4-0.55 V, lithium-cation-coordinated EC, DMC, and water molecules near the surface of graphite undergo one-electron reduction, producing solvated lithium radical cation intermediates, (3) At 0.55-0.2 V, the lithium-cation-coordinated solvents undergo further one- or two-electron reduction to form initial solid species, followed by the reaction of strong HF with the initial species, forming LiF and other species, (4) the intercalation of lithium ions into graphite becomes most favorable below 0.2 V; solvent molecules cannot get electrons through the electrode due

to the passivation layer that is formed. The SEI layer that is formed is believed to be ionic-conductive to lithium ions, but not conductive to electrons; thereby, the layer kinetically prevents further decomposition of the electrolyte unless it loses its effectiveness. Depending on the stability or the effectiveness of the SEI layer that is formed, the charge/discharge reversibility that leads to long-term cyclability is determined; thus, the properties of the SEI layer should be emphasized.

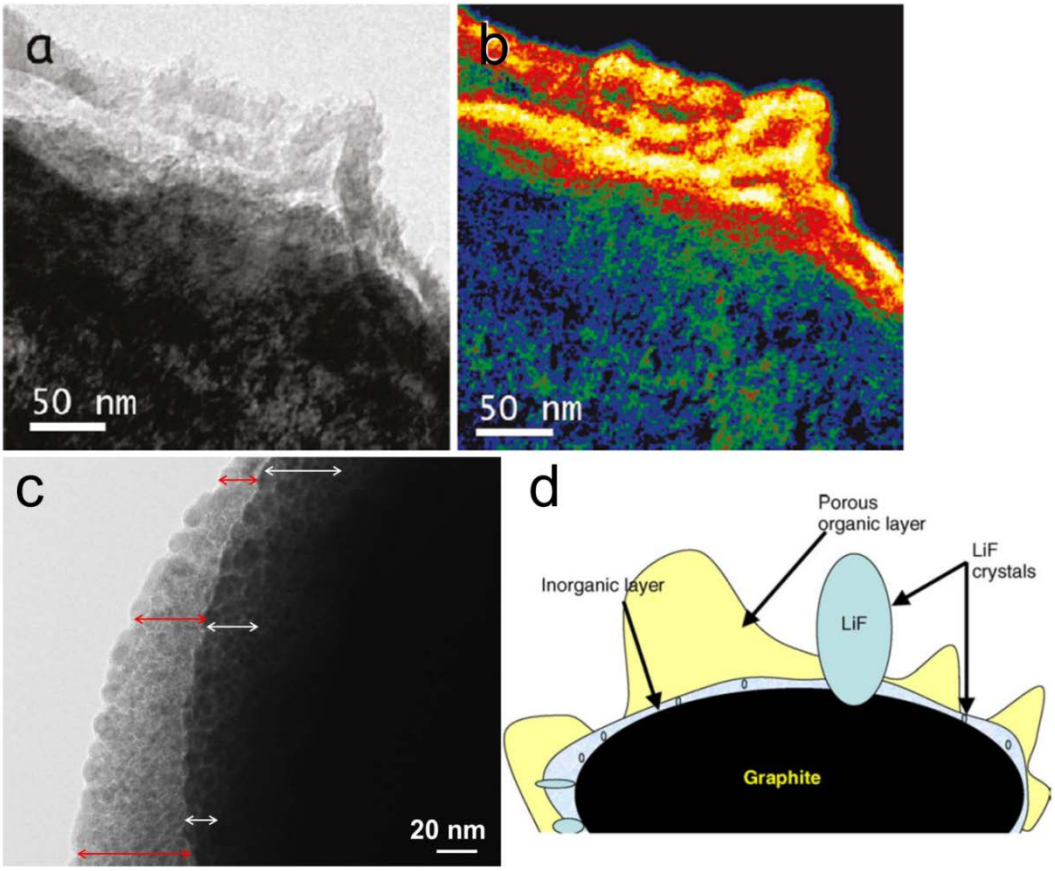

Figure 1-7. Morphology of the SEI layer that is formed on graphite: (a) TEM image of synthetic graphite (Alfa-Aesar) after lithiation to 10 mV and (b) its corresponding mapping of Li concentration [24]; (c) TEM image of Timcal SLP-30 graphite after cycling (by L. Liu); (d) a proposed schematic illustration of the SEI layer [25].

The SEI's morphology, including thickness, porosity, and uniformity, is considered to be a key factor in determining whether the SEI layer is effective and robust.

The morphology is strongly dependent on the salt, solvent, and graphite materials that are used; sponge-like, gel-like, and island-like films have been reported [21]. As illustrated by K. Edstrom *et al*., LiF is believed to distribute extensively throughout the SEI layer as a form of isolated crystallites (Fig. 1.7d) [25]. It is known that the SEI layer covers both the edge and basal planes of the graphite, as demonstrated by F. Wang *et al*. using Li concentration mapping (Fig. 1.7b). However, the SEI layer formed on the basal planes differs from the layer formed on the edge planes; the SEI layer on the basal planes is rich in organic compounds and relatively thinner than the SEI layer on edge planes, which contains abundant salt-reduction products (such as LiF and Li_2CO_3) [26]. The SEI layer can be described by a 3D-model, as proposed by Besenhard *et al*. [27]. They suggested that lithium-coordinated solvent molecules co-intercalate into the graphene layers to form a ternary graphite intercalation compound, and this model is generally accepted in the Li-ion battery community.

The thickness of the SEI layer has been a major topic of interest since the kinetics of the transfer of Li-ions at the interface is believed to be affected significantly by the thickness of the SEI layer. Figure 1.7 shows that the thickness of the SEI layer has been observed to be in the range of tens to hundreds of nanometers. The wide range of SEI thicknesses is mainly due to 1) the non-uniformity of the SEI (Fig 1.7c); 2) different graphites, electrolytes, and cycling; and 3) different measurement techniques. A thicker SEI layer increases the interfacial resistance at the anode and, hence, has critical influence on rate capability of a battery. Due to increase in the interfacial resistance, the available capacity can be reduced. However, recent studies have shown that not only the thickness of SEI but also the breakup of the lithium solvation sheath make significant

contributions to the diffusion of Li ions across the interface, which affects the interfacial impedance. As shown in Figure 1.8, K. Xu *et al*. claimed that the interfacial impedance, known as the combination of the so-called charge transfer and SEI resistance, is attributed to the de-solvation process of lithium ions, followed by diffusion/migration of the de-solvated Li ions through the SEI layer [28, 29]. Thus, facilitating the breakup of the Li-ion solvation sheath at the interface is another important factor in determining the kinetics of Li-ion transfer at the interface. It suggests that the composition and structure of the SEI should be formed or designed to facilitate the Li-ion de-solvation process in order to reduce the interfacial impedance at the anode.

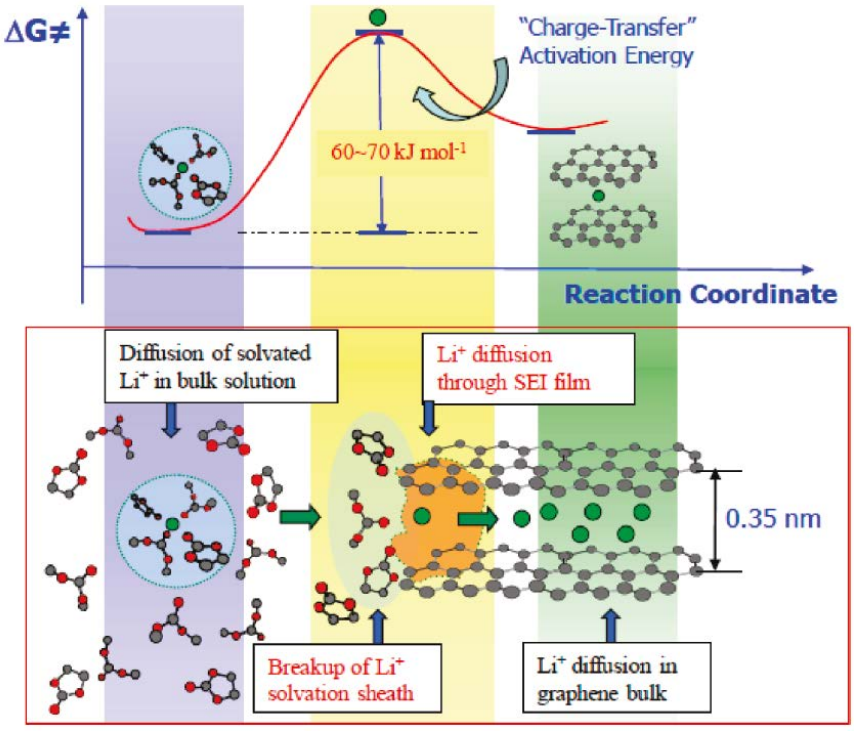

Figure 1-8. A schematic description of Li-ion transfer at the graphite/electrolyte interface [29].

Cathode/electrolyte interface

Unlike the SEI layer on the anode, the formation of the cathode surface layer does not occur during the initial cycles; rather, it tends to proceed gradually as the number of cycles increases, especially at high temperatures. Thus, in long-term cycling, the interfacial impedance is increased to a far greater extent at the cathode interface than it is at the anode interface. As shown in Figure 1.9a, it has been suggested that the cathode surface layer consists of organic and polymeric species, rather than inorganic species at the innermost part of the layer (close to the electrode), which differs from the SEI layer on the anode [30]. This different composition might deteriorate the passivation ability of the cathode film, allowing continuous reactions with the electrolyte. As shown in Figure 1.9b, the cathode surface layer typically ranges from a few nanometers to tens of nanometers. In spite of the relatively thin surface film, the impacts of the cathode interface on the battery's performance are very significant, demonstrating that the thickness and the morphology (such as porosity and uniformity) are critical to the reversibility of Li-ion intercalation. In a recent study, it was suggested that the less-compact or less-dense surface film that forms without an additive might contribute to greater dissolution of Mn [31]. Similar to the SEI layer, the thickness is dependent on the number of cycles, temperature, the cathode material, and the electrolyte.

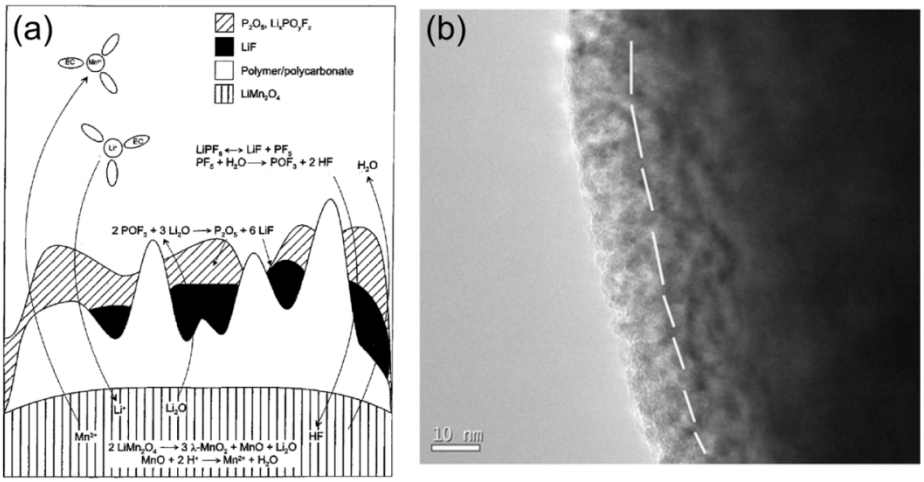

Figure 1-9. The surface layer that is formed on LMO cycled at elevated temperatures: (a) A schematic model [30] and (b) TEM image [31].

While it is generally believed that the cathode film is due to spontaneous reactions with the electrolyte, there is still a lack of understanding of the mechanisms involved in the formation of the cathode surface layer. Aurbach *et al*. summarized the possible reactions of the Li_xMO_y materials with the electrolyte at the cathode as follows: (1) acid-based interactions between the Li_xMO_y and HF, (2) nucleophilic attack of the electrophilic alkyl carbonate molecules by oxygen ions on the transition metal oxide, (3) surface-induced polymerization of cyclic alkyl carbonates to polycarbonates, and (4) redox reactions with the species in solution [32].

DEGRADATION OF THE ELECTRODE/ELECTROLYTE INTERFACE

Instability of the SEI layer: Chemical aspects

Since the graphite anode operates beyond the thermodynamic stability window of the electrolyte, further electrolyte decomposition can occur unless the SEI layer is stable. The initially accepted belief, i.e., that the SEI layer that is formed during initial cycles is

stable and maintains its passivation effect during prolonged cycling, is now largely discredited among many researchers. Rather, the parasitic reactions between the electrolyte and the electrode are ongoing during long-term cycling at a lower extent and at a lower rate, as demonstrated by the Dahn group using their high-precision coulometry technique [33]. The degradation of the SEI is attributed mainly to the chemical instability of the layer. As illustrated in Figure 1.10, the chemical degradation of the SEI layer does not originate from one single source, but from a number of processes and their interactions. Because of this, the SEI layer does not retain its original properties, which might be desirable for Li-ion transfer, and it is converted into a chemically-degraded or defective SEI layer. To date, the main causes of the degradation of the SEI are elevated temperatures and the deposition of transition metal ions, especially manganese.

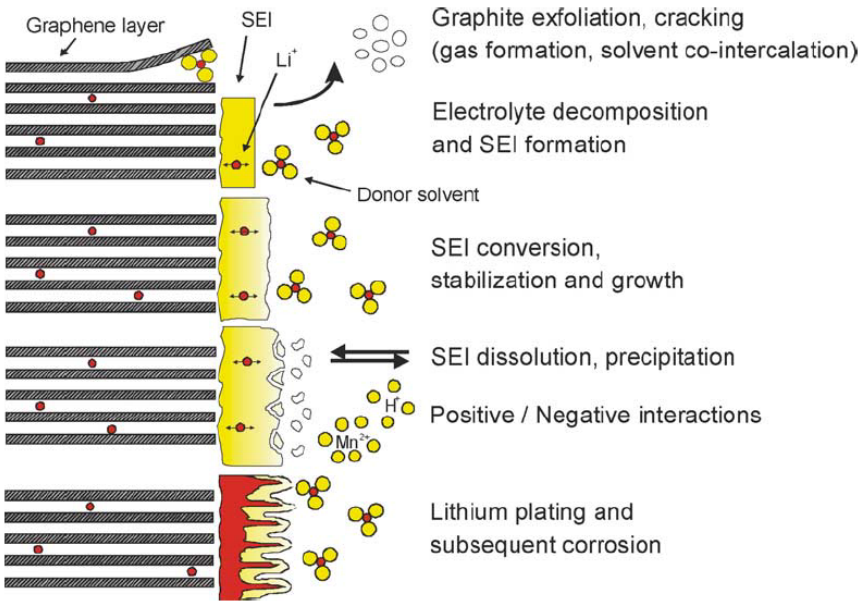

Figure 1-10. The degradation mechanisms that occur at the graphite/anode interface [13].

At elevated temperatures, the chemical instability of the SEI layer is pronounced, leading to additional decomposition of the electrolyte. As summarized in Table 1.4, it seems that SEI dissolution and growth occur simultaneously at elevated temperatures.

Table 1-4. SEI Growth or dissolution phenomena at elevated temperatures.

Techniques	Cells	Growth Vs. Dissolution	Observation	Ref
XPS	Li/C	Growth	After storing at 60 ºC for 7 days, the intensity of the graphite decreased	34
EIS	Li/C	Growth	After 8 days at 70 ºC storage, the film resistance increased	35
HRTEM	Li/C	Growth	After 1st cycle at 40 ºC, followed by 3 cycles at 20 ºC, thicker SEI layer was observed	36
XPS/FTIR	MCMB	Growth	After 4, 7, 10 days at 85 ºC storage, more decomposition products and the thicker surface film were observed	37
DSC	Li/C	Dissolution	The temperature-induced degradation of the SEI layer occurred first at 120-140 ºC	38
In-situ AFM	Li/HOPG	Dissolution	After 12h storage at high temperatures, the thickness of the SEI layer increased at 45 and 60 ºC, but decreased at 80 ºC	39
C80 calorimeter	Li/C	Dissolution	The metastable compounds in SEI film broke down when the temperature reached 61 ºC	40
IR microscopy	LNCO/C	Dissolution	After cycling the cell at 70 ºC for 2 weeks, IR spectroscopy detected no SEI remaining on the anode surface	41

It is believed that some of the SEI's species are dissolved thermally, decomposed, or converted; thereby, a portion of the anode's surface can be exposed locally to the electrolyte, so that additional formation of the SEI layer can contribute to its growth [34-41]. For instance, it has been reported that metastable organic SEI species, such as lithium alkyl carbonates, can be transformed to more stable inorganic species, such as Li_2CO_3 and LiF, at elevated temperatures. In addition, it has been suggested that the increased acid compounds, such as HF, can react with some of SEI species, forming other

SEI species. Because of these reactions, the SEI layer eventually grows, and the accumulated SEI species can decrease the pore size in the SEI layer, which contributes to a sluggish Li-ion transfer at the interface [21]. Conversely, low temperatures cause different types of parasitic side reactions, such as lithium plating and dendrite growth, possibly due to the sluggish diffusion of Li ions or trapped solvated Li ions at the interface between the anode and the electrolyte [13, 21].

Another origin of SEI instability is the transition metal ions that are dissolved from the cathode. The dissolved metal ions are transported to the anode where they deposit as various forms of chemical compounds, influencing both the chemical degradation of the SEI layer and the self-discharge of the lithiated graphite. The deposited metal ions might modify the original SEI layer to a defective SEI layer that cannot suppress further decomposition of the electrolyte. A representative example is the dissolved manganese ions that are released from the LMO cathode. Figure 1.11 shows that the Mn nanoparticles exist on the basal plane of the graphite and are surrounded by the SEI layer. These Mn nanoparticles can serve as a catalyst to accelerate the decomposition of both the SEI layer and the electrolyte [42, 44]. Although no agreement has been reached regarding the chemical state of the deposited Mn compounds, it seems that metallic Mn nanoparticles, MnF_2, and Mn oxides could be deposited on the anode, as shown in Figure 1.11c. As a consequence, the deposited metal compounds can hinder the reversibility of Li-ion intercalation.

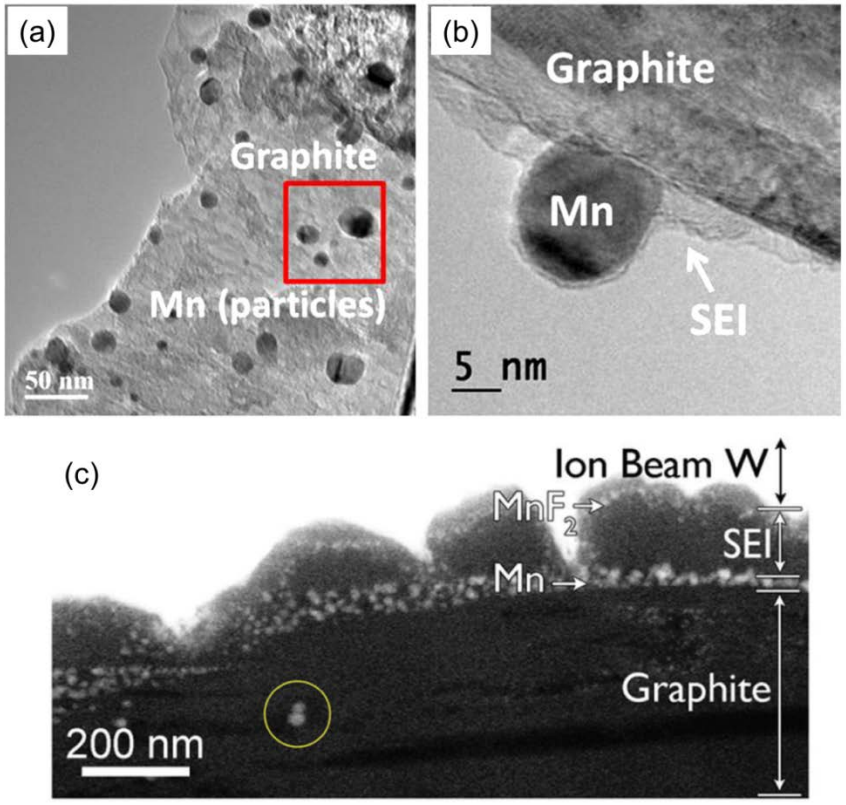

Figure 1-11. TEM images of the deposited Mn compounds on the graphite anode: (a) randomly distributed Mn nanoparticles, (b) Mn nanoparticles covered by the SEI layer, and (c) MnF_2 nanoparticles and metallic Mn nanoparticles on the surface of the graphite and a Mn nanoparticle inside the graphite [42, 43].

Instability of the SEI layer: Mechanical aspects

There have significantly fewer studies conducted to understand the mechanical degradation of the SEI layer than there have been to study its chemical degradation. This is not because it is of less importance; rather, it is because there has been less interest in the mechanical instability of the SEI layer than in the cracks or fractures of electrode particles, and there has been a lack of understanding of the mechanical degradation of the SEI layer. With the increasing interest in high-energy density anodes, such as Si, Co_3O_4, and SnO_2, many researchers are focusing their attention and their research on the mechanical degradation of both the anode and the SEI layer, because these types of

anodes undergo severe mechanical degradation resulting from lithiation-induced volume expansion and electrode pulverization. Repetitive volume changes during lithiation/delithiation are expected to cause fatigue stresses of both the anode and the SEI layer, which lead to fractures or cracks of both the anode and the SEI layer. The mechanical degradation induced by cracks or fractures in the SEI layer and the anode is closely coupled with the chemical degradation of the SEI, since additional decomposition of the electrolyte occurs on the exposed surface of the graphite through cracks or fractures, which results in additional loss of capacity.

It is believed that the SEI layer and the SEI/graphite region are affected significantly by the generation of stress. It has been reported that compressive and tensile stresses occur at anodes, such as graphite and Si materials, during lithiation and delithiation, respectively [45, 46]. The development of these stresses is associated mainly with the formation of the SEI layer and related phenomena, which can lead to the mechanical disintegration or mechanical instability of the SEI layer [46-48]. Mukhopadhyay *et al*. explained the generation of compressive stress during the formation of the SEI layer by using a nucleation-growth mechanism, as shown in Figure 1.12. The stress in the SEI layer is in the range of 218 MPa to 1 GPa, based on the assumption of the SEI layer that is approximately 100 nm thick [46-48]. These values are relatively high for the SEI layer that consists of soft organic/polymeric species and stiff inorganic components; thereby, large compressive stress in the layer can lead to buckling and delamination failures [47]. In addition, the observation that partial delamination of the graphite anode that occurs near the SEI/graphite interface also supports the conclusion that stress is localized largely in the SEI/graphite region, where there is a high possibility

of mechanical damage [49]. The gas evolution during the formation of the SEI layer also can contribute to the mechanical instability of the SEI layer.

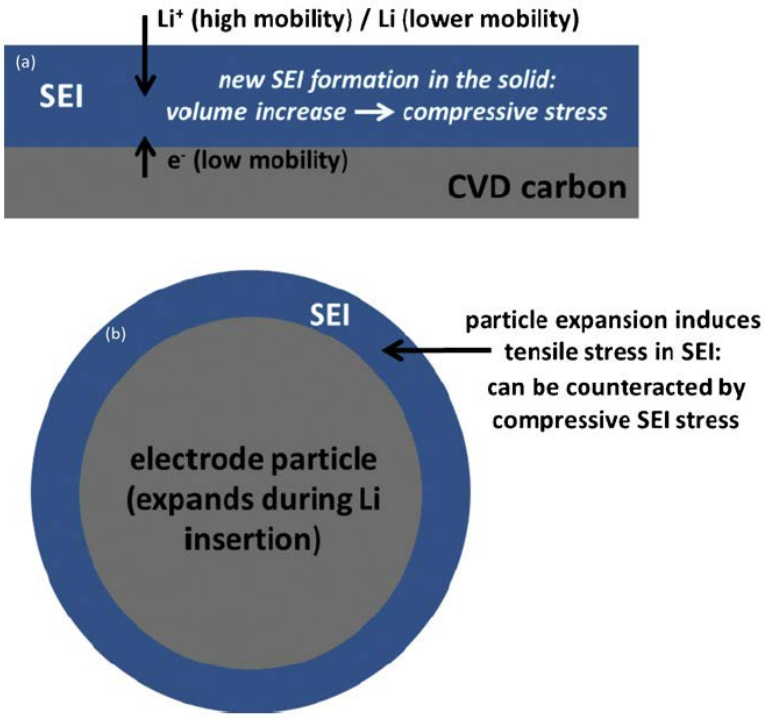

Figure 1-12. A schematic illustration of the formation of the SEI layer and the concomitant compressive stress that is generated in the SEI layer: (a) thin film electrode and (b) a particle of the graphite anode [47].

Instability of the cathode/electrolyte interface

Although the current cathode materials operate at potential voltages that are within the thermodynamic stability limits of the electrolytes, there has been significant evidence that cathode materials undergo spontaneous reactions with solvents, salts, and impurities, such as HF, indicating the instability of the cathode/electrolyte interface. This is why the formation of the surface film on the cathode tends to increase as the number of cycles and the storage time increase. At room temperature, the kinetics of the reactions on the surface of the cathode proceed at a slow rate and to a low extent. However, at

elevated temperatures, the kinetics of the reactions are accelerated, and the instability of the cathode/electrolyte interface becomes significant, leading to a considerable increase in the thickness of the surface layer, followed by an increase in the interfacial resistance at the cathode. The mechanisms by which the surface layer is formed remain less clear than those of formation of the SEI layer at the anode. This is because various processes are involved and interacted with each other during the formation of the surface layer at the cathode. For instance, the formation of the layer that forms on the $LiMn_2O_4$ cathode involves the following coupled reactions: (1) reactions of $LiPF_6$ decomposition products driven by the disproportionation process at the lithiated state, (2) electrolyte oxidation reaction coupled to insertion of Li ions at the delithiated state, and (3) electrolyte oxidation reaction coupled to a loss of oxygen from the spinel structure at the delithiated state [50]. The oxidation of the electrolyte at the surface of the cathode can be facilitated as a consequence of these coupled reactions, although the cathode operates within the thermodynamic stability limits of the electrolytes.

With increasing interest on high voltage cathodes, such as $LiCoPo_4$ (4.8 V), $LiNiPO_4$ (5.1 V), $LiCoPO_4F$ (4.9 V), and $LiNi_{0.5}Mn_{1.5}O_4$ (4.6 V), the issue regarding the instability of the cathode/electrolyte interface, which is an important problem, must be addressed further on the basis of the general consensus concerning the oxidative decomposition of the electrolyte above 4.5 V.

SCOPE OF THIS DISSERTATION

The aim of this dissertation was to elucidate the degradation mechanisms at the electrode/electrolyte interfaces in Li-ion batteries in order to understand how the

degradation processes at the interfaces are correlated with the loss of capacity and power in a battery. In particular, various degradation mechanisms of the electrode/electrolyte interfaces occurring at elevated temperatures were investigated and proposed using various experimental techniques and atomistic simulation tools.

The chemical instability of the SEI layer induced by elevated temperatures is discussed in Chapter 2. The degradation of the SEI layer at elevated temperatures was demonstrated based on the observations of changes in the thickness and chemical composition of the SEI layer and changes in the interfacial impedance at the anode. The mechanisms of SEI growth at elevated temperatures were suggested based on the results of electrochemical impedance spectroscopy (EIS). Chapter 3 describes the chemical degradation of the SEI layer induced by dissolved manganese ions, which was thoroughly investigated by artificially introducing soluble Mn ions into the electrolyte. In order to gain in-depth understanding of the influence of dissolved Mn ions on the degradation of the SEI, the chemical composition and the thickness of the SEI layer were determined using X-ray photoelectron spectroscopy (XPS) and atomic force microscopy (AFM). Deposited manganese compounds in the SEI layer were identified, and a possible deposition/reaction mechanism was proposed to explain the existence of dissolved manganese ions at the graphite/electrolyte interface. In Chapter 4, the mechanical aspects of the SEI layer are addressed; the elastic properties of the SEI layer were measured in the PeakForce QNM mode using AFM, and the elastic properties of individual SEI species were evaluated using atomistic simulations. The inhomogeneity of Young's moduli observed in the SEI layer was explained based on the results of atomistic scale simulations. It was determined that the elasticity of the SEI layer depended on its

component and microstructure (i.e., crystallinity). The influence of one of the electrolyte additives, i.e., fluoroethylene carbonate (FEC), on the anode and cathode interface is discussed in Chapter 5. The performances of the batteries with graphite/Li and LMO/Li half-cells were assessed at elevated temperatures, and the thermal stability of the electrode/electrolyte interface was investigated using electrochemical testing and several characterization tools. The adverse effects of FEC on the cathode interface were observed, and possible mechanisms were proposed for the formation of the surface layer at the cathode induced by the addition of FEC. In Chapter 6, the influence of dissolved Mn ions on the structural degradation of graphite is addressed. Structural changes (such as, average interlayer space in graphite and surface structural disordering in graphite) that were caused by the dissolved Mn ions were examined using X-ray diffraction (XRD) and Raman spectroscopy. As a complementary tool, density functional theory (DFT) calculations were performed using the Vienna ab-initio simulation package (VASP) to predict changes in the lattice parameters of graphite when Mn ions were intercalated. Chapter 7 summarizes the main results of the research that was conducted for this dissertation and provides suggestions for future research.

BIBLIOGRAPHY

[1] H. TAO, Z. Feng, H. Liu, X. Kan, and P. Chen, *TOMSJ*, **5**, 201 (2011).

[2] The U.S. Department of Energy website, http://energy.gov/eere/fuelcells/fuel-cell-technology-challenges (accessed Feb. 6, 2015).

[3] J. M. Tarascon, *Phil. Trans. R. Soc. A*, **368**, 3227 (2010).

[4] V. Etacheri, R. Marom, R. Elazari, G. Salitra, and D. Aurbach, *Energy Environ. Sci.*, **4**, 3243 (2011).

[5] T. Kim, J. Park, S. Chang, S. Choi, J. Ryu, and H. Song, *Adv. Energy Mater.*, **2**, 860, (2012).

[6] The EPA United States Environmental Protection Agency website, http://www.epa.gov/climatechange/ghgemissions/sources.html (accessed Feb. 8, 2015).

[7] M. M. Thackeray, *Encyclopedia of Energy*, **1**, 127, (2004).

[8] J. B. Goodenough, and K. Park, *J. Am. Chem. Soc.*, 135, 1167 (2013).

[9] R. J. Brodd, Batteries for sustainability: Selected entries from the encyclopedia of sustainability science and technology, Springer, New York, 2013, Chapter 2, pp 10-12.

[10] A. Manthiram, *J. Phys. Chem. Lett.*, **2**, 176 (2011).

[11] O. Park, Y. Cho, S. Lee, H. Yoo, H. Song, and J. Cho, *Energy Environ. Sci.*, **4**, 1621 (2011).

[12] J. Chen, *Materials*, **6**, 156 (2013).

[13] J. Vetter, P. Novak, M.R. Wagner, C. Veit, K.C. Moller, J.O. Besenhard, M. Winter, M. Wohlfahrt-Mehrens, C. Vogler, and A. Hammouche, *J. Power Sources*, **147**, 269 (2005).

[14] The website of Energy and Power Group at University of Oxford, http://epg.eng.ox.ac.uk/content/degradation-lithium-ion-batteries (accessed Feb. 12, 2015).

[15] A. Barre, B. Deguilhem, S. Grolleau, M. Gerard, F. Suard, and D. Riu, *J. Power Sources*, **241**, 680 (2013).

[16] J.M. Tarascon and M. Armand, *Nature*, **414**, 359 (2001).

[17] K. Xu, *Chem. Rev.*, **114**, 11503 (2014).

[18] M. Z. Winter, *Phys. Chem.*, **223**, 1395 (2009).

[19] P. B. Balbuena and Y. Wang, Lithium-ion batteries: Solid-Electrolyte Interphase, Imperial College Press, London, 2004, Chapter 8, pp 337-364.
[20] Y. Zhang and C. Wang, *J. Electrochem. Soc.*, **156**, A527 (2009).
[21] V. A. Agubra and J. W. Fergus, *J. Power Sources*, **268**, 153 (2014).
[22] P. Verma, P. Maire, and P. Novak, *Electrochim. Acta*, **55**, 6332 (2010).
[23] J. Yan, B. Xia, Y. Su, X. Zhou, J. Zhang, and X. Zhang, *Electrochim. Acta*, **53**, 7069 (2008).
[24] F. Wang, J. Graetz, M. S. Moreno, C. Ma, L. Wu, V. Volkov, and Y. Zhu, *ACS nano*, **5**, 1190 (2011).
[25] K. Edstrom, M. Herstedt, and D. Abraham, *J. Power Sources*, **153**, 380 (2006).
[26] E. Peled, D. Golodnitsky, A. Ulus, and V. Yufit, *Electrochim. Acta*, **50**, 391 (2004).
[27] J. O. Besenhard, M. Winter, J. Yang, and W. Biberacher, *J. Power Sources*, **54**, 228 (1995).
[28] K. Xu, *J. Electrochem. Soc.*, **154**, A162 (2007).
[29] K. Xu, A. Cresce, and U. Lee, *Langmuir*, **26**, 11538 (2010).
[30] T. Eriksson, A.M. Andersson, C. Gejke, T. Gustafsson, and J.O. Thomas, *Langmuir*, **18**, 3609 (2002).
[31] X. Zuo, J. Wu, C. Fan, K. Lai, J. Liu, and J. Nan, *Electrochim. Acta*, **130**, 778 (2014).
[32] D. Aurbach, B. Markovsky, G. Salitra, E. Markevich, Y. Talyossef, M. Koltypin, L. Nazr, B. Ellis, and D. Kovacheva, *J. Power Sources*, **165**, 491 (2007).
[33] A. J. Smith, J. C. Burns, X. Zhao, D. Xiong, and J.R. Dahn, *J. Electrochem. Soc.*, **158**, A447 (2011).
[34] A. Andersson, K. Edstrom, N. Rao, and A. Wendsjo, *J. Power Sources*, **81-82**, 286 (1999).
[35] R. Yazami and Y. Reynier, *Electrochim. Acta*, **47**, 1217 (2002).
[36] S. Lee and S. Pyun, *Carbon*, **40**, 2333 (2002).
[37] A. Xiao, W. Li, and B. Lucht, *J. Power Sources*, **162**, 1282 (2006).
[38] A. Pasquier, F. Disma, T. Bowmer, A. Gozdz, G. Amatucci, and J. Tarascon, *J. Electrochem. Soc.*, **145**, 472 (1998).
[39] M. Inaba, H. Tomiyasu, A. Tasak, S. Jeong, and Z. Ogumi, *Langmuir*, **20**, 1348 (2004).

[40] Q. Wang, J. Sun, X. Yao, and C. Chen, *J. Electrochem. Soc.*, **153**, A329 (2006).
[41] X. Zhang, P. Ross, R. Kostecki, F. Kong, S. Sloop, J. Kerr, K. Striebel, E. Cairns, and F. McLarnon, *J. Electrochem. Soc.*, **148**, A463 (2001).
[42] X. Xiao, D. Ahn, Z. Liu, J. Kim, and P. Lu, *Electrochem. Comm.*, **32**, 31 (2013).
[43] X. Xiao, Z. Liu, L. Baggetto, G. M. Veith, K. L. More, and R.R. Unocic, *Phys. Chem. Chem. Phys.*, **16**, 10398 (2014).
[44] S. Komaba, N. Kumagai, and Y. Kataoka, *Electrochim. Acta*, **47**, 1229 (2002).
[45] V.A. Sethuraman, N.V. Winkle, D.P. Abraham, A.F. Bower, and P.R. Guduru, *J. Power Sources*, **206**, 334 (2012).
[46] S.P.V. Nadimpalli, V.A. Sethuraman, G. Bucci, V. Srinivasan, A.F. Bower, and P.R. Guduru, *J. Electrochem. Soc.*, **160**, A1885 (2013).
[47] A. Mukhopadhyay, A. Tokranov, X. Xiao, and B. W. Sheldon, *Electrochim. Acta*, **66**, 28 (2012).
[48] A. Tokranov, B.W. Sheldon, P. Lu, X. Xiao, and A. Mukhopadhyay, *J. Electrochem. Soc.*, **161**, A58 (2014).
[49] S. Bhattacharya, A.R. Riahi, and A.T. Alpas, *J. Power Sources*, **196**, 8719 (2011).
[50] T. Eriksson, Ph.D. dissertation, Uppsala University, 2001, Chapter 6, pp38-39.

CHAPTER II.
DEGRADATION OF THE SEI INDUCED BY ELEVATED TEMPERATURES*

INTRODUCTION

Reductive decomposition and polymerization of the electrolyte on an anode leads to formation of the SEI (Solid Electrolyte Interphase) layer, which is conductive for lithium ions but electronically insulating to protect the anode from further electrolyte decomposition. It is well known that formation of such a layer on an anode affects initial irreversible capacity loss during initial formation cycles. It is believed that the SEI layer formed in a few cycles has a good passivating characteristic so that further electrolyte decomposition is inhibited during subsequent cycles, especially at room temperature. However, a recent study showed that the normal SEI layer is not stable, even at room temperature, which results in continuous SEI growth and reformation at a slow rate during long-term cycling or storage [1]. Thus, the stability of the SEI layer is closely related to battery performance, including cycle and calendar life. Nevertheless, the importance of SEI stability has been neglected due to the extremely low extents of electrolyte decomposition and lithium loss during normal cycling compared to the first cycle.

* This chapter includes content presented at the 16th IMLB conference and the UM/GM quarterly review meetings.

With regards to the issue of aggravated capacity loss of Li-ion batteries at elevated temperatures, the instability of the interface between the electrode and the electrolyte has received much attention. The causes of capacity fade at elevated temperatures are numerous and the instability of the SEI layer has emerged as one of the most prominent. This instability is related to changes in the characteristics of the layer formed at the interface [2-9]. For instance, a portion of the SEI layer can be dissolved or broken down at elevated temperatures [2-5]. At such temperatures, some of chemical species in the SEI layer are also converted [5, 10].

Although many efforts have been made to understand the behavior of the SEI layer, understanding of the SEI formation/growth mechanism at elevated temperatures has remained elusive. Because of this, there have been conflicting reports about the behavior of the SEI layer at elevated temperatures; both SEI dissolution and SEI growth have been suggested based on changes in the thickness and the composition of the SEI layer [2-9].

Tasaki *et al*. proposed a mechanism of SEI evolution or growth that can explain both SEI dissolution and growth phenomena [11]. Based on the solubility of lithium salts in dimethyl carbonate (DMC), they suggested that the SEI layer, which is phase-separated between the crystal and the amorphous phases, undergoes a continuous transformation of the SEI composition via salt dissolution, reduction, and decomposition; thereby a portion of inorganic species mainly contributes to the growth of the SEI layer.

However, this mechanism has not been supported by experimental results due to the inhomogeneity of SEI thickness and difficulties in measuring real-time changes of the SEI layer during cycling.

Electrochemical impedance spectroscopy (EIS) is considered as one of the most important electro-analytical techniques and provides information on the nature of the processes occurring at the electrode/electrolyte interfaces. Despite the ambiguity of correct EIS interpretation, EIS has been extensively used due to the following advantages: (1) it allows us to separately investigate a series of complex phenomena occurring inside a battery, including lithium-ion diffusion in the electrolyte, lithium ion migration through the surface layer, charge transfer at the interface, and lithium ion diffusion in the bulk of an active material; (2) it enables us to observe real-time changes in the complex phenomena in a non-destructive way.

EIS can be used to predict the behavior of the SEI layer by enabling us to observe real-time changes during cycling or storage. Previous studies have often used EIS to understand the behavior of the SEI layer and the charge transfer process at the interface [12-21]. In order to accurately observe the SEI layer on the anode, either a symmetric cell or a three-electrode cell is necessary, instead of a normal two-electrode cell [13-15, 17, 18, 21]. Using two-electrode EIS measurements, it is not possible to interpret the processes taking place at each electrode since the observed impedance represents cell impedance. The half-cells, such as Li/$LiMn_2O_4$ or Li/C cells, also give total cell impedance that includes the contribution of the Li/electrolyte interface. For instance, unless the contribution of the Li/electrolyte interface is eliminated in the Li/C cell, the graphite/electrolyte interface cannot be analyzed correctly due to the superposition of the graphite/electrolyte interface and the Li/electrolyte interface [22, 23].

In the work presented here, we investigate the stability of the SEI layer formed on the graphite anode at different temperatures. Since there is still a lack of consensus on

how the SEI layer is affected by elevated temperatures, we first examined the changes in the composition and the thickness of the SEI layer formed on graphite electrodes stored at different temperatures using X-ray photoelectron spectroscopy (XPS) with Ar-ion sputtering. Then we investigated the behavior of the SEI layer in order to elucidate the exact mechanism of SEI instability at elevated temperatures.

METHODS

Fabrication of electrodes and battery cells

To prepare the graphite electrode, a slurry was prepared by mixing synthetic graphite powder (90 wt%)(Timrex SLP30, Timcal) with a polyvinylidene fluoride (PVdF) binder (10 wt%)(Kureha 7208, Kureha America) dissolved in N-methyl-2-pyrrolidone (NMP) using a SpeedMixer (FlackTek Inc.). The resulting slurry was cast onto a 9 μm-thick copper foil at a constant speed using a 9-mil film applicator with a doctor-blade film coater (MTI corp.). To prepare a $LiMn_2O_4$ slurry, $LiMn_2O_4$ powder (95 wt%)(Electrochemical grade, particle size <5 μm, Sigma-Aldrich), carbon black (5 wt%)(Super C65, Timcal), and PVdF binder (5 wt %) dissolved in NMP solution were mixed and cast onto a 15 μm-thick aluminum foil using the procedure described above. All composite electrodes were then dried overnight in a vacuum oven at 110 °C. The dried electrodes were punched out as disks with an area of 0.785 cm^2 and vacuum-dried again before being used in the Swagelok cell assembly process. For assembly of three-electrode pouch cells (Fig. 2.1), an anode electrode (2.4×2.4 cm^2), a cathode electrode (2.3×2.3 cm^2), and a reference electrode (0.5×0.5 cm^2) were prepared and the mass ratio

of the cathode electrode to the anode electrode was adjusted according to the targeting capacity ratio (P/N ratio ~ 0.8).

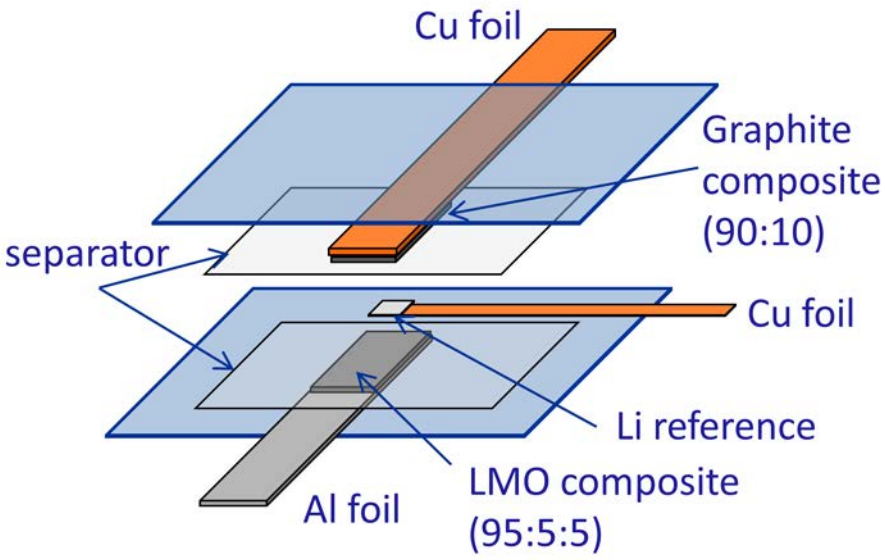

Figure 2-1. Configuration of the three-electrode pouch cell.

The electrolyte solution was 1M lithium hexafluorophosphate ($LiPF_6$, Sigma-Aldrich) dissolved in a mixture of ethylene carbonate (EC, Sigma-Aldrich) and dimethyl carbonate (DMC, Sigma-Aldrich) with a volume ratio of 1:1. The separator (Celgard 2320) was soaked in the electrolyte solution for at least 7 days before the use.

XPS measurements with Ar-ion sputtering

In order to investigate whether the SEI layer is stable at elevated temperatures, we compared the relative thickness of the SEI layer on a graphite anode stored at different temperatures using XPS measurements (Kratos Axis Ultra X-ray photoelectron spectrometer equipped with a monochromatic Al Kα excitation source ($h\nu$ = 1486.6 eV)) in conjunction with Ar-ion sputtering. The fabricated composite graphite anode was assembled with a counter electrode (Li) in a Swagelok cell and cycled four times between

1.0 V and 0.005V at a constant current (C/10 rate). At a voltage of 1.0 V (vs. Li/Li^+, delithiated state), the cell was disassembled in a glovebox. After disassembly, the graphite anode was carefully cut in half before storage tests. Since the graphite electrode was cycled at the same formation cycle condition, the same or similar characteristics (such as thickness and composition) of the SEI layer was expected to form on the two pieces of the anode. To precisely compare SEI thickness or composition at different conditions, it is important to ensure that initial SEI layer characteristics are the same before tests. The cycled graphite anodes were immersed into bottles containing 1 mL of electrolyte solution (1M $LiPF_6$, EC:DMC (1:1 v/v)) in the glovebox. These bottles were transferred to thermal chambers and stored at 25 ºC and 50ºC for 2 days or 7 days. After storage, the anode was vacuum-dried and sealed in the glovebox, in order for them to be transferred to the XPS instrument.

An area of 300 × 700 μm^2 on the anode was analyzed. The binding energy scale was adjusted based on the lithium fluoride (LiF) peak in the F 1s peak at 686 eV. Core spectra were recorded with 20 eV constant pass energy. Charge neutralization was used during the measurements. Depth profiles were obtained by Ar-ion beam sputtering using an ion beam voltage of 4 keV. The raster size was 2×2 mm^2 during the Ar-ion sputtering process.

EIS measurements using three-electrode pouch cells

To investigate how the change in an interfacial resistance of the anode is associated with SEI growth, EIS measurements were conducted during the SEI formation cycle. For this experiment, the cell was controlled by the anode potential. The cell was held at each anode potential (1V, 0.85V, 0.6V, and 0.3V vs. Li/Li^+) for 2h 30 min to

measure the impedance of the cell. Since the intercalation of lithium ions into graphite is commonly believed to start below 0.3 V (vs. Li/Li^+), the behavior of the interfacial resistance above 0.3 V was analyzed in this study.

To investigate the behavior of the SEI layer during cycling at elevated temperatures, the cell was cycled three times at a constant rate (C/15 rate) for SEI formation, followed by consecutive cycles (C/4 rate) including EIS measurements at different temperature conditions. During the consecutive cycles, EIS measurements were conducted after every two cycles in order to observe the impedance response at different temperature conditions. The cell that was controlled by the cathode potential was held at each 4.1 V, which corresponded to the anode potential 0.1 V, during the cycling. Before elevating the temperature, the cell was cycled at least 8 cycles to ensure stabilization of the electrode/electrolyte interfaces.

The impedance of the cell was measured by applying a 5 mV amplitude perturbation over the frequency range of 200 kHz to 10 mHz.

RESULTS AND DISCUSSION

Changes in the composition and thickness of the SEI Layer

To investigate the stability of the SEI layer at elevated temperatures, it is necessary to analyze changes in the composition of the layer. Figure 2.2 shows SEI composition of layers that formed on graphite anodes during storage tests. To ensure that a similar composition of the SEI layer was formed before storage tests, changes in SEI composition were precisely measured.

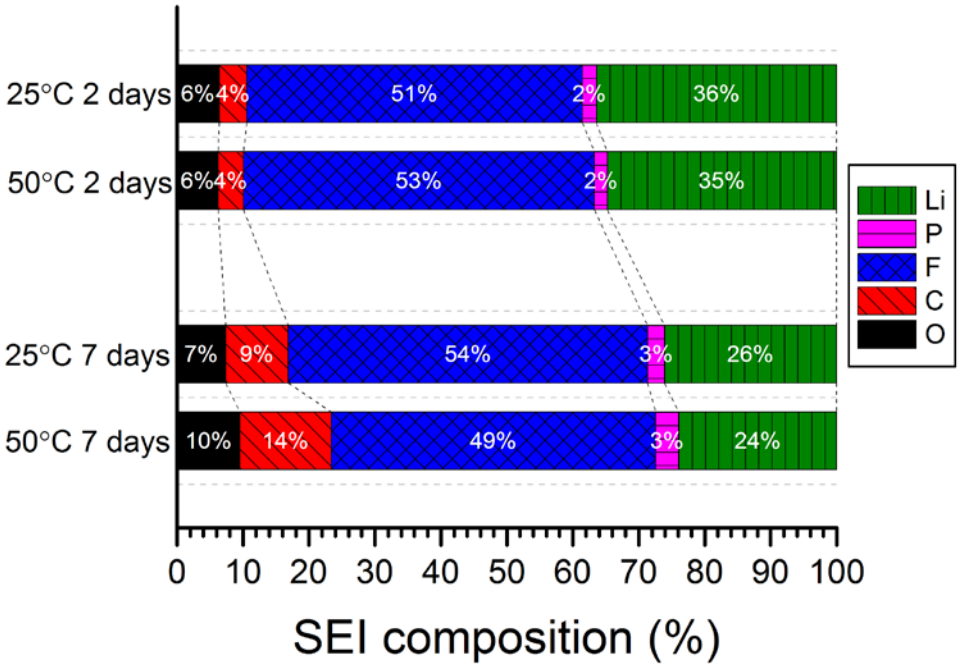

Figure 2-2. SEI compositions that formed on graphite electrodes stored at different temperatures.

After storage for 2 days at different temperatures, the difference in SEI composition was not significant. It might indicate that elevated temperatures do not significantly change the composition of the SEI layer during a short period of time, especially at the storage condition. However, noticeable difference in SEI composition was observed between the graphite anode stored at 25 °C and that stored at 50 °C after 7 days storage, compared to 2 days storage. Thus, the effect of elevated temperatures on the SEI composition increased with an increasing storage time. In particular, higher concentrations of oxygen and carbon elements were observed at the anode stored at high temperature than the anode stored at room temperature. It suggests that more of a surface layer containing C and O elements, possibly organic and polymeric species, was formed on the graphite surface during storage at high temperature. Note that the chemical

composition of the SEI layer was changed with an increasing storage time at 25 °C. It indicates that, even at room temperature, the SEI layer is not static but dynamic and suggests that storage time is also an important factor for SEI stability. Thus, as temperature and time increase, the SEI layer changes its chemical composition, which can affect the stability of the SEI layer.

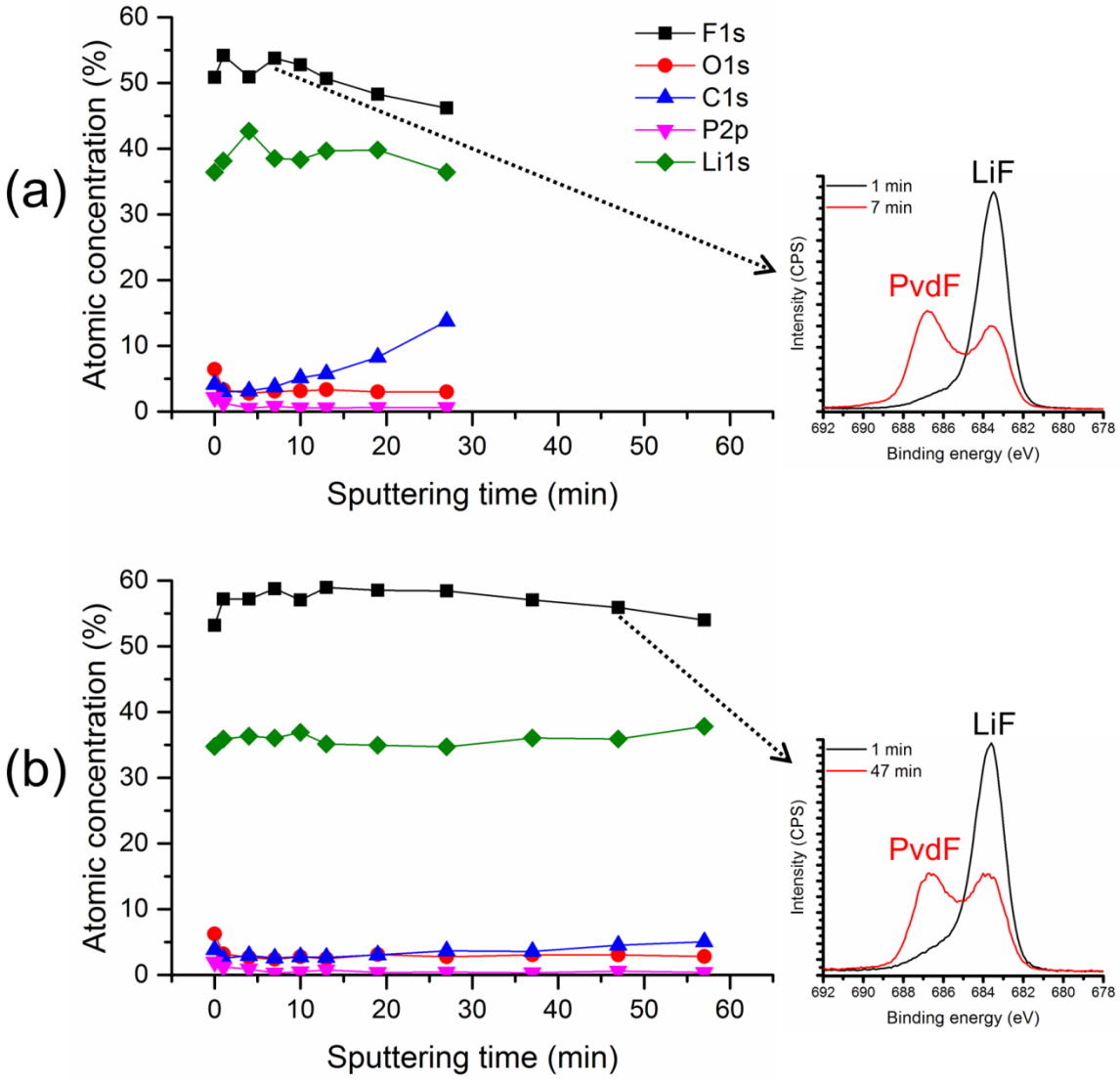

Figure 2-3. XPS depth-profiles of graphite electrodes stored for 2 days at (a) 25 °C and (b) 50 °C. The insets show changes in F 1s spectra during the sputtering process.

To further investigate the instability of the SEI layer at elevated temperatures, the thickness of the SEI layer needed to be evaluated. To confirm SEI growth or dissolution at elevated temperatures, XPS with Ar-ion sputtering was utilized. Since the raster area (2×2 mm^2) as well as the analyzed area is relatively large compared to other analytical techniques, XPS may give more accurate estimation on the inherently inhomogeneous SEI. Ar-ions were repeatedly sputtered to remove the SEI layer until the graphite-related peak or the PVdF binder-related peak started to appear in the carbon or fluorine core spectrum, respectively. The time required for the occurrence of the peaks (graphite or PVdF) was used to evaluate the thickness of the SEI layer.

Figure 2.3 shows XPS depth-profile of the graphite anode stored for 2 days. Although the difference in the composition of the SEI layer was not significant in the case of the graphite anodes after 2 days storage, the structure of the SEI layer as measured by its thickness varied. After a short sputtering time (~ 7min), the amount of carbon element in the SEI layer of the graphite stored at 25 °C (Fig. 2.3a) started to increase rapidly, showing the peaks related to the graphite and PVdF. At the same time, other elements (O, Li, F, and P) started to decrease with the exposure of the graphite surface. It indicates that the graphite covered by the SEI layer was being exposed with the removal of the SEI layer. The inset figure clearly shows the peak related to PVdF appeared with the decrease in the intensity of the peak associated with LiF. In contrast, a longer sputtering time (~ 47 min) was needed to remove the SEI layer of the graphite stored at 50 °C (Fig. 2.3b). It indicates that a thicker SEI layer was formed during storage at high temperature, suggesting that elevated temperatures result in further SEI growth.

On the basis of the above result, the results of the graphite anodes stored for 7 days (Figure 2.4) indicates that storage time as well as temperature affected the SEI growth.

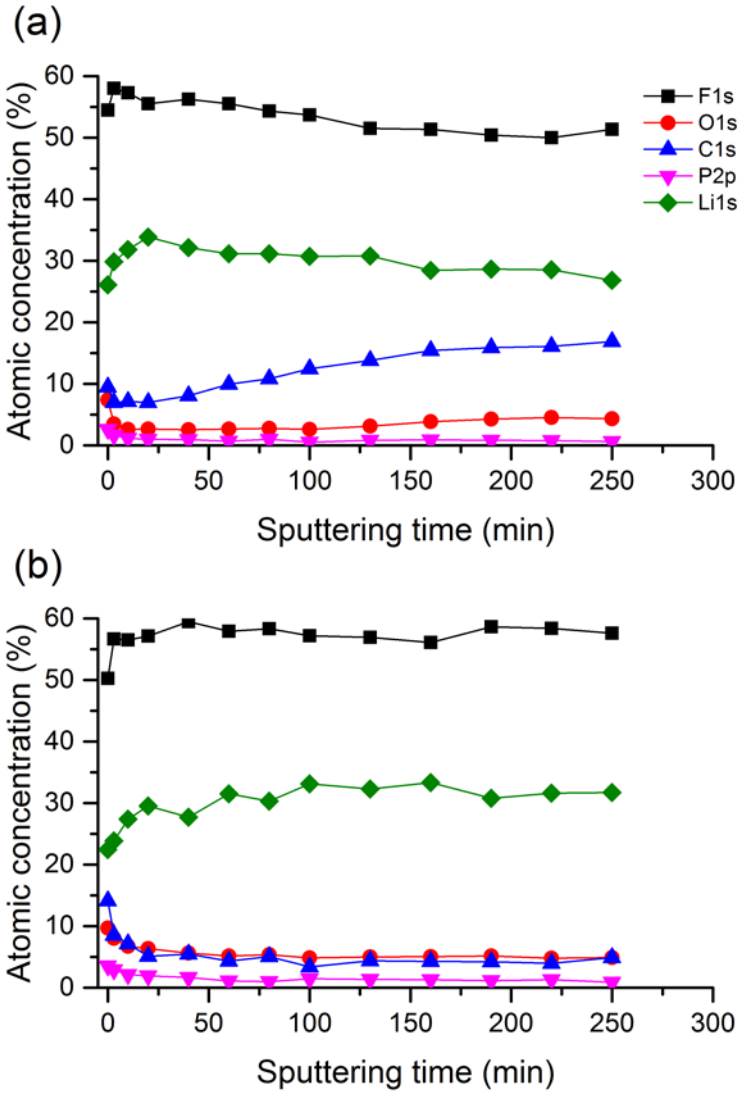

Figure 2-4. XPS depth-profiles of graphite electrodes stored for 7 days at (a) 25 °C and (b) 50 °C.

Compared with the graphite stored for 2 days at 25 °C (Fig. 2.3a), a longer sputtering time was spent to remove the SEI layer on the graphite stored for 7 days at 25 °C (Fig. 2.4a). The graphite-related peak began to appear at around 60 min in the case

of the graphite stored for 7 days. Consistent with the previous result (Fig. 2.1), this indicates that SEI growth proceeds even at room temperature.

The anode stored at 50 °C for 7 days did not show the increase of the amount of carbon element and the appearance of the graphite- or PVdF-related peak at the end of sputtering time; the graphite peak appeared with an increase of the amount of carbon element after 250 min. Thus, the SEI layer on the graphite stored for 7 days at 50 °C became much thicker than that stored at 25 °C, indicating high temperature promoted the growth of the SEI layer.

Note that the difference in the sputtering time needed to remove the SEI layer between 25 °C stored anode and 50 °C stored anode was considerably increased in the anodes after 7 days, compared to the anodes after 2 days.

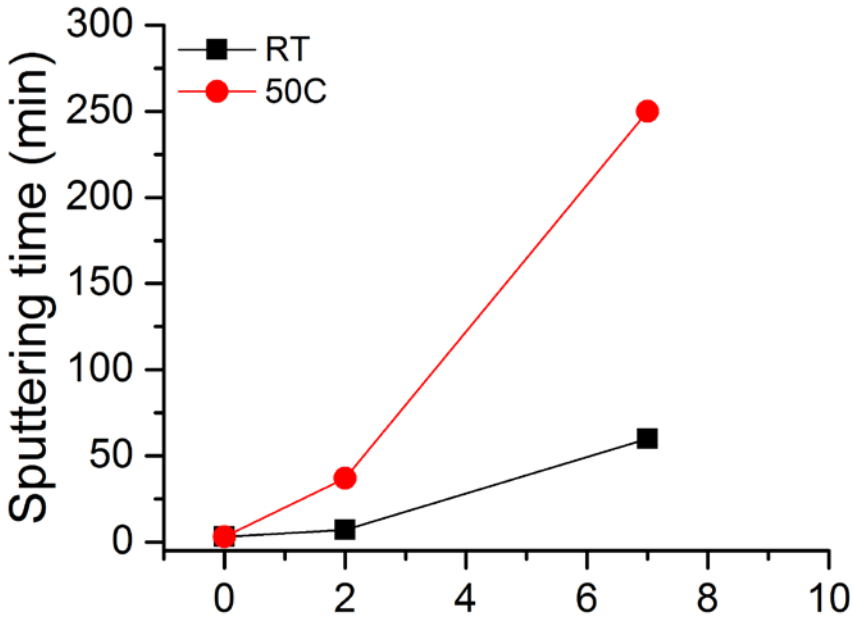

Figure 2-5. Comparison of the change in the sputtering time needed to remove the SEI layer on the graphite electrode stored at different temperatures.

Figure 2.5 show the comparison of the change in the sputtering time required to remove the SEI layer on the graphite anode. It shows the rate of SEI growth is much higher at higher temperature: the SEI layer stored at 50 °C grew faster than that stored at 25 °C. This is consistent with previously reported results [1, 24].

Compared to the literature, a relatively long sputtering time was required to remove the SEI layer on the graphite anode [25, 26]. This might be caused by the large amount of the electrolyte (1mL) used during storage, which could result in more electrolyte decomposition, resulting in a thicker SEI layer compared to that in a real battery cell.

With the help of XPS measurements, it was confirmed that the SEI layer eventually grew and the rate of SEI growth was accelerated at elevated temperatures. However, it was still not clear how the SEI layer grew at elevated temperatures. Next we will focus on the behavior of the SEI layer at elevated temperatures in order to elucidate the mechanism of the SEI growth.

Change in the interfacial resistance

The designed three-electrode pouch cell was first validated by comparing the impedance of the three-electrode cell and the impedance of the two-electrode cell. As shown in Figure 2.6a, the anode impedance and the cathode impedance were distinguished from the total impedance of the three-electrode cell using the three-electrode cell. It was observed that the anode impedance was much smaller than the cathode impedance. Figure 2.6b shows that the total impedance of the three-electrode cell was well matched with the two-electrode cell; it was determined that the deviation of

impedance value at open circuit voltage (OCV) between the three-electrode cell and the two-electrode cell was within 5%.

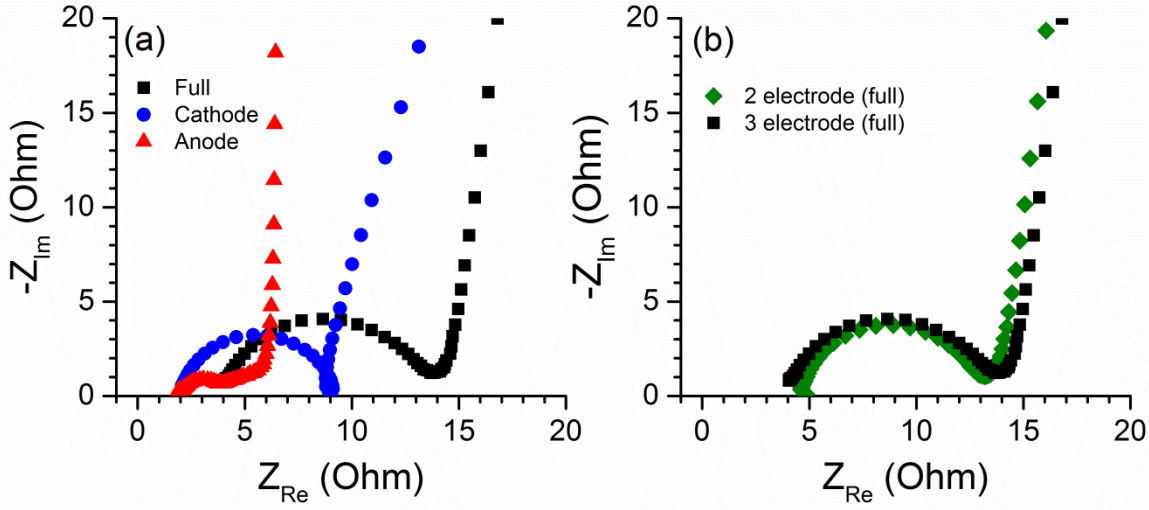

Figure 2-6. (a) OCV impedance spectra of the three-electrode pouch cell; (b) Comparison of the two-electrode and three-electrode pouch cells.

In order to understand how the interfacial resistance is associated with the SEI formation, the change in the interfacial resistance as a function of potential in the first charge cycle was investigated. Typically, the semicircles at high- and medium-frequency in the graphite electrode represent the migration of lithium ions through the SEI layer and the charge transfer process at the electrode/electrolyte interface, respectively. Since the two semicircles are related to interfacial processes at the interface, the combination of the semicircles is called as the interfacial resistance. The low-frequency Warburg impedance tail accounts for diffusion limitations in the electrode, which include diffusion through the electrolyte, the electrode surface layer, and the active material [27]. The ohmic resistance, which is expressed by the high frequency intercept on the real axis, includes the bulk electrolyte resistance and artifacts associated with cell design and measurement setting [27, 28].

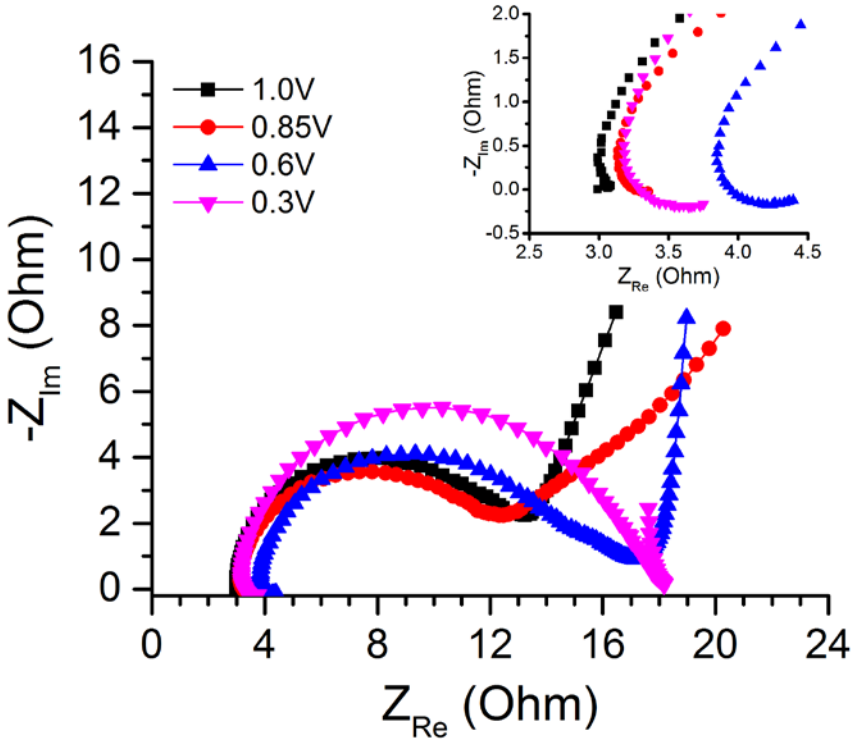

Figure 2-7. Changes in impedance spectrum of the graphite anode during the 1st charge process. The inset shows changes in the ohmic resistance of the graphite anode during the 1st charge.

Figure 2.7 shows that the impedance spectrum measured at each of the potentials in the first charge cycle. Unfortunately, the two semicircles observed at high- and medium-frequency were not clearly seen in our impedance spectra of the graphite anode, indicating that the two processes (SEI resistance and charge transfer resistance) had very close time constants. This is possibly due to the characteristics of the composite graphite electrode used in this study. The high-frequency arc is known to be associated with not only SEI resistance but also the characteristics of the composite anode [13, 20].

Upon decrease of the OCV to 0.85 V, the interfacial impedance did not show significant change, while the low frequency line that represented the blocking character of non-lithiated electrode (a slight slope line) changed its slope (around 45°). This can be

explained by the dominance of diffusion of the electrolyte to the electrode below 1.0 V. At the potential of 0.6 V, the interfacial impedance slightly increased, while the low frequency line again showed the blocking behavior (a straight line instead of a slope line). It indicates that a SEI layer with less conductive character was formed between 0.85 V and 0.6 V. It is well known that the reductive decomposition of the electrolyte starts to appear at around 0.7 V (vs. Li/Li^+) to form the SEI layer. It indicates that the behavior of the impedance spectrum correctly represented the SEI formation process. Note that the ohmic resistance noticeably increased at this potential. This can be attributed to the occurrence of electrolyte decomposition. The reduction process in the electrolyte can contribute to the increase of the ohmic resistance since the decomposed products increased in the electrolyte; the diffusion of the solvated Li-ions through the electrolyte might be sluggish due to the decomposition process.

Between 0.6 V and 0.3 V, the formation of the SEI layer proceeded further, leading to an increase of the interfacial resistance. This increase can be explained by the growth of the SEI layer. Note that the inductive behavior at the low frequency was observed at 0.3 V. Although there have been many explanations for this inductive behavior, we believe that this is related with the robustness of the SEI layer formed in the first cycle, which was also suggested by Gnanaraj *et al* [20]. The decreased ohmic resistance recovered at this potential, indicating that the decomposed products in the electrolyte were considerably reduced during SEI formation.

Based on the change in the interfacial resistance in the first charge cycle, where the SEI was grown mostly due to reductive decomposition of the electrolyte, it was confirmed that the interfacial resistance was closely associated with the behavior of the

SEI layer. It is important to note that the interfacial resistance is not only related to the SEI thickness, but also to SEI characteristics such as porosity and conductivity. Thus, depending on changes in the characteristics of the SEI layer, the interfacial resistance is expected to be affected.

To understand the behavior of the SEI layer at elevated temperatures, the behavior of the SEI layer at room temperature was first investigated.

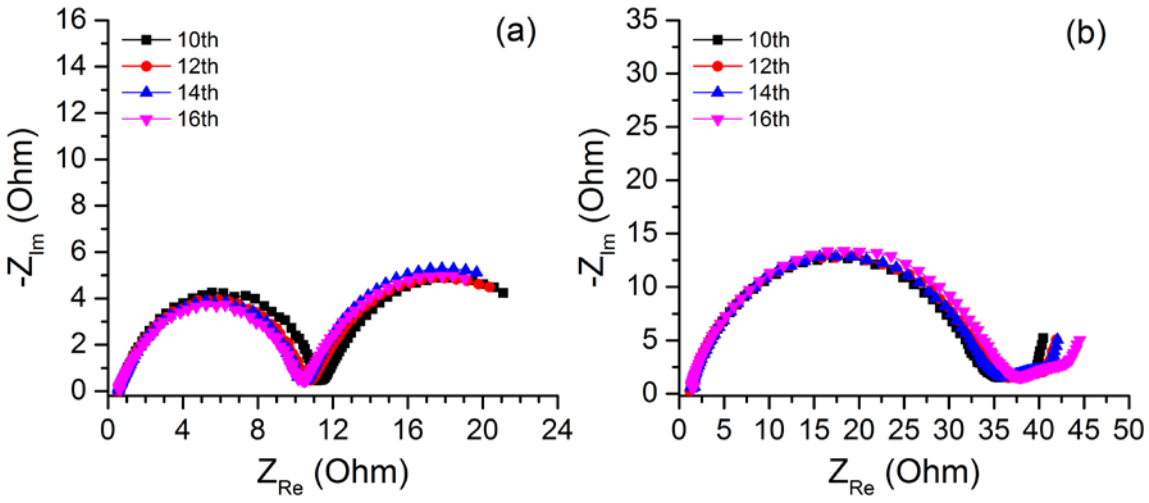

Figure 2-8. Changes in impedance spectra of (a) the graphite anode and (b) the $LiMn_2O_4$ cathode during cycling at room temperature.

As expected, the impedance of the anode (Fig. 2.8a) as well as the impedance of the cathode (Fig. 2.8b) did not change significantly during cycling at room temperature, as shown in Figure 2.8. In particular, the interfacial impedance remained nearly the same in both the cathode and anode until the 20th cycle. This indicates that the electrode/electrolyte interfaces were stable during cycling at room temperature. As the cycle number increases, it is expected to cause changes in the interfacial resistances of both the anode and the cathode; however, this is not related to the subject of this work.

To investigate the behavior of the SEI layer at elevated temperatures, the operating temperature was increased every two cycles during cycling. After each set of two cycles, EIS measurements were conducted at room temperature condition.

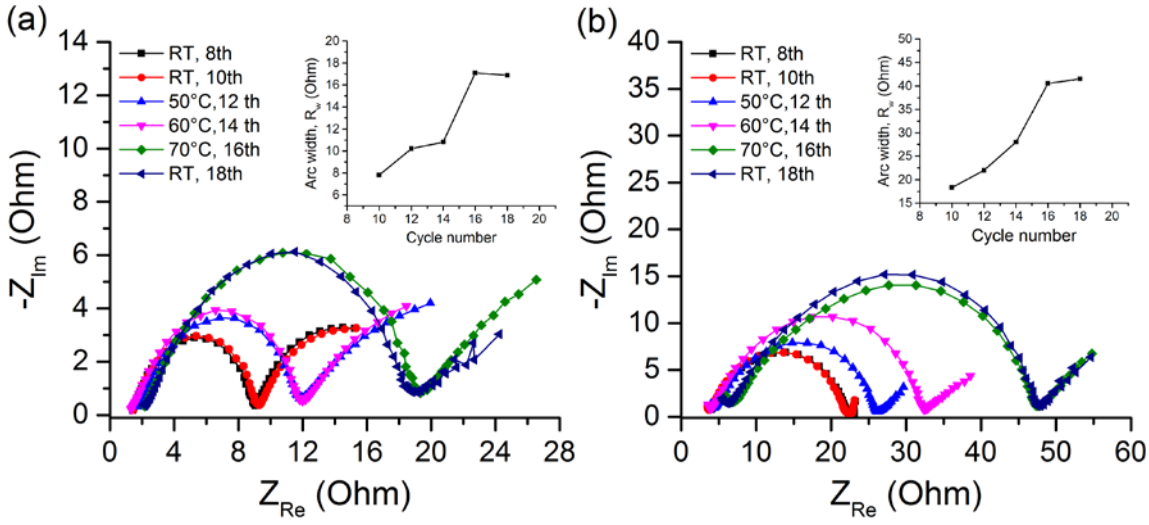

Figure 2-9. Changes in impedance spectra of (a) the graphite anode and (b) the $LiMn_2O_4$ cathode during cycling with increasing temperatures. The inset shows that change in the arc width (R_w) in the impedance spectra as a function of cycle number.

As shown in Figure 2.9, the interfacial impedance increased in both the anode (Fig. 2.9a) and the cathode (Fig. 2.9b) as temperature increased. However, the rise of the interfacial impedance of the anode showed a quite different pattern compared to that of the cathode. While the interfacial impedance of the cathode almost linearly increased with increasing temperature, the interfacial resistance of the anode monotonically increased. These patterns are clearly seen in the inset plots, which shows the change in the width of the semicircle as a function of cycle number.

The arc width (R_w) can be expressed based on the Arrhenius equation as follows [27]:

$$\frac{1}{R_w} = Aexp\left(-\frac{E_a}{RT}\right)$$

where A is a constant, E_a is the activation energy, R is the gas constant, and T is the temperature.

Based on this equation, increasing temperature should have reduced the interfacial resistance due to improved interface kinetics which is expressed by the charge transfer resistance. However, the opposite phenomena were observed experimentally in this study. This indicates that the interfacial resistance is mainly governed by the characteristics of the electrode/electrolyte interface, not by the charge transfer resistance, especially in the case of the anode.

The linear increase of the cathode impedance can be explained by the increase in side reactions such as the dissolution of manganese ions from the cathode and/or the formation of the cathode surface layer. The noticeable increase in the ohmic resistance with increasing temperatures in the cathode might due to the increased amount of dissolved manganese ions. The Li-ion transfer through the electrolyte can be interrupted by the increased dissolved manganese ions in the electrolyte, increasing the ohmic resistance. However, the electrolyte decomposition induced by elevated temperatures also would contribute to the increase of the ohmic resistance, since the increase in the ohmic resistance was also observed in the anode.

Compared to the cathode, the monotonic increase of the interfacial resistance in the anode is not straightforward to explain. It indicates that elevated temperature did not simply cause an increase in the thickness of the SEI layer. According to Abraham *et al*., the impedance of the anode is governed by composition and morphology of the SEI layer formed on the graphite anode [16]. It is postulated that the SEI dissolution mechanism is competing with the SEI growth mechanism at elevated temperatures. Since previous

studies reported that SEI dissolution or SEI growth phenomena at elevated temperatures, there is highly possibility that these processes coexist at elevated temperatures.

Depending on the competition between these two opposite effects, the interfacial resistance may decrease, increase, or remain unchanging according to the dominant mechanism at elevated temperatures. The hypothesis of the evolution of the SEI layer suggested by Tasaki *et al*. could be verified by this result [11].

To further investigate the instability of the SEI layer at high temperature, the increased temperature was kept during cycling. The Figure 2.10 shows changes in the interfacial resistances of the anode (Fig. 2.10a) and the cathode (Fig. 2.10b) during cycling at constant temperature 50 °C.

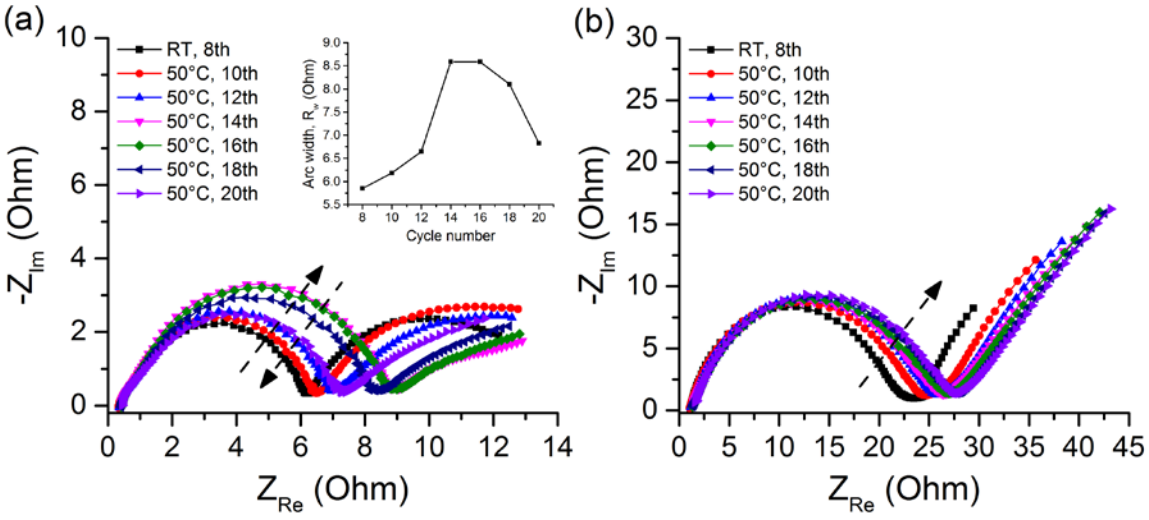

Figure 2-10. Changes in impedance spectra of (a) the graphite anode and (b) the $LiMn_2O_4$ cathode during cycling at 50°C. The inset shows that change in the arc width (R_w) in the impedance spectra as a function of cycle number.

While the interfacial resistance of the cathode increased as cycle number increased, the interfacial resistance of the cathode first increased and then decreased as cycle number increased. The oscillating behavior of the anode interfacial resistance might

reflect the behavior of the growth and dissolution of the SEI layer at elevated temperature, demonstrating the instability of the SEI layer at high temperature. This oscillating behavior of the anode interfacial resistance is consistent with a previous study; they observed the impedance of the SEI quickly decreased and increased in an oscillating manner when stored at 80 °C [18].

Based on the change in the anode interfacial resistance at elevated temperature, it is confirmed that the SEI dissolution and growth repeatedly occurs during cycling at elevated temperatures, which eventually leads to SEI growth. This behavior explains the instability of the SEI layer at elevated temperature.

CONCLUSIONS

In this work, the instability of the SEI layer at elevated temperatures was investigated by analyzing changes in the chemical composition and the thickness of the SEI layer as well as change in the interfacial resistance at the anode. The XPS results showed that the chemical composition of the SEI layer significantly changed as both temperature and storage time increased. The thickness of the SEI layer was also strongly affected by both elevated temperature and storage time. The rate of SEI growth was considerably higher at elevated temperature than at room temperature, which indicated that the degradation of the SEI layer was significantly accelerated at elevated temperatures.

The mechanism of the SEI growth was investigated by investigating changes in the interfacial resistance at the anode at elevated temperatures. The changes during the first cycle suggested that the interfacial resistance at the anode was closely associated

with the behavior of the SEI layer. At room temperature, the interfacial resistance at the anode was not significant, which indicated stability of the SEI layer. In contrast, the interfacial resistance at the anode increased and then decreased during cycling at 50 °C, which differed from the behavior of the interfacial resistance at the cathode. More interestingly, the interfacial resistance at the anode monotonically increased, while the interfacial resistance at the cathode linearly increased with increasing temperatures. Based on this behavior, it was proposed that the growth of SEI at elevated temperatures occurred as a consequence of a competitive mechanism between the dissolution and the precipitation of the SEI layer.

Thus, to enhance thermal stability of a SEI layer, the SEI layer must consist of chemical species that are less susceptible to the dissolution of SEI at elevated temperatures.

BIBLIOGRAPHY

[1] A. Smith, J. Burns, X. Zhao, D. Xiong, J. Dahn, *J. Electrochem. Soc.*, **158**, A447 (2011).

[2] A. Pasquier, F. Disma, T. Bowmer, A. Gozdz, G. Amatucci, J. Tarascon, *J. Electrochem. Soc.*, **145**, 472 (1998).

[3] M. Inaba, H. Tomiyasu, A. Tasak, S. Jeong, Z. Ogumi, *Langmuir*, **20**, 1348 (2004).

[4] Q. Wang, J. Sun, X. Yao, C. Chen, *J. Electrochem. Soc.*, **153**, A329 (2006).

[5] X. Zhang, P. Ross, R. Kostecki, F. Kong, S. Sloop, J. Kerr, K. Striebel, E. Cairns, F. McLarnon, *J. Electrochem. Soc.*, **148**, A463 (2001).

[6] A. Andersson, K. Edstrom, N. Rao, A. Wendsjo, *J. Power Sources*, **81-82**, 286 (1999).

[7] R. Yazami, Y. Reynier, *Electrochim. Acta*, **47**, 1217 (2002).

[8] S. Lee, S. Pyun, *Carbon*, **40**, 2333 (2002).

[9] A. Xiao, W. Li, B. Lucht, *J. Power Sources*, **162**, 1282 (2006).

[10] A. Andersson, D. Abraham, R. Haasch, S. MacLaren,, J. Liu, K. Amine, *J. Electrochem. Soc.*, **149**, A1358 (2002).

[11] K. Tasaki, A. Goldberg, J. Lian, M. Walker, A. Timmons, S. Harris, *J. Electrochem. Soc.*, **156**, A1019 (2009).

[12] C. Wang, A. Appleby, F. Little, *Electrochim. Acta*, **46**, 1793 (2001).

[13] M. Holzapfel, A. Martinent, F. Alloin, B. Gorrec, R. Yazami, C. Montella, *J. Electroanal. Chem.*, **546**, 41 (2003).

[14] S. Zhang, P. Shi, *Electrochim. Acta*, **49**, 1475 (2004).

[15] S. Zhang, *J. Power Sources*, **163**, 713 (2007).

[16] D. Abraham, M. Furczon, S. Kang, D. Dees, A. Jansen, *J. Power Sources*, **180**, 612 (2008).

[17] S. Xu, Q. Zhuang, L. Tian, Y. Qin, L. Fang, S. Sun, *J. Phys. Chem. C*, **115**, 9210 (2011).

[18] H. Lee, C. Wan, Y. Wang, *J. Electrochem. Soc.*, **151**, A542 (2004).

[19] S. Zhang, K. Xu, T. Jow, *Electrochim. Acta*, **51**, 1636 (2006).

[20] J. Gnanaraj, R. Thompson, S. Iaconatti, J. DiCarlo, K. Abraham, Electrochem. Solid. St., **8**, A128 (2005).

[21] A. Martinent, B. Gorrec, C. Montella, R. Yazami, *J. Power Sources*, **97-98**, 83 (2001).

[22] C. Chen, J. Liu, K. Amine, *J. Power Sources*, **96**, 321 (2001).

[23] M. Dolle, F. Orsini, A. Gozdz, J. Tarascon, *J. Electrochem. Soc.*, **148**, A851 (2001).

[24] L. Liu, J. Park, X. Lin, A.M. Sastry, W. Lu, *J. Power Sources*, **268**, 482 (2014).

[25] D. Bar-Tow, E. Peled, L. Burstein, *J. Electrochem. Soc.*, **146**, 824 (1999).

[26] V. Eshkenazi, E. Peled, L. Burstein, D. Golodnitsky, *Solid State Ionics*, **170**, 83 (2004).

[27] D. Abraham, E. Reynolds, P. Schultz, A. Jansen, D. Dees, *J. Electrochem. Soc.*, **153**, A1610 (2006).

[28] Y. Zhang, C. Wang, *J. Electrochem. Soc.*, **156**, A527 (2009).

CHAPTER III.
DEGRADATION OF THE SEI INDUCED BY THE DEPOSITION OF MANGANESE IONS*

INTRODUCTION

The capacity and power fading of lithium-ion (Li-ion) batteries are complicated processes that are very challenging to understand and resolve, especially at elevated temperatures [1-6]. Although the mechanisms responsible for the degradation of Li-ion batteries cannot be simplified and explained by one or two phenomena, the dissolution of the active materials and the instability of the solid electrolyte interface (SEI) are two of the key phenomena responsible for the degradation. These two phenomena, in particular, cannot be considered independent at elevated temperatures, since a significant amount of the ions dissolved at elevated temperatures move to the anode side and modify the SEI layer. Consequently, transition metal dissolution from the cathode materials not only influences the reversible capacity of the positive electrode, it also influences the reversible capacity of the negative electrode.

The dissolution of active materials from the cathode side clearly causes the loss of usable materials from the positive electrode. These dissolved transition-metal ions subsequently re-deposit on the positive electrode, forming an electrically insulating layer of oxides and fluorides [4, 7]. Moreover, the dissolved ions diffuse to the negative

* This chapter contains content from a published paper: H. Shin, J. Park, A.M. Sastry, and W. Lu, *Journal of Power Sources*, 284 (2015) 416-427.

electrode, where they are deposited, influencing both the chemical degradation of the SEI layer and the self-discharge of the lithiated anode [8, 9]. These phenomena are especially important for manganese-based electrodes, such as $LiMn_2O_4$, $LiMnO_2$, $Li_{1+x}Mn_2O_4$, and $Li_{1.05}(Ni_{1/3}Co_{1/3}Mn_{1/3})_{0.95}O_2$, since the manganese-based oxides are more vulnerable to dissolution in the electrolyte than other cathode materials, especially at elevated temperatures [10]. It has been also reported that the amount of Mn deposited is significantly greater than that of other transition metals, such as Ni and Co [11]. Thus, in manganese-based cells, a considerable amount of Mn ions is expected to be continuously dissolved and deposited during prolonged storage/cycling at elevated temperatures.

The instability of the SEI on the anode is severe especially at elevated temperatures; two factors, i.e., temperature and dissolved Mn ions, considerably contribute to the degradation of the SEI layer [2, 3, 8, 9]. Figure 3.1 shows a simple schematic of the degradation of the SEI on the graphite that occurs at elevated temperatures. As shown in the figure, two different mechanisms are associated with the chemical degradation of the SEI layer: (1) Elevated temperatures directly induce the dissolution, breakdown, and conversion of the SEI layer, which make the original SEI layer to be a defective layer [1-3]. This defective layer causes the consumption of cyclable lithium ions and additional decomposition of the electrolyte to reform the layer, resulting in the growth of the SEI layer. (2) The dissolved Mn ions also induce side reactions associated with the deposition of the Mn ions, resulting in a defective layer [8, 9, 12]. During the deposition process, Mn ions can interact with the chemical species in the SEI layer, and deposited Mn compounds can promote a catalytic reaction that results in more decomposition of the electrolyte. In addition, the deposition of the dissolved Mn

ions can make lithium ions in the lithiated graphite to deintercalate during the reduction process [8]. Thus, degradation of the SEI layer proceeds in the presence of the dissolved Mn ions, reducing capacity and power of a Li-ion battery. At elevated temperatures, these two phenomena simultaneously occur and are coupled to each other, which make understanding of the degradation mechanism of the SEI layer more complex.

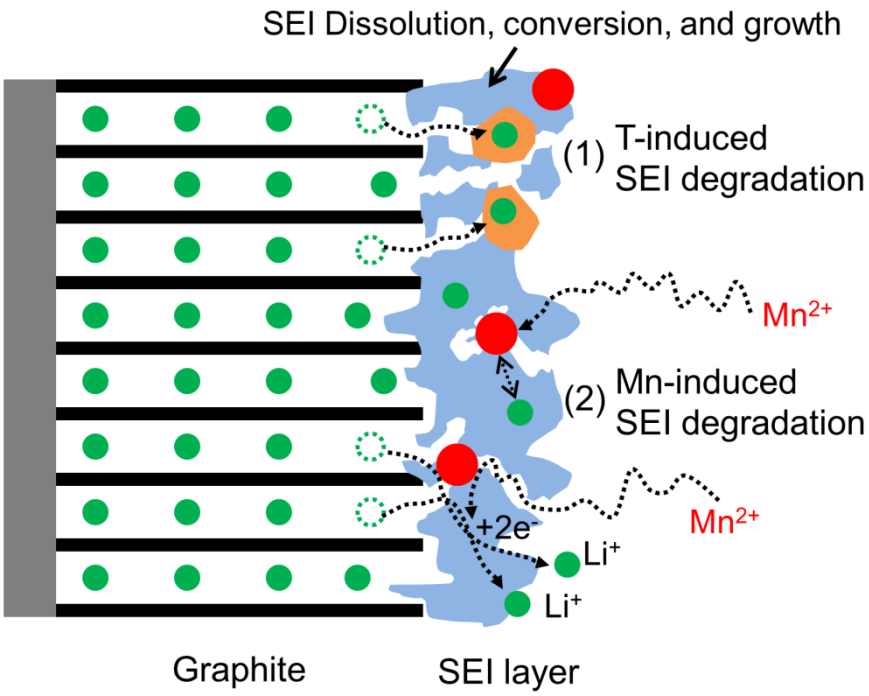

Figure 3-1. A schematic description of the SEI instability that occurs in cycled or stored Li-ion batteries at elevated temperatures.

To simplify the problem and get a better insight into the influence of Mn deposition on capacity fade, several studies have been conducted by artificially introducing soluble Mn ions into the electrolytes. Either a defined amount of the manganese perchlorate [$Mn(ClO_4)_2$] has been dissolved in $LiClO_4$-based electrolytes or the anodic dissolution of Mn metal has been carried out using electrolysis [9, 12-15]. These previous studies provide limited information that is only applicable to $LiClO_4$-

based electrolyte systems because, in each case, a lithium salt ($LiClO_4$) was used as the electrolyte. Moreover, the presence of hydrofluoric acid (HF), which is an important reason for Mn dissolution in $LiPF_6$-based electrolytes, has been ignored in $LiClO_4$-based electrolyte systems. A recent study tried to mimic the conditions in $LiPF_6$-based commercial cells by immersing $LiMn_2O_4$ powder in the electrolyte at the high temperature for several days [16]. However, this preparation could cause the degradation of the electrolyte during the storage, producing byproducts such as HF, PO_3F^{2-}, and $PO_2F_2^-$ in the electrolyte [17]. In addition, it is difficult to achieve the desired amount of dissolved Mn ions in the electrolyte.

So far, a number of efforts have been made to understand the influence of Mn deposition on anode performance, the interaction mechanism between dissolved Mn ions and the anode/electrolyte interface, and the oxidation state of the deposited Mn. The deterioration of anode performance induced by Mn deposition has been clearly observed with increased reduction current and interfacial impedance [12-16, 18]. However, earlier studies have shown conflicting results about the mechanism responsible for Mn compound deposition and the oxidation state of the deposited Mn compound. This makes it difficult to have a clear understanding of what happens at the anode/electrolyte interface as a result of the deposition of Mn ions. It was initially proposed that the dissolved Mn ions could be reduced electrochemically by the low potential, based on the known standard redox potential of Mn/Mn^{2+} (1.87 V vs. Li/Li^+) [12]. Another hypothesis was that the reduction of the Mn ions on the anode surface occurs chemically, via the chemical activity of the lithiated graphite [18]. Another possibility has recently been proposed that a metathesis reaction occurs between the dissolved Mn ions and some

species in the SEI layer, rather than the reduction reaction during Mn deposition on the anode [16]. Even when the deposited Mn compound was not clearly identified, the 2+ oxidation state of Mn deposited on anodes was predominantly observed [9, 13, 19]. However, recent studies also suggested that a metallic form of Mn can be formed on the anode [14, 20, 21]. The Mn compounds reported to date are summarized in Table 3.1.

Table 3-1. Summary of Mn compounds proposed to be deposited on the anode.

Detection techniques	Electrolyte employed	Proposed Mn compounds	Reference
XPS	1M $LiClO_4$ in EC/DEC with addition of 150 ppm $Mn(ClO_4)_2$	MnO or Mn_2O_3	S. Komaba *et al*. [13]
XPS	1M $LiPF_6$ in EC/DEC	MnO or MnO_2	L. Yang *et al*. [19]
XPS AFM	1M $LiClO_4$ in EC/DEC with 100 ppm Mn ions by the anodic dissolution of Mn metal (electrolysis)	Metallic Mn, $MnCO_3$, and $Mn(ClO_4)_2$	M. Ochida *et al*. [14]
XAS	1M $LiClO_4$ in EC/DEC with addition of 2.5mM $Mn(ClO_4)_2$	Mn(Ⅱ) such as $MnCO_3$	C. Delacourt *et al*. [9]
XAS XPS	1.2M $LiPF_6$ in EC/EMC with 20 ppm Mn ions dissolved from $LiMn_2O_4$ powder	Mn(Ⅱ) such as $MnCO_3$ and MnF_2	C. Zhan *et al*. [16]
TEM XPS	1M $LiPF_6$ in EC/DEC	Metallic Mn and MnF_2	X. Xiao *et al*. [21]
XAS	1M $LiClO_4$ in EC/DEC with addition of 200 ppm $Mn(ClO_4)_2$	Metallic Mn and Mn(Ⅱ)	S. R. Gowda *et al*. [20]

Despite the research described above, the precise mechanism of the interaction between dissolved Mn ions and the anode/electrolyte interface is still being debated and remains a challenging topic. To shed further light on the mechanism of capacity fade driven by deposited Mn, it is necessary to understand how the dissolved Mn ions cause SEI degradation. The identification and spatial distribution of Mn compounds at the anode/electrolyte interface are also essential to understand the mechanisms of Mn deposition as well as the Mn-induced SEI degradation. The goals of this work are to

improve an understanding of how the composition and structure of the SEI layer are modified by dissolved Mn ions and how these modifications degrade battery performance. In order to reveal the deposition/reaction mechanism of dissolved Mn ions, we identified the Mn compounds that form on both the graphite anode and individual SEI species, and investigated how the Mn is distributed at the graphite/electrolyte interface.

METHODS

A binder-free highly oriented pyrolytic graphite (HOPG, SPI supplies) was chosen as the working electrode in order to investigate the difference in SEI layer compositions that forms in the Mn-free electrolyte and the Mn-containing electrolyte. The presence of polyvinylidenedifluoride (PVdF) in conventional composite anodes makes it difficult to achieve a detailed and conclusive analysis of the SEI composition, since peaks associated with the PVdF binder overlap with the peaks of SEI chemical species in X-ray photoelectron spectroscopy (XPS) spectra. The HOPG electrode was prepared as a square sheet with sides of 5 mm and a thickness of 1 mm. For other purposes, the composite electrode was prepared by spreading a mixture of 90 wt % synthetic graphite powder (TIMREX SLP 30, Timcal) and 10 wt % PVdF binder dissolved in anhydrous N-methyl-2-pyrrolidone (99.5% NMP, Sigma-Aldrich) onto a 9 μm-thick Cu foil (MTI corp.). The electrode sheet was then vacuum-dried at 110 °C for one day to remove the NMP. Lithium metal (Alfa Aesar) and the Celgard 2320 were used as a counter electrode and a separator, respectively, in the coin-cell assembly process. All 2032-type coin cells (MTI Corp.) were assembled in an argon-filled glove box (MBraun) containing less than 0.1 ppm oxygen and moisture. The electrolyte solution was 1 M

lithium hexafluorophosphate ($LiPF_6$, Sigma-Aldrich) dissolved in a mixture (1:1, v/v) of ethylene carbonate (EC, Sigma-Aldrich) and dimethyl carbonate (DMC, Sigma-Aldrich). The Mn-containing electrolyte was prepared by dissolving a known amount of synthesized manganese hexafluorophosphate [$Mn(PF_6)_2$] into the base electrolyte. The $Mn(PF_6)_2$ salt was synthesized by reacting manganese chloride ($MnCl_2$, Sigma-Aldrich) with the silver hexafluorophosphate ($AgPF_6$, Sigma-Aldrich) in ethanol. The mixture was then filtered and distilled to isolate the synthesized $Mn(PF_6)_2$. The $Mn(PF_6)_2$ was vacuum-dried at 90 °C overnight before use. The concentration of dissolved Mn ions in the electrolyte was analyzed using inductively coupled plasma optical emission spectrometry (ICP-OES).

For the investigation of cycling performance and SEI composition, the assembled HOPG/Li cells containing the Mn-free or the Mn-containing (200 ppm) electrolyte were charged to 0.01 V and then discharged to 1.5 V at a constant rate of C/15 in the first 3 cycles, followed by 25 times between 0.01 and 1 V at a constant rate of C/7, using a battery test system (Biologic). The open-circuited cells at 1.0 V were disassembled in an argon-filled glove box.

For the identification of the deposited Mn compound, the composite electrode cell was charged at a rate of C/15 to 1.0 V, which is below the standard redox potential of Mn/Mn^{2+} (1.87 V vs. Li/Li^{+}), and then held there for 24 hr. This condition was used to examine whether or not the Mn ions were reduced and deposited as metallic Mn under the reduction conditions. To prevent other effects caused by solvent reduction, the potential was held at 1.0 V, which is higher than the known solvent reduction potential 0.8 V. In addition, the cell held at 1.0 V was discharged at a rate of C/15 to 2.5 V, which

is above the redox potential, and then kept at this potential for 24 hr. Under this condition, oxidation is expected to be favorable at the anode surface. To clearly identify the chemical state of the deposited Mn, we used the electrolyte with dissolved Mn ions at a concentration of around 2500 ppm.

To investigate the ion-exchange mechanism, lithium fluoride (LiF, Sigma-Aldrich), which is known to be one of the main components of the SEI, was immersed in both the Mn-free electrolyte and the Mn-containing electrolyte for one week. After soaking, the LiF was extracted from the electrolytes, and then vacuum dried overnight. The same procedure was performed using lithium carbonate (Li_2CO_3, Sigma-Aldrich), except for the storage time. Due to the lower solubility of Li_2CO_3 in the electrolyte, compared with LiF, the Li_2CO_3 was immersed for two weeks [22]. To exclude the possibility of HF reacting with the dissolved Mn ions, lithium perchlorate ($LiClO_4$, Sigma-Aldrich) was used as a salt and manganese perchlorate ($Mn(ClO_4)_2$, Sigma-Aldrich) was added to the electrolyte (1M $LiClO_4$ in EC:DMC (1:1, v/v)). The received $Mn(ClO_4)_2 \cdot 6H_2O$ was vacuum-dried at 100 °C for 24 h to remove any hydrated water residue.

For the investigation of the Mn distribution throughout the SEI layer, a composite electrode with Mn-containing electrolyte (2500 ppm) was cycled five times at a rate of C/15 and charged to 0.005 V. Then, it was stored at open-circuit potential for 1 month at room temperature.

Except for the samples taken to identify the Mn compounds that form on the anode and salts (LiF and Li_2CO_3), other cycled samples (HOPGs) were rinsed with the DMC solvent for 3 min to remove residual salts on samples. Rinsed and non-rinsed

samples were vacuum-dried overnight and then vacuum-sealed in a glove box in order to transfer them to the XPS instrument for the chemical analysis of the layer that formed during the experiment. XPS measurements were conducted using a Kratos Axis Ultra X-ray photoelectron spectrometer equipped with a monochromatic Al Kα excitation source ($h\nu$ = 1486.6 eV) in the University of Michigan Electron Microbeam Analysis Laboratory (EMAL). The area of the SEI layer analyzed was 300 × 700 μm^2. The binding energy scale was calibrated from intrinsic hydrocarbon contamination using the C 1s peak at 285 eV. Core spectra were recorded with 20 eV and 40 eV constant pass energy. The fitting of core peaks were performed using the Shirley background correction and Gaussian-Lorentzian curve synthesis (70% Gaussian, 30% Lorentzian). Charge neutralization was used during the measurements. Depth profiles were obtained by Ar-ion beam sputtering using an ion beam voltage of 4 keV.

Atomic force microscopy (AFM) was carried out on the HOPG sample to get the thickness profile of the SEI layer. After the 10th cycle, a square area of 2 × 2 μm^2 was scratched out in the contact mode at a constant force of 500 nN in order to remove the SEI layer from the surface. In the lateral force mode, the area was scraped off until the non-uniform friction, which was due to the SEI, changed to uniform friction, allowing observation of the appearance of the flat HOPG surface. Then, an area of 6 × 6 μm^2 which contains the scratched area was scanned again with a force less than 500 nN. Finally, 20 scan lines in the dotted square area of the height image were averaged to get the average height profile (Fig. 3.6), since the non-uniform SEI layer made it difficult to determine the SEI layer thickness.

RESULTS AND DISCUSSION

Influence of the dissolved Mn ions on the performance of the HOPG/Li cell

Figure 3.2 shows the cycling performance of HOPG/Li cells containing electrolytes with or without dissolved Mn ions, after the formation cycle. With the addition of dissolved Mn ions at a concentration of 200 ppm, the capacity degradation occurs more severely over 25 cycles. After 25th cycle, the Mn-free cells retain 85% of their original capacity, while the Mn-containing cells retain only 70%. The decrease in reversible capacity due the addition of Mn ions is consistent with the findings of other studies [12, 13, 16].

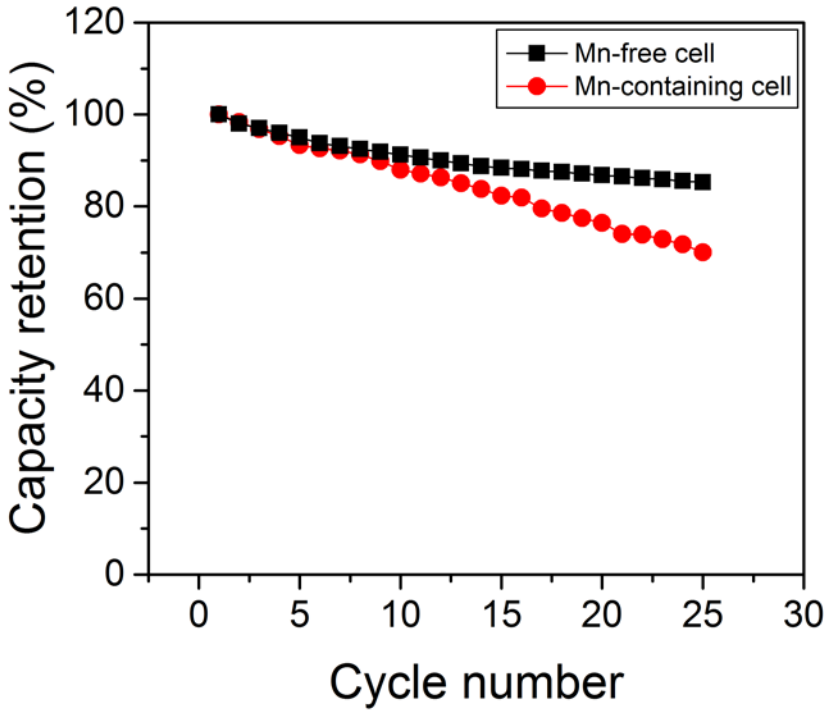

Figure 3-2. Discharge capacity retention of the HOPG/Li cell without/with dissolved Mn ions (200 ppm).

According to the previous studies, side reactions related to the deposition of Mn that accompanies the loss of electric charge are the main contributors to the reduction in

capacity [23]. In addition, continuous electrolyte decomposition products induced by the deposited Mn compounds may hinder the intercalation of lithium into the graphite, thereby reducing the reversibility of the lithium intercalation [12]. It has also been suggested that the capacity fade is caused by modification of the SEI layer, which is continuously reacting with dissolved Mn ions [16]. The capacity degradation of the cell due to the addition of Mn ions could be even more severe in the full-cell, such as a graphite/$LiMn_2O_4$ cell, which has an absolute capacity. The reduction in the number of cyclable lithium ions caused by the deposition of Mn and SEI reformation/growth additionally contributes to the capacity fade. In the graphite/Li half-cell used in this study, the capacity loss caused by the consumption of cyclable lithium is not considered due to the abundance of cyclable lithium.

Effects of the dissolved Mn ions on SEI chemical composition and growth

The differences between the SEI layers that form in electrolytes with and without Mn ions can be assessed by investigating the elemental compositions of these SEI layers. Figure 3.3 shows the relative amounts of the elements present in the SEI layers that form in Mn-free and the Mn-containing electrolytes after the 1st and 25th cycles. Note that the concentration of Mn cannot be determined in the Mn-containing (200 ppm) cells, since the Mn signal is barely detectable. It seems that the quantity of deposited Mn is below the detection limit (~1000 ppm) of XPS [11]. In reality, the Mn signal can be detected after a very long data-collection time (above 100 core scans), indicating that a very small concentration of Mn (below 0.1%) exists at the surface. Nevertheless, there is a noticeable difference in the chemical compositions of the SEI layers that form in the presence of electrolytes with and without dissolved Mn ions.

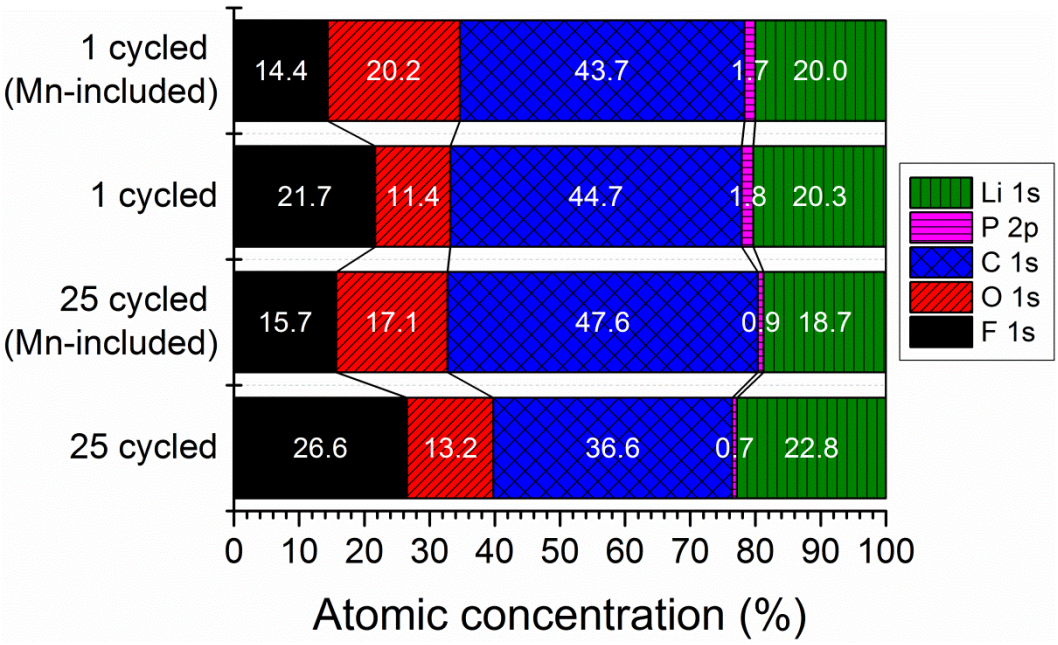

Figure 3-3. Comparison of the elemental compositions (atom %) of SEI layers formed in Mn-free and the Mn-containing electrolytes after the 1st cycle and the 25th cycle.

The SEI layer that forms in the Mn-containing electrolyte contains a higher concentration of oxygen, but a lower concentration of fluorine, than the SEI layer that forms in the presence of the Mn-free electrolyte. The difference in SEI composition is due to the formation of a number of oxygen-containing products caused by the Mn deposition. The oxygen-rich SEI layer might be attributed to either the deposition of oxygen-containing manganese compounds (MnO, Mn_2O_3, and $MnCO_3$), or the deposition of additional solvent decomposition products that result from the catalytic effect of the deposited Mn compounds. It has been reported that manganese oxides act as oxidation catalysts, promoting organic compound decomposition [12, 24]. Since a very low Mn concentration (below 0.1 %) is found in the SEI layer that forms in the Mn-containing electrolyte, the increased amount of oxygen in the Mn-containing cell must be mainly due

to the formation of more oxygen-containing organic/polymeric compounds, not oxygen-containing Mn compounds.

In the Mn-containing cell, the relative amounts of carbon and oxygen in the SEI layer are still significant after 25 cycles. On the other hand, a lower amount of carbon and a similar amount of oxygen are observed in the SEI layer that forms in the presence of Mn-free electrolyte after 25 cycles. It seems that the content of LiF increases considerably in the SEI layer during cycling, resulting in a significant increase in the quantity of fluorine in the Mn-free electrolyte. In contrast, a small increase in the fluoride content of the SEI layer that forms in Mn-containing electrolyte after 25 cycles indicates that the amount of organic/polymeric components (which consist of carbon and oxygen) in the SEI layer is greater than the increased amount of LiF over cycling. This also suggests that the SEI layer that forms in the Mn-containing electrolyte includes more organic/polymeric compounds (containing C and O) than the SEI layer that forms in the Mn-free electrolyte. This finding is further supported by the results of depth profiling (Fig. 3.4).

In the Mn-free cell, the amount of oxygen rapidly decreases after only 2 min of sputtering, declining below half the initial amount of oxygen. The observed trend of decreasing oxygen is consistent with the results of other studies [25-28]. In the Mn-containing cell, however, the oxygen content decreases more gradually, requiring 8~10 min of sputtering in order to decline below half the initial oxygen concentration. It is known that the initial decrease in oxygen content mainly originates from the removal of polymer and solvent reduction products, such as polyethylene oxide (PEO) and alkyl carbonates [25-27]. Thus, this result indicates that more oxygen-containing products

(possibly the organic/polymeric compounds) are present in the deeper SEI layer that forms in the Mn-containing cell. As mentioned above, since the quantity of Mn compounds observed in the SEI layer is extremely low, the contribution of oxygen-containing Mn compounds to the change in the oxygen content is negligible. Except for the oxygen, the changes in other elements as a function of depth are very similar in the Mn-free and the Mn-containing cells, following the generally observed trends [25-28].

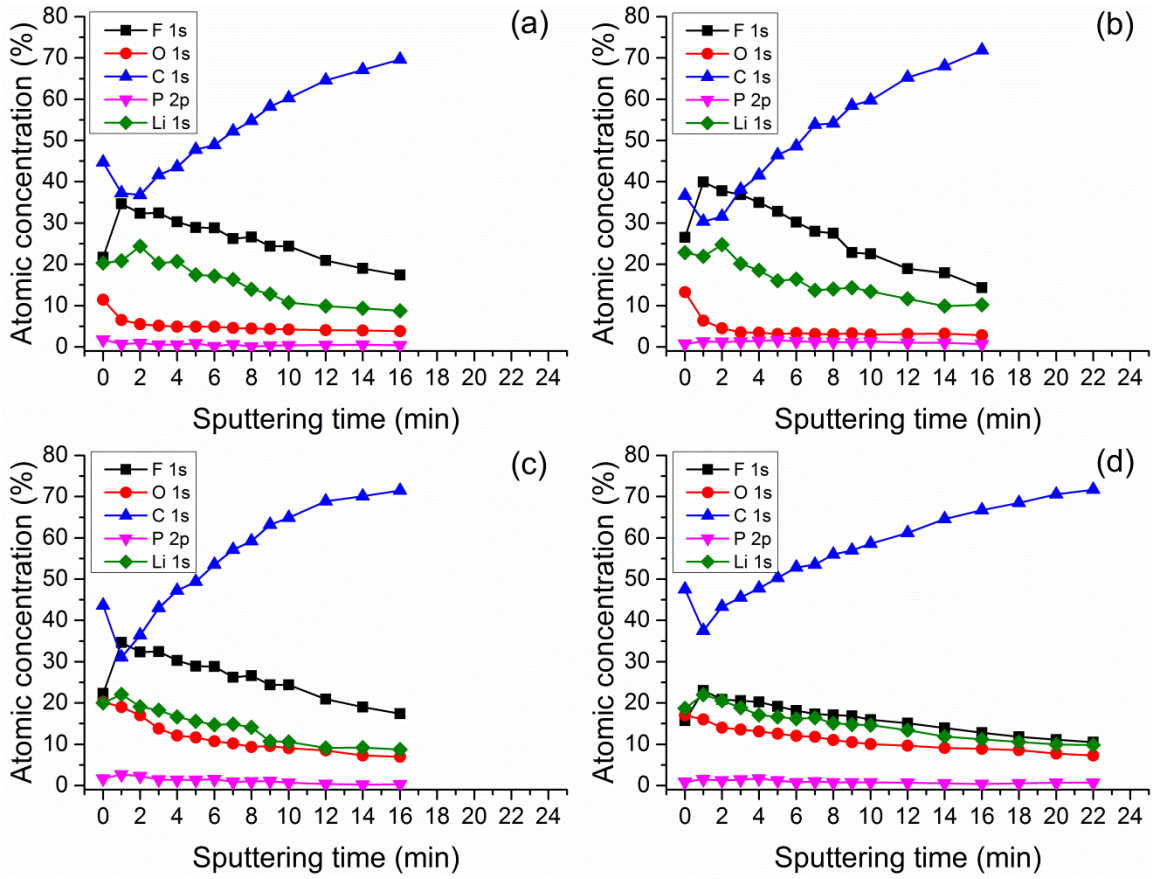

Figure 3-4. Depth profiles of HOPG surfaces after: (a) the 1st cycle, (b) the 25th cycle in Mn-free electrolyte; as well as after: (c) the 1st cycle, and (d) the 25th cycle in Mn-containing electrolyte.

The concentration of carbon initially decreases, which reflects the reduction of organic/polymeric species, and then increases with sputtering time, due to the contribution of the gradual exposure of the HOPG underlying the SEI layer. The initial

increases in fluorine and lithium reflect the increase in LiF content with the decrease in the organic/polymeric thin layer. The fluorine content decreases continuously with the gradual removal of LiF, while the lithium content decreases due to the reduction of lithium-containing organic and inorganic components, such as alkyl carbonates and Li_2CO_3.

Based on the sputtering time needed for the carbon content to exceed 70 %, the thickness of the SEI layer that forms in the Mn-containing electrolyte can be compared to that of the SEI layer that forms in the Mn-free electrolyte. After the 1st cycle, the thickness of the SEI layer that forms in the presence of Mn-containing electrolyte (Fig. 3.4c) is quite similar to that of the SEI layer that forms in the presence of the Mn-free electrolyte (Fig. 3.4a). It is well known that SEI formation mostly occurs in the 1st cycle, due to the reduction of the electrolyte. Thus, this result indicates that the influence of the dissolved Mn ions on the initial SEI layer growth is not significant during the formation process. However, the effect is clearly seen after the 25th cycle. The thickness of the SEI layer in the Mn-containing cell noticeably increases after 25th cycle. In the Mn-free cell, the thickness of the SEI layer after the 25th cycle (Fig. 3.4b) is almost identical with the thickness of the SEI layer after the 1st cycle (Fig. 3.4a). This result suggests that the SEI layer that forms without deposited Mn effectively suppresses further electrolyte decomposition, thereby limiting SEI growth. In contrast to the normal SEI layer, the SEI layer that forms with deposited Mn allows additional electrolyte decomposition over repeated cycles, showing a thicker SEI layer after the 25th cycle (Fig. 3.4d) than after the 1st cycle (Fig 3.4c).

The instability of the SEI layer due to the deposited Mn leads to the continuous growth of the SEI layer during cycling. As mentioned earlier, it is quite likely that the Mn compounds deposited in the SEI layer act as oxidation catalysts, promoting further electrolyte decomposition. As shown in the depth profile of the SEI layer that forms in the presence of Mn-containing electrolyte after the 25th cycle, a considerable amount of oxygen-containing products are deeply distributed throughout the outer part of SEI layer. This supports the possibility that deposited Mn compounds catalyze the decomposition of organic compounds.

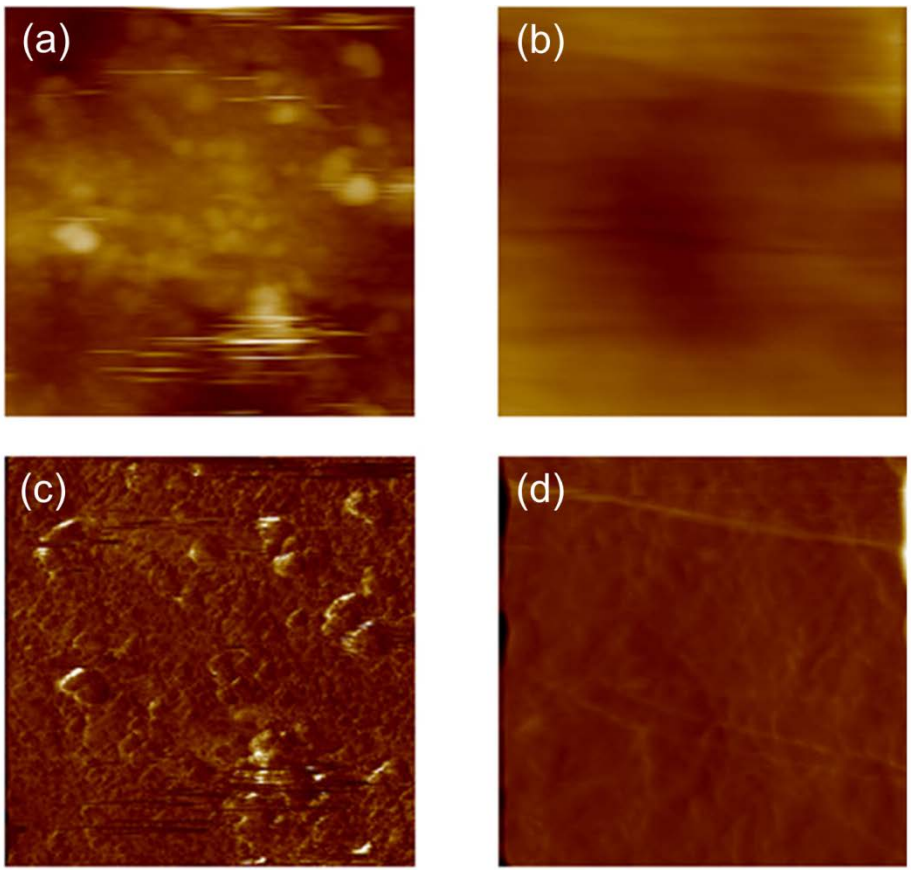

Figure 3-5. AFM height (a, b) and friction (c, d) images (2×2 μm^2) of HOPG after 10 cycles before scratching (a, c) and after scratching (b, d).

The increase in SEI thickness due to Mn deposition is also confirmed by AFM measurements. Figure 3.5 shows the changes in the AFM height and friction images on a HOPG basal plane. Non-uniform particle-like precipitates (SEI layer) form on the flat HOPG surface after cycling, which is consistent with the results of other studies [2, 14, 15]. In the lateral (friction) signals, the non-uniform friction image after cycling also indicates that the SEI layer completely covers the HOPG surface. After scraping the layer off using several repeated scans, the height and friction images of the scraped area become almost uniform, indicating that the HOPG surface is fully exposed.

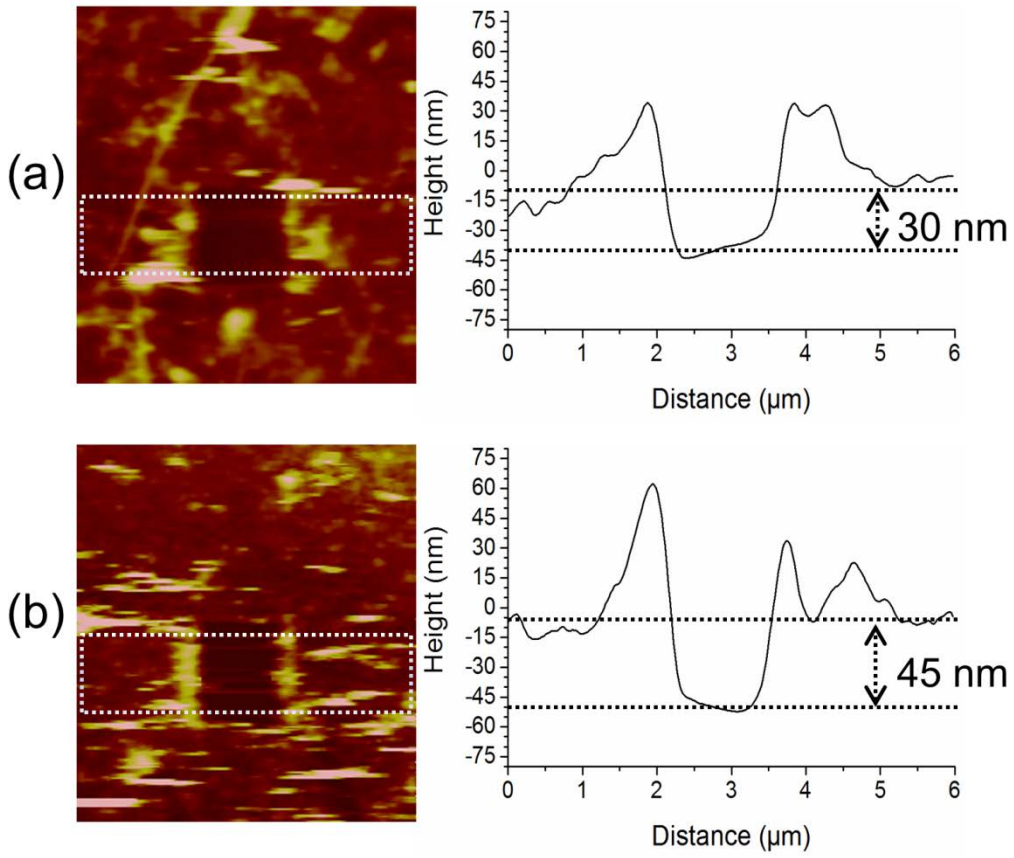

Figure 3-6. AFM height images and their corresponding averaged cross-sectional profiles of HOPGs cycled in (a) Mn-free electrolyte and (b) Mn-containing electrolyte.

The thickness of the SEI layer is estimated from the difference in height between the scratched and unscratched areas (Fig. 3.6). Due to the roughness of the SEI layer, the 20 scan lines in the dotted square area of the height image were averaged to get the average SEI height profile. It seems that the hills observed near the left and right of the scraped area are formed by the accumulation of material from the SEI layer removed during the scratching process. The thickness of the SEI layer formed in the presence of Mn-containing electrolyte is estimated to be roughly 45 nm, while the SEI layer formed in the presence of the Mn-free electrolyte has a thickness of about 30 nm. This implies that deposited Mn promotes electrolyte decomposition, resulting in a thicker SEI layer, which is consistent with the result obtained using XPS depth profiles.

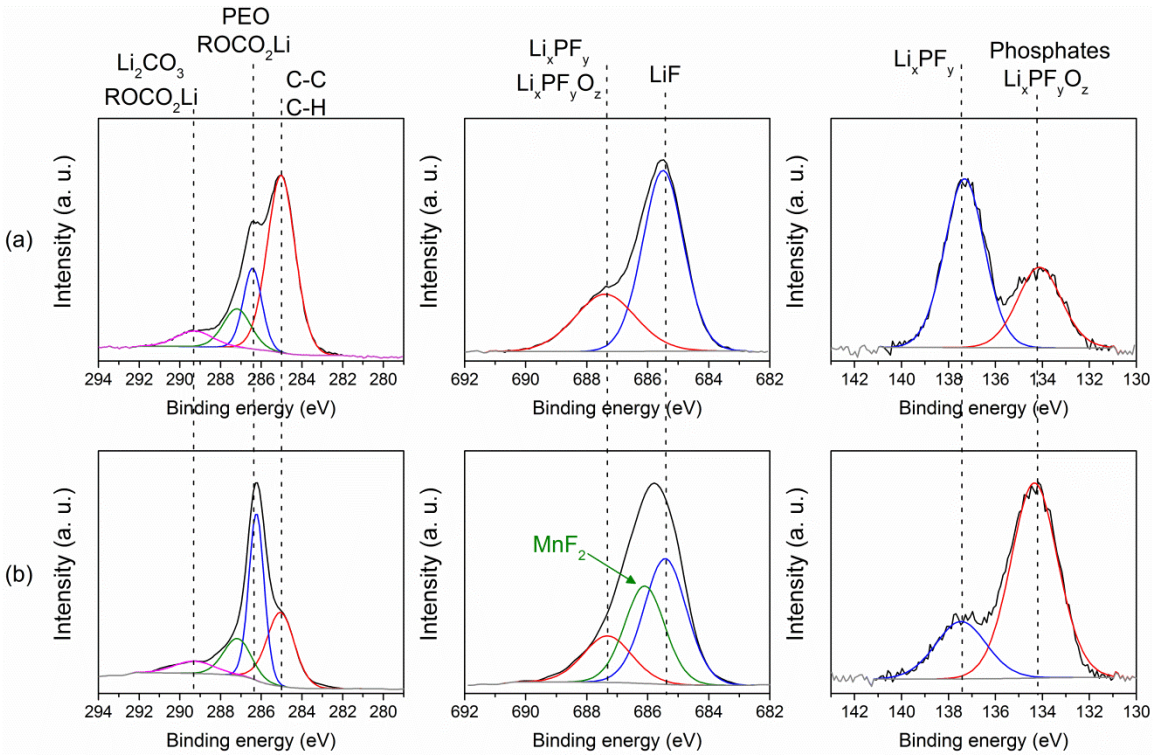

Figure 3-7. C 1s, F 1s, and P 2p XPS spectra of HOPGs cycled 25 times with: (a) Mn-free electrolyte and (b) Mn-containing electrolyte.

In order to further investigate the changes in SEI composition resulting from the deposited Mn compounds, high-resolution XPS spectra after the 25th cycle are compared (Fig. 3.7). In the C 1s spectra, the peak at 284.3 eV, assigned to graphite, is not observed, indicating that the HOPG surface is fully covered by the SEI layer. The C 1s spectra can be deconvoluted into three main peaks with an additional shoulder. The first peak, at 285.0 eV, is attributed to intrinsic hydrocarbons and alkane products (C-C and C-H bonds) [29, 30]. The second peak, at 286.3 eV with a small shoulder at 287.3 eV, could be assigned to ether carbons within the oligomeric polyethylene oxide (PEO) species ($-CH_2-CH_2-O-)_n$ and the lithium alkyl carbonates ($ROCO_2Li$). The presence of PEO and $ROCO_2Li$ in the SEI layer has been widely described in the literature [27-32]. The third peak, at 289.5 eV, which corresponds to $-CO_3-$ bonds, is associated with carbonate species such as lithium carbonate (Li_2CO_3) and lithium alkyl carbonate ($ROCO_2Li$) [27-32]. In the Mn-containing cell, this peak may also be associated with manganese carbonate ($MnCO_3$), which may have been deposited on the anode. Unfortunately, it is difficult to verify the presence of $MnCO_3$, since the peak at 289.5 V is relatively weak and broad. Based on the analysis of the C 1s spectra, the SEI species that form in the Mn-containing electrolyte are similar to those that form in the Mn-free electrolyte. However, the relatively high intensity is seen in the 286 ~ 287 eV region of the XPS spectrum of the sample cycled in the presence of the Mn-containing electrolyte, compared with the sample cycled in the Mn-free electrolyte. This result indicates that a considerable amount of organic species, such as PEO and $ROCO_2Li$, are formed during cycling in the Mn-containing cell. The increase of these compounds explains the formation of the oxygen-rich SEI layer in the Mn-containing cell, which is shown in Fig. 3.3 and Fig. 3.4. Thus,

these results provide additional evidence that the deposition of Mn compounds induces a greater amount of organic compound decomposition.

Noticeable differences are also observed in the F 1s and the P 2p spectra of the Mn-free and the Mn-containing samples. The F 1s spectra show that the SEI layers of both samples are composed of salt decomposition products, such as Li_xPF_y and/or $Li_xPF_yO_z$ (687.4 eV), and LiF (685.4 eV) [29]. The dominant peak from the sample cycled in the presence of the Mn-containing electrolyte is broadened and shifted to a higher binding energy (685.9 eV). This is also observed in the sample cycled in the presence of the Mn-free electrolyte. The broadened and shifted peak might be attributed to the presence of an additional compound near the peak at 685.9 eV. We suspect that the formation of MnF_2 might contribute to this shifting and broadening of the dominant peak. The P 2p spectra of both samples show two distinct peaks at 137.3 eV and 134.2 eV, regardless of the presence of deposited Mn. The peak at 137.3 eV can be assigned to an insoluble P-F compound (Li_xPF_y). The peak at 134.2 eV can be associated with $Li_xPF_yO_z$ compounds such as Li_2PFO_3 $LiPOF_2$, and/or phosphate compounds such as phosphate-ending PEO oligomer species [29-31]. The sample cycled in the Mn-containing electrolyte shows that the intensity of the peak at 134.2 eV increases relative to that of the peak at 137.3 eV. The increase in peak intensity at 134.2 eV indicates that more decomposition products of $LiPF_6$ are produced in the presence of the deposition of Mn compounds. This observation is similar to the results from samples cycled at high temperatures [29]. It was reported that $LiPF_6$ decomposition considerably increases at high temperatures and the reaction between highly reactive PF_5 and solvents produces some polymeric species [29, 33]. It seems that the deposition of Mn compounds causes

$LiPF_6$ instability, which could be another mechanism by which polymeric species are generated.

Identification of the Mn compounds deposited on the anode

To positively identify the Mn compounds that are deposited on the anode, a high concentration of Mn ions was dissolved in the electrolyte. As shown in Fig. 3.8, the amount of Mn compounds deposited increases as the concentration of Mn ions in the electrolyte increases. When the electrolyte contains Mn ions at a concentration of 200 ppm, the intensity of the peak corresponding to Mn is extremely low (almost invisible in the survey spectrum). Therefore, a considerably long scan time is required to detect the Mn signal in the core spectrum. The insufficient intensity of the Mn spectra may cause misinterpretation of the chemical state of the manganese species deposited on the anode, since determination of the position of the Mn $2p_{3/2}$ peak is confusing in the Mn 2p spectrum. Due to blurred signals in the XPS spectra caused by the small amount of Mn deposited on the anode, previous studies have experienced difficulties conclusively identification of the deposited Mn compound [11, 13, 19].

With a high concentration of dissolved Mn-ions (around 2500 ppm) in the electrolyte, the relative concentration of the element Mn on the anode surface is determined to be 2.2%, showing a clear Mn signal in the survey spectrum. The multiplet splitting of Mn 2p and Mn 3s peaks, in addition to the position of the Mn $2p_{3/2}$ peak are analyzed in an attempt to confirm the chemical state of the deposited Mn.

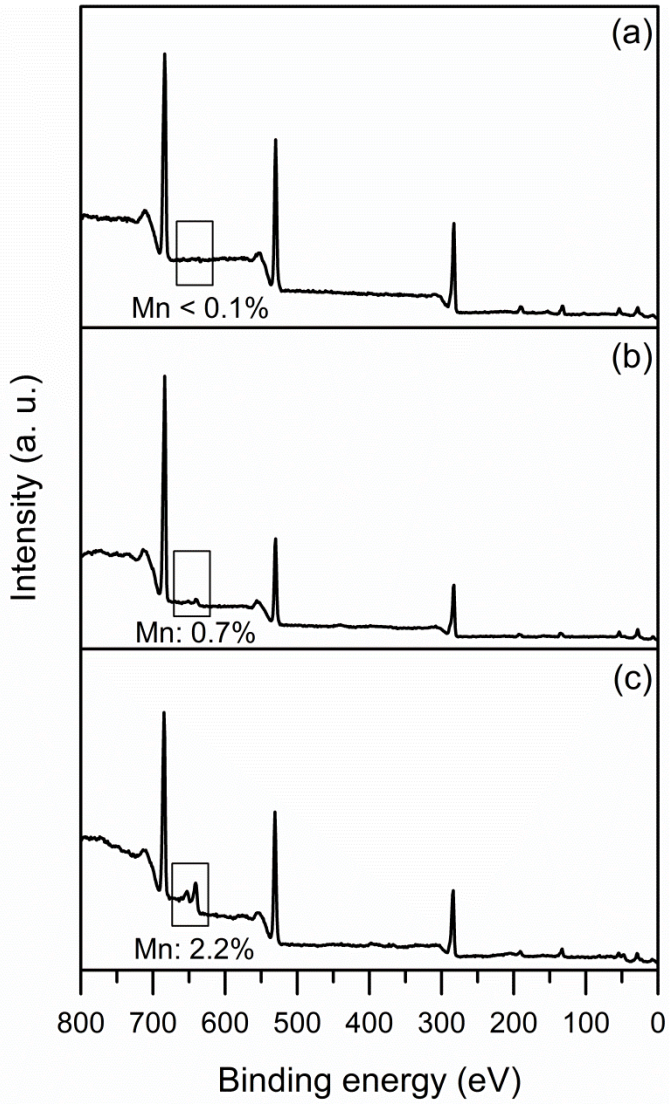

Figure 3-8. XPS survey spectra of negative electrodes after the 1st cycle in the presence of electrolytes containing Mn ions at concentrations of: (a) 200 ppm, (b) 1000 ppm, and (c) 2500 ppm.

It is believed that the dissolved Mn-ions may be reduced to form Mn metal during the deposition because of the standard redox potential of the Mn to Mn(Ⅱ) transition (1.87 V vs. Li/Li^+). To assess the electrochemical reduction of Mn-ions driven by the lowered potential, the cell is charged to 1.0 V. To prevent the influence of solvent reductions on the deposition of Mn, the cell is not charged below 1.0 V. Under this condition, which

favors reduction at the anode surface, MnF_2 is mainly formed; metallic Mn is not deposited on the anode surface (Fig. 3.9).

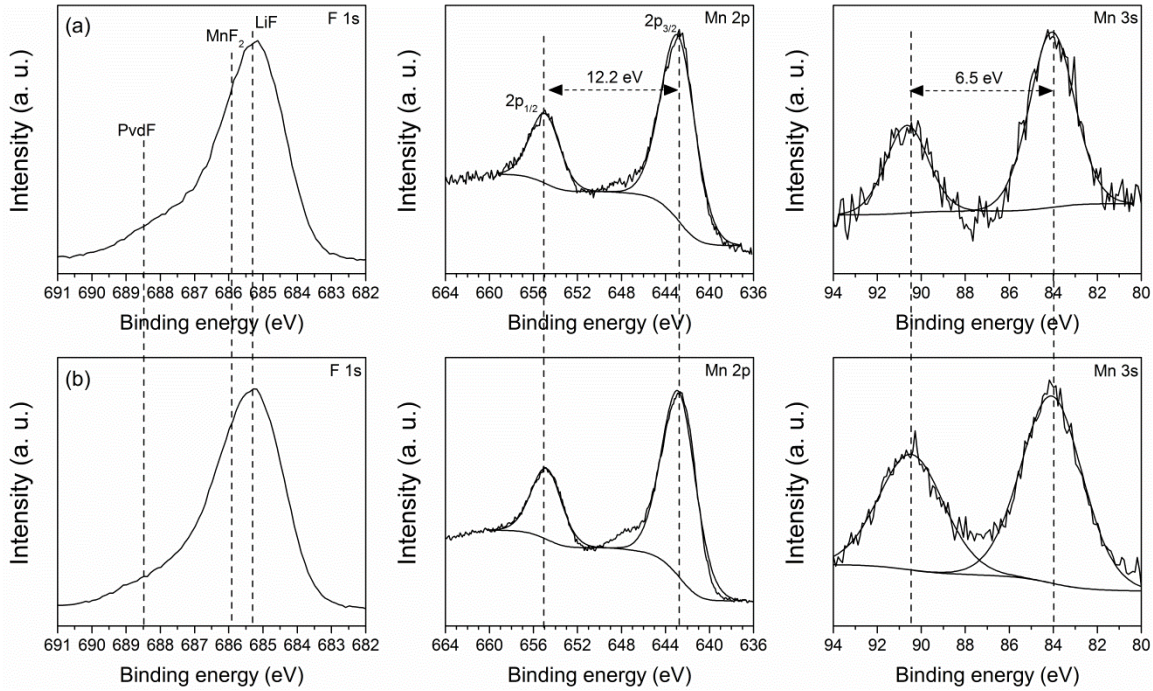

Figure 3-9. F 1s, Mn 2p, Mn 3s spectra of composite electrodes held for 24 h at (a) 1.0 V during the 1st charge (i.e., reductive condition at the anode) and (b) 2.5 V during the 1st discharge after the potential is held at 1.0 V (i.e., oxidative condition at the anode)

The asymmetry of the dominant peak (685.3 eV) in the F 1s spectrum (Fig. 3.9a) may be due to contributions from both LiF and MnF_2 (near 685.8 eV) formed on the surface. The formation of MnF_2 is also supported by analyses of the Mn 2p and Mn 3s spectra. In the Mn 2p core spectrum, the peak maximum of Mn $2p_{3/2}$ is observed at around 642.9 eV, which is very close to the maxima found in our reference MnF_2 (643 eV) and in other reports (642.7, 642.8 eV) [34, 35]. This peak position is far from that expected for metallic Mn (639.2 eV) and clearly higher than those observed for other Mn compounds, such as MnO (641.5, 641.7 eV) and $MnCO_3$ (642 eV) [34-36]. In addition, the multiplet splitting of the Mn 2p peak, which is the difference in binding energy

between the Mn $2p_{1/2}$ and the Mn $2p_{3/2}$, is 12.2 eV. The observed value is higher than the values found in metallic Mn (11.0 eV) and MnO (11.6 eV) [37, 38]. The observed value is similar to the values found for $MnCO_3$ (12.2 eV) and MnF_2 (12.1 eV), which are measured in our reference samples. The presence of MnF_2 on the surface is further confirmed by the observed multiplet splitting of the Mn 3s (6.5 eV) peak, which is the same as the values measured for the reference MnF_2 (6.5 eV) in this study and close to the values found in previous reports (6.3, 6.5 eV) [35, 39]. The observed multiplet splitting of the Mn 3s peak is significantly different than the value observed for metallic Mn (3.7 eV) [40]. The measured reference $MnCO_3$ shows a lower value (6.1 eV) and the values reported for other possible Mn compounds, such as MnO (5.5 eV), Mn_2O_3 (5.4 eV), and MnO_2 (4.6 eV), are considerably lower than the observed value (6.5 eV) [35].

Based on these observations, we believe that the majority of Mn is deposited in the form of MnF_2 particles, not metallic Mn. Our observation of MnF_2 formation is consistent with the results of a recent study [21]. They used TEM images to demonstrate that MnF_2 nanoparticles were formed at the graphite/electrolyte interface. However, it is possible that small amounts of the metallic Mn and other Mn compounds, such as $MnCO_3$ and the MnO, exist on the anode surface, as suggested by other researchers [9, 14, 20]. Note that the formation of Mn metal is mainly detected in the $LiClO_4$-based cells, as summarized in Table 3.1. This suggests that Mn metal might be formed predominantly in $LiClO_4$-based cells, rather than $LiPF_6$-based cells. In $LiPF_6$-based cells, MnF_2 compounds, which play the role of an electric insulator, seem to be formed initially on the surface, suppressing the further formation of metallic Mn on the surface [21].

To construct conditions favorable for oxidation at the anode surface, the cell is charged and held at 1.0 V, and then discharged and kept at 2.5 V, which is higher than the standard redox potential of Mn/Mn(Ⅱ). As shown in Fig. 3.9b, the MnF_2 that forms is not changed significantly, due to the oxidative conditions at the anode. This result indicates that the formation of MnF_2 on the anode surface is an irreversible reaction. It seems that the deposition of Mn ions and the formation of Mn compounds are not significantly affected by redox reactions or anode potentials, as suggested by a recent study [16]. They proposed that a metathesis reaction occurs between Mn ions and species in the SEI layer at the anode surface during Mn deposition, rather than a reduction reaction. Consistent with the study, we speculate that LiF in the SEI layer can react with the Mn^{2+} ions to form MnF_2 according to the following reactions:

$$LiPF_6 \leftrightarrow LiF\ (s) + PF_5 \qquad (1)$$

$$2LiF + Mn^{2+} \rightarrow MnF_2 + 2Li \qquad (2)$$

Alternatively, MnF_2 can be formed due to the acid HF environment. It has been suggested that the acid HF is considered as the main reason for MnF_2 formation on the cathode. The mechanism of MnF_2 formation on the cathode is as follows [41]:

$$2LiMn_2O_4 + 4HF \rightarrow 3MnO_2 + MnF_2 + 2LiF + 2H_2O \qquad (3)$$

In a similar manner, the formation of MnF_2 can occur at the anode according to the following series of reactions:

$$LiPF_6 \leftrightarrow LiF\ (s) + PF_5 \qquad (4)$$

$$PF_5 + H_2O \rightarrow POF_3 + 2HF \qquad (5)$$

$$2HF + Mn^{2+} \rightarrow MnF_2 + H_2 \qquad (6)$$

Thus, we believe that MnF_2 formation is caused by either ion-exchange reactions or the reactions of HF with Mn ions.

Mechanism of the formation of Mn compounds on the graphite anode

Two potential mechanisms of MnF_2 formation were introduced in the previous section. One involves ion-exchange reactions with Mn ions, and the other involves the reaction of HF with Mn ions. To elucidate the mechanism of the formation of Mn compounds, LiF and Li_2CO_3, which are known to be the main SEI products that form on the anode, were immersed in the Mn-containing electrolyte. To exclude the possibility of the HF-induced reaction mechanism, we used $LiClO_4$ and $Mn(ClO_4)_2$ salts, instead of $LiPF_6$ and $Mn(PF_6)_2$ salts in the electrolyte.

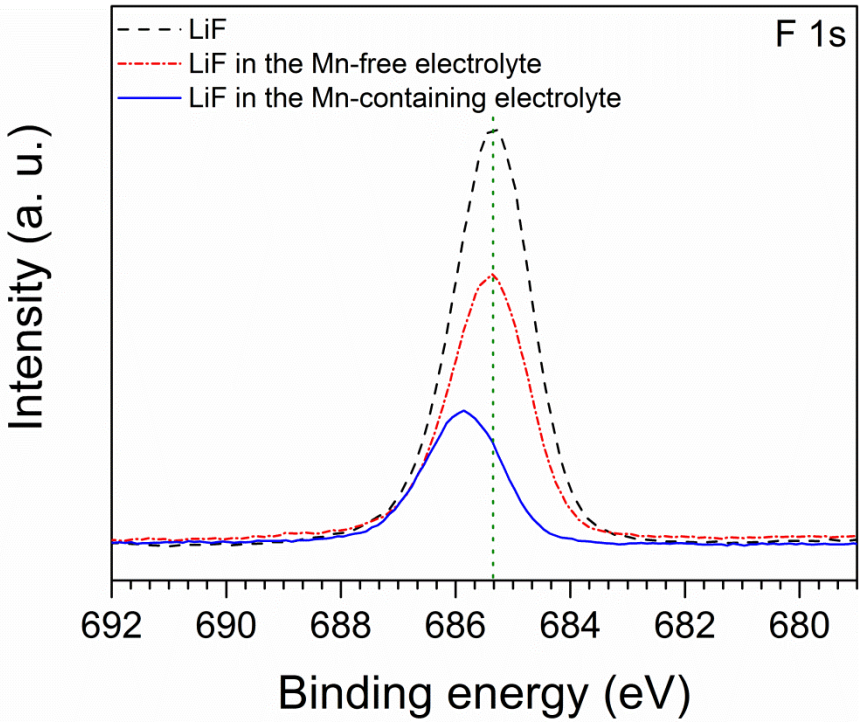

Figure 3-10. Changes in the F 1s spectrum of LiF after soaking in an electrolyte with or without Mn ions.

Figure 3.10 shows that LiF powder (685.3 eV in F 1s spectrum) does not change its binding energy in the presence of a normal electrolyte. The intensity of the LiF in the electrolyte is slightly reduced compared with that of bare LiF, since the residual solvents and decomposition products cover the LiF powder. However, the peak associated with LiF is shifted to higher binding energy (685.8 eV) in the Mn-containing electrolyte. The peak observed at the higher binding energy can be explained by the fact that the fluorine is bonded to manganese, which has a higher electronegativity than lithium. This result indicates that LiF reacts with Mn ions in the electrolyte, forming MnF_2. The formation of MnF_2 is confirmed by the Mn 2p spectrum shown in Fig. 3.11.

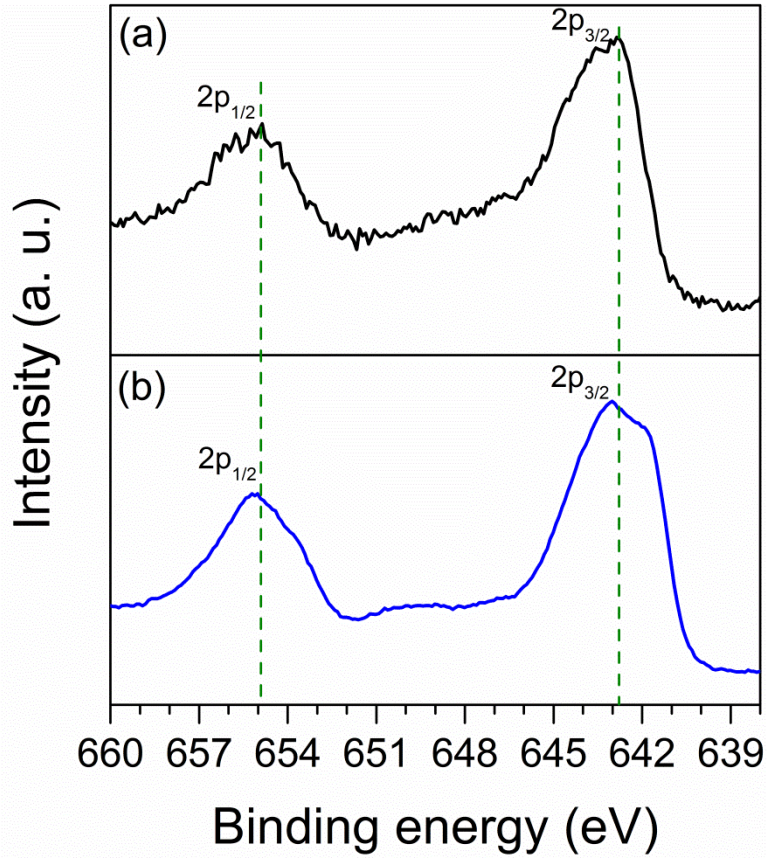

Figure 3-11. Comparison of the Mn 2p spectra of (a) LiF soaked in Mn-containing electrolyte and (b) a reference sample of MnF_2.

The Mn 2p spectrum of LiF soaked in the Mn-containing electrolyte is very similar to that of the reference MnF_2 compound. It suggests that a portion of the LiF is converted to MnF_2. Note that the peak intensity in the F 1s spectrum (Fig. 3.10) decreases more in the Mn-containing electrolyte than in the normal electrolyte. This may indicate that the process responsible for the formation of MnF_2 promotes further solvent decomposition. In conclusion, it is clear that the ion-exchange phenomenon happens between the LiF that forms in the SEI layer and dissolved Mn ions at the graphite/electrolyte interface and that further solvent decomposition can occur during the reaction process.

Soaking Li_2CO_3 powders in Mn-free electrolyte and in Mn-containing electrolyte allows further examination of this mechanism.

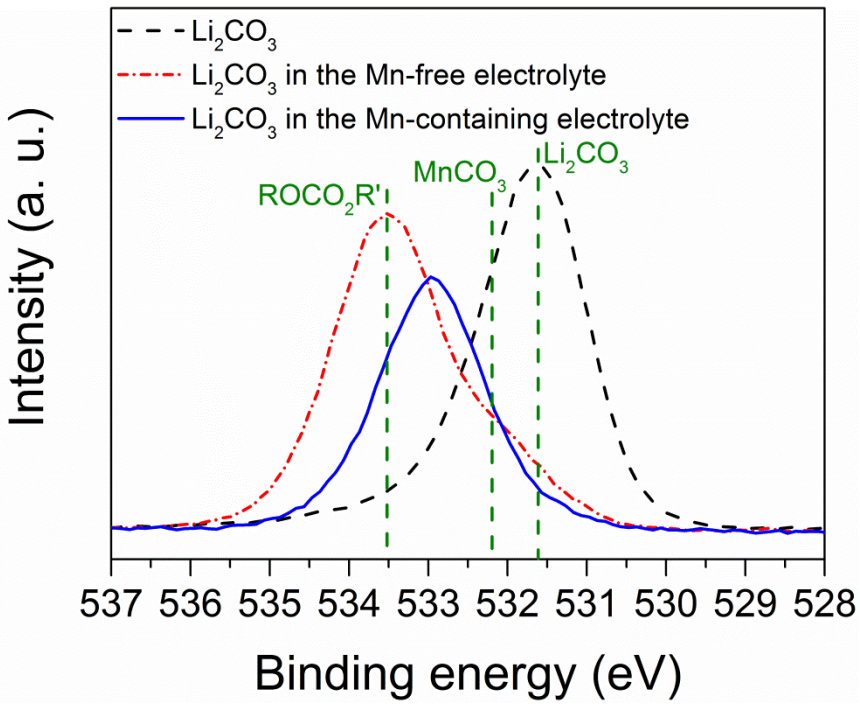

Figure 3-12. Changes in the O 1s spectrum of Li_2CO_3 after soaking in an electrolyte with or without Mn ions.

As shown in Fig. 3.12, the peak associated with the bare Li_2CO_3 is located at 531.6 eV in the O 1s spectrum. The Li_2CO_3 powder soaked in the Mn-free electrolyte has a dominant peak (533.5 eV) with a small shoulder (531.5-532.5 eV). The shoulder can be assigned to Li_2CO_3, while the peak at 533.5 eV corresponds to carbonate esters ($ROCO_2R'$) that originate from solvent residues and decomposition products, such as lithium alkyl carbonate species. The strong peak is shifted to lower binding energy (533 eV) in the presence of Mn ions in the electrolyte. This may result from an additional contribution from $MnCO_3$ (532.2 eV), which has a slightly higher binding energy than Li_2CO_3 (531.6 eV) [42]. As in the case of LiF, the reduced intensity of the dominant peak is also observed. The Mn 2p spectrum supports the formation of $MnCO_3$. The Mn 2p spectrum collected from the Li_2CO_3 powder soaked in the Mn-containing electroltye resembles that of reference $MnCO_3$, as shown in Fig. 3.13.

The Mn $2p_{3/2}$ peak maximum is located at approximately 642 eV, showing multiplet splitting of 12.2 eV. In addition, the presence of two satellite peaks near both the Mn $2p_{3/2}$ and $2p_{1/2}$ (marked as S in Fig. 3.13) is very similar to the satellite structure of the reference $MnCO_3$. Satellite structure is an important factor that has been used to identify Mn chemical states. The spectrum of MnO has satellite peaks associated with both the Mn $2p_{3/2}$ and Mn $2p_{1/2}$ peaks, while the spectra of Mn_2O_3 and MnO_2 have satellite peaks associated with only their Mn $2p_{1/2}$ peaks [38]. Although MnO has also two satellite peaks associated with its Mn $2p_{3/2}$ and Mn $2p_{1/2}$ peaks, the peak positions of Mn $2p_{3/2}$ (640.6 eV) and O 1s (529.6 eV) are much lower than those of $MnCO_3$ [38]. This clearly indicates that the observed Mn 2p spectrum corresponds to that of $MnCO_3$, not

MnO. Thus, the results show that the Li_2CO_3 is partially converted to $MnCO_3$ through the ion exchange reaction.

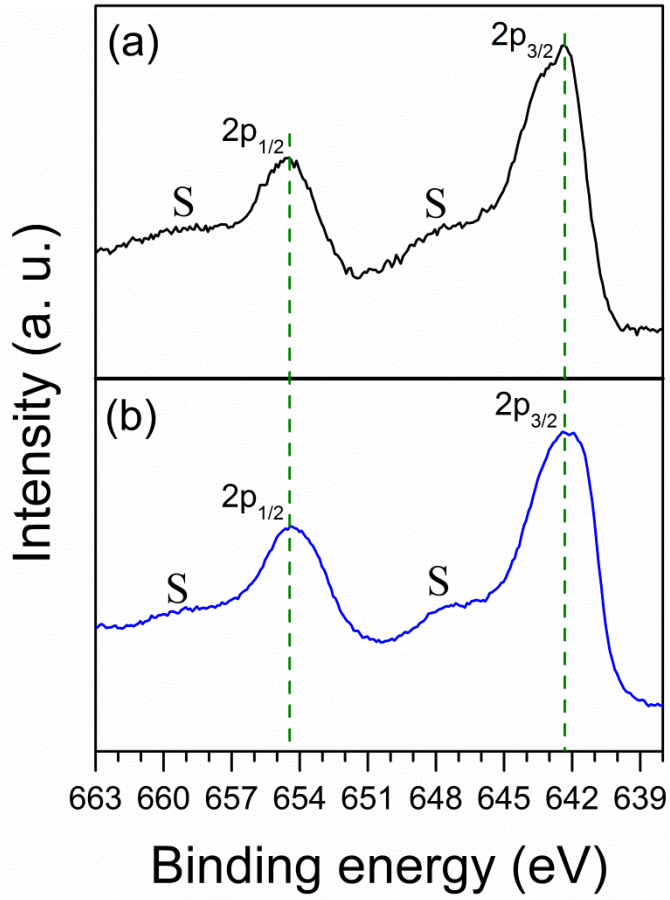

Figure 3-13. Comparison of the Mn 2p spectra of (a) Li_2CO_3 soaked in Mn-containing electrolyte and (b) a reference sample of $MnCO_3$.

Based on these findings, we propose that reactions can occur between inorganic species and dissolved Mn ions, transforming SEI species into diverse Mn compounds, such as MnF_2 and $MnCO_3$. During the reaction process, additional decompositions of the electrolyte may take place at the anode/electrolyte interface.

Spatial distribution of the Mn compounds at the graphite/electrolyte interface

In order to gain further information about the interactions of dissolved Mn ions at the anode/electrolyte interface, it is necessary to understand how the deposited Mn is distributed at the anode/electrolyte interface. Figure 3.14 shows the depth profile of the aged anode, revealing the distribution of Mn element throughout the graphite/electrolyte interface. The Mn profile shows that Mn is not uniformly distributed at the graphite/electrolyte interface. A small amount of the Mn is observed at the top surface of the interface, indicating that the deposition of dissolved Mn ions is not severe in the region of the porous organic layer. Mn reaches its maximum after about 60 minutes of Ar-ion sputtering, at which point the graphite anode starts to appear, as evidenced by a sharp increase in carbon. This result suggests that the dissolved Mn ions are mostly deposited near the inorganic layer/graphite interface, suggesting that the inorganic layer can be significantly affected by the dissolved Mn ions. It seems that the dissolved Mn ions easily diffuse through the porous organic SEI layer and interact with the inorganic species, possibly as a result of the ion exchange mechanism, as evidenced by previous results.

The tendency of Mn accumulation in the inorganic layer/graphite interfacial region is consistent with the results observed in aged commercial cells [11]. The diffusion of lithium ions may be more hindered by the deposition of inorganic Mn compounds, such as MnF_2 and $MnCO_3$, which can limit the capacity of the Li-ion battery. Note that Mn is still observable at the end of sputtering, at which point the graphite surface is almost fully exposed by removal of the SEI layer. The small amount of Mn that can be detected inside the graphite suggests that dissolved Mn ions may co-intercalate or move

into the graphite interlayer via either defects in the SEI layer or cracks in the graphite. It has been recently observed that Mn nanoparticles are present within cracks in the graphite, suggesting that Mn compounds can be deposited internally [21].

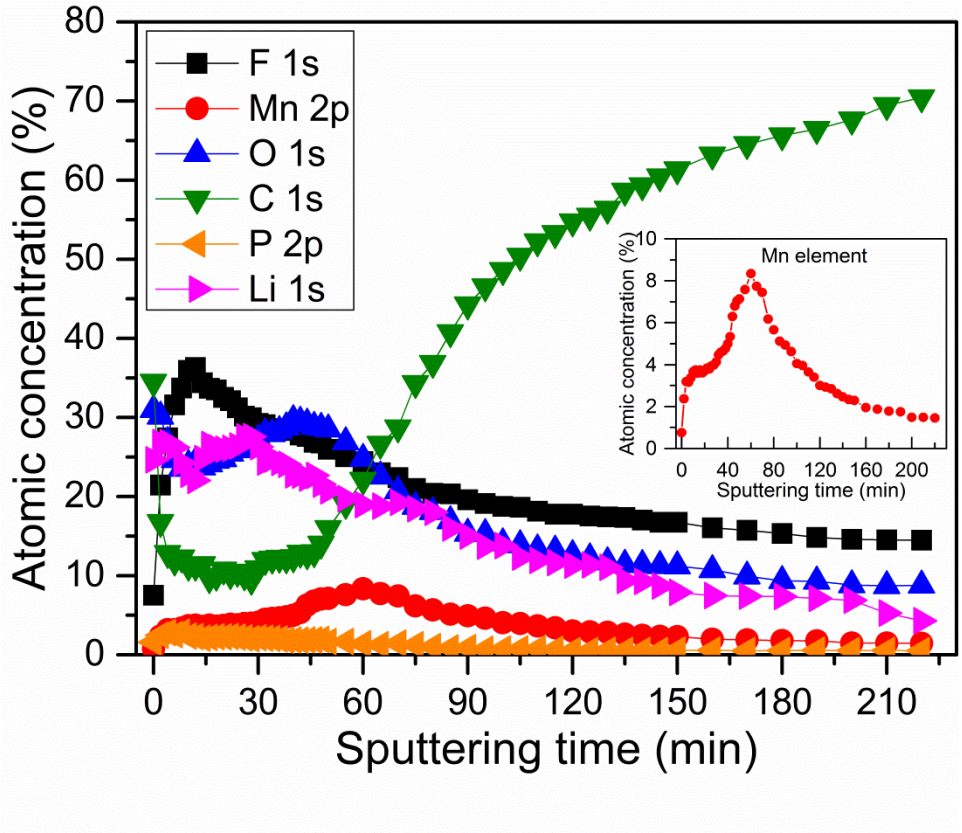

Figure 3-14. XPS depth profile of a composite electrode cycled in Mn-containing electrolyte during formation, and then stored for one month. The inset contains an enlargement of the profile of the Mn element.

In addition, disorder in the graphite surface structure due to deposition of iron has been observed [43]. Although the observed Mn content may be associated with an artifact of the sputtering process that can cause the re-deposition of sputtered Mn, there is a strong possibility that Mn ions are deposited between graphite interlayers, which may inhibit the contraction and expansion of the graphite during the (de)intercalation process.

The structural disorder of the graphite due to Mn deposition and its effects are currently under investigation.

CONCLUSIONS

Deterioration of the SEI layer due to the deposition of dissolved Mn ions significantly contributes to the degradation of Li-ion battery capacity. In this work, the chemical degradation of the SEI layer induced by dissolved Mn ions and its mechanism has been systematically investigated. The chemical composition of the SEI layer formed in the presence of dissolved Mn ions shows a more oxygen-rich layer. This layer originates from an increased amount of organic/polymeric species that result from additional electrolyte decompositions catalyzed by Mn deposition and interaction processes of the dissolved Mn ions. XPS and AFM measurements revealed that SEI growth is accelerated by the deposition of dissolved Mn ions, showing a thicker SEI layer on the anode. The dissolved Mn ions easily diffuse through the porous SEI layer and mostly deposit at the inorganic layer/graphite interface region, where the Mn ions interact with inorganic SEI species via the ion-exchange mechanism. The main Mn compound formed on the anode surface is identified as MnF_2, which is not much affected by reductive/oxidative conditions. The dissolved Mn ions may diffuse or co-intercalate into the graphite through both defects in the SEI layer and cracks in the graphite due to structural disordering induced by Mn deposition.

The findings from this work deepen our understanding of SEI degradation mechanisms at elevated temperatures. Both the high temperature itself and the increased deposition of dissolved Mn-ions significantly affect the instability of the SEI layer.

Improving the stability of the SEI layer at elevated temperatures will require strategies that that suppress the interaction of dissolved Mn ions with the SEI layer, as well as the development of a thermally stable SEI layer.

BIBLIOGRAPHY

[1] J. Vetter, P. Novak, M.R. Wagner, C. Veit, K.C. Moller, J.O. Besenhard, M. Winter, M. Wohlfahrt-Mehrens, C. Vogler, A. Hammouche, *J. Power Sources*, **147**, 269 (2005).

[2] M. Inaba, H. Tomiyasu, A. Tasaka, S.K. Jeong, Z. Ogumi, *Langmuir*, **20**, 1348 (2004).

[3] T. Zheng, A.S. Gozdz, G.G. Amatucci, *J. Electrochem. Soc.*, **146**, 4014 (1999).

[4] T. Aoshima, K. Okahara, C. Kiyohara, K. Shizuka, *J. Power Sources*, **97-8**, 377 (2001).

[5] Y. Terada, Y. Nishiwaki, I. Nakai, F. Nishikawa, *J. Power Sources*, **97-8**, 420 (2001).

[6] Y. Matsuo, R. Kostecki, F. McLarnon, *J. Electrochem. Soc.*, **148**, A687 (2001).

[7] D. Kim, S. Park, O.B. Chae, J.H. Ryu, Y.U. Kim, R.Z. Yin, S.M. Oh, *J. Electrochem. Soc.*, **159**, A193 (2012).

[8] I.H. Cho, S.S. Kim, S.C. Shin, N.-S. Choi, *Electrochem. Solid St.*, **13**, A168 (2010).

[9] C. Delacourt, A. Kwong, X. Liu, R. Qiao, W.L. Yang, P. Lu, S.J. Harris, V. Srinivasan, *J. Electrochem. Soc.*, **160**, A1099 (2013).

[10] W. Choi, A. Manthiram, *J. Electrochem. Soc.*, **153**, A1760 (2006).

[11] D.P. Abraham, T. Spila, M.M. Furczon, E. Sammann, *Electrochem. Solid St.*, **11**, A226 (2008).

[12] S. Komaba, N. Kumagai, Y. Kataoka, *Electrochim. Acta*, **47**, 1229 (2002).

[13] S. Komaba, T. Itabashi, T. Ohtsuka, H. Groult, N. Kumagai, B. Kaplan, H. Yashiro, *J. Electrochem. Soc.*, **152**, A937 (2005).

[14] M. Ochida, Y. Domi, T. Doi, S. Tsubouchi, H. Nakagawa, T. Yamanaka, T. Abe, Z. Ogumi, *J. Electrochem. Soc.*, **159**, A961 (2012).

[15] M. Ochida, T. Doi, Y. Domi, S. Tsubouchi, H. Nakagawa, T. Yamanaka, T. Abe, Z. Ogumi, *J. Electrochem. Soc.*, **160**, A410 (2013).

[16] C. Zhan, J. Lu, A. Jeremy Kropf, T. Wu, A.N. Jansen, Y.K. Sun, X. Qiu, K. Amine, *Nat. Comms.*, **4**, 2437 (2013).

[17] A.V. Plakhotnyk, L. Ernst, R. Schmutzler, *J. Fluorine Chem.*, **126**, 27 (2005).

[18] K. Amine, J. Liu, S. Kang, I. Belharouak, Y. Hyung, D. Vissers, G. Henriksen, *J. Power Sources*, **129**, 14 (2004).

[19] L. Yang, M. Takahashi, B.F. Wang, *Electrochim. Acta*, **51**, 3228 (2006).

[20] S.R. Gowda, K.G. Gallagher, J.R. Croy, M. Bettge, M.M. Thackeray, M. Balasubramanian, *Phys. Chem. Chem. Phys.*, **16**, 6898 (2014).

[21] X. Xiao, Z. Liu, L. Baggetto, G.M. Veith, K.L. More, R.R. Unocic, *Phys. Chem. Chem. Phys.*, **16**, 10398 (2014).

[22] K. Tasaki, A. Goldberg, J.J. Lian, M. Walker, A. Timmons, S.J. Harris, *J. Electrochem. Soc.*, **156**, A1019 (2009).

[23] T. Tsujikawa, K. Yabuta, T. Matsushita, M. Arakawa, K. Hayashi, *J. Electrochem. Soc.*, **158**, A322 (2011).

[24] Y.F. Shen, R.P. Zerger, R.N. Deguzman, S.L. Suib, L. McCurdy, D.I. Potter, C.L. Oyoung, *Science*, **260**, 511 (1993).

[25] D. Bar-Tow, E. Peled, L. Burstein, *J. Electrochem. Soc.*, **146**, 824 (1999).

[26] A.M. Andersson, K. Edstrom, *J. Electrochem. Soc.*, **148**, A1100 (2001).

[27] V. Eshkenazi, E. Peled, L. Burstein, D. Golodnitsky, *Solid State Ionics*, **170**, 83 (2004).

[28] A.M. Andersson, A. Henningson, H. Siegbahn, U. Jansson, K. Edstrom, *J. Power Sources*, **119**, 522 (2003).

[29] A.M. Andersson, D.P. Abraham, R. Haasch, S. MacLaren, J. Liu, K. Amine, *J. Electrochem. Soc.*, **149**, A1358 (2002).

[30] R. Dedryvere, S. Laruelle, S. Grugeon, L. Gireaud, J.M. Tarascon, D. Gonbeau, *J. Electrochem. Soc.*, **152**, A689 (2005).

[31] R. Dedryvere, H. Martinez, S. Leroy, D. Lemordant, F. Bonhomme, P. Biensan, D. Gonbeau, *J. Power Sources*, **174**, 462 (2007).

[32] H. Tavassol, J.W. Buthker, G.A. Ferguson, L.A. Curtiss, A.A. Gewirth, *J. Electrochem. Soc.*, **159**, A730 (2012).

[33] X. Zhang, P.N. Ross, R. Kostecki, F. Kong, S. Sloop, J.B. Kerr, K. Striebel, E.J. Cairns, F. McLarnon, *J. Electrochem. Soc.*, **148**, A463 (2001).

[34] A. Aoki, *JPN. J. Appl. Phys.*, **15**, 305 (1976).

[35] J.C. Carver, T.A. Carlson, Schweitz.Gk, *J. Chem. Phys.*, **57**, 973 (1972).

[36] J. Yuan, J. Zhu, H. Bi, Z. Zhang, S. Chen, S. Liang, X. Wang, *RSC Adv.*, **3**, 4400 (2013).

[37] A. Lebugle, U. Axelsson, R. Nyholm, N. Martensson, *Phys. Scr.*, **23**, 825 (1981).

[38] M. Oku, K. Hirokawa, S. Ikeda, *J. Electron. Spectrosc. Relat. Phenom.*, **7**, 465 (1975).

[39] C.S. Fadley, D.A. Shirley, A.J. Freeman, P.S. Bagus, J.V. Mallow, *Phys. Rev. Lett.*, **23**, 1397 (1969).

[40] V. Dicastro, G. Polzonetti, *J. Electron. Spectrosc. Relat. Phenom.*, **48**, 117 (1989).

[41] O.K. Park, Y. Cho, S. Lee, H.C. Yoo, H.-K. Song, J. Cho, *Energy Environ. Sci.*, **4**. 1621 (2011).

[42] O.W. Duckworth, S.T. Martin, Geochim. *Cosmochim. Acta*, **68**, 607 (2004).

[43] Y. Lai, Z. Cao, H. Song, Z. Zhang, X. Chen, H. Lu, M. Jia, J. Li, *J. Electrochem. Soc.*, **159**, A1961 (2012).

CHAPTER IV.
COMPONENT-/STRUCTURE-DEPENDENT ELASTICITY OF THE SEI IN Li-ION BATTERIES[*]

INTRODUCTION

The performance of a Li-ion battery—such as irreversible capacity loss, 1st cycle columbic efficiency, and cycle/calendar life—is closely related to the properties of the solid electrolyte interface (SEI) layer [1–5]. The SEI layer that formed on the negative electrode during the initial few cycles is known as an ionic conductor for lithium but not an electronic conductor, thereby it protects the electrode from further reductive decomposition of the electrolyte during subsequent cycles. It enables a Li-ion battery to maintain its good capacity retention even if the battery operates below the reduction potential of electrolytes. This is the case, however, only if a perfect and stable SEI layer is formed and maintained during the cycling. In reality, the SEI layer does not keep its initial configuration and properties [6]. The aging or degradation process of the SEI layer proceeds to a low extent and at a low rate for the whole cycle/calendar life of Li-ion batteries [5, 6]. For instance, dissolution/breakdown, conversion, and growth of the SEI layer can occur during prolonged storage and cycling, especially at high temperatures [3, 5, 7–9]. The phenomena cause changes in SEI layer properties, such as composition and morphology, so that the electrons and solvents could be permeable in a defective SEI

[*] This chapter includes content from a published paper: H. Shin, J. Park, S. Han, A.M. Sastry, and W. Lu, *Journal of Power Sources*, 277 (2015) 169-179.

layer, leading to additional electrolyte decomposition. Continuous decomposition reactions promote further SEI formation or SEI reconstruction, thickening the SEI layer and consuming cyclable lithium-ions. It has been shown that the SEI growth rate slows with time but never stops entirely during long-term storage and cycling [5]. However, if the initially formed SEI layer has desirable and effective properties for SEI stability, the SEI growth rate can be diminished or even come close to stopping entirely, improving the capacity retention of Li-ion batteries. Thus, having an understanding and clarification of the SEI properties in terms of mechanical and chemical aspects is the first important step in achieving the stability of the SEI layer, and eventually the enhancement of the cycle/calendar life of Li-ion batteries.

Many efforts have been made recently to elucidate the structure, morphology, chemical composition, and thickness of the SEI layer on a negative electrode. Inhomogeneous mosaic-type or multilayered-type SEI structure models have been proposed based on the SEI layer formation process via 2D surface reduction [10, 11]. A 3D SEI model, including the intercalation of decomposition products into the graphite interlayer, as well as the attachment of the products to the graphite surface, has been also suggested [12]. Although no consensus on the detailed SEI structure has yet been reached, it is generally accepted that the SEI layer is composed of two distinct layers: a thin, dense layer of inorganic species close to the electrode side, and a thick, porous layer of organic and polymeric compounds close to the electrolyte side. The inorganic species such as lithium fluoride (LiF), lithium carbonate (Li_2CO_3), and lithium oxide (Li_2O) are typically believed to exist as a polycrystalline or crystalline phase, while the organic components such as dilithium ethylene dicarbonate ($[CH_2OCO_2Li]_2$, Li_2EDC), lithium methyl

carbonate ($LiOCO_2CH_3$, LiMC), and lithium ethyl carbonate ($LiOCO_2C_2H_5$, LiEC) are commonly reported to present as a form of amorphous structure [9, 13, 14]. In addition, the formation of a long-chain oligomer or polymeric compound such as polyethylene oxide (PEO) has also been reported [14, 15]. The chemical composition of the SEI layer is dependent on the solvents and salts used as the electrolytes. The thickness of the SEI layer has been observed to be in the range of tens to hundreds of nanometers [13, 16]. Since SEI thickness as well as SEI composition can be influenced by artifacts in measurements and different experimental conditions, the reported values vary from one another.

While numerous studies have been aimed at elucidating SEI formation mechanisms and physical/chemical properties of the SEI layer, relatively little attention has been paid to the mechanical properties of the SEI layer, especially SEI elasticity. During the repeated cycles, the particles of the negative electrode experience volume change, stress, and pressure build-up due to intercalation-induced strain and gas production, which can initiate the physical damage or the instability of the SEI layer as well as the particle surface of the electrode [16, 17]. It has recently been observed that stress change at the surface of a negative electrode is closely related to the SEI layer formation [18]. If a stiff SEI layer is formed on the surface of a negative electrode, the SEI layer can be partially broken down due to the stress caused by the intercalation of the Li-ions, which promotes further SEI layer formation by re-exposing the new electrode surface to the electrolyte. This SEI formation and regrowth contributes to a continuous decrease in the capacity of Li-ion batteries. Therefore, an endurable SEI layer is desirable

to maintain the mechanical stability of the SEI layer, and to get better adhesion between the electrode and the SEI layer in order to keep the passivation effect.

Recently, a few experimental or computational studies have been conducted to evaluate the elastic properties of the SEI layer. The Atomic Force Microscopy (AFM)-based nano-indentation technique has been used to quantitatively investigate the elastic modulus of the SEI layer. A different surface contact stiffness of the SEI layer on a silicon anode was observed by adding the silane additive in the electrolyte [19]. It was also found that the Young's modulus of the SEI layer on an MnO anode changes during the SEI formation process [20]. In addition to experimental observations, atomistic simulations were used to predict the elastic modulus of the SEI layer. A molecular dynamics simulation using the ReaxFF potential suggested that ethylene carbonate (EC)-based SEI layer is stiffer than the dimethyl carbonate (DMC)-based SEI layer [21].

As mentioned earlier, the composition and structure of the SEI layer is quite dependent on the system including the anode material, the electrolyte, and the initial formation environment. Furthermore, the mechanical properties of the SEI layer are closely related to the composition and structure of the SEI layer. Previous studies, however, have not provided SEI elasticity based on its chemical composition and structure [19, 20]. Consequently, a study on the component-/structure-dependent SEI elasticity can provide useful guidance for building a more robust SEI layer.

Previous experimental studies have used the probe-based indentation technique to investigate elastic properties of the SEI layer [19, 20]. Nanoindenter and AFM have been widely used for the probe-based nano-indentation technique to characterize the nano-mechanical properties of various materials. However, the technique is comparatively very

slow, which makes detailed topographical mapping difficult. In addition, relatively large deformation depths can lead a sample getting damaged, resulting in a poor lateral resolution. The large deformation depth can lead the measured values to be unreliable due to the substrate effect, since SEI layer thickness is typically very thin. It is commonly believed that the indentation depth should be less than a tenth of the film thickness to avoid the substrate effect [22]. The PeakForce Quantitative Nanomechanical (PF-QNM) mode with AFM, which was recently introduced, has allowed quantitative mechanical property mapping at the nanoscale with a high resolution and fast scanning for a range material firmness, from soft to hard [23–29]. It directly controls the maximum normal force to be constant, enabling small load forces with very small deformation depths of a sample, which can minimize the effect of a substrate on the measured modulus [22].

In this work, SEI elasticity is investigated based on a coupled technique: AFM with PF-QNM mode and X-ray photoelectron spectroscopy (XPS) measurements. Also, atomistic calculations are conducted to decompose the component and structure effects on the mechanical properties of the constituents of the SEI layer, which is not possible in the measurement.

METHODS

Experimental: Sample preparation

A 2032 type-coin cell (MTI Corp.) was assembled in an argon-filled glove box (M Braun). The cell was assembled with a 0.75 mm thick lithium foil (99.9%, Alfa Aesar) as the counter electrode (12.7 mm in diameter circle), a highly oriented pyrolytic graphite (HOPG; SPI-2 grade, 5 × 5 × 1 mm, SPI supplies) as the working electrode, and a

separator (Celgard 2320, 15.88 in diameter circle) soaked in an electrolyte. The separator was immersed into the electrolyte in an aluminum container for 7 days before use. The electrolyte solution was 1 M lithium hexafluorophosphate ($LiPF_6$; ≥ 99.99 %, Sigma-Aldrich) dissolved in a mixture of ethylene carbonate (EC; 99%, < 0.005 % H_2O, Sigma-Aldrich) and dimethyl carbonate (DMC; ≥ 99%, < 0.002 % H_2O, Sigma-Aldrich) with a volume ratio of 1:1. All electrolyte preparation and handling was carried out in an argon-filled glovebox with water and oxygen contents lower than 0.1 ppm. The HF content of the electrolyte was less than 80 ppm, as determined by a non-aqueous titration method. In order to form the SEI layer on a HOPG sample, the assembled cell was cycled 25 times between 0.01 V and 1 V at a constant current density of 50 $\mu A/cm^2$ using a battery test system (Biologic). After cycling, the cell was disassembled in an argon-filled glove box for characterizations. To fully understand the chemical composition of the SEI layer, both the 1st cycled sample and the 25th cycled sample were examined with XPS measurements. The HOPG electrode covered by the SEI layer was rinsed with the DMC solvent for 3 minutes, and was then vacuum-dried overnight to remove any residual salts on the sample.

Experimental: Chemical analysis with XPS

To analyze the chemical species existing in the SEI layer on the samples, XPS measurements were conducted on a Kratos Axis Ultra X-ray photoelectron spectrometer using a monochromatic Al Kα excitation source ($h\nu$ = 1486.6 eV). The rinsed HOPG was vacuum-sealed in the glove box, and then transferred to the XPS instrument. The sample was briefly exposed to air during the transportation into the analysis chamber. It has been confirmed that a short air exposure—anything less than 2 minutes—does not significantly

change the surface chemistry on the sample [30]. The analyzed area of the SEI layer was 300 × 700 μm^2. The binding energy scale was calibrated from intrinsic hydrocarbon contamination using the C 1s peak at 285 eV. Core spectra were recorded with 20 eV constant pass energy. The fitting of core peaks were performed using the Shirley background correction and Gaussian-Lorentzian curve synthesis (70% Gaussian, 30% Lorentzian). Charge neutralization was used in measurements.

Experimental: Mechanical analysis with AFM

A mechanical property mapping was performed via PeakForce tapping mode using Bruker's Dimension Icon AFM. PF-QNM measurements were done with silicon probes (TAP525A, Bruker) under ambient conditions. A probe was chosen for measuring both stiff and soft portions of the SEI layer. The deflection sensitivity of the cantilever was measured on a clean sapphire sample for the calibration of the probe. A nominal spring constant was used and then the tip radius was calibrated using a reference sample (highly ordered pyrolytic graphite, Bruker) with a known elastic modulus (18 GPa). The tip radius was adjusted until the observed modulus data matched the known modulus value. After calibrating the probe, topology and elastic modulus images were collected over a 2×2 μm^2 area at a resolution of 512 pixels × 512 pixels. The line scanning rate was set to 0.5 Hz. Each set of Young's modulus measurements on the sample is based on 512 × 512 force-separation curves. To prevent damage to the SEI layer formed on the surface of the HOPG, the 2 nN tip force was applied to obtain the elastic modulus map before the scratch. The tip force was then increased to 100 nN to peel off the outer part of the SEI layer, which consists mostly of organic and polymeric species. After the scratch, the 2 nN tip force was set again to acquire the elastic modulus map for the scratched area. The PF-

QNM measurement was performed in three different region of the sample. The Young's modulus of the SEI layer was determined by fitting the Derjaguin-Muller-Toporov (DMT) model to the retracting curves of the obtained force-separation curves, as shown in Fig 4.1.

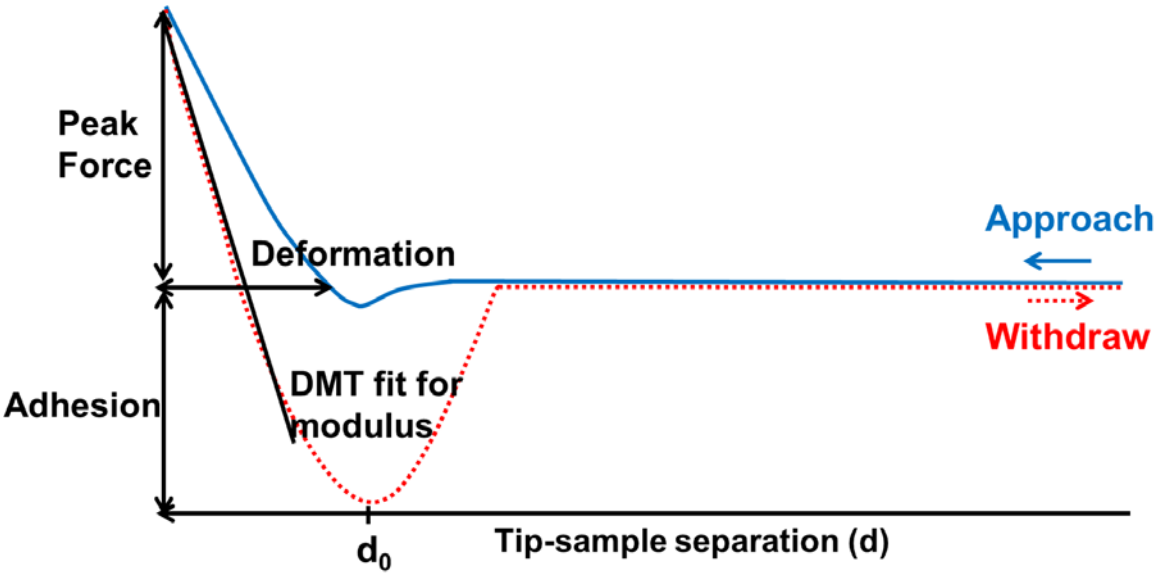

Figure 4-1. A schematic diagram of a force vs. separation curve in the PeakForce tapping mode.

According to the DMT model, the force that describes the tip-surface interaction behavior can be expressed as [31]:

$$F - F_{adh} = \frac{4E^* \sqrt{R(d - d_0)^3}}{3}$$

where F is the tip-sample interaction force, F_{adh} is the adhesion force during the contact, E^* is the reduced elastic modulus obtained from the DMT fit, R is the tip end radius, and $d-d_0$ is the deformation of the sample. The Young's modulus of the sample can be derived using the equation:

$$E^* = \left[(1 - \nu_s^2)/E_s + (1 - \nu_{tip}^2)/E_{tip}\right]^{-1}$$

where E_s is the Young's modulus of the sample, ν_s is the Poisson's ratio of the sample, ν_{tip} is the Poisson's ratio of the probe, and E_{tip} is the Young's modulus of the probe. In the PF-QNM measurement, the second term of the above equation was neglected, based on the assumption that $E_s \ll E_{tip}$. The Poisson's ratio of the sample was assumed to be equal to 0.3. The maps obtained using these methods were post-processed with NanoScope Analysis software (Bruker).

Computational: Molecular dynamics simulation

To predict the elastic properties of each SEI layer component, the COMPASS (Condensed-phase Optimized Molecular Potentials for Atomistic Simulation Studies) force field was used as potential functional parameters due to its high accuracy in predicting the condensed-phase properties for a broad range of organic, inorganic, and polymeric materials [32]. It has been shown that the COMPASS force field is capable of accurately predicting the elastic properties of organic and polymeric materials [33–36]. With the COMPASS force field, the solubility of lithium salts (organic and inorganic materials) found in the SEI layer was also calculated, showing trends similar to those in experimental observations [9]. For further validation of the force field, a lattice constant and a bulk modulus of crystalline inorganic materials were first compared with available experimental values as well as values of Density Functional Theory (DFT) calculations in the present study.

For the inorganic SEI layer component, both crystalline and amorphous structures were generated for the calculations. However, only amorphous structures were

considered for the organic and polymeric SEI layer components, since the organic and polymeric species in the SEI layer have been observed to exist as an amorphous phase [37–39]. Based on our XPS results, LiF and Li_2CO_3 were observed as the main inorganic components, thus these two components were considered in the numerical calculations. The initial unit cells of LiF and Li_2CO_3 crystal structures were imported from the available crystallographic data [40, 41], while amorphous structures were generated using the Amorphous Cell module of the Material Studio software package (version 6.0, Accelrys Inc.). The size of each simulation cell was in the range of 20Å to 30Å, depending on the types of SEI layer components. The generated structure was first subjected to a geometry optimization, followed by the isobaric-isothermal (NPT) dynamics at 10^5 Pa and 298 K for 1 ns in order to equilibrate the structure. The Nose-Hoover thermostat and Berdensen barostat were used for the NPT ensemble. Finally, a 200-ps production run was conducted to calculate the properties of the structure. To get the average values of properties, ten equilibrated structures were chosen in the production run. The Ewald summation was used to compute the non-bonded interactions, such as van der Waals and electrostatic interactions.

For the calculation of the elastic properties, the static approach with constant strains was employed [42]. This methodology has been adopted as a useful approach for estimating the elastic properties of various materials [42–46]. For each equilibrated configuration, the maximum strain amplitude was set to 0.003 so that the minimized structure was strained under a set of 12 deformations (three pairs of uniaxial tension/compression and three pairs of pure shear). The strained structure was then re-

minimized following each deformation. The internal stress tensor was then obtained from the analytically calculated virial expression as follows:

$$\boldsymbol{\sigma} = \frac{1}{V_0}\sum_i \left[-m_i \mathbf{v}_i \otimes \mathbf{v}_i + \frac{1}{2}\sum_{j \neq i} \mathbf{r}_{ij} \otimes \mathbf{f}_{ij} \right]$$

where index i runs over all atoms 1 through N (total number of atoms), m_i, $\mathbf{v}_i$ m_i and v_i are the mass and velocity of atom i, $\mathbf{r}_{ij}$ is the relative position vector between atom i and atom j, $\mathbf{f}_{ij}$ denotes the force acting on atom i by atom j, V_o is the undeformed system volume, and $\otimes$ is the cross product. The elastic stiffness coefficients were finally determined by estimating the first derivatives of the stress with respect to strain.

$$\mathbf{C}_{\mathrm{ijkl}} = \partial \boldsymbol{\sigma}_{\mathrm{ij}} / \partial \boldsymbol{\varepsilon}_{\mathrm{kl}}$$

where C is the elastic stiffness tensor, σ is the stress tensor, and ε is the strain tensor. The elastic constants were then averaged over ten equilibrated configurations. In order to predict the elastic aggregate properties of the bulk (B) and shear modulus (G), the Voigt-Reuss-Hill (VRH) approximation method was used by averaging the elastic constants of the single crystal over all orientations [47].

$$\mathrm{B_{Voigt}} = 1/9[\mathrm{C_{11}} + \mathrm{C_{22}} + \mathrm{C_{33}} + 2(\mathrm{C_{12}} + \mathrm{C_{13}} + \mathrm{C_{23}})]$$

$$\mathrm{B_{Reuss}} = [\mathrm{S_{11}} + \mathrm{S_{22}} + \mathrm{S_{33}} + 2(\mathrm{S_{12}} + \mathrm{S_{13}} + \mathrm{S_{23}})]^{-1}$$

$$\mathrm{G_{Voigt}} = 1/15[\mathrm{C_{11}} + \mathrm{C_{22}} + \mathrm{C_{33}} - \mathrm{C_{12}} - \mathrm{C_{13}} - \mathrm{C_{23}} + 3(\mathrm{C_{44}} + \mathrm{C_{55}} + \mathrm{C_{66}})]$$

$$\mathrm{G_{Reuss}} = 15[4(\mathrm{S_{11}} + \mathrm{S_{22}} + \mathrm{S_{33}} - \mathrm{S_{12}} - \mathrm{S_{13}} - \mathrm{S_{23}}) + 3(\mathrm{S_{44}} + \mathrm{S_{55}} + \mathrm{S_{66}})]^{-1}$$

The Hill value is defined as the average of values obtained by the other two approaches, namely, $B_{Hill}=(B_{Voigt} + B_{Reuss})/2$ and $G_{Hill}=(G_{Voigt} + G_{Reuss})/2$ [48]. From the averaged bulk and shear modulus, the Young's modulus (Y) of an aggregate can be estimated based on the bulk modulus and the shear modulus as follows [49].

$$Y = 9B_{Hill}G_{Hill}/(G_{Hill} + 3B_{Hill})$$

Here, we used the value obtained by the Hill approach to represent the bulk and shear modulus of each SEI layer component.

RESULTS AND DISCUSSION

Experimental: Chemical components of the SEI layer on a HOPG

To identify the chemical composition of the SEI layer formed on a HOPG surface, an XPS analysis was conducted. Figure 4.2 shows high-resolution XPS spectra of the SEI layer formed on the HOPG basal plane after the 25th cycle. The graphite peak at 284.3 eV in the C 1s spectrum is not identified, indicating that the HOPG surface is fully covered by the SEI layer. The chemical composition of the SEI layer consists of various chemical species, including solvent reduction/decomposition products, polymeric species, and salt reduction/decomposition products.

Based on the peak fitting of the C 1s spectrum, five peaks can be assigned. The peak at 285 eV, assigned to C-C, C-H bonds, is attributed to the intrinsic hydrocarbon, alkanes (C-H), and polymers which consist of hydrocarbons (-CH_2-CH_2- type bonds) [50-55]. The second peak at near 286.3 eV corresponding to C-O bonds associates with oxygen-containing polymeric species such as polyethylene oxide PEO (-CH_2-CH_2-O-)n

and lithium alkyl carbonates $ROCO_2Li$ [30, 50, 52, 55]. The two peaks in the vicinity of 287.3~288.5 eV originate from the contribution of the $ROCO_2Li$ [30, 50, 55]. The lithium alkyl carbonates $ROCO_2Li$ are formed due to the reduction of solvents, and have widely been considered to be one of the main components of the SEI layer on negative electrodes. The formation of PEO oligomers has also been suggested by a ring-opening mechanism of the solvent EC, leading to the formation of CO_2 [14, 15]. In O 1s spectrum, the broad asymmetric peak is due to a convolution of Li_2CO_3 (531.5 eV) and $ROCO_2Li$ (532.3 eV). A shoulder at 533.9 eV originates from PEO oligomers and a portion of $ROCO_2Li$ [30, 50]. The small peak near 528.7 eV corresponds to the formation of Li_2O, which is known as a consequence of Li_2CO_3 decomposition or trace amounts of water in the electrolyte [50, 51, 54, 56]. The presence of Li_2O in the SEI layer remains a matter of debate. Previous study reported that the observed Li_2O could be an artifact of the sputtering process rather than a true SEI component [56]. However, there is an agreement that the Li_2O is not a major component of the SEI layer. In this work, a small amount of Li_2O is found in the SEI layer without any sputtering process.

Besides the solvent reduction products, salt reduction or decomposition compounds are clearly detected as a portion of SEI layer. The inorganic LiF (685.5 eV in F 1s, 56 eV in Li 1s) and salt residues, including $LiPF_6$ and Li_xPF_y (near 687.5 eV in F 1s) are also formed at the surface [30, 52–54]. The strong peak at 137.3 eV in the P 2p supports that salt residues or its reduction products are formed considerably in the SEI layer. A small amount of $Li_xPF_yO_z$ (134.2 eV in the P 2p) due to the hydrolysis of $LiPF_6$ is observed in the SEI layer as well [30].

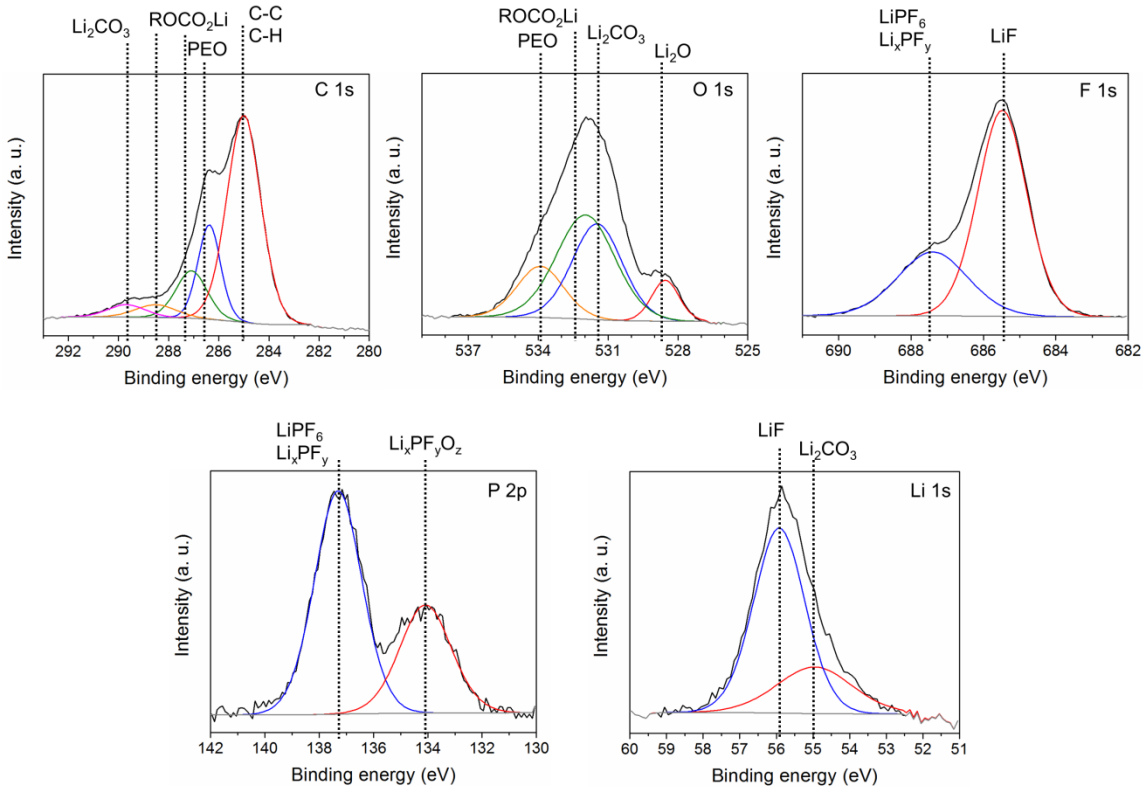

Figure 4-2. F 1s, O 1s, C 1s, P 2p, Li 1s XPS high-resolution spectra of the 25th cycled HOPG.

In order to obtain more clear information on chemical composition of the formed SEI layer after the 25th cycle, the 1st cycled HOPG was compared to the 25th cycled HOPG, as shown in Fig. 4.3. The main difference is that an undetected peak at 289.7 eV is visible after the 25th cycle, indicating the formation of the lithium carbonate Li_2CO_3 during the cycling (Fig. 4.3a). This result suggests that less stable compounds partially converted to the Li_2CO_3 over repeated cycling. It has been previously observed that the metastable $ROCO_2Li$ can decompose to form the more stable Li_2CO_3 at high temperature and over repeated cycling [30, 57]. It is supported by an observation that the intensity of dominant peaks associated with $ROCO_2Li$ and PEO (near 286~287 eV in Fig. 4.3a) decreases after the 25th cycle.

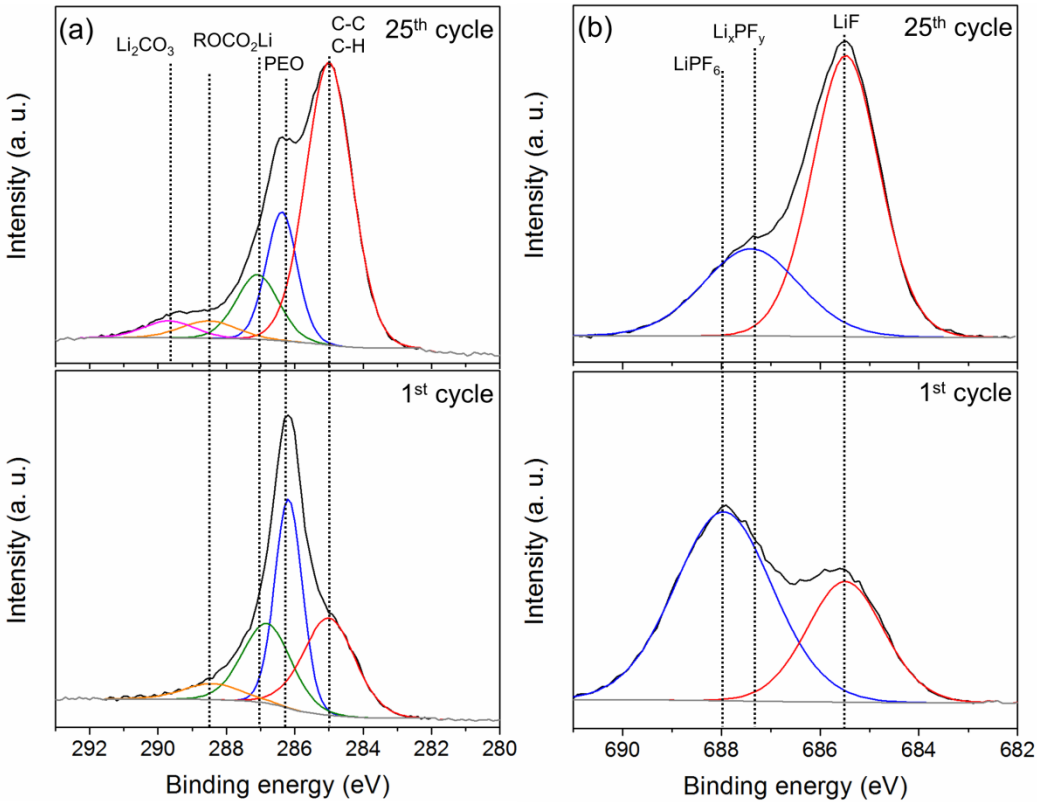

Figure 4-3. Comparison of the 1st cycled and the 25th cycled HOPG: (a) C 1s XPS spectrum, (b) F 1s XPS spectrum.

Compared to the Li_2CO_3, the inorganic LiF (685.5 eV in Fig. 4.3b), which is observed in the SEI layer formed after the 1st cycle, is still seen after the 25th cycle (Fig. 4.3b). However, the significant increase of peak intensity at 685.5 eV after the 25th cycle indicates that the extent of the LiF considerably increases over repeated cycling. That is, a considerable amount of the LiF is included in the SEI layer after the 25th cycle compared to the SEI layer formed after the 1st cycle. Consequently, it is expected that the SEI layer formed after the 25th cycle is stiffer than after the 1st cycle. As the SEI layer after 25 cycles is thicker than that after 1st cycle, it implies that the inorganic LiF considerably exists in the outer part as well as the inner part of the SEI layer. It has been

suggested that the LiF widely distributes throughout the SEI layer as a form of isolated crystallites rather than a solid layer [55, 56]. In addition, the peak (688 eV) related to the salt residue $LiPF_6$ shifts to the lower binding energy (687.5 eV) due to the formation of the degradation products Li_xPF_y after the 25th cycle [53]. That is, the salt residue and reduction products are also distributed throughout the SEI layer, thereby those species can be found on the surface. Therefore, it is expected that these stiff components such as Li_2CO_3, LiF, $LiPF_6$, Li_xPF_y, and $Li_xPF_yO_z$ significantly contributes to the elastic modulus of the SEI layer.

Experimental: Elastic modulus of the SEI layer

Figure 4.4 shows the measured DMT modulus maps with the corresponding cross-section plots using PeakForce QNM imaging mode for a fresh HOPG (Fig. 4.4a), a 25-time cycled HOPG before scratching (Fig. 4.4b), and the same sample as in Fig. 4.4b but scratched (Fig. 4.4c). As shown in Fig. 4.4a, the elastic modulus of the fresh HOPG basal plane is about 10.9 ± 2.9 GPa, which is in good agreement with the reported Young's modulus of 10.5 GPa that was found in the literature [58]. Although the elastic modulus is quite consistent over the scan area, a slight variation still exists in the observed elastic modulus. This variation may come from the surface roughness and defects of the HOPG samples. The dulled or contaminated tip while scanning the surface may also contribute to the variation.

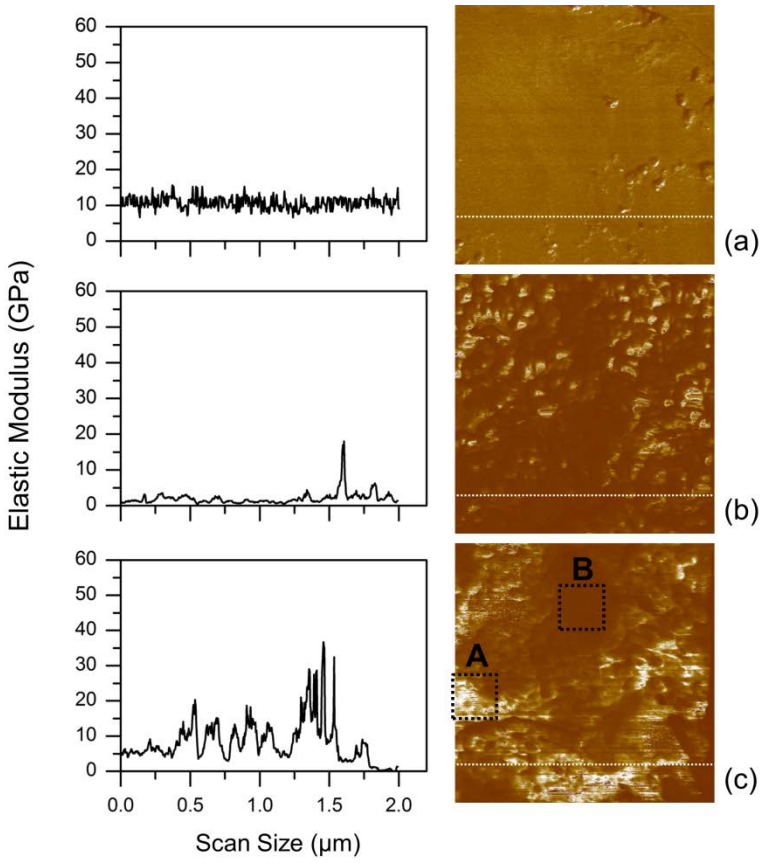

Figure 4-4. Representative maps of DMT modulus with corresponding cross sections: (a) HOPG before cycling, (b) SEI layer formed on HOPG after 25 cycles, (c) SEI layer formed on HOPG after scratching.

As confirmed by the XPS measurements above, an SEI layer is formed after cycling, and the formed SEI layer in the cycled HOPG consists of various chemical components (Fig. 4.4a). Figure 4.4b shows a change of modulus after the sample is cycled; a lower elastic modulus is observed compared to the fresh HOPG. The average elastic modulus measured in the entire scan area (2×2 μm^2) shows 3.8 ± 5.6 GPa. The observed large deviation is mainly due to the observed inhomogeneous elastic modulus as well as the non-uniform SEI surface. In the image, the bright (white color) spots indicate a relatively high elastic modulus compared to the dark (brown color) area. Our XPS results show that the SEI layer is composed of organic/polymeric compounds, inorganic

compounds, and salts residues. In general, inorganic materials have higher elastic moduli compared to organic materials, thus it is expected that the higher modulus is associated with partially exposed inorganic compounds through porous organic outer layer, and $LiPF_6$ salt residues and its decomposition products (LiF, Li_xPF_y, and $Li_xPF_yO_z$) on the surface. It is supported by the previous XPS results: the salt decomposition species (mainly the LiF) exist in a significant way on the surface after 25 cycles. The lower modulus can be explained by the existence of organic and polymeric species. In order to further confirm our observation, the outer portion of the SEI layer is scraped off by increasing the tip force during the scan.

Figure 4.4c shows the elastic modulus map and corresponding cross-section profile of the SEI layer after the scratch. The average elastic modulus in the whole scan area increases to 8.3 ± 11.5 GPa. As mentioned, the large deviation is due to distinct difference in the elastic modulus (bright vs. dark) within the scan area. The DMT modulus plots at the same cross-section line (Fig. 4.4b vs. Fig. 4.4c) clearly prove that the elastic modulus significantly increases after the scratch. The increased modulus is related to the increased amounts of inorganic component portions of the SEI layer after the scratch. It has been known that dense inorganic components that are present at the inner portion of the SEI layer close to the electrode and porous organic/polymeric species mainly consist of the outer portion of the SEI layer. During the scratch, it seems that soft organic and polymeric species are easily removed, revealing more inorganic compounds that exist at the inner part of the SEI layer.

Note that the organic/polymeric species are still observed in some regions, suggesting that one scratch is not enough to entirely remove the outer part of SEI layer.

Only one scratch was conducted to minimize the effect of the dulled or contaminated tip on the modulus measurements. The histograms illustrated in Fig. 4.5 provide a clear difference in the elastic modulus before (Fig. 4.5a) and after the scratch (Fig. 4.5b), corresponding to the maps shown in Fig. 4.4b and Fig. 4.4c, respectively.

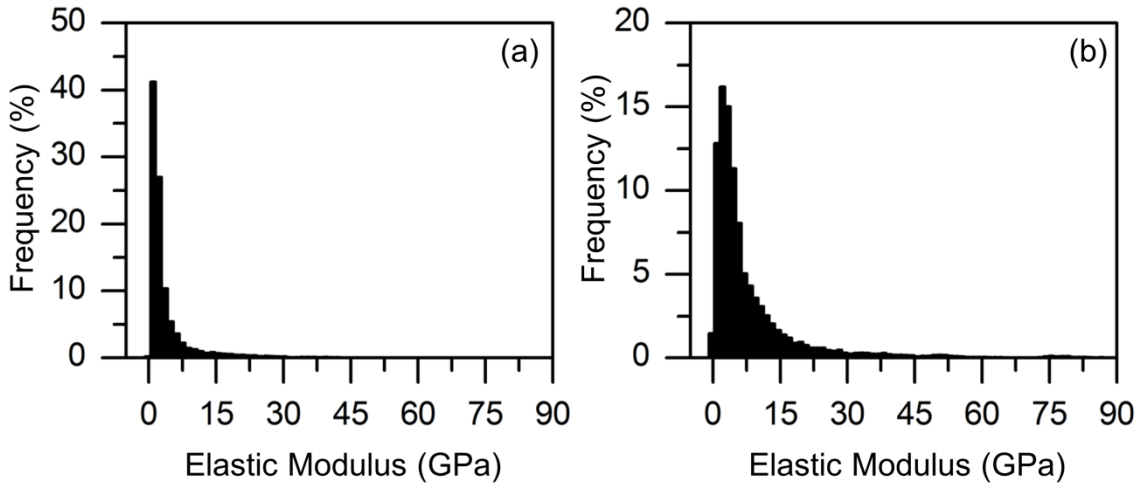

Figure 4-5. Histograms of DMT modulus: (a) SEI layer before scratching, (b) HOPG after scratching.

Before the scratch, the measured elastic modulus of the SEI layer is mostly in the range from 0.2 to 4.5 GPa, showing around 84% of the elastic modulus values below 4.5 GPa. After the scratch, the amount of species exhibiting low elastic moduli decreases, while the amount of species with high elastic moduli increases, showing around 47% of the elastic modulus values above 4.5 GPa. It indicates that SEI compounds other than organic and polymeric species in abundance on the surface, which implies the more exposure of inorganic species due to the scratch.

On zooming into the inorganic region that shows a considerable number of high elastic moduli (Dotted square area A in Fig. 4.4c), the histogram indicates that the modulus is mainly in the range from 20 to 85 GPa, as shown in Fig. 4.6a. The histogram

of area B (Fig. 4.6b) shows 1.0 ± 0.2 GPa, which is in a similar range of polymeric and organic phase materials [25, 26, 59–62].

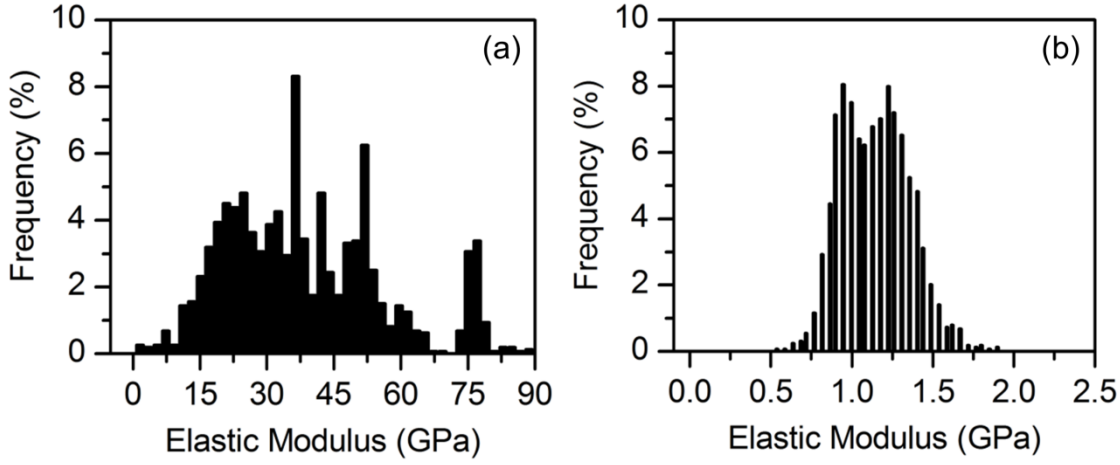

Figure 4-6. Histograms of DMT modulus: (a) The dotted square area A in Fig. 4.3c (Inorganic region), (b) The dotted square area B in Fig. 4.3c (Organic/polymeric region).

Note that a wider range of elastic moduli is measured at the region identified as inorganic species than the region of the organic and polymeric phase region. This may come from two reasons related to the chemical and structural characteristics of the inorganic components of the SEI layer. First, a wide variance in the elastic moduli of the inorganic components (LiF, Li_xPF_y, $Li_xPF_yO_z$, Li_2CO_3, and salt residues) can contribute to the observed wide range of elastic moduli. Second, crystallinity and crystal orientation may result in the broad range of inorganic species' elastic moduli. It has been reported that the elastic properties of various materials strongly depend on its degree of crystallinity and crystal orientation [62–65]. The elastic modulus versus the crystallinity linear relationship has been observed in polyethylene [63]. A DFT calculation has shown that a variation of Young's modulus can be around 70 GPa depending on the angle between the crystal c-axis and the direction of strain [65]. In the literature, it has been

reported that the organic components exist as an amorphous phase, while the inorganic components form a (poly)crystalline phase. However, it is still possible that a portion of the inorganic SEI layer exists as a form of an amorphous phase during the SEI formation and evolution process. In the next session, this structure-dependent SEI elasticity is discussed.

Computational: Structure-dependent SEI layer elasticity

Based on our XPS measurements and other literature, LiF and Li_2CO_3 are recognized as the main inorganic components of the SEI layer. These components are chosen to explore the structure-elastic property relationship of the individual inorganic SEI layer components. Table 4.1 lists the cell lattice parameters of the equilibrated crystalline structures calculated in this work, including experimental data and other calculations for comparison [41, 66–69].

Table 4-1. Experimental and calculated lattice parameters (a, b, and c in Å) and angle (β in °) of inorganic crystalline species.

	LiF	Li_2CO_3
Experiment	4.03 [a]	8.36/4.97/6.19/114.79 [c]
Calculation	3.88 ~ 4.13 [b]	8.41/5.03/6.30/114.80 [d] 8.32/4.93/5.90/116.07 [e]
This work	4.18	8.94/5.11/6.19/119.53

[a] From Ref. 66, [b] From Ref. 67, [c] From Ref. 41, [d] From Ref. 68, [e] From Ref. 69

The cell lattice parameters of the equilibrated crystalline structures in this work are quite close to the experimental values, showing less than a 6% deviation from the experimental values. Depending on the calculation methods or the force field used, the

calculated values in the literature vary up to around 7% of each other, as shown in Table 4.1.

To evaluate whether the equilibrated structures represent the characteristics of a crystalline or an amorphous structure, the total pair distribution function, g(r), which describes the distribution of the distances between pairs of atoms in a given volume, is plotted in Fig. 4.7.

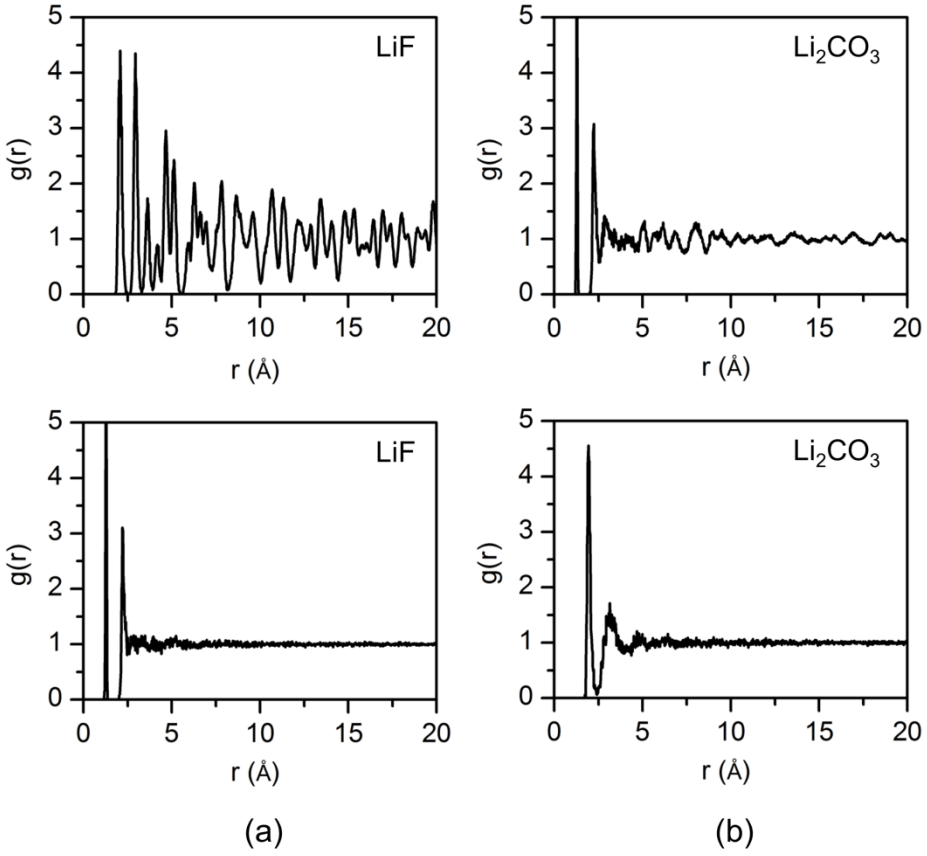

Figure 4-7. Total pair distribution function, g(r): (a) LiF, (b) Li_2CO_3; Upper and bottom figures represent crystalline and amorphous structures, respectively.

Compared to the equilibrated crystalline structures showing an existence of long-range order, the equilibrated amorphous structures show a short-range order because they show the presence of peaks over a much shorter distance compared to the crystalline

structures. Therefore, the equilibrated amorphous structures do a good job of reproducing the features of an amorphous solid.

In order to investigate the effect of the crystallinity of the SEI layer components on the elastic properties, the estimated bulk, shear modulus, and B/G ratio values of the SEI inorganic components are calculated, as shown in Table 4.2.

Table 4-2. Predicted elastic properties (B, G in GPa) of inorganic LiF and Li_2CO_3 with different crystal structures (Crystalline vs. Amorphous).

	LiF		Li_2CO_3	
	Crystalline	Amorphous	Crystalline	Amorphous
Bulk modulus (B)	89.4	45.5	50.5	43.1
Shear modulus (G)	54.2	21.1	22.2	13.3
B/G	1.65	2.16	2.27	3.24

The calculated bulk modulus of crystalline LiF (89.4 GPa) is within the other calculated values that vary from 60 to 95 GPa, and is close to the experimental values of 69.9, 73.0 GPa [67, 70]. The calculated bulk modulus of crystalline Li_2CO_3 (50.5 GPa) also shows good agreement with other calculated values in the range of 41.7 to 55.5 GPa [69]. Based on Pugh's criterion (B/G ratio) of a brittleness material [71], the crystalline LiF behaves in a brittle manner (B/G < 1.75), while the crystalline Li_2CO_3 is a ductile material (B/G > 1.75). Other theoretical calculations based on DFT also predict that the monoclinic Li_2CO_3 is a ductile material, showing B/G values above 2 [69]. Generally, the bulk modulus of an amorphous structure has a lower value than that of the crystalline structure of the same material. For the amorphous phase, the bulk moduli of LiF and Li_2CO_3 are 45.5 and 43.1 GPa, respectively. Similar trends can be found in the shear

modulus and the Young's modulus. Figure 4.8 clearly shows the structure dependence of the SEI elasticity.

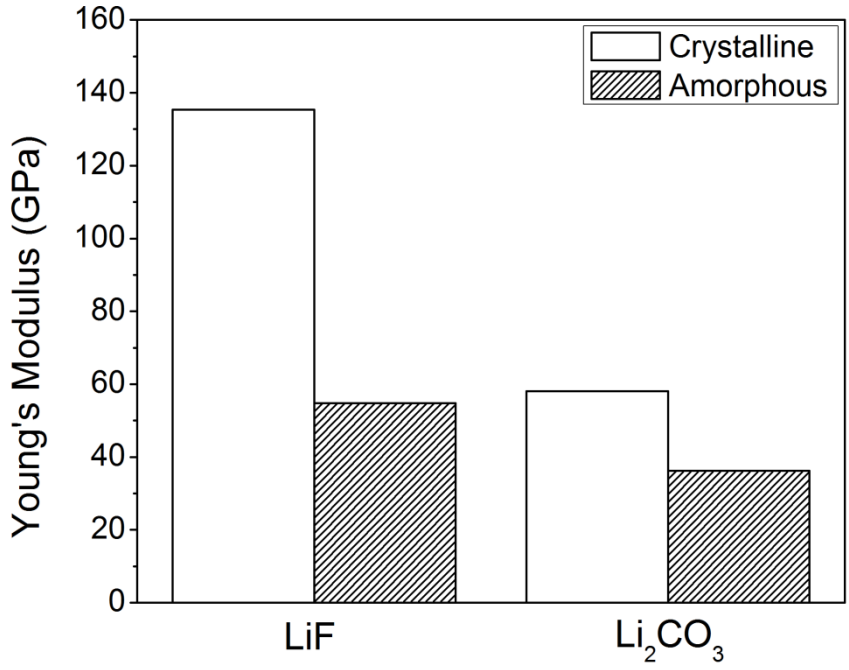

Figure 4-8. The predicted Young's modulus of inorganic SEI component with different crystal structures (Crystalline vs. Amorphous).

The crystalline LiF shows 135.3 GPa, which is close to the experimental value (~ 125 GPa) [72], while the amorphous LiF has a considerably lower value of 58.1 GPa. Similarly, the Young's modulus of crystalline Li_2CO_3 (54.8 GPa) is also quite higher than the amorphous phase of Li_2CO_3 (36.2 GPa). Note that the influence of the microstructure on the elastic properties is much larger for the LiF than for the Li_2CO_3. The change in the structure of the LiF not only decreases the modulus, but also changes the brittle and ductile behavior of the LiF material. According to the B/G ratio shown in Table 4.2, the LiF component behaves as a ductile material under an amorphous state, while it behaves

as a brittle material under a crystalline state. However, the Li_2CO_3 component exists as a ductile material regardless of its being in a crystalline or amorphous phase.

Since an SEI layer is not homogenous and it is formed on a composite anode material with crystalline (graphite) and amorphous (binder) features, pure Li_2CO_3 and LiF with crystalline features might not be formed or changed during the SEI formation and growth. It has been observed that pure Li_2CO_3 with a crystalline feature can be changed to an amorphous feature of Li_2CO_3 as the Li_2CO_3-Al_2O_3 composite solid electrolyte is synthesized due to chemical reactions between the composite components [73]. Several chemical reactions, such as salt/solvent decompositions and reactions between SEI species and the electrolyte are involved in SEI formation and growth. Thus, it is possible for the inorganic LiF and Li_2CO_3 to exist as forms of a polycrystalline or even amorphous phase, rather than a pure crystalline phase. It has also been found that thin film LiF with the preferred orientation changes to a completely random structure as it grows on an amorphous substrate [74]. Thus, the SEI growth on the composite anode and the inhomogeneous SEI layer itself could make it difficult to form well-ordered structures, even though pure LiF and Li_2CO_3 show high crystalline features. Consequently, the observed wide range of the elastic modulus—especially at the inorganic regions compared to organic regions—can be explained by the atomistic calculation results in this section. If the inorganic components can exist as different crystal structures in the SEI layer, the inorganic SEI layer shows a large variation of the elastic modulus.

Computational: Component-dependent SEI layer elasticity

Figure 4.9 shows the atomic structure of each SEI layer component used in the calculations. These components have been known as the main chemical species typically

found in the SEI layer in the EC/DMC-based electrolyte. Our XPS results also confirm that the formed SEI layer on the HOPG surface mainly consists of these organic, polymeric, and inorganic chemical components, such as Li_2EDC, LiEC, LiMC, PEO, LiF, and Li_2CO_3.

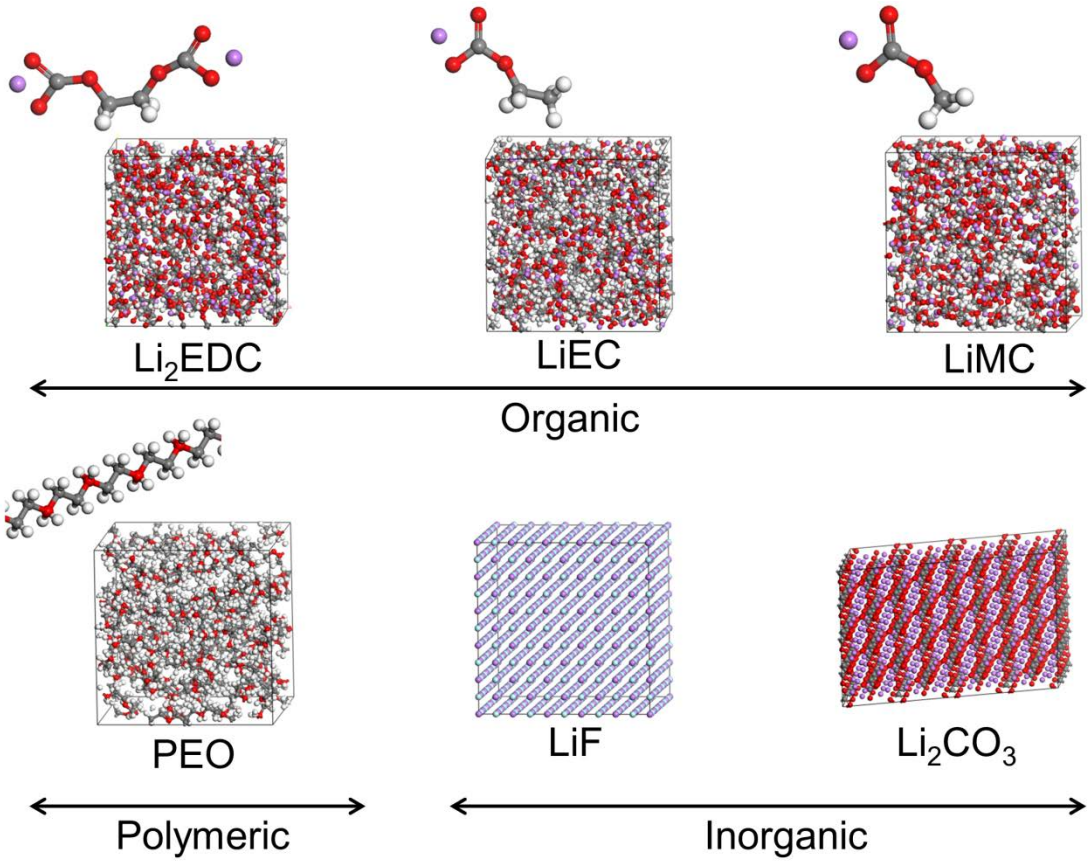

Figure 4-9. The chemical structures of SEI components (Organic, polymeric, and inorganic species) used in simulations.

The calculated bulk (B) and shear (G) modulus of each amorphous organic/polymeric component with its B/G value are listed in Table 4.3. The bulk modulus of organic/polymeric species ranges from 2.5 GPa to 18.9 GPa in the order of PEO < LiEC < LiMC < Li_2EDC, which is similar to the order in the previous work [21].

The discrepancy between the calculated and measured values may be due to the simulations performed on defect-free materials or experimental assumptions, such as Poisson's ratio and the DMT model. Note that the calculated values of organic/polymeric species are considerably lower than those of inorganic species (Table 4.2) regardless of the crystal structure.

Table 4-3. Predicted elastic properties (B, G in GPa) of main organic and polymeric SEI components.

	Li_2EDC	LiEC	LiMC	PEO
Bulk modulus (B)	18.9	5.8	8.9	2.5
Shear modulus (G)	8.4	3.1	4.1	0.9
B/G	2.25	1.87	2.17	2.77

The shear modulus follows the same order as the bulk modulus (PEO < LiEC < LiMC < Li_2EDC). The organic species of the SEI layer have a higher elastic modulus than the polymeric PEO of the SEI layer. Among organic species, the elastic modulus of Li_2EDC, which is known as a primary component in the EC-based SEI layer, is relatively high compared to other organic species. One of the main decomposition products in the DMC-based SEI layer, LiMC, also has a lower modulus than the Li_2EDC. According to our simulation results, it seems that the EC-based SEI layer is stiffer than the DMC-based SEI layer. The trend is in a good agreement with the previous observation [21]. As expected, all organic and polymeric species of an SEI layer show ductile behaviors based on the calculated B/G values (> 1.75). Specifically, the organic species (Li_2EDC and LiMC) of EC and DMC decomposition products are less ductile than the polymeric PEO.

Figure 4.10 compares the Young's modulus of each SEI layer component constructed as an amorphous structure. The figure illustrates the component dependence

of the SEI elasticity. It clearly shows that the SEI elasticity is linked with the chemical composition of the SEI layer. The Young's moduli of different SEI components range from 2.4 GPa to 58.1 GPa in order of the polymeric, organic, and inorganic components, specifically PEO < LiEC < LiMC < Li_2EDC < Li_2CO_3 < LiF. The inorganic LiF is the stiffest component of the SEI layer, while the polymeric PEO is the most flexible part of the SEI layer. Even if the inorganic components are assumed to be amorphous, a considerable difference is still observed between the Young's moduli of inorganic and organic/polymeric species. The elasticity difference between organic layers and inorganic layers in the SEI layer is even more significant if inorganic species exist as crystalline or polycrystalline phase. Therefore, the extremely high modulus values observed in our experiments are possibly due to crystalline LiF and other crystalline inorganic species.

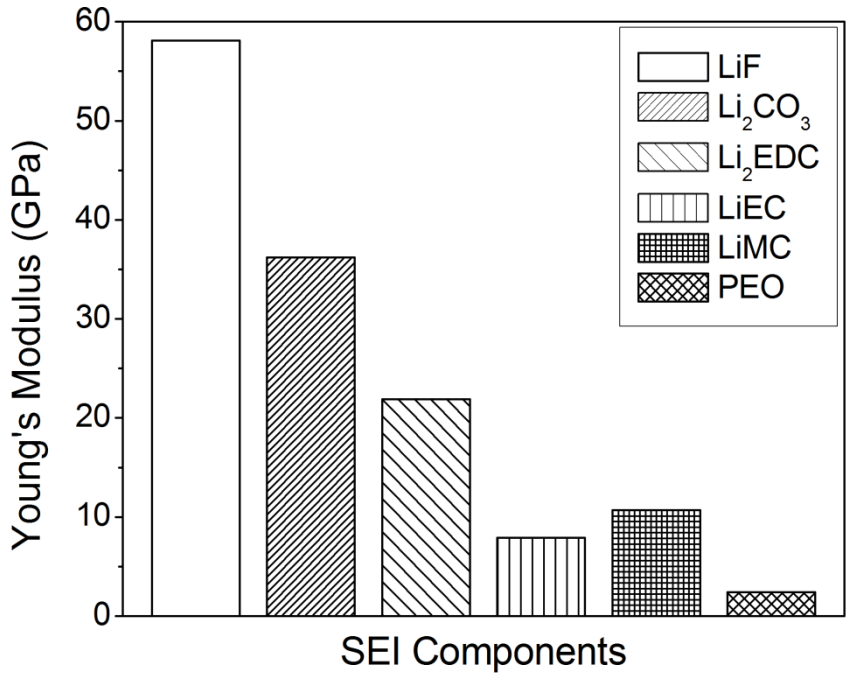

Figure 4-10. Predicted Young's modulus of each individual SEI component.

The flexible organic/polymeric layer that exists at the outer part of the SEI layer is possibly less affected by a large strain due to volume changes during intercalation and deintercalation. On the other hand, the stiff inorganic layer that forms at the inner part of the SEI layer would be difficult to withhold from large strain, causing mechanical degradation of the inorganic inner layer. Especially, the inner part that consists of LiF species rather than Li_2CO_3 is likely to experience a failure or cracking of the SEI layer due to the induced stress. For this reason, as an example, for a silicon anode with such a huge volume change, Li_2CO_3 would be a more favorable component than LiF as an inorganic layer keeping a good passivation characteristic. In a similar way, as an organic layer, the formation of polymeric PEO rather than other organic species is more effective for SEI elasticity, building a more flexible SEI layer. Therefore, it is important to control SEI chemical composition to achieve desirable SEI elasticity, especially an electrode with a large change in volume.

CONCLUSIONS

In this work, the SEI elasticity has been studied both experimentally and computationally. To characterize the SEI elasticity, the SEI layer formed on a HOPG electrode in an electrolyte (1M $LiPF_6$ in EC:DMC (1:1, v/v)) has been investigated using PF-QNM and atomistic calculations. Both experimental and computational results have shown that SEI elasticity is strongly affected by the SEI chemical composition. We have found significant differences in the SEI elastic properties between organic/polymeric components and inorganic components of SEI layer. Experimental results have revealed that the inner layer contains considerably more of the stiff species than the outer layer

does. Computational results have shown the component and its structure dependence of SEI elasticity. The elasticity of each main SEI component has been determined, showing stiffer behavior in the order of LiF > Li_2CO_3 > Li_2EDC > LiMC > LiEC > PEO. In addition, it has also been shown that the elasticity of SEI inorganic component varies significantly depending on its crystal structure. In particular, the elasticity of LiF is more easily affected than Li_2CO_3 by change in the crystal structure.

The findings from this work can be used in controlling the SEI layer to minimize damage to the SEI layer. The mechanical stability (adhesion, elasticity, etc.) of the SEI layer can be achieved by changing formation conditions and electrolytes (salts, solvents, and additives). For instance, the formation of an inorganic layer with an amorphous feature, and of a PEO polymeric layer rather than an EC- or DMC-based organic layer would be desirable for forming a flexible SEI layer. This strategy focused on mechanical stability would be critically important for new promising materials like silicon in which the main challenge is to mitigate the mechanical instability.

BIBLIOGRAPHY

[1] D. Aurbach, B. Markovsky, I. Weissman, E. Levi, Y. Ein-Eli, *Electrochim. Acta*, **45**, 67 (1999).

[2] R. Yazami, Y.F. Reynier, *Electrochim. Acta*, **47**, 1217 (2002).

[3] M. Inaba, H. Tomiyasu, A. Tasaka, S.K. Jeong, Z. Ogumi, *Langmuir*, **20**, 1348 (2004).

[4] T. Yoshida, M. Takahashi, S. Morikawa, C. Ihara, H. Katsukawa, T. Shiratsuchi, J. Yamaki, *J. Electrochem. Soc.*, **153**, A576 (2006).

[5] A.J. Smith, J.C. Burns, X. Zhao, D. Xiong, J.R. Dahn, *J. Electrochem. Soc.*, **158**, A447 (2011).

[6] J. Vetter, P. Novak, M.R. Wagner, C. Veit, K.C. Moller, J.O. Besenhard, M. Winter, M. Wohlfahrt-Mehrens, C. Vogler, A. Hammouche, *J. Power Sources*, **147**, 269 (2005).

[7] A. Du Pasquier, F. Disma, T. Bowmer, A.S. Gozdz, G. Amatucci, J.M. Tarascon, *J. Electrochem. Soc.*, **145**, 472 (1998).

[8] T. Zheng, A.S. Gozdz, G.G. Amatucci, *J. Electrochem. Soc.*, **146**, 4014 (1999).

[9] K. Tasaki, A. Goldberg, J.-J. Lian, M. Walker, A. Timmons, S.J. Harris, *J. Electrochem. Soc.*, **156**, A1019 (2009).

[10] A. Zaban, D. Aurbach, *J. Power Sources*, **54**, 289 (1995).

[11] E. Peled, D. Golodnitsky, G. Ardel, *J. Electrochem. Soc.*, **144**, L208 (1997).

[12] J.O. Besenhard, M. Winter, J. Yang, W. Biberacher, *J. Power Sources*, **54**, 228 (1995).

[13] P. Verma, P. Maire, P. Novak, *Electrochim. Acta*, **55**, 6332 (2010).

[14] R. Dedryvere, S. Laruelle, S. Grugeon, L. Gireaud, J.M. Tarascon, D. Gonbeau, *J. Electrochem. Soc.*, **152**, A689 (2005).

[15] H. Tavassol, J.W. Buthker, G.A. Ferguson, L.A. Curtiss, A.A. Gewirth, *J. Electrochem. Soc.*, **159**, A730 (2012).

[16] H.L. Zhang, F. Li, C. Liu, J. Tan, H.M. Cheng, *J. Phys. Chem. B*, **109**, 22205 (2005).

[17] R. Deshpande, M. Verbrugge, Y.-T. Cheng, J. Wang, P. Liu, *J. Electrochem. Soc.*, **159**, A1730 (2012).

[18] H. Tavassol, M.K.Y. Chan, M.G. Catarello, J. Greeley, D.G. Cahill, A.A. Gewirth, *J. Electrochem. Soc.*, **160**, A888 (2013).

[19] W. Xu, S.S.S. Vegunta, J.C. Flake, *J. Power Sources*, **196**, 8583 (2011).

[20] J. Zhang, R. Wang, X. Yang, W. Lu, X. Wu, X. Wang, H. Li, L. Chen, *Nano Lett.*, **12**, 2153 (2012).

[21] S.-P. Kim, A.C.T. van Duin, V.B. Shenoy, *J. Power Sources*, **196**, 8590 (2011).

[22] H. Cabibil, H. Celio, J. Lozano, J.M. White, R. Winter, *Langmuir*, **17**, 2160 (2001).

[23] P. Trtik, J. Kaufmann, U. Volz, *Cem. Concr. Res.*, **42**, 215 (2012).

[24] G. Pletikapic, A. Berquand, T.M. Radic, V. Svetlicic, *J. Phycol.*, **48**, 174 (2012).

[25] M.E. Dokukin, I. Sokolov, *Langmuir*, **28**, 16060 (2012).

[26] T.J. Young, M.A. Monclus, T.L. Burnett, W.R. Broughton, S.L. Ogin, P.A. Smith, *Meas. Sci. Technol.*, **22**, 125703 (2011).

[27] K. Sweers, K. van der Werf, M. Bennink, V. Subramaniam, *Nanoscale Res. Lett.*, **6**, 270 (2011).

[28] P. Schon, K. Bagdi, K. Molnar, P. Markus, B. Pukanszky, G.J. Vancso, *Eur. Polym. J.*, **47**, 692 (2011).

[29] J. Adamcik, A. Berquand, R. Mezzenga, *Appl. Phys. Lett.*, **98**, 193701 (2011).

[30] A.M. Andersson, D.P. Abraham, R. Haasch, S. MacLaren, J. Liu, K. Amine, *J. Electrochem. Soc.*, **149**, A1358 (2002).

[31] B.V. Derjaguin, V.M. Muller, Y.P. Toporov, *J. Colloid Interface Sci.*, **52**, 314 (1975).

[32] H. Sun, *J. Phys. Chem. B*, **102**, 7338 (1998).

[33] M. Grujicic, Y.P. Sun, K.L. Koudela, *Appl. Surf. Sci.*, **253**, 3009 (2007).

[34] S.S. Jang, W.A. Goddard, III, M.Y.S. Kalani, *J. Phys. Chem. B*, **111**, 1729 (2007).

[35] A. Sturcova, G.R. Davies, S.J. Eichhorn, *Biomacromolecules*, **6**, 1055 (2005).

[36] W.A.W. Hassan, I. Hamerton, B.J. Howlin, *PLoS One*, **8**, e61179 (2013).

[37] P. Poizot, S. Laruelle, S. Grugeon, L. Dupont, J.M. Tarascon, *Nature*, **407**, 496 (2000).

[38] S. Chattopadhyay, A.L. Lipson, H.J. Karmel, J.D. Emery, T.T. Fister, P.A. Fenter, M.C. Hersam, M.J. Bedzyk, *Chem. Mater.*, **24**, 3038 (2012).

[39] S. Shi, P. Lu, Z. Liu, Y. Qi, L.G. Hector, Jr., H. Li, S.J. Harris, *J. Am. Ceram. Soc.*, **134**, 15476 (2012).

[40] R.W.G. Wyckoff, *Crystal Structures*, **1**, 85 (1963).

[41] Y. Idemoto, J.W. Richardson, N. Koura, S. Kohara, C.K. Loong, *J. Phys. Chem. Solids*, **59**, 363 (1998).

[42] D.N. Theodorou, U.W. Suter, *Macromolecules*, **19**, 139 (1986).

[43] S.L. Teich-McGoldrick, J.A. Greathouse, R.T. Cygan, *J. Phys. Chem. C*, **116**, 15099 (2012).

[44] K. Wasanasuk, K. Tashiro, *Macromolecules*, **45**, 7019 (2012).

[45] H. Liu, M. Li, Z.-Y. Lu, Z.-G. Zhang, C.-C. Sun, T. Cui, *Macromolecules*, **44**, 8650 (2011).

[46] N.B. Shenogina, M. Tsige, S.S. Patnaik, S.M. Mukhopadhyay, *Macromolecules*, **45**, 5307 (2012).

[47] G. Simmons, H. Wang, Single Crystal Elastic Constants and Calculated Aggregate Properties: A HANDBOOK, 2nd ed., The M.I.T. Press, Cambridge, Massachusetts, and London, (1971).

[48] R. Hill, *P. Phys. Soc. Lond. A*, **65**, 349 (1952).

[49] B.H. Billings, D.E. Gray, American Institute of Physics handbook, 3rd ed., McGraw-Hill, New York, (1972).

[50] A.M. Andersson, A. Henningson, H. Siegbahn, U. Jansson, K. Edstrom, *J. Power Sources*, **119**, 522 (2003).

[51] D. Bar-Tow, E. Peled, L. Burstein, *J. Electrochem. Soc.*, **146**, 824 (1999).

[52] R. Dedryvere, H. Martinez, S. Leroy, D. Lemordant, F. Bonhomme, P. Biensan, D. Gonbeau, *J. Power Sources*, **174**, 462 (2007).

[53] S. Leroy, H. Martinez, R. Dedryvere, D. Lemordant, D. Gonbeau, *Appl. Surf. Sci.*, **253**, 4895 (2007).

[54] A. Xiao, L. Yang, B.L. Lucht, S.-H. Kang, D.P. Abraham, *J. Electrochem. Soc.*, **156**, A318 (2009).

[55] A.M. Andersson, K. Edstrom, *J. Electrochem. Soc.*, **148**, A1100 (2001).

[56] K. Edstrom, M. Herstedt, D.P. Abraham, *J. Power Sources*, **153**, 380 (2006).

[57] L. Zhao, I. Watanabe, T. Doi, S. Okada, J. Yamaki, *J. Power Sources*, **161**, 1275 (2006).

[58] A. Richter, R. Ries, R. Smith, M. Henkel, B. Wolf, *Diam. Relat. Mater.*, **9**, 170 (2000).

[59] D. Tahk, H.H. Lee, D.-Y. Khang, *Macromolecules*, **42**, 7079 (2009).

[60] I. Zlotnikov, D. Shilo, Y. Dauphin, H. Blumtritt, P. Werner, E. Zolotoyabko, P. Fratzl, *RSC Adv.*, **3**, 5798 (2013).

[61] W. Kiridena, V. Jain, P.K. Kuo, G.Y. Liu, *Surf. Interface Anal.*, **25**, 383 (1997).

[62] J.-C. Tan, P.J. Saines, E.G. Bithell, A.K. Cheetham, *Acs Nano*, **6**, 615 (2012).

[63] S. Humbert, O. Lame, R. Seguela, G. Vigier, *Polymer*, **52**, 4899 (2011).

[64] M.J. Doyle, *Polym. Eng. Sci.*, **40**, 330 (2000).

[65] J.L. Laugesen, *Cem. Concr. Res.*, **35**, 199 (2005).

[66] P. Cortona, *Phys. Rev. B: Condens. Matter.*, **46**, 2008 (1992).

[67] K. Doll, H. Stoll, *Phys. Rev. B: Condens. Matter.*, **56**, 10121 (1997).

[68] Y. Duan, D.C. Sorescu, *Phys. Rev. B: Condens. Matter.*, **79**, 014301 (2009).

[69] S.-L. Shang, L.G. Hector, Jr., S. Shi, Y. Qi, Y. Wang, Z.-K. Liu, *Acta Mater.*, **60**, 5204 (2012).

[70] N.A. Smirnov, *Phys. Rev. B: Condens. Matter.*, **83**, 014109 (2011).

[71] S.F. Pugh, *Philos. Mag. A*, **45**, 823 (1954).

[72] J. Maniks, I. Manika, R. Grants, R. Zabels, K. Schwartz, M. Sorokin, R.M. Papaleo, *Appl. Phys. A*, **104**, 1121 (2011).

[73] M. Sulaiman, A.A. Rahman, N.S. Mohamed, *ICCM*, (2011).

[74] L.G. Schulz, *J. Chem. Phys.*, **17**, 1153 (1949).

CHAPTER V.
EFFECTS OF FLUOROETHYLENE CARBONATE ON ANODE AND CATHODE INTERFACES AT ELEVATED TEMPERATURES[*]

INTRODUCTION

It is well known that lithium-ion batteries experience significant capacity fade during cycling or storage at elevated temperatures. However, the mechanisms responsible for the capacity fade at elevated temperatures are poorly understood because the capacity fade is caused by several interdependent factors. On anode side, most previous studies have identified the degradation of the solid electrolyte interphase (SEI) as the factor primarily responsible for the capacity loss seen at elevated temperatures [1-4]. Temperature-induced reactions, such as SEI decomposition, redox reaction, and electrolyte decomposition, cause changes in the morphology and composition of the SEI layer [3]. Deposition of transition metal ions, which are dissolved from cathode active materials at elevated temperatures, onto the anode/electrolyte interface also contributes significantly to the degradation of the SEI layer [5-7]. Degradation of the SEI layer results in SEI reformation and growth, during which cyclable lithium ions are consumed additionally. Thus, the degraded SEI layer cannot sustain its original properties, which affects the degradation of anode performance [1, 3, 7]. For instance, an increase in the

[*] This chapter includes content from an unpublished paper in review: H. Shin, J. Park, W. Lu, and A.M. Sastry, *Journal of the Electrochemical Society*.

level of inorganic components present in the SEI layer can lower the ionic conductivity of the SEI layer, which hinders lithium ion transport into/from the anode [4].

While degradation of the SEI layer has been considered the main contributor to the fade in capacity at the anode side, several factors has been proposed as reasons for the capacity fade that comes from the cathode side. In particular, $LiMn_2O_4$ shows the most severity in terms of (i) the dissolution of cathode materials due to the disproportionation reaction and hydrofluoric acid (HF) attack; (ii) formation of cathode surface films due to continuous decomposition and oxidation of the electrolyte; (iii) irreversible phase and structure transition (i.e. Jahn-Teller distortion); and (iv) structural instability at higher potential (i.e. transformation of the unstable two-phase structure to a more stable single-phase structure via the loss of MnO and Mn_2O_3) [4,8-10].

Several modifications have been made to the cathode side in order to improve the poor performance observed at elevated temperatures. For instance, a considerable degree of Mn dissolution, as well as structural instability, have been suppressed by partially substituting Mn with transition metals, such as Co, Cr, or Ni, and coating the surface with diverse metal oxides [11, 12]. Nevertheless, considerable decay in performance was still observed at elevated temperatures in $LiMn_2O_4$/graphite Li-ion cells [12]. Thus, problems associated with the electrode/electrolyte interfaces have attracted considerable attention as key issues that need to be addressed to solve the battery degradation at elevated temperatures. In particular, the instability or poor characteristics of the SEI layer formed on the anode has been identified as a main issue that must be addressed to further enhance battery performance at elevated temperatures.

The use of electrolyte additives has been considered one of the most effective and economical ways to construct a robust and thermally stable SEI layer on the anode side. Electrolyte additives are electrochemically decomposed on the graphite anode before the reductive decomposition of the main organic solvents, thereby ensuring the stability of the SEI layer. The reduction-type additives, such as vinylene carbonate (VC), vinyl ethylene carbonate (VEC), and fluoroethylene carbonate (FEC), have typically been selected to modify the SEI layer on the anode, thereby enhancing battery performance at both room and high temperatures [13]. VC has been widely using to improve the electrochemical performance and thermal stability of Li-ion batteries [14-22]. It has been reported that adding less than 2% VEC to the electrolyte helped improve cell performance due to the modified SEI layer [23-25].

Many studies have recently been conducted on the effects of FEC on anode performance. It was reported that adding FEC was beneficial to performances of graphite and silicon anodes because it formed a desirable SEI layer [26-32]. However, a recent study showed a conflicting result, suggesting the detrimental effect of FEC on anode performance [33]. Thus, the impact of FEC on the anode still remains unclear.

In addition, the fundamental mechanism of FEC decomposition is still controversial in the literature. One potential mechanism suggested that FEC might lose hydrogen fluoride (HF) through dehydrofluorination to form polymers of VC [13, 31]. In this case, lithium fluoride (LiF) and poly(vinylene carbonate) were reported as the main species present in the SEI layer on the anode. Another decomposition mechanism involved opening of the five-membered ring, which led to the formation of lithium poly(vinyl carbonate), LiF, and some dimers [34]. A recent ab initio molecular dynamics

simulation proposed that both one- and two-electron mechanisms led to the rapid release of F^- to form LiF [35]. Due to these different decomposition mechanisms, there are still discrepancies regarding the nature of the chemical species that constitute the SEI layer formed on the anode side [29-32].

While several studies have attempted to elucidate the effects of electrolyte additives on battery performance, emphasizing the properties of the SEI layer on the anode, relatively little attention has been paid to understanding of the effects of electrolyte additives on the cathode side. Recently, Burns *et al*. claimed that reduced electrolyte oxidation at the cathode side is primarily responsible for the enhanced capacity retention observed at elevated temperatures due to the addition of VC and that the effect of VC at the anode is less important [19]. In addition, it was reported that the addition of VC considerably suppressed Fe dissolution from $LiFePO_4$ cathode material at elevated temperatures [17]. However, this is not the case for $LiCoO_2$ cathode material. It was suggested that the VC remaining after formation of the SEI layer reacts with the cathode surface, leading to Co dissolution during storage at high temperature [20]. It was also shown that the addition of VEC had significant effects on the surface of the cathode, improving the electrochemical performance of a $LiNo_{0.8}Co_{0.2}O_2$ /Li cell at 50 °C [36]. Thus, the use of electrolyte additives not only affects the anode side but also the cathode side. An in-depth understanding of the cathode/electrolyte interface driven by electrolyte additives is necessary to fully evaluate the effects of electrolyte additives on the performance of Li-ion batteries. To the best of our knowledge, this is the first effort to systematically study the effects of FEC on the cathode interface at elevated temperatures.

The goal of this work is to improve our understanding of the influence of FEC on both the anode and cathode sides. We first investigate the effects of FEC on anode (graphite) performance at elevated temperatures. Next, we conduct a comprehensive investigation of the effects of FEC on the performance of the cathode ($LiMn_2O_4$) at elevated temperatures, identifying its mechanisms of action by focusing on Mn dissolution and surface film formation at the surface of the cathode electrode.

METHODS

Preparation of electrodes and battery cells

Composite electrodes were prepared to investigate effects of FEC on the performance of a graphite anode and a $LiMn_2O_4$ (LMO) cathode. To prepare the graphite electrode, a slurry was prepared by mixing synthetic graphite powder (90 wt%)(Timrex SLP30, Timcal) with a polyvinylidene fluoride (PVdF) binder (10 wt%)(Kureha 7208, Kureha America) dissolved in N-methyl-2-pyrrolidone (NMP) using a SpeedMixer (FlackTek Inc.). The resulting slurry was cast onto a 9 μm-thick copper foil at a constant speed using a 9-mil film applicator with a doctor-blade film coater (MTI Corp.). To prepare a LMO slurry, LMO powder (95 wt%)(Electrochemical grade, particle size <5 μm, Sigma-Aldrich), carbon black (5 wt%)(Super C65, Timcal), and PVdF binder (5 wt%) dissolved in NMP solution were mixed and cast onto a 15 μm-thick aluminum foil using the procedure described above. All composite electrodes were then dried overnight in a vacuum oven at 110 °C. The dried electrodes were punched out as disks with an area of 0.785 cm^2 and vacuum-dried again before being used for coin-cell assembly. To assemble 2032-type coin cells, the working electrode was assembled in a half-cell configuration

with a Li foil counter/reference electrode (0.75 mm thick, 99.9%, Alfa Aesar) and a separator (Celgard 2320) soaked in electrolyte solution The base electrolyte was 1.0 M lithium hexafluorophosphate ($LiPF_6$) (Battery grade, <50 ppm HF, <15ppm H_2O, Sigma Aldrich) dissolved in a 1:1 (by volume) mixture of ethylene carbonate (EC) and dimethyl carbonate (DMC). FEC (5 wt%) (99% fluoroethylene carbonate, Sigma-Aldrich) was added to the base electrolyte in an aluminum container in order to prepare the FEC-containing electrolyte. The HF content of the FEC-containing electrolyte was less than 50 ppm, as determined by using a non-aqueous titration method. All electrolyte preparation and cell assembly operations were carried out in an argon-filled glovebox (M. Braun) at moisture and oxygen levels below 0.1 ppm.

Electrochemical testing: Graphite/electrolyte interface

The graphite/Li half-cells described above were used for electrochemical experiments, including electrochemical impedance spectroscopy (EIS) measurements, using a battery cycler (Biologic). To evaluate the effects of FEC on the performance of a graphite electrode at room and high temperatures, the half-cells were discharged (lithiation) and charged (de-lithiation) between 5 mV and 1.0 V at constant current (C/18 rate) during the formation process (first 8 cycles). At each cutoff voltage, the voltage was held until the current reached 70% of the applied current. Subsequent cycles (C/3 rate) before the 31st cycle were performed at room temperature. These cycles were followed by an additional 30 cycles (C/3 rate) at room temperature or 55 °C, using a same charge-discharge scheme used in the formation process. All C-rates are based on the theoretical capacity (372 mAh/g) of graphite.

To understand the characteristics of the SEI layer formed in the presence of FEC, the interfacial resistances of the cells after the formation cycles and the high temperature cycles (55 °C) were measured using EIS. Before the EIS measurements, the potential was held at 1.0 V for 5 h after each cycling. The frequency was scanned from 150 kHz to 50 mHz using a 5 mV amplitude perturbation. To investigate the stability of the FEC-derived SEI layer at elevated temperature, the change in total reduction charge of the FEC-containing cell, which is the sum of the reversible and irreversible discharge capacities, was compared with that of the FEC-free cell. The cycled cells (8 cycles for formation, followed by 22 cycles at room temperature) were stored at 55 °C for 7 days under an open-circuit condition, and then cycling was continued, starting with a reduction current, i.e., discharge of the half-cells.

To further confirm the stability of the FEC-derived SEI layer, the amount of Li-ions consumed during SEI reformation or recovery after high temperature storage was estimated by integrating the currents during constant voltage holds at 0.4 V, which is higher than the potential required for Li-ion intercalation in graphite (below 0.25 V vs. Li/Li^+). For this electrochemical analysis, the cells were cycled at a rate of C/10 between 5 mV and 1.0 V, including the constant voltage holds at each 0.4 V with a cutoff current of <1.5 μA, as shown in Figure 5.1. With this potential window (1.0 ~ 0.4 V), it was assumed that a major portion of the Li-ions would be consumed by SEI (re)formation and that the electron flow would be completely balanced by that Li-ion consumption, since Li-ion intercalation was excluded or at least minimized, as described in a previous study [37]. After 15 cycles, the cells were stored at 55 °C for 7 days, and then cycling was continued using the same procedure at room temperature.

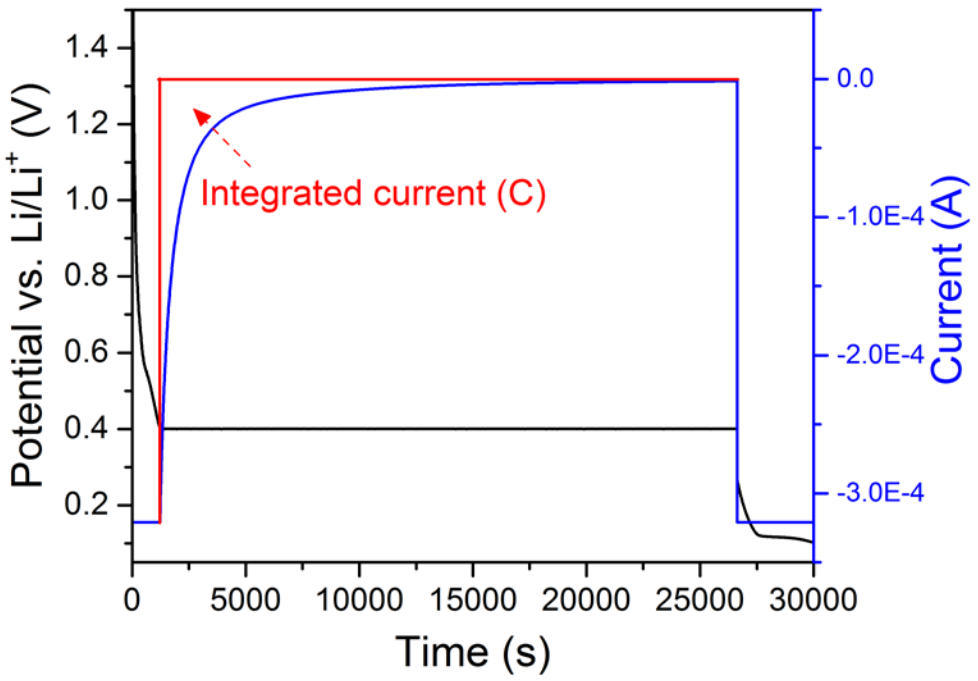

Figure 5-1. Variations in current (blue) and potential (black) over time during a constant voltage hold at 0.4 V.

Electrochemical testing: LMO/electrolyte interface

To investigate the effects of FEC on the performance of the LMO cathode at room and high temperatures, the LMO/Li half-cells were cycled between 3.5 V and 4.3 V at a constant current (C/3 rate) during the formation process (first 5 cycles). This was followed by 50 cycles at the same rate, but at different temperatures (RT vs. 50 °C). For the EIS measurements, the potential was held at 3.5 V for 3 hours and the impedance of the cell was measured by applying a 5 mV amplitude perturbation over the frequency range of 150 kHz to 50 mHz.

Characterization

The graphite particle morphology of the anode was examined by scanning electron microscopy (SEM) with an accelerating voltage of 10 kV.

For the surface analysis of the cycled LMO cathode, X-ray photoelectron spectroscopy (XPS) was conducted using a Kratos Axis Ultra X-ray photoelectron spectrometer equipped with a monochromatic Al Kα excitation source ($h\nu$ = 1486.6 eV). The cycled LMO electrode was rinsed with DMC solvent for 3 min and then vacuum-dried to remove residual salts. Rinsed samples were vacuum-sealed in a glovebox and then transferred to the XPS instrument for analysis. An area of the cathode surface layer analyzed was 300 × 700 μm^2. The binding energy scale was calibrated based on the graphite peak in the C 1s peak at 284.3 eV. Core spectra were recorded with 20 eV constant pass energy. Charge neutralization was used during the measurements. Depth profiles were obtained by Ar-ion beam sputtering using an ion beam voltage of 4 keV.

To assess the dissolution of manganese from the LMO cathode, the composite LMO electrode was immersed in the electrolyte (1M $LiPF_6$ in EC:DMC) with or without 5 wt% FEC in an aluminum container in a glovebox. These aluminum containers were then stored in a vacuum oven for several days. After storage at elevated temperature, the content of Mn dissolved in the electrolyte was determined by inductively coupled plasma optical emission spectrometry (ICP-OES).

To investigate the formation of HF upon thermal aging, the HF content of the electrolyte was measured by using an acid-based neutralization titration method.[38] To ensure the accuracy of the measurement, the non-aqueous titration was performed in a glovebox, where the moisture content was maintained below 0.1 ppm. This titration was

performed using a 0.01 mol L^{-1} titrating reagent that was prepared by dissolving trimethylamine (Sigma-Aldrich) in DMC (Sigma-Aldrich) and a methyl orange indicator (Sigma-Aldrich). Using this non-aqueous titration method in an inert environment, the HF level of the same electrolyte was determined to be below 50 ppm (~ 38 ppm), which is in excellent agreement with the reported value (< 50 ppm) by the manufacturer.

RESULTS AND DISCUSSION

Effects of FEC on the graphite/electrolyte interface

Figure 5.2 shows the differential capacity (dQ/dV) curves for the first charging (Li intercalation) of Li/graphite half cells with or without added FEC. A peak, which is associated with the reduction of EC, is observed at 0.6 ~ 0.7 V (vs. Li/Li^+) was observed in the normal cell, while reduction peaks are observed at higher potential region (1.0 ~ 0.7 V) in the FEC-containing cell.

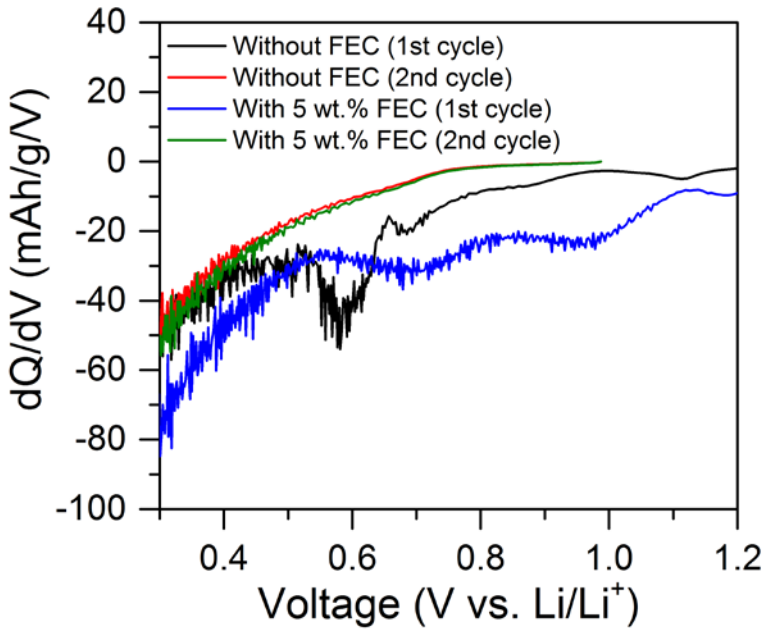

Figure 5-2. Differential capacity plots of Li/graphite cells with or without added FEC.

The reductions peaks at higher potentials are associated with the reduction of FEC, since LUMO energy (0.98 eV) of FEC is lower than that of EC (1.17 eV) [27]. This indicates that the reduction of FEC occurred on the anode surface prior to the reduction of EC. Thus, a FEC-derived layer, which consists of decomposition products of FEC, was formed in the FEC-containing cell, and this modified SEI layer might affect the performance of graphite electrodes.

Figure 5.3 shows the cycling performance of graphite electrodes in FEC-containing and FEC-free solutions at room temperature (Fig. 5.3a) and at 55 °C (Fig. 5.3b). Graphite/Li cells were cycled at a C/18 rate during the formation process (first 8 cycles), and then at a C/3 rate during the subsequent cycles at different temperatures.

A gap in the initial specific discharge capacity between the FEC-containing cell and the FEC-free cell was observed. A lower reversible capacity was observed from the FEC-free cell, compared with the FEC-containing cell. It seems that the intercalation/deintercalation of lithium ions into the graphite through an SEI layer derived from a normal electrolyte (1M $LiPF_6$ in EC:DMC) is extremely slow, so that the cell cannot attain the maximum capacity of the graphite electrode, even at a C/18 rate. The faster kinetics of lithium intercalation/deintercalation seen in the presence of FEC can be attributed to a modification of the characteristics of the SEI layer caused by the added FEC [39, 40]. As a result, a reversible capacity of 360~370 mAh/g, which is close to the theoretical maximum capacity of graphite (372 mAh/g), was achieved simply by adding 5 wt% FEC to the electrolyte. This implies that the mobility of lithium ions through the FEC-derived SEI layer was superior to that in the conventional SEI layer, delivering almost the full capacity of graphite at a C/18 rate.

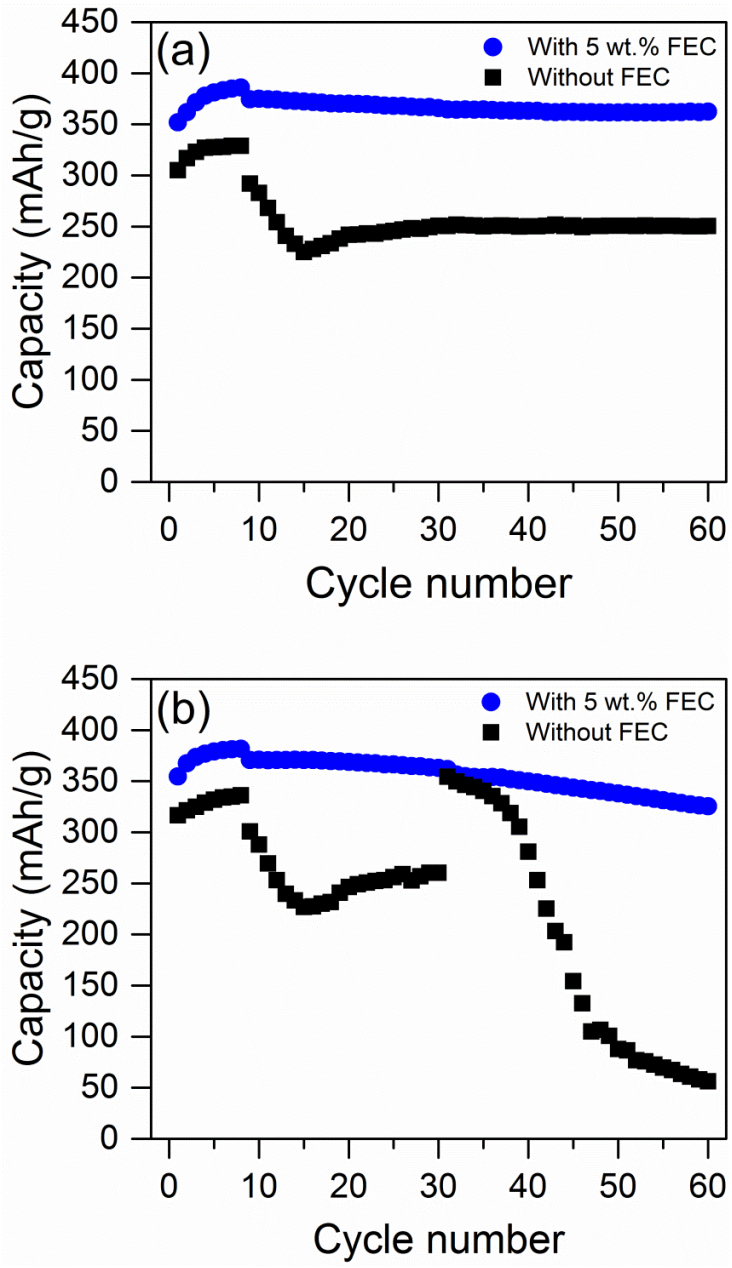

Figure 5-3. The cycling behavior of Li/graphite cells with/without FEC at (a) room temperature and (b) elevated temperature.

Note that the slight increase in reversible capacity during the formation process (first 8 cycles) was observed regardless of the use of FEC additive. The increased capacity during the initial cycles is consistent with the results of a previous study, in which the same graphite (SLP 30) was used [41]. The increase is due to the slow

electrolyte wetting rate in the porous electrode, which consisted of hydrophobic graphite and PvdF [42, 43]. Transport of the electrolyte into the pore networks of the electrode is greatly affected by the porosity and thickness of the electrode, as well as the particle morphology of the graphite; a combination of these factors determines the wetting rate of the electrolyte.

After the formation process, the rate was increased to C/3 during subsequent cycles. In the FEC-free cell, the capacity decreased dramatically and reached its lowest point at 46.4% of the maximum capacity obtained at the C/18 rate. The decreased capacity recovered slightly within a few cycles and the capacity remained at this recovered level through the rest of the cycles. In contrast, the FEC-containing cell showed only a slight drop in capacity when the cycling rate was increased and the cell retained this capacity during cycling.

As shown in Figure 5.4, the graphite used in this work had a relatively large particle size (d_{90} = 32 μm) with a potato shape that exhibited a high degree of preferential orientation. It has been reported that these rate effects are more pronounced with this type of graphite (large particles with a non-spherical shape) because there are longer diffusion lengths for the lithium ions in the particles and longer pathways for Li^+ transport from the bulk electrolyte to the graphite surface [42, 44-46]. The sudden drop in capacity at the C/3 rate was somewhat associated with this type of particle morphology. However, this was not the main parameter affecting the rate capability of the graphite electrode. Surprisingly, the decrease in capacity at a C/3 rate was considerably reduced with the addition of FEC. In other words, the change in SEI properties was sufficient to overcome the drawbacks of the graphite electrode, allowing remarkable improvement in the rate

capability. Thus, the poor rate capability observed in the FEC-free cell can be attributed to a disruption of the SEI layer formed at the anode/electrolyte interface.

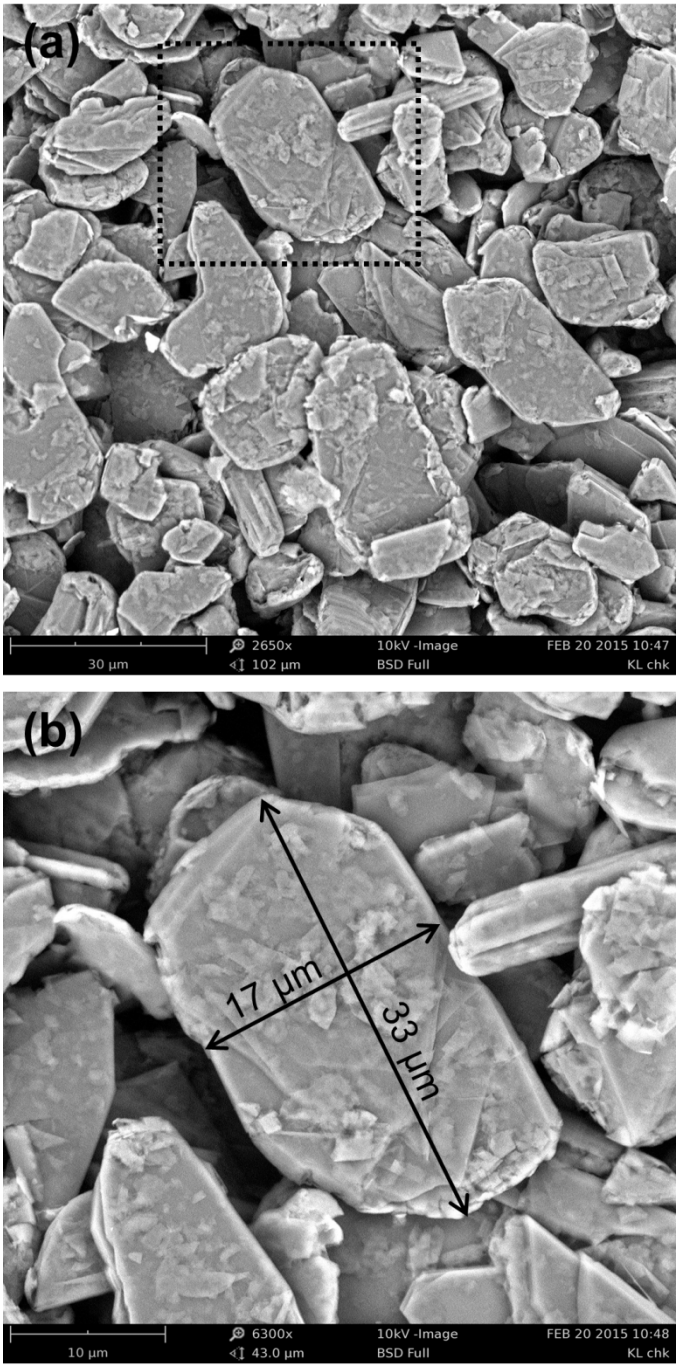

Figure 5-4. SEM image of graphite (Timrex SLP 30): (a) Many graphite particles have a high degree of preferential orientation. (b) Close-up image of the square box (a), showing one particle exhibiting dimensions of 17 × 33 µm.

The result implies that the sluggish transport of lithium ions through the SEI layer is primarily responsible for the decrease in capacity at the increased rate, rather than the diffusion length for lithium ions in the graphite particles or the length of the pathways for Li^+ transport to the graphite surface. Thus, modification of the SEI layer is a more important factor for improving poor rate capability than morphological modification of the graphite particles. It can be concluded that the modified SEI layer driven by the addition of FEC exhibited desirable properties for the fast transport of lithium ions and better chemical and mechanical stability at a high rate.

In the FEC-free cell, the observation of a slight recovery of capacity from its lowest point might indicate that the mechanical instability of the conventional SEI layer also contributes to the observed capacity drop at the increased cycling rate. It seems that partial defects in the SEI layer occurred due to the stresses generated during fast intercalation and deintercalation of lithium ions and reformation of the SEI layer, exposing new graphite surfaces [47]. Similar to the previous explanation for the capacity increase during the initial cycles, electrolyte wetting of the new graphite surfaces, as well as restoration of the damaged SEI layer, could result in a slight increase in capacity within a few cycles. It is believed that the local current density and lithium concentration on the particle surface are relatively high for large particles of graphite [42]. The high current density and lithium concentration are likely to cause fast local SEI formation as well as fast local volume changes, with a greater probability of cracks or defects in the SEI layer [42].

When the temperature increased, most of the reduced reversible capacity was initially recovered in the cell with no additive (Fig. 5.3b). The increased temperature

facilitated the kinetics of lithium ion transfer at the interface, allowing considerable intercalation of lithium ions at the given rate. However, the capacity quickly decreased during cycling at the elevated temperature. This is mainly due to the instability of the SEI layer, as well as SEI growth, at elevated temperatures. SEI growth decreases the conductivity of the graphite agglomerate, and reduces the reversible capacity due to decreases in the amount of active material and in the kinetics of lithium insertion.[48] Capacity retention at elevated temperature improved significantly in the FEC-containing cell, indicating the stability of the FEC-derived SEI layer at elevated temperatures. Therefore, the FEC-derived SEI layer is expected to have desirable properties for the kinetics of lithium ion transfer and excellent stability at high temperature.

The effectiveness of the FEC-derived SEI layer was confirmed by the impedance spectra, as shown in Figure 5.5. Compared with the FEC-derived SEI layer, the conventional SEI layer formed in the absence of additive showed higher interfacial resistance, which was displayed as two semicircles in the high and medium frequency ranges, after the formation cycle. Typically, these two suppressed semicircles represent the processes of Li^+ transport through the SEI layer at higher frequencies and the so-called charge-transfer at lower frequencies [18, 28, 49]. Recent studies have pointed out that the "charge-transfer" process at the graphite/electrolyte interface can be understood as an "ionic transfer" process involving two distinct, but closely interwoven steps: (1) Li^+ desolvation (i.e. stripping of the Li^+ solvation sheath), and (2) the migration of the "naked" Li-ions through the SEI layer [50, 51]. Thus, the observed semicircles are correlated with these Li^+ transport processes at the graphite/electrode interface.

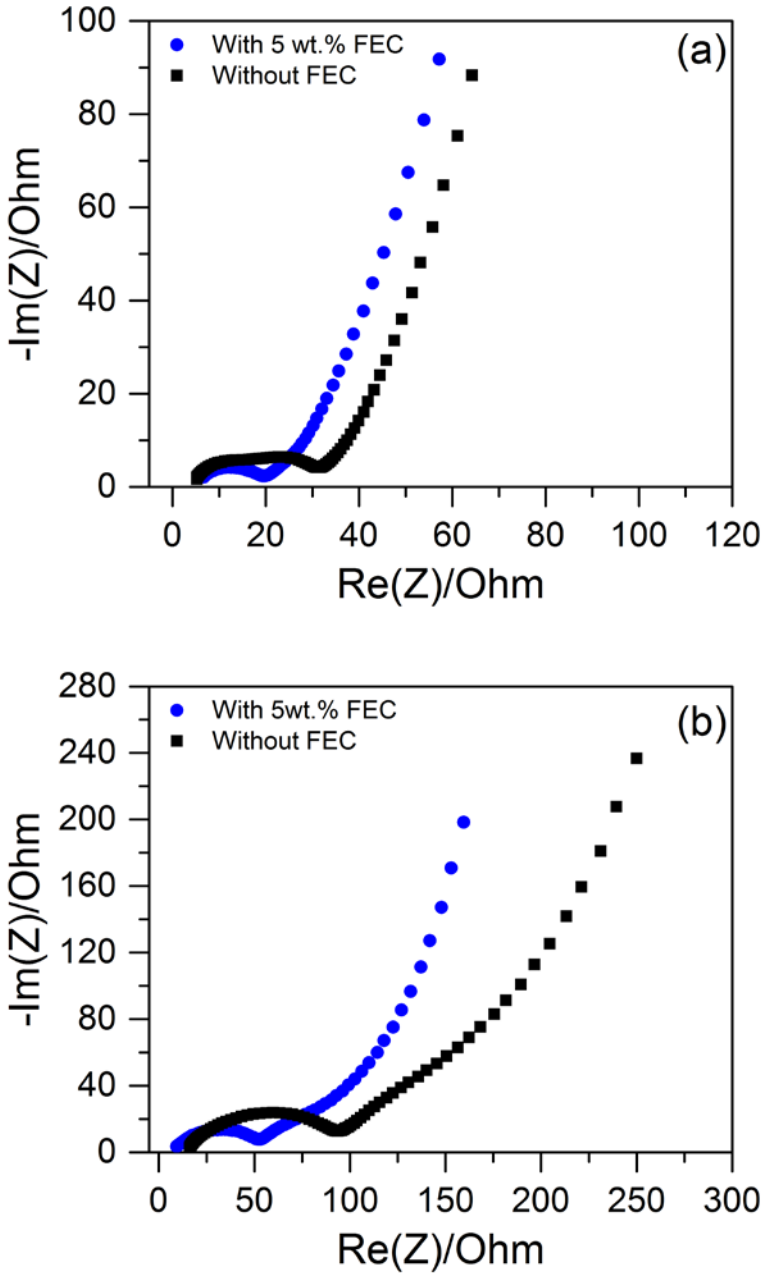

Figure 5-5. Impedance spectra, represented as Nyquist plots, of Li/graphite cells with or without added FEC after (a) the formation cycle and (b) the 50th cycle at 55 °C.

As shown in Fig. 5.5a, the lower interfacial resistance proved that the FEC-derived SEI layer had desirable properties—such as a compact/flexible chemical structure, decreased thickness, and better Li^+ conductance—for the faster Li^+ transport at the interface. There has been good agreement that the FEC-derived SEI layer is much thinner

and denser than the EC-derived SEI layer [12, 29, 32, 33]. Although there was some discrepancy regarding the composition of the SEI layer derived from the FEC additive, it seems that this SEI layer had better mechanical stability, which allowed it to withstand the stresses that occur during fast intercalation/deintercalation, as well as better passivation, which minimized reactions between anode and electrolyte. As suggested by previous studies, the dense polymeric or oligomeric species that result from FEC decomposition were likely to improve the passivation and flexibility of the SEI layer [12, 32, 33].

Figure 5.5b shows that the stability of the FEC-derived SEI layer was well maintained, even at elevated temperatures. After cycling at high temperature, the increase in the interfacial resistance observed in the cell with added FEC additive was significantly lower than that of the cell with no additive. This result implies that the passivation effect of the FEC-derived SEI layer was still effective at elevated temperatures, suppressing further electrolyte decomposition and SEI growth. In contrast, a considerable increase in the interfacial resistance of the normal cell indicates that the conventional SEI layer failed to maintain the passivation and its integrity, possibly due to the dissolution or disruption of the SEI species, leading to continuous electrolyte decomposition and SEI growth. Consequently, a thick and resistive SEI layer could significantly interrupt Li-ion transport at the graphite/electrolyte interface. In addition, the conductivity of the graphite agglomerate would decrease due to poor contact between particles that were covered by the thick SEI layer.

Another noticeable difference was observed at the intercept on the real axis at high frequency, which reflects an ohmic resistance that includes the electrolyte resistance,

the electronic resistance between active materials and current collectors, and the external connection resistance [49]. After cycling at high temperature, a higher ohmic resistance was observed in the cell without additive compared with the FEC-containing cell. This was due to increased electrolyte resistance that may originate from severe electrolyte decomposition and from the chemical species dissolved or decomposed from the SEI layer at elevated temperature. Since the FEC-derived SEI layer was chemically stable at elevated temperature, electrolyte decomposition and SEI dissolution was successfully restrained, allowing no increase in the ohmic resistance.

Next, we further investigated the stability of the SEI layer at elevated temperatures by comparing the results of the total reduction charge over cycling test.

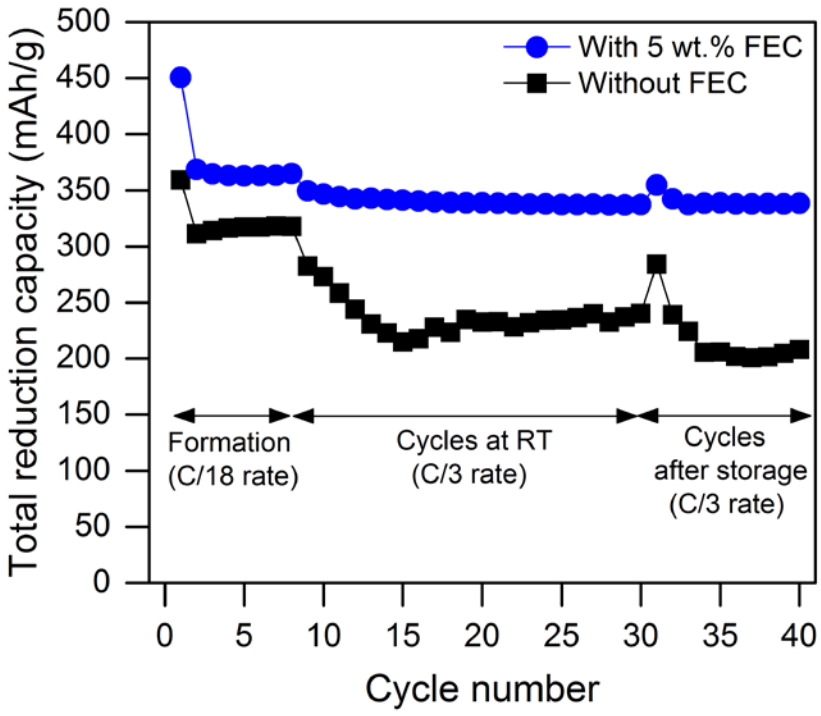

Figure 5-6. Variations in the total reduction capacity after 55 °C storage with or without added FEC.

As shown in Figure 5.6, the stability of the FEC-derived SEI layer was compared with that of the conventional SEI layer by examining the total reduction capacity (the sum of the reversible and irreversible discharge capacity) using a method adopted in a previous study [3]. The cells cycled (30 times) at room temperature were stored at 55°C in their deintercalated states, and then cycled again (10 times) at room temperature. The cell with added FEC exhibited a small increase in total reduction charge (17.5 mAh/g) at the 31st cycle, while the cell without additive showed a relatively large increase in total reduction charge (43.9 mAh/g). The additional reduction capacity observed at the 31st cycle was mainly due to the additional reduction of electrolyte, as suggested by the previous study [3]. This result suggests that damage or disruption of the SEI layer formed without additive was severe at elevated temperature, compared with that formed in the presence of added FEC. That is, the FEC-derived SEI layer had better stability against elevated temperature. Note that the total reduction capacity of the cell without additive was slightly lost during continued cycling after storage at high temperature. This indicates that the reconstructed SEI layer did not function as well as the original SEI layer, affecting the reversibility capacity by disturbing the intercalation and deintercalation of lithium ions.

To further confirm the stability of the FEC-derived SEI layer, we investigated the integrated current, which is indicative of the amount of Li consumed during SEI formation or reformation. Figure 5.7 displays the consumption of Li ions during the SEI formation process (inset figure) as well as during the SEI reformation process, after storage at high temperature.

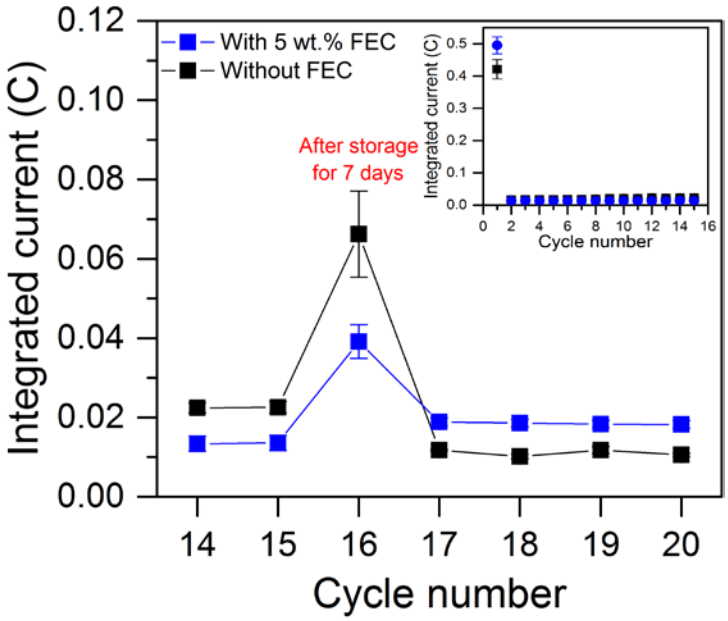

Figure 5-7. Variations in the integrated current before and after 55 °C storage with (blue) or without (black) added FEC; the inset figure shows variation of the integrated current during the first 15 cycles.

As shown in the inset of Figure 5.7, a considerable integrated current occurred during the first cycle, although it decreased significantly after the first cycle. This suggests that the SEI layer was predominantly formed and a major fraction of the Li ions was consumed during the first cycle. This result confirmed that the integrated current could be used as an indicator for estimating this behavior during SEI formation. The cell with added FEC showed a larger integrated current during the first cycle, compared with the cell with no additive. When we considered the fact that the FEC-derived SEI layer was thinner than the normal layer, it might imply that the addition of FEC led to form a denser SEI layer, which might require greater Li-ion consumption.

The thermal stability of the FEC-derived SEI layer is demonstrated in the main figure. After storage at high temperature, the FEC-containing cell displayed a slight increase in the integrated current at the 16th cycle, compared with the cell without

additive. This result suggests that elevated temperature caused little disruption of the FEC-derived SEI layer, which resulted in a small amount of Li-ion consumption during SEI reformation or SEI recovery. In contrast, the cell without additive consumed a large amount of Li-ions in order to reconstruct the SEI layer that was significantly damaged by elevated temperature.

Effects of FEC on the LMO/electrolyte interface

Figure 5.8 shows a comparison of the cycle performance of the LMO electrode in FEC-containing and FEC-free electrolytes at room temperature and 55°C. At room temperature, there was no distinct difference in capacity retention between the FEC-containing cell and the FEC-free cell, which is quite consistent with a previous report [12]. However, when the cells were cycled at elevated temperature, the FEC-containing cell exhibited worse cycle performance than FEC-free cell.

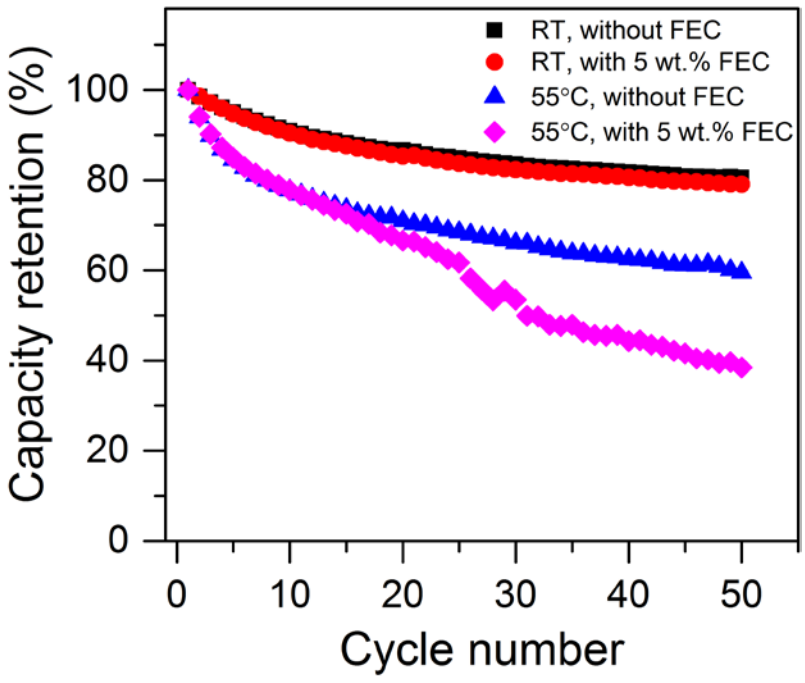

Figure 5-8. Cycling retentions of Li/LMO cells at room and high temperatures with or without added FEC.

We believe that the poor cycle performance at elevated temperature in the FEC-containing cell originated from the LMO/electrolyte side, rather than the Li/electrode side, since it is known that FEC has a positive effect on the Li metal electrode, preventing deposition and dissolution of a lithium metal [52].

The authors of a previous report concluded that there was little effect of FEC on the cathode surface or on the interfacial properties of $LiMn_2O_4$, assuming that the added FEC was quite stable on the positive electrode [12]. It seems that they reached a hasty conclusion without considering the LMO electrode and its surface at elevated temperature. Here, our results clearly displayed the adverse effect of added FEC on the LMO electrode at elevated temperature. This indicates that the enhanced performance of the FEC-containing LMO/graphite full cell at elevated temperature originates from the superior improvement of the graphite/electrolyte interface due to the addition of FEC, despite of its negative effects, to some extent, on the LMO electrode. Thus, it can be inferred that the FEC remaining after formation of the FEC-derived SEI layer on the anode continuously reacted on the cathode surface, influencing the cathode side, especially at elevated temperature. This suggests that complete consumption of the FEC additive during SEI formation by either controlling the formation procedure or adjusting the FEC content might be necessary to prevent further reactions at the cathode side. A previous study regarding the effects of VC lends support to our suggestion. They revealed that VC remaining after formation of the SEI layer on the graphite anode would react continuously on the surface of the cathode, resulting in abrupt evolution of gases, such as CO_2 [20]. They also suggested that the dissolution of metal elements on the cathode surface could occur as a result of this reaction. We believe that similar phenomena can

occur when FEC is added to the cell. It is important to note that there is a still a chance to further improve the performance of the FEC-containing Li-ion cell containing at elevated temperature by identifying and solving the problems induced at the positive electrode by added FEC. Thus, the rest of this work focused on identifying the reasons behind the poorer cyclability of the LMO electrode in FEC-containing electrolyte, especially at elevated temperature.

Figure 5.9 shows the impedance spectra of LMO/Li half cells after the 50th cycle in FEC-free and FEC-containing electrolytes at room temperature and 55 °C. Consistent with the cycle performance observed above, the impedance of cells containing FEC was very similar to that of FEC-free cells after cycling at room temperature, while there was a clear difference in the cell impedance at high temperature.

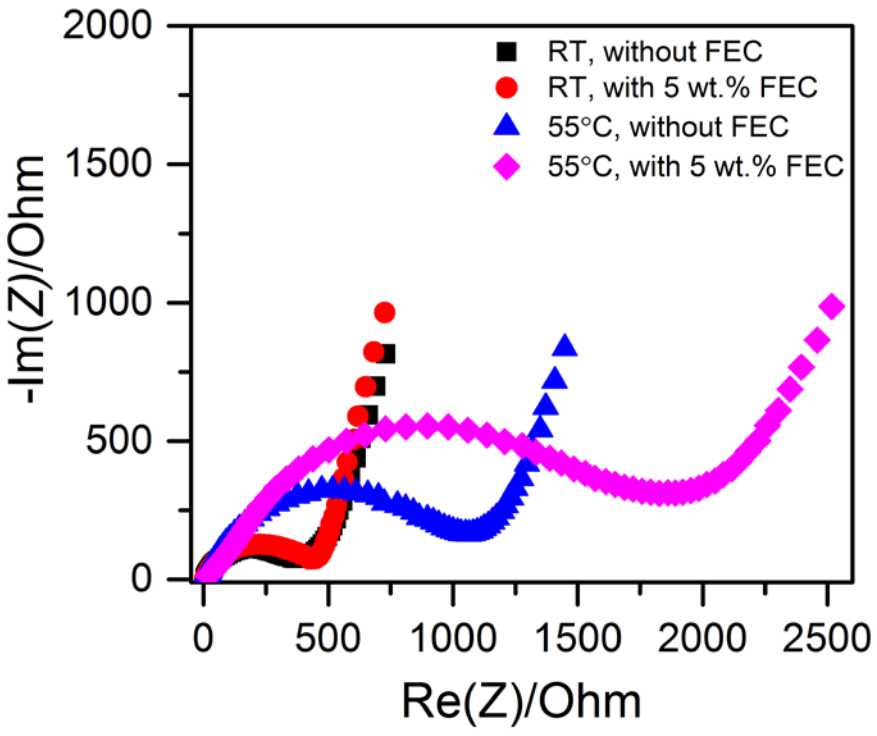

Figure 5-9. Impedance spectra of Li/LMO cells at room and high temperatures with or without added FEC.

The difference was primarily observed in the semicircle at the high-to-medium frequency, which represents an interfacial resistance associated with lithium-ion diffusion in the cathode surface layer and the charge transfer process at the cathode/electrolyte interface. Thus, the FEC-containing cell exhibited a rapid increase in interfacial resistance during cycling at elevated temperature, while a similar interfacial resistance was observed after cycling at room temperature, when compared with the FEC-free cell.

The increase in interfacial resistance (surface film and charge transfer resistances) at elevated temperature might be attributed to poorly conductive organic and inorganic species resulting from the decomposition of the electrolyte and the inter-particle contact loss induced by manganese dissolution. Since the dissolution of manganese leads to the loss of inter-particle contact as well as the subsequent re-deposition of Mn ions, as MnO, MnO_2, and $MnF_{2,}$ on the surface, the charge transfer resistance is closely coupled with the surface film resistance. The observation of increased interfacial resistance gave us a clue concerning the origin of the poor cycle performance shown by the FEC-containing cell at elevated temperature. It was speculated that added FEC altered the kinetics of surface reactions at elevated temperature. These altered kinetics might accelerate the formation of a surface layer on LMO particles as well as Mn dissolution, lowering Li-ion transport at the LMO/electrolyte interface as well as the electronic conductivity of the LMO electrode.

To confirm the above assumption and investigate the surface reactions that occur in the presences of added FEC, we analyzed the thickness and chemical composition of the cathode surface layers that form with/without FEC. The thickness of the surface layer that formed on the cycled LMO electrode in FEC-containing and FEC-free electrolytes was compared based on the depth profile of the surface of the LMO electrode (Fig. 5.10).

The relative amounts of the elements (C, F, O, and Mn) changed as a function of sputtering time, since the surface compounds (e.g. surface layer) that covered the LMO electrode were being sputtered away. In particular, the Mn concentration increased as more of the LMO electrode was exposed. After sputtering for at a certain time, the Mn concentration became uniform, indicating that the surface layer was fully removed. The dotted line (black) represents a sputter time at which the Mn concentration became uniform. Based on the sputtering time needed for the Mn content to become uniform, the thickness of the cathode surface layer was compared. As shown in Fig. 5.10a and 5.10b, the addition of FEC did not result in a significant change in the thickness of the surface layer that formed after cycling at room temperature. That is, the thickness of the FEC-derived surface layer was very similar to that of the surface layer derived from the normal electrolyte.

In contrast, there was a considerable difference in the thickness of the surface layer when the FEC-containing cell was cycled at elevated temperature. After cycling at 55 °C, the LMO electrode in the FEC-containing cell was covered with a thicker surface layer (Fig. 5.10d), compared with the FEC-free cell (Fig. 5.10c). As mentioned earlier, it seems that FEC-driven surface reactions were more pronounced at elevated temperature, which accelerated the formation of a surface layer on the LMO particles. Thus, the thicker surface layer formed in the FEC-containing cell can hinder fast Li-ion transfer at the interface, contributing to the capacity fade of the cell.

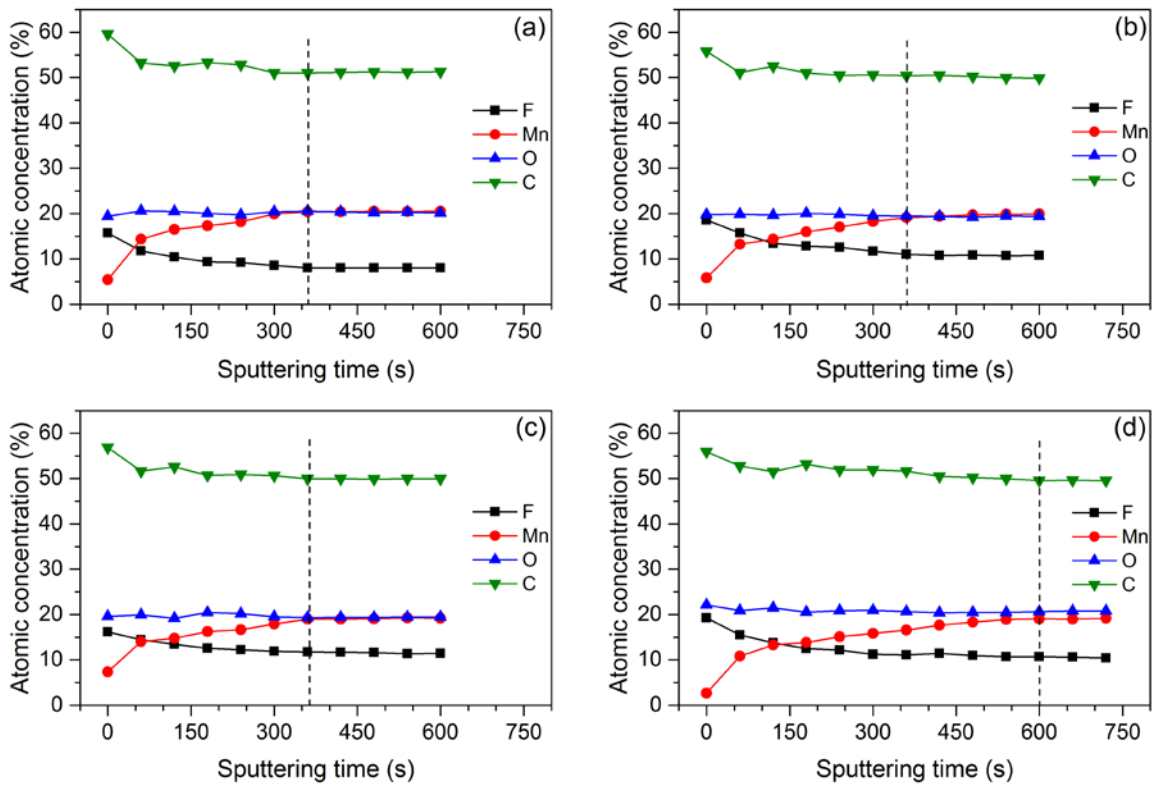

Figure 5-10. Depth profiles of LMO electrodes after cycling without added FEC at (a) room temperature and (c) 55 °C; and with added FEC at (b) room temperature and (d) 55 °C. The dotted line (black) represents a sputtering time at which the surface layer is removed and the bulk LMO is fully exposed.

Note that there was no significant difference between the thickness of the surface layer formed after cycling at room temperature (Fig. 5.10a) and at elevated temperature (Fig. 5.10b) in the FEC-free cell. This means that the observed decrease in capacity of the FEC-free cell at elevated temperature was mostly caused by increased Mn dissolution at high temperature, rather than by the increased thickness of the cathode surface layer. In the case of the FEC-containing cell, however, the decrease in capacity of the cell at elevated temperature originated not only from increased Mn dissolution but also from the formation of a thicker surface layer on the LMO electrode.

To reveal the mechanisms of surface reactions driven by the addition of FEC, high-resolution XPS spectra were collected from LMO electrodes cycled in FEC-free and FEC-containing electrolytes and compared.

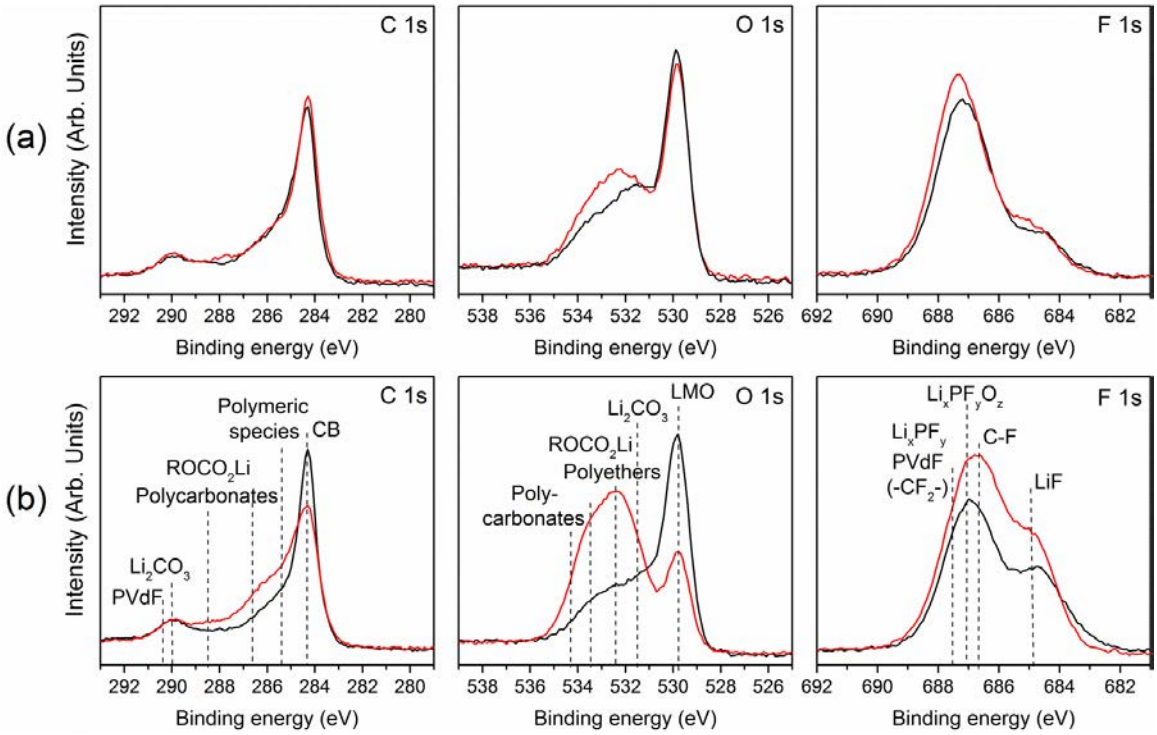

Figure 5-11. Comparison of XPS spectra of the surface of cycled LMO electrodes with (red) and without (black) added FEC at (a) room temperature and (b) 55 °C

As expected, very similar surface layer compositions was observed in FEC-containing and FEC-free cells after cycling at room temperature (Fig. 5.11a). However, a significant difference in the composition of the surface layer was observed after cycling at high temperature, as shown in Fig. 5.11b. The FEC-containing cell cycled at high temperature displayed lower intensities of the peaks associated with carbon black (CB, 284.3 eV in C 1s) and lithium manganese oxide (LMO, 529.8 eV in O 1s). This result indicates that the LMO electrode cycled in FEC-containing electrolyte at 55 °C was covered by a relatively thick surface layer compared with the FEC-free cell cycled at

55 °C. This result is consistent with the result of depth profiling described above. Therefore, it was observed that the intensities of other peaks related to the surface layer increased considerably in the FEC-containing cell at elevated temperature. It is important to note that the use of FEC yields positive effects on the anode side due to the formation of a thin and dense SEI layer, while it has a negative effect on the cathode side due to the formation of a thick surface layer.

Detailed analysis of the C 1s and O 1s spectra suggested that the main difference between the cells cycled at 55 °C in FEC-containing and FEC-free electrolytes was an abundance of polymeric species and polycarbonates at the LMO surface. The peak at 285.4 eV in the C 1s spectrum was assigned to polymeric species which might originate from a pure hydrocarbon compound and/or polyethylene oxide (PEO, $(-CH_2-CH_2-O-)_n$) [53, 54]. The peaks at 286.7 eV and 287.5-289.5 eV were associated with ether and carbonate functional groups, respectively [53, 54]. It is commonly known that these peaks correspond to lithium alkyl carbonates ($ROCO_2Li$) and/or polycarbonates [10, 53, 54]. Andersson *et al*. suggested that the carbonate species were probably polycarbonates based on the observation that the transformation of metastable $ROCO_2Li$ into Li_2CO_3 was not seen at elevated temperature in the case of a positive electrode, which was different from the result observed in the case of a negative electrode [53]. Eriksson *et al*. proposed that the polymerized carbonate formed at elevated temperature resulted from the polymerization of ethylene carbonate (EC), which was initiated by either EC oxidation or the strong Lewis acid PF_5 [54]. We also believe that the increased intensities of the peaks at 286.7 eV and 287.5-289.5 eV were mostly associated with the formation of polycarbonates, since the intensity of the peak (289.9 eV) assigned to Li_2CO_3 did not

increase significantly with increasing temperature in our study. Nevertheless, there was still a possibility that the surface layer formed after cycling at room temperature could contain $ROCO_2Li$ species, as suggested in previous studies.

The abundant presence of PEO-type polymers and polycarbonates in the surface layer derived from the FEC additive at elevated temperature was supported by the dominant intensities of the peaks at 532.5 eV and 533.5~534.4 eV in the O 1s spectra. The peak at 532.5 eV could be assigned to polyethers ($-CH_2O-$), which may have originated from oligomers of PEO, while the peak at 533.5~534.4 eV could correspond to polycarbonates that resulted from EC polymerization and/or polymerization of the FEC additive. Still, the contribution of $ROCO_2Li$ (533.5 eV (C-O-C), 532.5 eV (C=O)) to these peaks, to some extent, cannot be neglected. Thus, it can be inferred that the surface layer formed in the FEC-containing electrolyte contained a significant amount of polycarbonates and polymeric species compared with that formed in the FEC-free electrolyte, especially after cycling at elevated temperature.

The PEO polymer-rich surface layer that formed in the FEC-containing cell can be attributed to additional reactions of $LiPF_6$ with FEC, similar to the reaction of $LiPF_6$ with EC. It has been known that EC polymerization is caused by an acid-catalyzed ring-opening reaction. PF_5, which is a strong Lewis acid, reacts with EC at elevated temperatures, producing PEO polymers and CO_2 [55].

The presence of abundant polycarbonates in the FEC-derived surface layer was likely due to the decomposition and/or side reactions of the FEC additive, initiated or accelerated by elevated temperature. Due to the strong electrostatic field close to the

cathode surface, FEC, which is highly polar, is likely to be the preferred target for electrophilic and nucleophilic attack at the cathode.

Although the reduction/oxidation or decomposition mechanisms of FEC are not clearly understood, one plausible mechanism is that FEC can be transformed to vinylene carbonate (VC), by the loss of an HF molecule (FEC → VC + HF) [13]. Polymerization of the resulting VC could occur, forming polycarbonate species such as poly(VC). This reaction pathway was previously invoked to explain a high content of polycarbonates in the FEC-derived SEI layer at the anode [31, 32]. Similarly, we speculated that vinylene carbonates resulting from FEC decomposition underwent cationic polymerization initiated by protonic and Lewis acids during cycling, producing polycarbonate species on the LMO electrode. Aurbach *et al*. suggested that oligomers of VC could be produced by cationic polymerization on delithiated oxides (at potentials > 4.2 V vs. Li/Li^+) [14]. They reported that an LMO electrode cycled in VC-containing electrolyte exhibited a surface film that mostly contained polycarbonates, possibly poly(VC). Thus, the dehydrofluorination of FEC seems to be the origin of the poly(VC) that forms on the LMO electrode cycled in FEC-containing electrolyte. It was speculated that the dehydrofluorination of FEC was considerably accelerated by elevated temperature; thus, the majority of the polycarbonates were detected in the surface layer on the LMO electrode cycled in FEC-containing electrolyte at high temperature.

Additional evidence for the dehydrofluorination of FEC can be found in the F 1s spectra shown in Fig 5.11b. Assuming that the amounts of LiF generated by the decomposition of $LiPF_6$ ($LiPF_6 \rightarrow LiF + PF_5$) in the FEC-containing cell and the FEC-free cell were similar, the increase in the quantity of LiF seen in the FEC-containing cell

was possibly due to the reaction of Li^+ with HF or F^- from the decomposition of FEC at elevated temperature. More interestingly, a peak near 687 eV was observed to have higher intensity in the FEC-containing cell. It was difficult to precisely interpret the peak, due to the contribution of several compounds (PVdF, Li_xPF_y, and $Li_xPF_yO_z$). Based on the assumption that the decomposition of $LiPF_6$ was not significantly affected by the addition of FEC, the amount of decomposed products, Li_xPF_y and $Li_xPF_yO_z$, were believed to be very similar in both cells. This assumption seemed reasonable because FEC, which has a high dielectric constant, increases the ionization of $LiPF_6$ ($LiPF_6 \leftrightarrow Li^+ + PF_6^-$), thereby suppressing dissociation or decomposition of non-ionized $LiPF_6$ ($LiPF_6 \rightarrow LiF + PF_5$) [56]. Therefore, the peak was expected to be of lower intensity in the FEC-containing cell than the FEC-free cell, since the thicker surface layer derived from FEC obscured more of the LMO electrode, including the PVdF binder, as observed in the peaks (CB and LMO) of the C 1s and O 1s spectra. Based on this expectation, it was speculated that additional F-containing compounds were responsible for the increased intensity of the 687 eV peak observed in spectra of the FEC-containing cell cycled at high temperature. According to recent studies, the additional compounds might be related to dimers containing C-F bonds and/or C-F containing organic products that resulted from FEC decomposition [33, 57].

As mentioned earlier, the decrease in capacity of the FEC-containing cell at elevated temperature could not be solely explained by the formation of a thicker surface layer on the LMO electrode. Mn dissolution from the LMO electrode was another source of degradation within the cell. According to the mechanism suggested above (FEC → VC + HF), we expected that the FEC-containing electrolyte would produce more HF as a

result of FEC decomposition, or side reactions accelerated by elevated temperature, promoting Mn dissolution. The acid dissolution catalyzed by HF is known to be one of the mechanisms for manganese dissolution at elevated temperature [42]. Thus, any increase in the concentration of HF was likely to lead to considerable dissolution of manganese into the electrolyte.

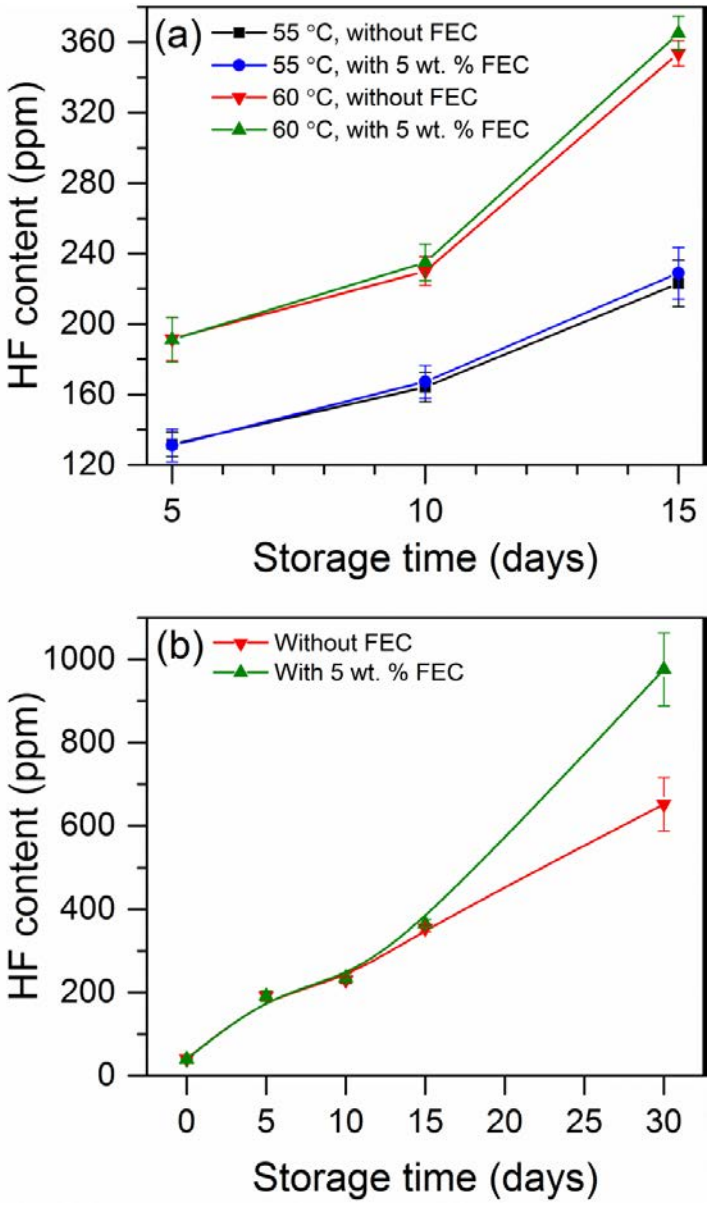

Figure 5-12. Variation of the amount of HF produced during thermal aging with/without added FEC; (a) 15 days storage at 55 °C and 60 °C, (b) 30 days storage at 60 °C.

To further prove the mechanism at elevated temperature, the amount of HF generated as a function of storage time was investigated at elevated temperatures. Figure 5.12a shows the temperature and time dependence of the quantity of HF in the electrolyte with/without added FEC. Regardless of the use of FEC, the amount of HF in the electrolyte increased with increasing temperature, indicating more $LiPF_6$ decomposition catalyzed by increasing temperature.

The decomposition of $LiPF_6$ typically starts with the following reaction:

$$LiPF_6 \rightarrow LiF + PF_5 \qquad (1)$$

which is followed by a reaction between phosphorous pentafluoride and water to form HF and POF_3, as follows:

$$PF_5 + H_2O \rightarrow POF_3 + 2HF \qquad (2)$$

Reaction (1) is negligible at room temperature, so $LiPF_6$ is in equilibrium with LiF and PF_5. However, the equilibrium of the reaction is shifted to the right due to the interaction between PF_5 and the solvent at elevated temperatures, lowering the stability of $LiPF_6$ [55, 56, 58]. The reaction rate is dependent on the solvent and the temperature [55, 56]. Thus, the increased amount of the strong Lewis acid PF_5 reacts with water, increasing the HF content. Furthermore, the formation of additional HF can be accelerated by the following reactions [56, 58]:

$$POF_3+H_2O \rightarrow POF_2(OH) + HF \qquad (3)$$

$$H^+ + PF_6^- \rightarrow HF + PF_5 \qquad (4)$$

In addition to the dependence of HF formation on temperature, the time-dependent formation of HF upon thermal aging of the electrolyte was clearly observed. It has been reported that only a small amount of water is needed to start the decomposition reaction and this reaction is accelerated during thermal aging due to various autocatalytic reactions [58-60]. For instance, the released CO_2 from the carbonates during the aging process can be an additional reaction source [59].

More interestingly, the FEC-containing electrolyte produced more HF than the normal electrolyte as storage time increased at elevated temperatures. At room temperature, the amount of HF did not increase until 30 days of storage. Therefore, there was no significant difference in HF content between the FEC-containing electrolyte and the normal electrolyte. The difference in the amount of HF produced in the electrolytes during thermal aging became more significant as the temperature and storage time increased. As shown in Fig. 5.12b, the difference was quite small and unclear until the storage reached 10 days, but it was clearly seen after 10 days. As speculated earlier, it seems that FEC decomposition (such as dehydrofluorination), or side reactions involving FEC, were accelerated by elevated temperature, producing more HF in the FEC-containing electrolyte. Thus, the results suggest that an increased amount of HF leads to dissolution of manganese in the LMO cathode. They also imply that the FEC-derived SEI layer effectively protects the electrode from HF attack. Thus, the layer was not significantly affected by elevated temperature, compared with the SEI layer formed in the FEC-free electrolyte.

Figure 5.13 shows the changes in the amount of manganese dissolved from the LMO cathode that was soaked in different electrolytes at elevated temperature as a

function of storage time. As expected, we found that the increase in Mn dissolution was accelerated with the use of FEC at elevated temperature. The difference in the amount of dissolved Mn was distinct at the end of 30 days storage. A higher amount of dissolved Mn ions in the FEC-containing electrolyte was associated with the increased HF as a result of FEC dehydrofluorination, which induced attack at the LMO cathode by the increased HF.

We expected that the effect of increased HF would be more significant during cycling at elevated temperature, since the disproportionation reaction of Mn^{3+} is promoted by the increased concentration of HF and the thermodynamic instability of delithiated lithium manganese spinel makes it vulnerable to attack by HF; thereby producing more Mn dissolution in the electrolyte [4, 61].

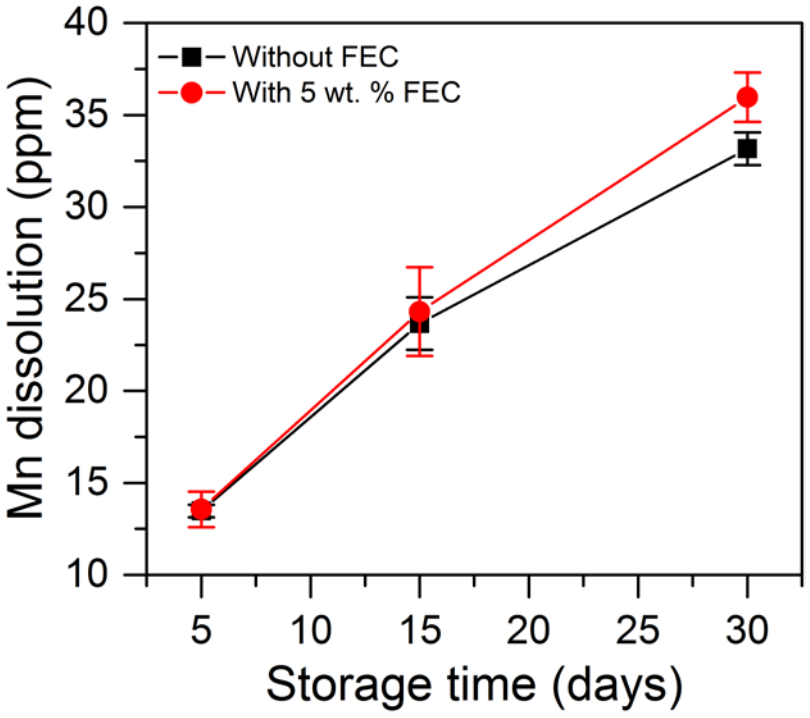

Figure 5-13. Variation of the amount of dissolved manganese ions with (red) or without (black) added FEC as a function of storage time.

A previous study claimed that the VC-derived SEI layer on the graphite electrode was thermally more stable and could more effectively protect the electrode from the deposition of Mn ions, compared with the FEC-derived SEI layer at elevated temperature [11]. This was based on the assumption that similar amounts of manganese ions were dissolved from the cathode side in the FEC-containing and VC-containing cells. Based on our results, however, it is highly possible that more manganese ions were dissolved from the LMO cathode in the FEC-containing electrolyte than were dissolved in the VC-containing electrolyte. Thereby, the FEC-derived SEI layer was believed to have a difficulty in protecting the graphite/electrolyte interface from Mn deposition due to the considerable amount of dissolved manganese ions released from the cathode side.

Based on our findings, the poor cyclability of the LMO electrode in the FEC-containing electrolyte at elevated temperature was attributed to the increased Mn dissolution and a thicker surface layer as a consequence of acceleration of FEC defhydroluorination in the electrolyte at elevated temperatures.

CONCLUSIONS

The effects of the electrolyte additive FEC on electrochemical performance and the electrode/electrolyte interface were thoroughly investigated using graphite/Li cells and LMO/Li cells. The addition of FEC to the normal electrolyte (1M $LiPF_6$ in EC:DMC (1:1 v/v) solution) remarkably improved the performance of graphite/Li cells at room temperature and at elevated temperature. This performance improvement was attributed to the stability and effectiveness of the SEI layer resulting from the FEC additive. The FEC-derived SEI layer imparted desirable properties to graphite/Li cells at room

temperature, including higher reversibility and excellent rate capability. The lower interfacial resistance observed after the formation cycles of the FEC-containing cell, compared with that of the FEC-free cell, demonstrated that the FEC-derived SEI layer was effective in facilitating Li-ion transfer at the graphite/electrolyte interface. The superior thermal stability of the FEC-derived SEI layer was also confirmed, showing excellent performance during cycling and storage at elevated temperature.

On the other hand, the adverse effect of FEC on the performance of LMO/Li cells was observed at elevated temperature, while there was no clear difference in the performance of LMO/Li cells at room temperature. For the FEC-containing cell, formation of a thick surface layer on the LMO cathode and increased Mn dissolution catalyzed by elevated HF levels were responsible for the poor performance observed, resulting in a dramatic increase in the interfacial resistance as well as accelerated capacity fading at elevated temperature. It was proposed that the origin of the thick surface layer and the increased Mn dissolution was an FEC dehydrofluorination reaction and/or its side reactions at the LMO surface, initiated or accelerated by elevated temperature. This suggestion was supported by the observation of abundant polycarbonates, possibly poly(VC), on the LMO surface and an increased HF content in the FEC-containing cell at elevated temperature.

Based on our findings, it is suggested that the FEC remaining after formation of the SEI layer on the anode side is detrimental to the cathode side, especially at elevated temperature. It is, therefore, important to optimize the amount of FEC added to the electrolyte in order to minimize the adverse effect of residual FEC on the cathode side.

This strategy can be an effective way to further improve the performance of LMO/graphite cells at elevated temperature.

BIBLIOGRAPHY

[1] A. M. Andersson, K. Edstrom, N. Rao, and A. Wendsjo, *J. Power Sources*, **81**, 286 (1999).

[2] T. Zheng, A. S. Gozdz, and G. G. Amatucci, *J. Electrochem. Soc.*, **146**, 4014 (1999).

[3] A. M. Andersson and K. Edstrom, *J. Electrochem. Soc.*, **148**, A1100 (2001).

[4] J. Vetter, P. Novak, M. R. Wagner, C. Veit, K. C. Moller, J. O. Besenhard, M. Winter, M. Wohlfahrt-Mehrens, C. Vogler, and A. Hammouche, *J. Power Sources*, **147**, 269 (2005).

[5] S. Komaba, N. Kumagai, and Y. Kataoka, *Electrochim. Acta*, **47**, 1229 (2002).

[6] H. Tsunekawa, S. Tanimoto, R. Marubayashi, M. Fujita, K. Kifune, and M. Sano, *J. Electrochem. Soc.*, **149**, A1326 (2002).

[7] C. Delacourt, A. Kwong, X. Liu, R. Qiao, W. L. Yang, P. Lu, S. J. Harris, and V. Srinivasan, *J. Electrochem. Soc.*, **160**, A1099 (2013).

[8] M. Mohamedi, D. Takahashi, T. Itoh, and I. Uchida, *Electrochim. Acta*, **47**, 3483 (2002).

[9] T. Doi, M. Inaba, H. Tsuchiya, S.-K. Jeong, Y. Iriyama, T. Abe, and Z. Ogumi, *J. Power Sources*, **180**, 539 (2008).

[10] H. Duncan, D. Duguay, Y. Abu-Lebdeh, and I. J. Davidson, *J. Electrochem. Soc.*, **158**, A537 (2011).

[11] I. H. Cho, S.-S. Kim, S. C. Shin, and N.-S. Choi, *Electrochem. Solid St.*, **13**, A168 (2010).

[12] M.-H. Ryou, G.-B. Han, Y. M. Lee, J.-N. Lee, D. J. Lee, Y. O. Yoon, and J.-K. Park, *Electrochim. Acta*, **55**, 2073 (2010).

[13] S. S. Zhang, *J. Power Sources*, **162**, 1379 (2006).

[14] D. Aurbach, K. Gamolsky, B. Markovsky, Y. Gofer, M. Schmidt, and U. Heider, *Electrochim. Acta*, **47**, 1423 (2002).

[15] D. Aurbach, J. S. Gnanaraj, W. Geissler, and M. Schmidt, *J. Electrochem. Soc.*, **151**, A23 (2004).

[16] H. Ota, Y. Sakata, A. Inoue, and S. Yamaguchi, *J. Electrochem. Soc.*, **151**, A1659 (2004).

[17] H.-C. Wu, C.-Y. Su, D.-T. Shieh, M.-H. Yang, and N.-L. Wu, *Electrochem. Solid St.*, **9**, A537 (2006).

[18] L. Chen, K. Wang, X. Xie, and J. Xie, *J. Power Sources*, **174**, 538 (2007).

[19] J. C. Burns, G. Jain, A. J. Smith, K. W. Eberman, E. Scott, J. P. Gardner, and J. R. Dahn, *J. Electrochem. Soc.*, **158**, A255 (2011).

[20] J.-Y. Eom, I.-H. Jung, and J.-H. Lee, *J. Power Sources*, **196**, 9810 (2011).

[21] N. N. Sinha, A. J. Smith, J. C. Burns, G. Jain, K. W. Eberman, E. Scott, J. P. Gardner, and J. R. Dahn, *J. Electrochem. Soc.*, **158**, A1194 (2011).

[22] B. Li, Y. Wang, H. Rong, Y. Wang, J. Liu, L. Xing, M. Xu, and W. Li, *J. Mater. Chem. A*, **1**, 12954 (2013).

[23] Y. S. Hu, W. H. Kong, L. Hong, X. J. Huang, and L. Q. Chen, *Electrochem. Commun.*, **6**, 126 (2004).

[24] Y. S. Hu, W. H. Kong, Z. X. Wang, H. Li, X. J. Huang, and L. Q. Chen, *Electrochem. Solid St.*, **7**, A442 (2004).

[25] H. Xiang, J. Chen and H. Wang, *Ionics*, **17**, 415 (2011).

[26] R. McMillan, H. Slegr, Z. X. Shu, and W. D. Wang, *J. Power Sources*, **81**, 20 (1999).

[27] N.-S. Choi, K. H. Yew, K. Y. Lee, M. Sung, H. Kim, and S.-S. Kim, *J. Power Sources*, **161**, 1254 (2006).

[28] I. A. Profatilova, S.-S. Kim, and N.-S. Choi, *Electrochim. Acta*, **54**, 4445 (2009).

[29] H. Nakai, T. Kubota, A. Kita, and A. Kawashima, *J. Electrochem. Soc.*, **158**, A798 (2011).

[30] S. Dalavi, P. Guduru, and B. L. Lucht, *J. Electrochem. Soc.*, **159**, A642 (2012).

[31] V. Etacheri, O. Haik, Y. Goffer, G. A. Roberts, I. C. Stefan, R. Fasching, and D. Aurbach, *Langmuir*, **28**, 965 (2012).

[32] A. Bordes, K. Eom, and T. F. Fuller, *J. Power Sources*, **257**, 163 (2014).

[33] N. N. Sinha, J. C. Burns, and J. R. Dahn, *J. Electrochem. Soc.*, **160**, A709 (2013).

[34] X. Chen, X. Li, D. Mei, J. Feng, M. Y. Hu, J. Hu, M. Engelhard, J. Zheng, W. Xu, J. Xiao, J. Liu, and J.-G. Zhang, *Chemsuschem*, **7**, 549 (2014).

[35] K. Leung, S. B. Rempe, M. E. Foster, Y. Ma, J. M. M. del la Hoz, N. Sai, and P. B. Balbuena, *J. Electrochem. Soc.*, **161**, A213 (2014).

[36] J. Li, W. Yao, Y. S. Meng, and Y. Yang, *J. Phys. Chem. C*, **112**, 12550 (2008).

[37] A. Mukhopadhyay, A. Tokranov, X. Xiao, and B. W. Sheldon, *Electrochim. Acta*, **66**, 28 (2012).
[38] S. H. Youn, Method for measuring HF content in lithium secondary battery electrolyte and analytical reagent composition used in the same, in *U.S. Patent* (2013).
[39] K. Abe, H. Yoshitake, T. Kitakura, T. Hattori, H. Y. Wang, and M. Yoshio, *Electrochim. Acta*, **49**, 4613 (2004).
[40] J. Vetter, H. Buqa, M. Holzapfel, and P. Novak, *J. Power Sources*, **146**, 355 (2005).
[41] S. F. Lux, T. Placke, C. Engelhardt, S. Nowak, P. Bieker, K. E. Wirth, S. Passerini, M. Winter, and H. W. Meyer, *J. Electrochem. Soc.*, **159**, A1849 (2012).
[42] H. Buqa, D. Goers, M. Holzapfel, M. E. Spahr, and P. Novak, *J. Electrochem. Soc.*, **152**, A474 (2005).
[43] W. Pfleging and J. Proella, *J. Mater. Chem. A*, **2**, 14918 (2014).
[44] T. D. Tran, J. H. Feikert, R. W. Pekala, and K. Kinoshita, *J. Appl. Electrochem.*, **26**, 1161 (1996).
[45] K. Zaghib, X. Song, A. Guerfi, R. Kostecki, and K. Kinoshita, *J. Power Sources*, **124**, 505 (2003).
[46] M. Yoshio, H. Y. Wang, K. Fukuda, T. Umeno, T. Abe, and Z. Ogumi, *J. Mater. Chem.*, **14**, 1754 (2004).
[47] L. Mickelson, H. Castro, E. Switzer, and C. Friesen, *J. Electrochem. Soc.*, **161**, A2121 (2014).
[48] C. S. Wang, A. J. Appleby, and F. E. Little, *J. Electroanal. Chem.*, **497**, 33 (2001).
[49] Y. Zhang and C.-Y. Wang, *J. Electrochem. Soc.*, **156**, A527 (2009).
[50] K. Xu, *J. Electrochem. Soc.*, **154**, A162 (2007).
[51] K. Xu, A. von Cresce, and U. Lee, *Langmuir*, **26**, 11538 (2010).
[52] R. Mogi, M. Inaba, S. K. Jeong, Y. Iriyama, T. Abe, and Z. Ogumi, *J. Electrochem. Soc.*, **149**, A1578 (2002).
[53] A. M. Andersson, D. P. Abraham, R. Haasch, S. MacLaren, J. Liu, and K. Amine, *J. Electrochem. Soc.*, **149**, A1358 (2002).
[54] T. Eriksson, A. M. Andersson, C. Gejke, T. Gustafsson, and J. O. Thomas, *Langmuir*, **18**, 3609 (2002).
[55] S. E. Sloop, J. B. Kerr, and K. Kinoshita, *J. Power Sources*, **119**, 330 (2003).

[56] T. Kawamura, S. Okada, and J. Yamaki, *J. Power Sources*, **156**, 547 (2006).

[57] E. Markevich, G. Salitra, K. Fridman, R. Sharabi, G. Gershinsky, A. Garsuch, G. Semrau, M. A. Schmidt, and D. Aurbach, *Langmuir*, **30**, 7414 (2014).

[58] S. F. Lux, J. Chevalier, I. T. Lucas, and R. Kostecki, *ECS Electrochem. Lett.*, **2**, A121 (2013).

[59] L. Terborg, S. Weber, F. Blaske, S. Passerini, M. Winter, U. Karst, and S. Nowak, *J. Power Sources*, **242**, 832 (2013).

[60] A. V. Plakhotnyk, L. Ernst, and R. Schmutzler, *J. Fluorine. Chem.*, **126**, 27 (2005).

[61] J. Wang, Q. Zhang, X. Li, Z. Wang, H. Guo, D. Xu, and K. Zhang, *Phys. Chem. Chem. Phys.*, **16**, 16021 (2014).

CHAPTER VI.
INFLUENCE OF DISSOLVED MANGANESE IONS ON STRUCTURAL DEGRADATION OF GRAPHITE IN Li-ION BATTERIES[*]

INTRODUCTION

Understanding the degradation mechanisms of a Li-ion battery is of considerable importance to achieve longer battery lifetime. As the applications of Li-ion batteries gradually extend to large-scale systems, such as electric vehicles and energy storage systems, a much longer cycle and calendar lifetime is necessary for such systems [1]. In a Li-ion battery, the degradation process involves several physical, mechanical, and chemical processes that are interdependent [2]. This complexity of the degradation mechanisms makes it difficult to remedy the performance degradation of the battery over time.

Although many efforts are currently being paid to the development of novel anodes, including silicon- and tin-based anodes, graphite is being still used extensively as an anode in commercial Li-ion batteries, and it is expected to continue being the primary option for anode materials in the near future [1]. However, structural degradation of a graphitic anode is commonly observed from cycled or stored Li-ion batteries, which aggravates the batteries' performance [3-10]. Several factors are responsible for the performance degradation of the graphitic anode. Upon intercalation/deintercalation of Li-

[*] This chapter includes content from an unpublished paper in progress: H. Shin, J. Park, and W. Lu, *Journal of Power Sources*.

ions during cycling, stress is generated by the repeated expansion and contraction of the crystal structure in graphite (~10% of volumetric change), which can cause structural damage to the graphitic anode [5-9, 11]. The structural damage can be also caused by co-intercalation of solvents together with Li-ions. It was suggested that co-intercalated solvents induce exfoliation and structural degradation of the graphite's particles [3, 12-14]. In addition, a buildup of internal stress in the graphite due to gas evolution during decomposition of the electrolyte can result in structural degradation [7, 10].

The structural degradation or damage in the graphite is more severe near the surface than in the bulk of the graphite [3, 5-7]. This is because the current density and the concentration of Li-ions are predominantly localized on the surface of the graphite, especially at the edge planes [3, 6]. Hence, the graphite is susceptible to structural damage at the surface. This damage is commonly described as 'surface structural disordering', which represents the significant extent of the edge planes or lattice defects [3-7]. In other words, surface structural disordering can account for deformation of the interlayers and breaking of the C-C bonds in graphite [7]. This disordering in graphite becomes more pronounced upon prolonged cycling (i.e., numerous intercalations/deintercalations of Li-ions), especially at high charge/discharge rates, elevated temperatures, and high-voltage regions (i.e., early stages of Li-ion intercalation) [3, 5, 6].

The surface structural disordering of the graphitic anode can alter the kinetics of Li-ion transfer at the electrode's surface [3, 9]. More importantly, the structural damage of the graphite can modify or create cracks in the solid electrolyte interphase (SEI), which promotes further decomposition of the electrolyte and the growth of the SEI layer,

gradually reducing the capacity of a battery over prolonged cycling. Consequently, the surface structural disordering of the graphitic anode significantly affects the long-term performance of Li-ion batteries. Thus, identifying the cause of surface structural disordering in graphite is important to improve the long-term performance of Li-ion batteries.

One of the causes of the structural disordering in graphite is the dissolved transition metal ions that come from the cathode. Y. Lai *et al*. showed that the deposition of the dissolved iron (Fe) ions on the graphitic anode aggravated surface structural disordering in graphite, resulting in a thicker SEI layer [15]. They suggested that the deposition of Fe ions might cause structural breakdown of graphite, leading to the exposure of new edge planes. Our recent study suggested that the dissolved manganese (Mn) ions might intercalate into graphite or present in graphite, which in turn might cause the surface structural disordering of the graphite [16]. A recent study reported that the dissolved Mn-ions from the cathode deposit at the graphite/electrolyte interface, and some manganese compounds present within cracks of the graphite [17]. However, there is still a lack of understanding about how the dissolved Mn-ions are related to the structural degradation of the graphitic anode.

This work aims to investigate the correlation between the dissolved Mn-ions and the structural degradation of the graphitic anode using a combination of experimental measurements and theoretical analysis. First, we investigate the effects of the dissolved Mn ions on both change in the interlayer spacing and the surface structural disordering of graphite using X-ray diffraction (XRD) and Raman spectroscopy, respectively. Then, the

reason for the structural degradation in graphite due to the dissolved Mn-ions is analyzed from the results predicted by density function theory (DFT) calculations.

METHODS

Experimental: Cell fabrication and characterization (XRD & Raman)

The slurry of the graphite electrode was prepared by mixing synthetic graphite powder (90 wt%)(Timrex SLP30, Timcal) with a polyvinylidene fluoride (PVdF) binder (10 wt%)(Kureha 7208, Kureha America) dissolved in N-methyl-2-pyrrolidone (NMP) using a SpeedMixer (FlackTek Inc.). The resulting slurry was cast onto a 9 μm-thick copper foil at a constant speed using a 9-mil film applicator with a doctor-blade film coater (MTI Corp.). The composite electrode was then dried overnight in a vacuum oven at 110 °C. The dried electrodes were punched out as disks with an area of 0.785 cm^2 and vacuum-dried again before being used for coin-cell assembly. To assemble 2032-type coin cells, the working electrode was assembled in a half-cell configuration with a Li foil counter/reference electrode (0.75 mm thick, 99.9%, Alfa Aesar) and a separator (Celgard 2320) soaked in electrolyte solution The base electrolyte was 1.0 M lithium hexafluorophosphate ($LiPF_6$) (Battery grade, <50 ppm HF, <15ppm H_2O, Sigma Aldrich) dissolved in a 1:1 (by volume) mixture of ethylene carbonate (EC) and dimethyl carbonate (DMC). The Mn-containing electrolyte was prepared by dissolving a known amount of synthesized manganese hexafluorophosphate [$Mn(PF_6)_2$] into the base electrolyte. The $Mn(PF_6)_2$ salt was synthesized by the same method introduced in our previous study [16]. The concentration of dissolved Mn-ions in the electrolyte was analyzed using inductively coupled plasma optical emission spectrometry (ICP-OES).

For XRD measurements, the Mn-containing (1000 ppm) and Mn-free cells were charged (i.e., lithiation) at a constant current (C/50 rate) to three voltages – 0.18 V, 0.1 V, and 0.005 V (vs. Li/Li^+) – and held at each voltages until the current dropped to approximately 1μA. The cells were disassembled in a glovebox and the graphite electrode was washed with DMC to remove residual salts. After 15 min of drying, the electrode was sealed with a Kapton tape in the glovebox to avoid exposure to the atmosphere. In order to compare the average interlayer spacing of graphite cycled in Mn-free electrolyte with that of graphite cycled in Mn-containing electrolyte, *ex-situ* X-ray diffraction was employed using the electrode that had been wrapped in Kapton tape. All X-ray diffraction data were obtained by using an X-ray diffractometer (Rigaku rotating anode) with Cu Kα radiation.

For Raman spectroscopy measurements, the Mn-containing (250 ppm and 1000 ppm) and Mn-free cells were cycled three times at a constant current (C/50 rate) between 5 mV and 1.5 V (vs. Li/Li^+) using a battery cycler (Biologic). The cycled graphite electrode was disassembled at the delithiated state (1.5 V vs. Li/Li^+) in a glovebox and washed with DMC to remove residual salts. The electrode was dried in the glovebox for 8 hr and placed in an air-tight spectroscopic cell (Fig. 6.1) to avoid exposure to the atmosphere. Raman spectra were recorded with a Raman microscope (Renishaw inVia) with a HeNe laser (λ=633nm, 1mW) as the excitation source. 690 Raman spectra were collected over an area of approximately 180 μm × 140 μm and the intensity ratio of the D-band to G-band (I_D/I_G) was calculated from each Raman spectrum in order to acquire the surface Raman maps of the I_D/I_G ratio.

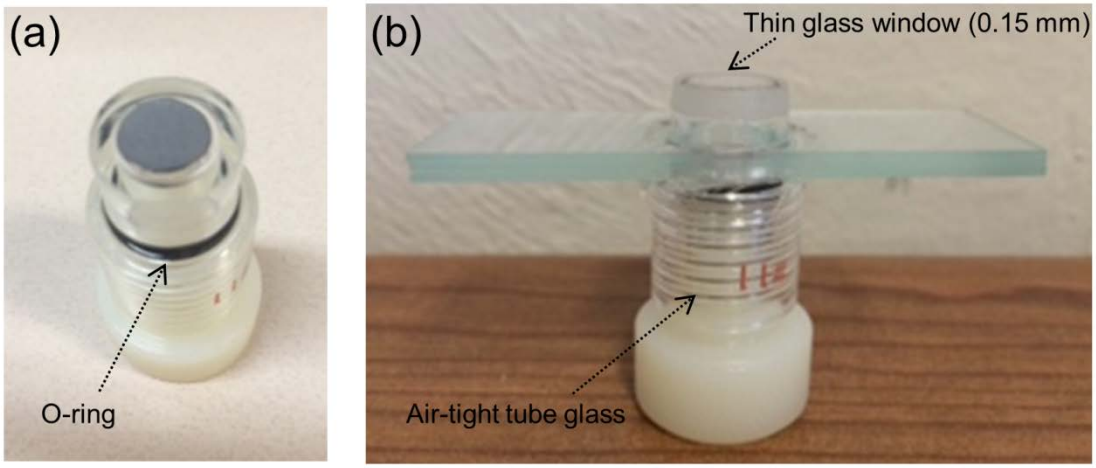

Figure 6-1. Pictures of the designed air-tight spectroscopic cell: (a) top view and (b) side view.

Computational: DFT calculations

To investigate the effects of intercalated manganese ions on the interlayer expansion or contraction of the graphite, DFT calculations with various vdW correction methods were conducted using the Vienna *ab initio* simulation package (VASP). Since it was known that the generalized gradient approximations (GGA) failed to reproduce the reasonable interlayer spacing of lithium graphite intercalation compound (Li-GIC), we first used different vdW correction methods with GGA and the local density approximation (LDA) to successfully reproduce changes in the interlayer spacing of Li-GICs [18-21]. As shown in Figure 6.2, unit cells of graphite (C_4) and different stages of Li-GIC, such as LiC_{18}, LiC_{12}, and LiC_6, were used in this work. For the LiC_{18} structure, two different types of GICs were previously investigated, and researchers suggested that LiC_{18} with the αABA stacking was more favorably formed than LiC_{18} with the αAAA stacking [18]. Here we used LiC_{18} with αABA stacking in our calculations. The unit cells

were created using the crystallographic data of lithium intercalated graphite compounds [18].

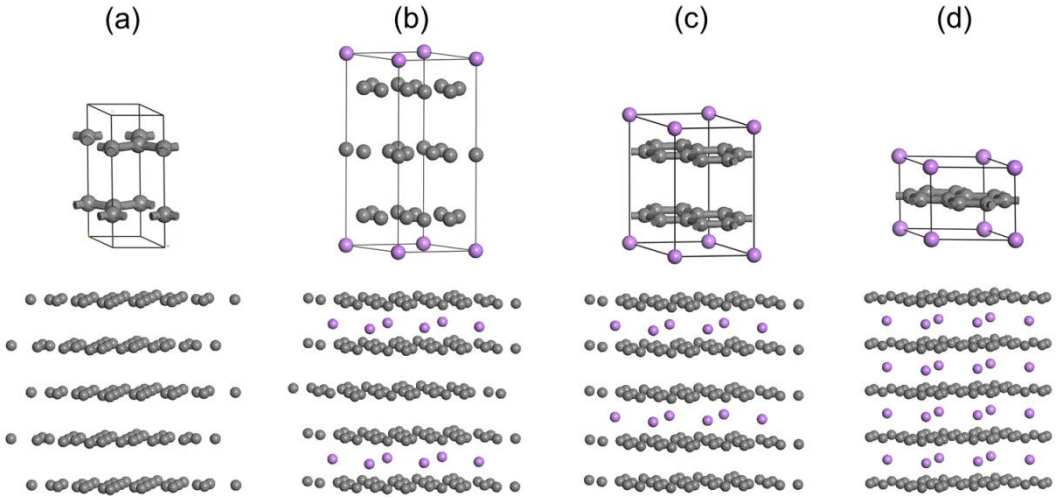

Figure 6-2. Unit cells (upper) and supercells (bottom) of Li-GICs used in this work: (a) graphite, (b) LiC_{18} (αABAα), (c) LiC_{12}, and (d) LiC_6.

After comparing the calculated lattice parameter of the Li-GIC with its corresponding experimental data, we chose a vdW correction method to predict the changes in the interlayer spacing of the Mn-intercalated graphite. Since there was no information about structures of Mn-GICs and where the Mn ions could be located in the interlayer of the Li-GIC, various hypothetical structures were considered in our calculations. Figure 6.3 shows the Mn-intercalated Li-GIC structures used in the calculations. In addition, change in the interlayer spacing of the Mn-GIC as a function of Mn ions was investigated based on the assumption that the structures of Mn-GICs are the same as those of Li-GICs.

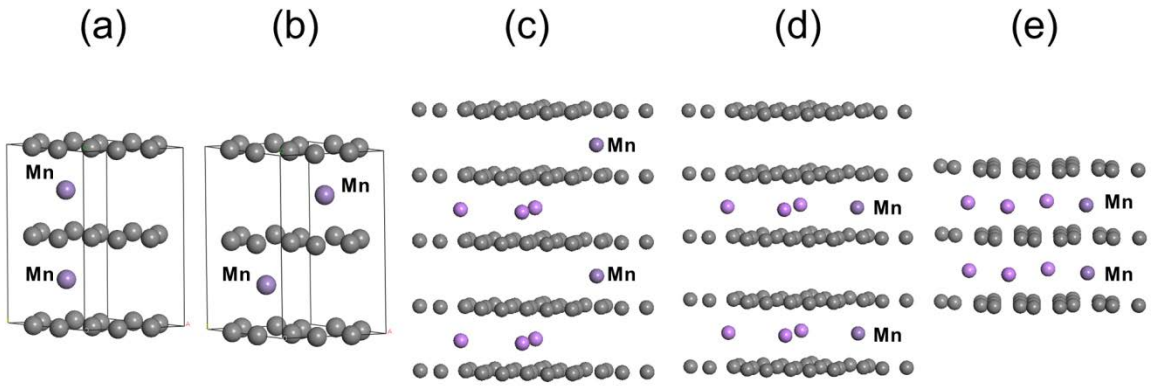

Figure 6-3. Atomic structures of Mn-intercalated compounds considered in this work: (a) MnC_6 (αAαA), (b) MnC_6 (αAβA), (c) $Li_{0.75}Mn_{0.25}C_6$ (stage 2, Mn-intercalated into empty interlayers), (d) $Li_{0.75}Mn_{0.25}C_6$ (stage 2, Mn-intercalated into the interlayers with Li-ions), and (e) $Li_{0.75}Mn_{0.25}C_6$ (stage 1).

In addition to calculating the average interlayer spacing of the Li-GIC, the intercalation energy was calculated for Li-GICs and various Mn-intercalated graphite structures. In order to examine the energetics of intercalation into graphite, i.e., the intercalation energy, which was defined as the energy required to insert a cation atom from the bulk to the graphite, was calculated using the following equation:

$$E^{\text{int}}{}_{AC_n} = E_{AC_n} - E_{C_n} - \frac{1}{i} E_A^{metal}$$

where i is the number of intercalated atoms in a cell for a metal.

For DFT calculations, the structures were optimized by simultaneously minimizing all degrees of freedom via a conjugated gradient method. The electronic degrees of freedom were converged to 10^{-6} eV/cell with a plane wave cutoff energy of 1000 eV for all structures. The integration in reciprocal space was performed with Monkhorst-Pack grids 11×11×4, 11×11×4, 8×8×4, and 6×6×7 for graphite, LiC_{18}, LiC_{12}, and LiC_6, respectively.

RESULTS AND DISCUSSION

Experimental: X-ray diffraction and Raman spectroscopy

First, we investigated how the dissolved Mn-ions affect the structural change of the graphite. Figure 6.4 shows the change in the graphite (002) peak, which was taken at OCV, 0.18 V, 0.1 V, 0.07 V, and 0.005 V (vs. Li/Li^+). The (002) peak corresponds to the average interlayer spacing between the graphene layers in graphite. The (002) peak shifted to a lower angle as the cell voltage decreased, which indicates that the average interlayer spacing expands upon the intercalation of Li-ions. The stage-4 phase of Li-GIC was formed at 0.18 V. Stage-4 phase (near 25.84°) changed to stage-2 phase (near 25.32°) at 0.1 V. At 0.07 V, the coexistence of stage-1 and stage-2 (i.e., two-phase) was clearly observed, and LiC_6 (i.e., stage-1 phase) was finally formed at the end of charge (0.005 V). The phase change was quite consistent with the result of a previous study [22], which indicates that the result of our *ex-situ* experiments shows the stage phenomenon that occurs in graphite.

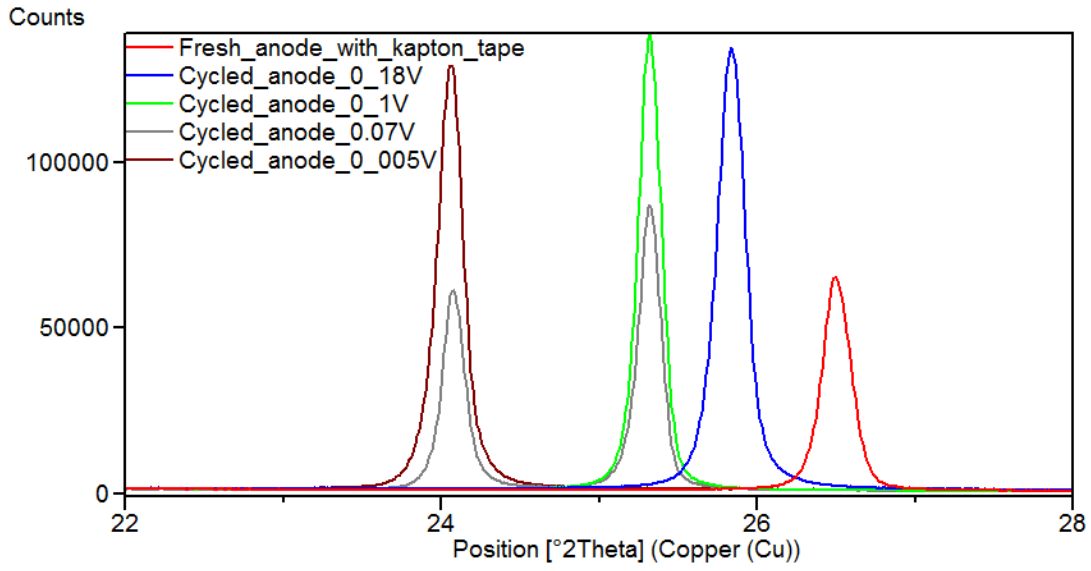

Figure 6-4. Change in the (002) peak of X-ray diffraction as a function of potential.

As shown in Figure 6.5, the change of the average interlayer spacing of graphite as a function of x in Li_xC_6 measured in our study was also consistent with previous studies [22, 23].

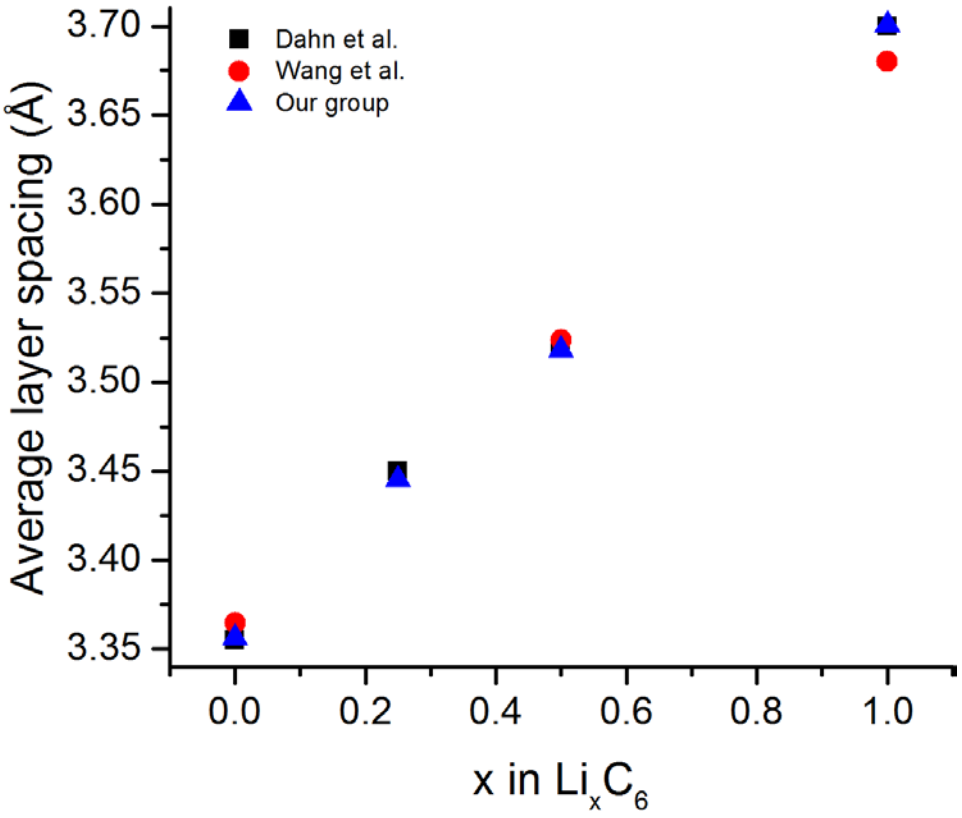

Figure 6-5. Change in the average interlayer spacing of the graphite anode cycled without Mn-ions.

In the case of the graphite electrode cycled with the Mn-containing electrolyte (1000 ppm), the (002) peak also shifted toward lower angles, showing similar staging phenomena. As shown in Figure 6.6, the average interlayer spacing observed in the Mn-containing cell was not significantly different from that observed in the Mn-free cell. It seems that the amount of co-intercalated Mn-ions is very low or the intercalation of Mn-

ions does not occur, which makes it difficult to observe the effect of the intercalated Mn-ions on the interlayer spacing in graphite.

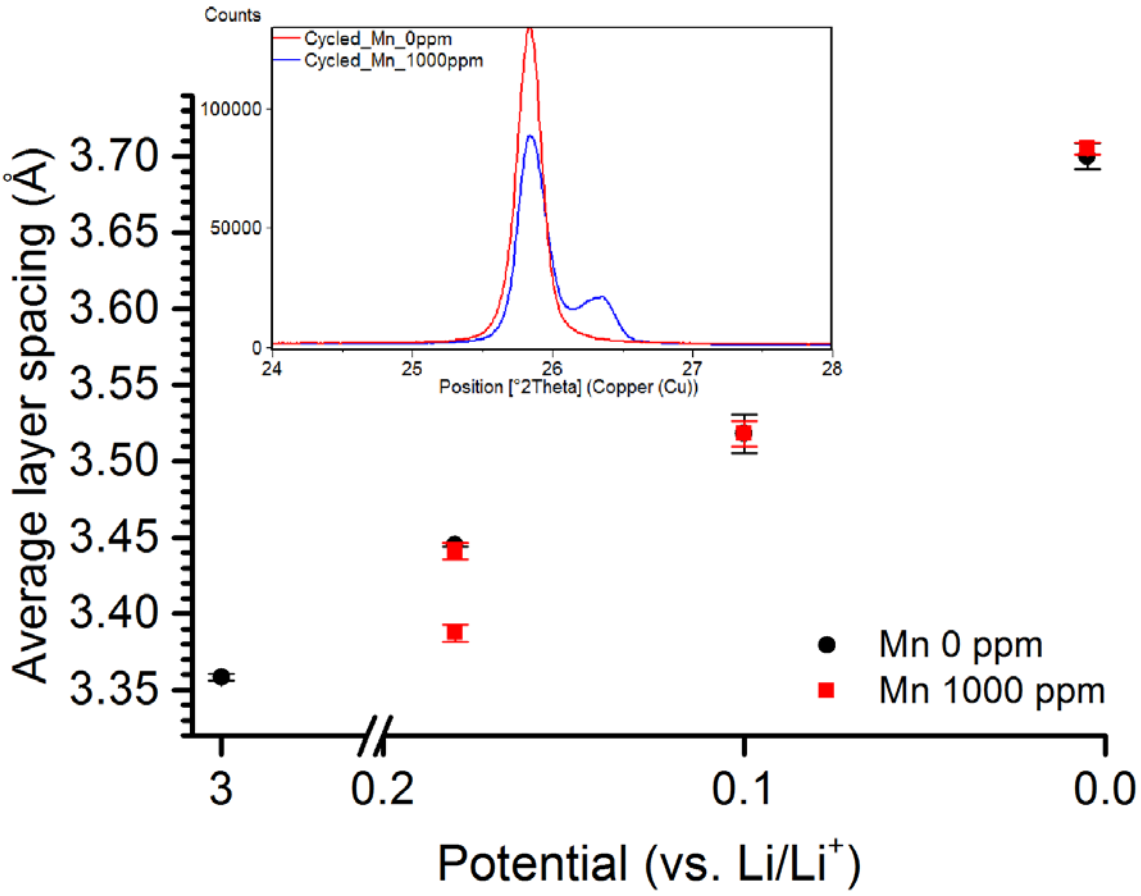

Figure 6-6. Change in the average interlayer spacing of the graphite anode cycled with Mn-ions (1000 ppm).

However, a noticeable difference was observed at the early stage of Li-ion intercalation, i.e., at 0.18 V. At the potential, the graphite in the Mn-containing cell showed two peaks, which indicates the coexistence of two different phases. One peak (near 25.84°) was clearly stage-4 phase, while the other peak (near 26.35°) was close to dilute stage-1 phase. In the presence of dissolved Mn-ions, the graphite anode still underwent the transition stage (i.e., from the dilute stage-1 to stage-4), and the phase

change to stage-4 was not completed. This might be due to co-intercalated Mn-ions in graphite. Since the voltage was held for a long time (more than 5 days) in order to allow complete intercalation at the potential, we suspected that some of the interlayer spaces in the graphite did not expand well due to a small amount of co-intercalated Mn-ions, which might hinder the phase transition (from dilute stage-1 to stage-4).

The results indicate that the effect of dissolved Mn-ions on change in the interlayer space in graphite is only pronounced at the early stage of Li-ion intercalation, i.e., when the amount of intercalated Li-ion is very small. Since the majority of the interlayer spaces in graphite is occupied by Li-ions at the middle and end stages of intercalation, the interlayer spaces in graphite are likely to be affected primarily by a large amount of Li-ions such that the impact of co-intercalated Mn-ions will be small and only observed locally.

Based on our XRD results, it is suggested that a small amount of co-intercalated Mn-ions occur, which might affect local structural damage in graphite. Thus, the influence of the dissolved Mn ions on the surface structural disordering of graphite was further investigated using Raman spectroscopy.

In the Raman spectra of the graphite anodes cycled, two apparent bands were present at ~1350 and ~1580 cm^{-1}. The D-band observed at 1350 cm^{-1}, which is assigned to the A_{1g} vibrational mode, is associated with the breakage of symmetry occurring at edge planes and defects of the graphene sheets [3, 5]. The D-band is referred to as the 'disorder band'. The G-band observed at 1580 cm^{-1}, which is assigned to the E_{2g} vibration mode, can be attributed to the relative motion of sp^2 carbon atoms in rings as well as

chains [5, 6]. To determine the extent of structural disorder in graphite, the peak intensity ratio I_D/I_G is extensively used [3-6].

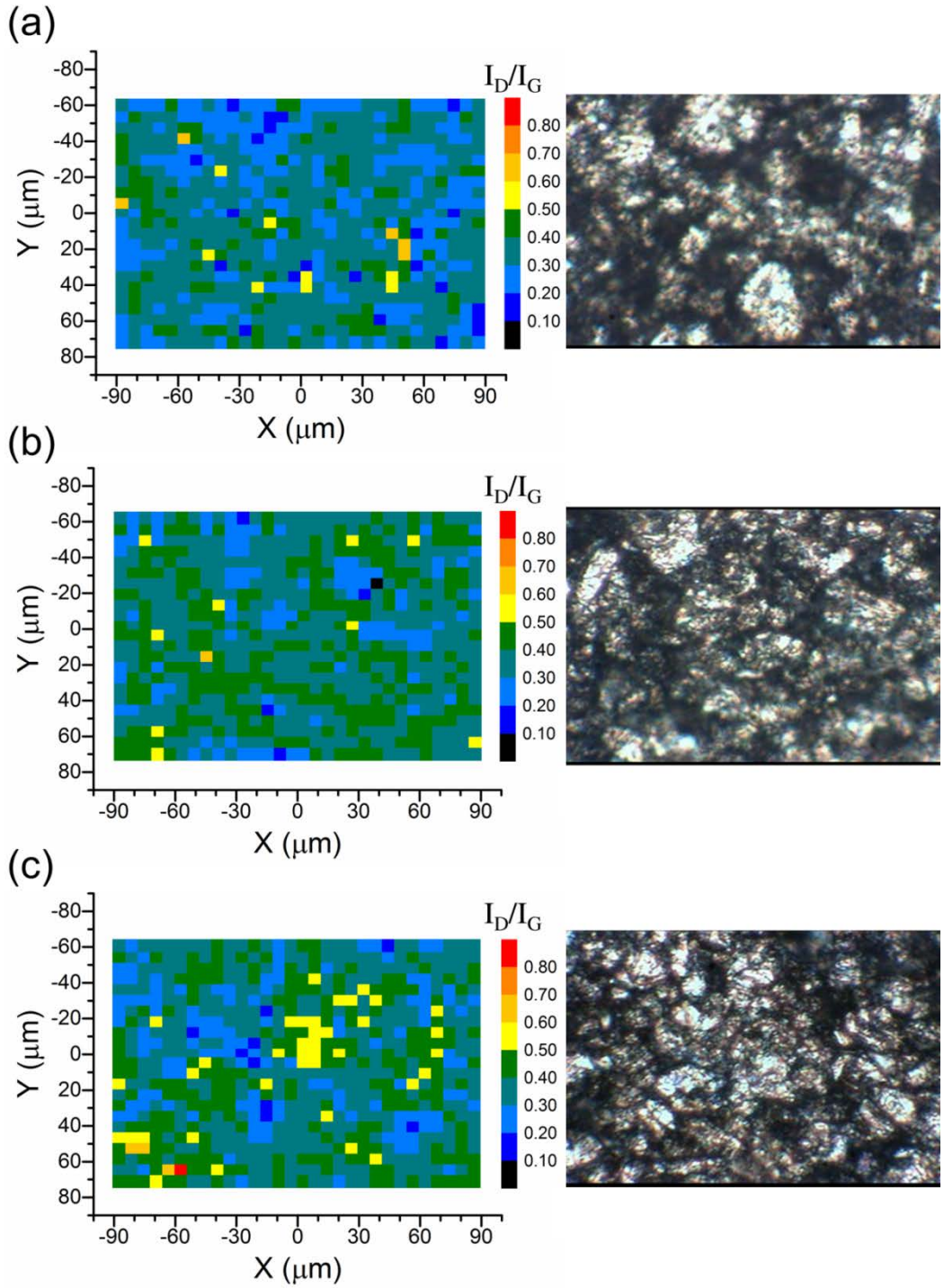

Figure 6-7. Raman maps of the I_D/I_G ratio and their corresponding microscope images: (a) No Mn-ions, (b) 250 ppm Mn-ions, and (c) 1000 ppm Mn-ions.

Figure 6.7 shows Raman maps of the I_D/I_G ratio from the area of 180 × 140 μm^2 of cycled graphite anodes with/without dissolved Mn-ions. The graphite anodes were only cycled three times at a very slow rate (C/50 rate) to exclude other factors that cause the surface structural disordering, such as the number of cycle and high charging rate.

As shown in Figure 6.7a, the cycled anode without Mn-ions displayed highly graphitic carbons with low I_D/I_G ratios, which corresponds to green and blue dots on the map. Yellow, orange, and red dots represent relatively high intensity ratio of the G band to D band (I_D/I_G), which accounts for the significance of the structural disordering in graphite. Only a few disorders with high I_D/I_G ratios were locally observed in the cycled anode without Mn-ions. Similarly, the cycled anode with the electrolyte containing Mn-ions dissolved at a concentration of 250 ppm (Fig. 6.7b) also showed a few disorders; however, the extent of the overall structural disordering increased compared to the anode cycled without Mn-ions, as shown in Table 6.1.

Table 6-1. Average I_D/I_G ratio values from Raman maps.

The quantity of Mn-ions	0 ppm	250 ppm	1000 ppm
Avg. I_D/I_G ratio	0.333 ± 0.07	0.372 ± 0.07	0.374 ± 0.09

The extent of the local structural disordering in graphite was noticeably higher in the case of the anode cycled with 1000 ppm Mn-ions (Fig. 6.7c). This indicates that severe local structural disordering occurred in graphite due to the dissolved Mn ions. Note that the surface disordering appeared “locally”. This indicates that the surface structural degradation of graphite induced by the dissolved Mn-ions proceeded in a highly non-uniform manner. This severe local structural disorder might be due to some co-intercalated Mn-ions, as suggested by the XRD results.

To explain the observed structural degradation in graphite due to the dissolved Mn ions, the next section investigates how the lattices of Li-GICs are affected by the intercalated Mn ions using DFT calculations.

Computational: DFT calculations

First, various dispersion-corrected DFT methods were evaluated by comparing the DFT calculations with existing experimental data. All functionals reproduced the experimental a-lattice parameter of the graphite and the Li-GIC compounds, implying that the in-plane C-C bonds were well described; however, the c-lattice parameter, which was perpendicular to the graphene layers, displayed much larger deviations from the experimental value, reflecting the challenge of reproducing van der Waals interactions by DFT calculations.

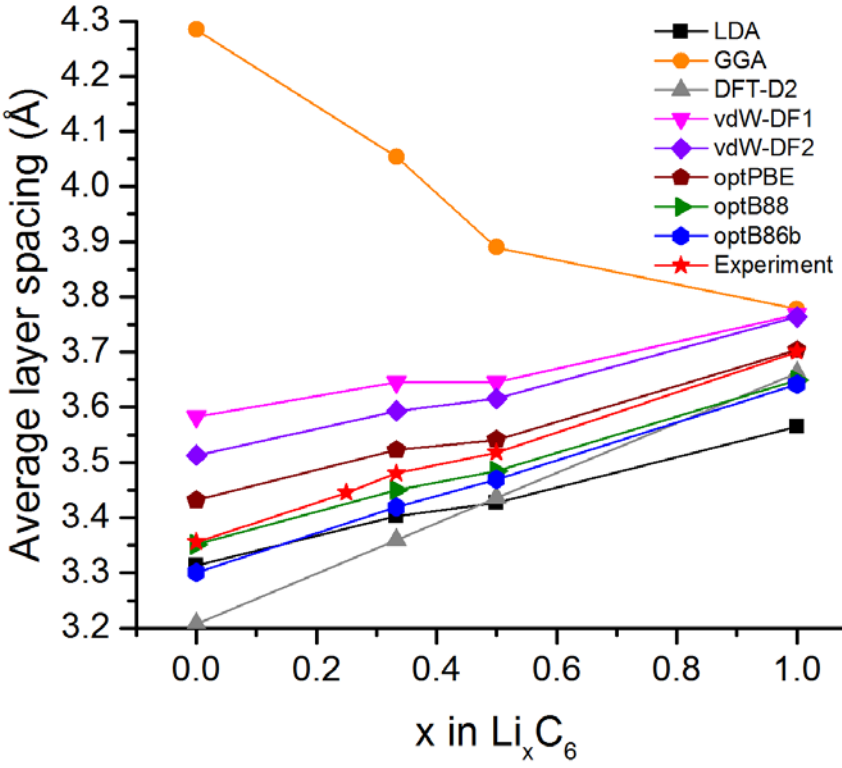

Figure 6-8. Change in the average interlayer space between graphene layers as a function of Li content.

Figure 6.8 showed the changes in the average layer spacing of the graphite and Li-GIC compounds. Compared to GGA, all vdW functionals improved the treatment of interplanar interaction by introducing dispersion. The vdW-DF1, vdW-DF2, and optPBE underestimated the interlayer interaction, leading to a wider interlayer space. In contrast, the optB88, optB86b, LDA, and DFT-D2 overestimated the interlayer interaction. Overall, the optB86b functional yielded the best agreement with the experimental value [18].

In order to estimate the intercalation energy or the enthalpy of formation of Li-GICs, the functionals were also applied to a lithium metal. As listed in Table 6.2, the GGA, vdW-DF, optPBE, and optB86b functional were in good agreement with the experimental value [24]. Thus, those functionals were good candidates for the calculation of the intercalation energy.

Table 6-2. Calculated values of the lattice parameter and cohesive energy of a lithium metal.

	LDA	GGA	DFT-D2	vdW-DF	vdW-DF2	optPBE	optB88	optB86b	Exp.
Lattice parameter (Å)	3.363	3.436	3.270	3.451	3.294	3.438	3.411	3.452	3.509
Cohesive E (Kcal/mol)	-41.7	-37.0	-39.9	-35.1	-33.8	-37.1	-36.2	-37.5	-36.5

In this work, optB86b was used to calculate the formation enthalpy of Li-GICs. Endothermic enthalpy of formation indicates that the compound is unstable with respect to the reference state of the pure elements, while the exothermic enthalpy of formation implies that the structure is stable. The absolute value of the formation energy can be used to evaluate relative stability. Figure 6.9 showed the calculated formation energy of Li-GICs with the experimental value [25]. The calculated values of LiC_{12} and LiC_6 were well matched with the experimental value. Although all of the Li-GICs considered were

energetically favorable, the most stable compound was LiC_{12}. Note that LiC_6 was less stable than LiC_{12}. This might indicate that the interlayer of the graphite started to limit the intercalating Li-ions. Thus, the compounds, such as LiC_4 and LiC_3 had difficulty holding the intercalated Li-ions, due to their unstable structures. That is why only one Li-ion can be positioned within the six carbon atoms.

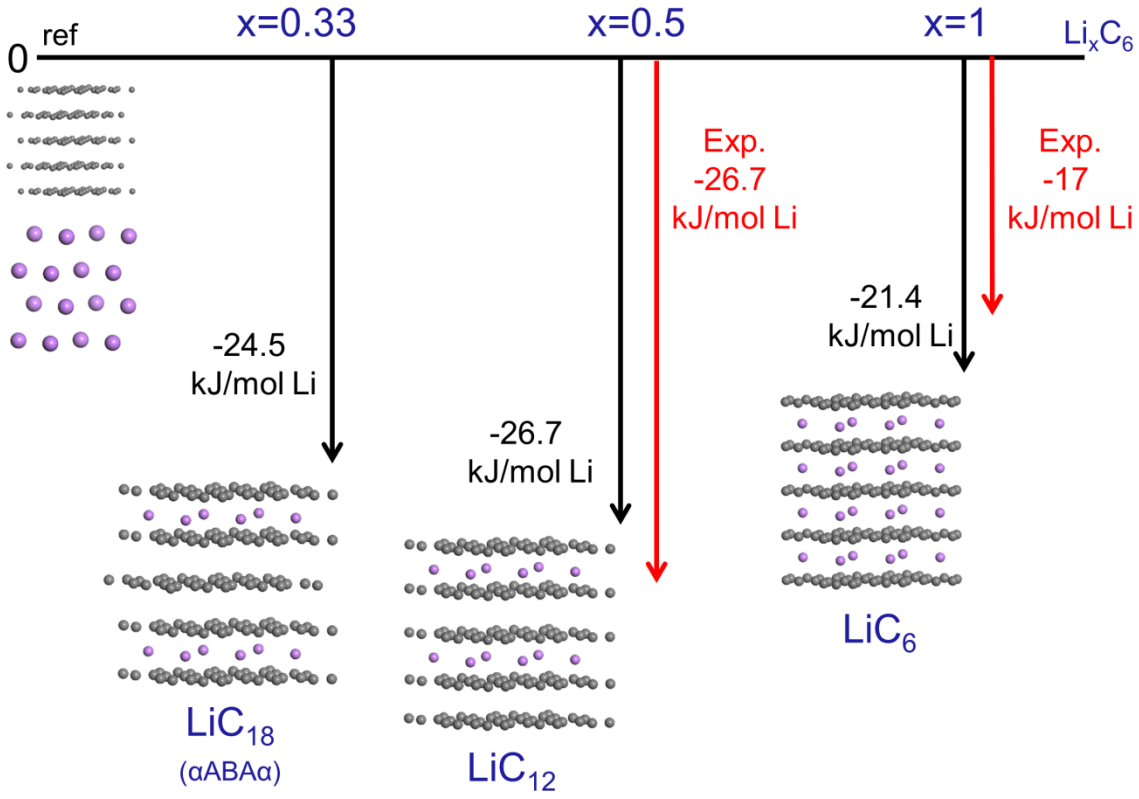

Figure 6-9. Calculated formation energy of the Li-GIC compounds.

Since the optB86b functional aptly reproduced the experimental values of lattice parameters and the intercalation energy, it was used to predict the effects of intercalated Mn ions on change in lattices in graphite. As shown in Figure 6.3, five different types of structures were considered in this work. The first two structures (a, b) were reported by a previous study of the stage-1 binary graphite transition metal (TM) intercalated

compounds [26]. The other structures were modifications of stage-2 (LiC_{12}) and stage-1 (LiC_6) of Li-GIC by replacing some of the Li-ions with Mn-ions.

Table 6.3 shows the results of the energies and lattice parameters of the MnC_6 structures predicted by the optB86b functional. It was observed that the lattice parameters of Mn-GICs were strongly dependent upon the magnetic character of the structure. Among the structures considered here, the structure of MnC_6 (αAβA) with the ferromagnetic tended to form more than the others. The c-lattice parameters of MnC_6 structures were smaller than those of LiC_6, except for MnC_6 (αAαA, antiferromagnetic). Since the MnC6 (αAαA) with antiferromagnetic showed a higher energy than the other structures, it is not preferable to other structures. Thus, MnC_6 is believed to be a smaller c-lattice than LiC_6. In contrast, the a-lattice parameter of MnC_6 was smaller than that of LiC_6. These trends were consistent with a previous study [26]. Thus, when some of the Mn-ions are intercalated into graphite, the interlayer space and a-lattice of graphite might be contracted and expanded, respectively. This might cause local stresses in lattices in graphite, resulting in an increase in structural disordering in graphite.

Table 6-3. Energies and lattice parameters of MnC_6 structures calculated by optB86b.

	Energy (eV)	c-lattice (Å)	a-lattice (Å)
MnC_6 (αAαA)	-104.5 [a], -103.8 [b]	3.568 [a], 3.723 [b]	4.352 [a], 4.342 [b]
MnC_6 (αAβA)	-104.8 [a], -104.6 [b]	3.254 [a], 3.215 [b]	4.366 [a], 4.370 [b]
LiC_6	-100.2	3.610	4.325

a: ferromagnetic structures, b: antiferromagnetic structures.

We further investigated the structures that consisted of Li and Mn ions ($Li_{0.75}Mn_{0.25}C_6$ (c, d, e), as shown in Figure 6.3. These structures included the same amount of intercalated Mn-ions in Li-GICs. Similar to the result of MnC_6, the average interlayer spaces of these structures were smaller than those of their corresponding Li-

GICs (Table 6.4). In particular, the contraction of the interlayer spacing was larger when Mn ions were intercalated into the interlayer space that occupied by Li-ions (2.13%) than when they were intercalated into an empty interlayer space between graphene layers (0.32%). The interlayer space in Li-GIC decreased further when Mn ions were intercalated into all of the interlayer spaces (-3.41%). Thus, the extent of structural disordering in graphite can be dependent upon where the co-intercalated Mn-ions are positioned in the interlayer spaces in graphite.

Table 6-4. Average interlayer spaces of the $Li_{0.75}Mn_{0.25}C_6$ structures calculated by optB86b.

	Average interlayer spacing (Å)
Stage-2, $Li_{0.75}Mn_{0.25}C_6$, (c) structure in Fig. 6.3	3.459 (-0.32%)
Stage-2, $Li_{0.75}Mn_{0.25}C_6$, (d) structure in Fig. 6.3	3.396 (-2.13%)
Stage-2, LiC_{12}	3.470
Stage-1, $Li_{0.75}Mn_{0.25}C_6$, (e) structure in Fig. 6.3	3.487 (-3.41%)
Stage-1, LiC_6	3.610

In this work, the Mn-intercalated structures and Mn-GICs showed positive formation energies that were different from Li-GICs. This indicates that these structures are not energetically favorable, suggesting that the Mn-ions are difficult to intercalate into graphite. The positive formation energies might be due to the incorrect energy value of a manganese metal calculated by optB86b. The optimized lattice parameter of a manganese metal was 2.763 Å, which was significantly lower than the experimental value, 3.081 Å [27]. Also, the predicted magnetic moment of the manganese metal was zero, which was different from the values found in previous theoretical works [28, 29]. We believe that the GGA-U method might be more appropriate for accurately predicting the formation energies of such transition metal (TM) graphite intercalation compounds (TM-GICs).

Based on the calculated energies, Mn-ions may be difficult to intercalate into graphite by means of the normal intercalation process; however, we believe that Mn-ions can be co-intercalated into graphite together with Li-ions and solvents in the early stage of the intercalation process, as suggested by the XRD results. In the early stage of intercalation, it is known that solvent molecules, such as EC, PC, and PF_6, can co-intercalate into graphite along with Li-ions, which significantly expand the interlayer space between the graphene sheets [30, 31]. With this large expansion due to co-intercalation of solvent molecules, the Mn-ions might be easily intercalated into graphite.

In summary, our DFT calculations suggested that the co-intercalation of Mn-ions into graphite can cause the contraction of the interlayer space between graphene layers and expansion of in-plane C-C bonds in graphene sheets. This might induce local stresses in the lattice, resulting in surface structural disordering in graphite. Thus, we believe that the increase in the structural disordering due to the dissolved Mn-ions can be attributed to the change of lattices in graphite induced by the co-intercalated Mn-ions. In addition, the co-intercalated Mn ions might limit or hinder the intercalation of Li-ions into the graphite, thereby affecting the capacity fade of a Li-ion battery.

CONCLUSIONS

Our experimental and computational works showed that dissolved manganese ions from the cathode can result in the structural degradation of graphite. XRD results suggested that a small amount of Mn-ions can intercalate along with Li-ions into graphite in the early stage of the Li-ion intercalation process. From the results of Raman spectroscopy, it was found that the extent of surface structural disordering was severe in

Mn-containing cells, even at a very low cycle rate (C/50 rate) and very short cycle (3 cycles). Raman maps of I_D/I_G ratio clearly indicated that the surface structural disordering of graphite occurred locally due to the dissolved Mn-ions. This might be due to the co-intercalation of Mn-ions into graphite. DFT calculations showed that the intercalated Mn-ions contract the interlayer space between graphene sheets and expand the in-plane C-C bonds in graphene sheets in the graphitic anode.

Thus, if some of the dissolved Mn-ions are diffuse and present at the interlayer space of the graphite through cracks or defects in particles of the graphite anode and the SEI layer, the structural degradation of graphite can be accelerated during cycling.

BIBLIOGRAPHY

[1] T. Kim, J. Park, S. Chang, S. Choi, J. Ryu, and H. Song, *Adv. Energy Mater.*, **2**, 860, (2012).

[2] J. Vetter, P. Novak, M.R. Wagner, C. Veit, K.C. Moller, J.O. Besenhard, M. Winter, M. Wohlfahrt-Mehrens, C. Vogler, and A. Hammouche, *J. Power Sources*, **147**, 269 (2005).

[3] R. Kostecki and F. McLarnon, *J. Power Sources*, **119**, 550 (2003).

[4] L.J. Hardwick, H. Buqa and P. Novak, *Solid State Ionics*, **177**, 2801 (2006).

[5] L.J. Hardwick, M. Marcinek, L. Beer, J.B. Kerr, and R. Kostecki, *J. Electrochem. Soc.*, **155**, A442 (2008).

[6] V.A. Sethuraman, L.J. Hardwick, V. Srinivasan, and R. Kostecki, *J. Power Sources*, **195**, 3655 (2010).

[7] S. Bhattacharya, A.R. Riahi, and A.T. Alpas, *J. Power Sources*, **196**, 8719 (2011).

[8] V.A. Sethuraman, N.V. Winkle, D.P. Abraham, A.F. Bower, and P.R. Guduru, *J. Power Sources*, **206**, 334 (2012).

[9] H. Nakagawa, Y. Domi, T. Doi, M. Ochida, S. Tsubouchi, T. Yamanaka, T. Abe, and Z. Ogumi, *J. Power Sources*, **206**, 320 (2012).

[10] H. Zhang, F. Li, C. Liu, J. Tan, and H. Cheng, *J. Phys. Chem. B*, **109**, 22205 (2005).

[11] Y. Qi and S.J. Harris, *J. Electrochem. Soc.* **157**, A741 (2010).

[12] J. O. Besenhard, M. Winter, J. Yang, and W. Biberacher, *J. Power Sources*, **54**, 228 (1995).

[13] M. Inaba, Z. Siroma, A. Funabiki, and Z. Ogumi, *Langmuir*, **12**, 1535 (1996).

[14] E. Peled, D. Bar Tow, A. Merson, A. Gladkich, L. Burstein, and D. Golodnitsky, *J. Power Sources*, **97/98**, 52 (2001).

[15] Y. Lai, Z. Cao, H. Song, Z. Zhang, X. Chen, H. Lu, M. Jia, and J. Li, *J. Electrochem. Soc.*, **159**, A1961 (2012).

[16] H. Shin, J. Park, A.M. Sastry, and W. Lu, *J. Power Sources*, **284**, 416 (2015).

[17] X. Xiao, Z. Liu, L. Baggetto, G.M. Veith, K.L. More, and R.R. Unocic, *Phys. Chem. Chem. Phys.*, **16**, 10398 (2014).

[18] Y. Imai and A. Watanabe, *J. Alloys Compd.*, **439**, 258 (2007).

[19] Y. Qi, H. Guo, L.G. Hector, and A. Timmons, *J. Electrochem. Soc.*, **157**, A558 (2010).

[20] K.R. Kganyago and P.E. Ngoepe, *Phys. Rev. B*, **68**, 205111, (2003)

[21] S. Thinius, M.M. Islam, P. Heitjans, and T. Bredow, *J. Phys. Chem. C*, **118**, 2273 (2014).

[22] J.R. Dahn, *Phys. Rev. B*, **44**, 9170 (1991).

[23] X. Wang, K. An, L. Cai, Z. Feng, S.E. Nagler, C. Daniel, K.J. Rhodes, A.D. Stoica, H.D. Skorpenske, C. Liang, W. Zhang, J. Kim, Y. Qi, and S.J. Harris, *Nature, Scientific Reports*, **2**, 747 (2012).

[24] R. A. Silverman and W. Kohn, *Phys. Rev.*, **80**, 912 (1950).

[25] V.V. Avdeev, A.P. Savchenkova, L.A. Monyakina, I.V. Nikolskaya, and A.V. Khvostov, *J. Phys. Chem. Solids*, **57**, 947 (1996).

[26] R. Singh and S. Prakash, *Carbon*, 48, 1341 (2010).

[27] J. Kubler, *J. Magn. Magn. Mater.*, **20**, 107 (1980).

[28] T. Asada and K. Terakura, *Phys. Rev. B.*, **47**, 15992 (1993).

[29] N.E. Brener, G. Fuster, J. Callaway, J. L. Fry, and Y.Z. Zhao, *J. Appl. Phys.*, **63**, 4057 (1988).

[30] M.R. Wagner, J.H. Albering, K.C. Moeller, J.O. Besenhard, M. Winter, Electrochem. Commun. **7**, 947 (2005).

[31] K. Tasaki, *J. Phys. Chem. C*, **118**, 1443 (2014).

CHAPTER VII.
CONCLUSIONS AND FUTURE WORKS

To achieve the integration of large-scale Li-ion batteries in transportation and grid storage applications, these batteries must meet higher specifications in terms of high energy density, long lifetime, excellent power capability, low cost, and safety. Along with the development of new materials (anodes, cathodes, and electrolytes) for high energy and power densities, many efforts are focusing on probing the battery's degradation mechanisms in order to achieve long lifetime without degradation of performance. However, the phenomena that contribute to the degradation of these batteries are still problematic and challenging since the degradation process involves several physical, mechanical, and chemical processes that are interdependent.

To shed light on one of the most important degradation mechanisms, i.e., interface degradation, this research focused on the investigation of the dynamic properties of the surface layer and the chemical processes that occur at the electrode/electrolyte interface in order to identify the mechanisms that lead to the degradation of the interface and the concomitant phenomena. Various types of cells and experimental methodologies were designed, and several electrochemical and analytical techniques (including EIS, SEM, XPS, AFM, XRD, ICP-OES, Raman, and acid-based titration) were utilized to gain insights into changes in properties of (1) the surface layer at the electrode/electrolyte interface, (2) the electrodes (graphite and LMO), and (3) the electrolytes. The atomistic

simulations using molecular dynamics (MD) and density functional theory (DFT) were used as a complementary tool to provide experimentally-inaccessible information as well as explanations and fundamental understandings of what was observed.

This research showed the importance of the mechanical and chemical stability of the SEI layer and emphasized their interdependence; the mechanical degradation of the SEI layer influenced the chemical degradation of the SEI and vice versa. The stability of the SEI layer was related closely to the degradation of the battery's performance during cycling, especially in the case of high rates of cycling and cycling at elevated temperatures.

The stability of the SEI layer was highly dependent on the properties of the SEI layer. As a representative example, the FEC-derived SEI layer exhibited superior cell performances, showing excellent rate capability and enhanced thermal stability (Chapter 5). These were attributed to the SEI's chemical structure and composition, i.e., a thinner and denser layer that consisted of abundant polymeric species as a consequence of the reduction of FEC during the formation cycle. Thus, forming an effective and desirable SEI layer was indispensable for facilitating Li-ion transport at the electrode/electrolyte interface as well as for suppressing the growth of the SEI layer due to additional decomposition of the electrolyte.

The effectiveness of the FEC-derived SEI layer can be understood based on the mechanical stability of the SEI layer, i.e., the elasticity of the SEI layer, which was one of the subjects in this research. The experimental and computational results in Chapter 4 showed that the elasticity of the SEI layer was affected significantly by the chemical composition of the SEI layer, suggesting the importance of controlling its chemical

composition. The experimental work demonstrated that the inner layer of the SEI contains considerably more of the stiff species than the outer layer, and the elasticity of each main component of the SEI was determined by computational results, showing stiffer behavior in the order of LiF > Li_2CO_3 > Li_2EDC > LiMC > LiEC > PEO. Based on these findings, it was suggested that the formation of a polymeric layer (such as PEO) rather than an EC- or DMC-based organic layer, would be desirable to have flexibility of the SEI layer in order to minimize its mechanical instability. Thus, the abundance of polymeric species in the FEC-derived SEI layer, which resulted from the reduction of FEC prior to the reduction of EC, was believed to be effective in preserving the mechanical stability of the SEI layer. The flexible layer that exists at the inner layer of the FEC-derived SEI layer possibly was helpful in protecting the SEI layer from a large strain due to intercalation-induced and gas formation-induced volume changes, especially during extreme cycling conditions.

The passivating effect of the SEI layer was degraded or eliminated by the chemical degradation of the SEI layer, leading to further formation and growth of the SEI layer. The XPS results in Chapter 2 showed that the chemical composition and thickness of the SEI layer that was formed during storage at elevated temperature differed significantly from the SEI layer formed at room temperature; a thicker SEI layer with higher concentrations of carbon and oxygen was formed at elevated temperature, suggesting that dissolution, breakdown, or conversion of the SEI layer occurred at elevated temperatures. EIS measurements indicated that the SEI layer was not stable at elevated temperatures; the interfacial resistance at the anode had an oscillating behavior, which was different from the behavior of the interfacial resistance at room temperature.

Based on the observation of a monotonic relationship between temperature and the interfacial resistance at the anode, it was proposed that the growth of SEI at elevated temperatures occurred as a consequence of a competitive mechanism between the precipitation and the dissolution of the SEI layer. According to this mechanism, it was inferred that the thermal stability of the FEC-derived SEI layer possibly was associated with the chemical composition of the FEC-derived SEI layer, which consisted of chemical species that were less susceptible to the dissolution of SEI at elevated temperatures (Chapter 5).

The chemical degradation of the SEI layer was promoted by the dissolution of SEI as a direct result of elevated temperature and also by the deterioration of SEI induced by the deposition of dissolved manganese ions, which was an indirect result of the elevated temperature. In Chapter 3, the process and mechanism of the chemical degradation of SEI induced by the deposited manganese ions were determined. The results showed that dissolved manganese ions diffused through a porous layer and were deposited mainly in the form of MnF_2 at the inorganic/graphite interface, allowing ion-exchange reactions to occur between the species comprising the SEI and deposited manganese ions. During the deposition and/or interactions of dissolved manganese ions, additional electrolyte decompositions were catalyzed, forming a more oxygen-rich layer. Consequently, a thicker SEI layer was formed at the interface of the anode in the presence of dissolved manganese ions.

The dissolved manganese ions that affected the deterioration of the SEI layer also contributed to the structural degradation of graphite, which were addressed in Chapter 6. Based on results from XPS depth profiling and XRD measurements, the possibility of

manganese co-intercalation was proposed. Using hypothetical Li-GIC structures, including manganese ions, the DFT calculations predicted that intercalated manganese ions would lead to the contraction of the interlayer space in graphite, suggesting the possibility of structural disordering and defects in the graphite. Raman mapping results demonstrated that the structural disordering of graphite occurred in the presence of dissolved manganese ions. The results placed more emphasis on the development of an effective SEI layer that can protect the anode side from the attack of dissolved transition metal ions.

In Chapter 5, the necessity of evaluating the effect of the electrolyte additive on the cathode side was emphasized in order to improve the thermal stability of a battery. While the chemical and mechanical instabilities of the SEI layer were overcome by using the FEC additive in the electrolyte, adverse effects of FEC on the cathode side were observed, especially at elevated temperatures. The capacity of the LMO/Li cell containing FEC was decreased dramatically at elevated temperatures, compared to that of the cell without FEC. EIS results showed that the increase in the interfacial resistance at the cathode was significant in the case of the FEC-containing cell. One of the reasons for the rapid increase of the interfacial resistance at the cathode was the formation of a thicker surface layer with high concentrations of polymeric and polycarbonate species. In addition, the increase in the amount of dissolved Mn was accelerated due to the increased amount of hydrofluoric acid (HF) in the FEC-containing cell. The study demonstrated that these adverse effects was initiated or provoked by the thermal decomposition or dehydrofluorination of the FEC additive. Based on these findings, it was suggested that the residual FEC after formation of the SEI layer on the anode side was detrimental to the

cathode at elevated temperatures. Thus, it was necessary to optimize the amount of FEC to achieve further improvement of a battery at elevated temperature.

The findings from this research can provide a fundamental understanding of chemical and physical processes that underlie the degradation of the SEI layer and concomitant other degradation phenomena. Such an understanding is essential to gain insights into strategies for controlling or optimizing the properties of the SEI to provide the mechanical and chemical stability of the electrode/electrolyte interface. This work can guide the direction of many approaches in the "design" of the SEI layer.

Based on this work, the following future work is proposed:

- The modified SEI layers derived by electrolyte additives should be studied further by investigating the thermal dissolution behavior of the SEI layer and the protective behavior of the SEI layer against the attack of transition metal ions.
- A comparative study on the effects of other deposited transition metal ions (such as Ni, Co, and Fe) on the properties of the SEI layer is needed to clarify the degradation mechanism of SEI induced by the deposition of transition metal ions.
- DFT calculations are required to investigate the possibility of co-intercalation of other transition metal ions and its effects on the contraction/expansion behaviors of the interlayer spacing in graphite. In addition, the investigation on the mechanical stability of graphite that contains different co-intercalated transition metal ions is recommended.
- To investigate the cracking behavior of the SEI on graphite or silicon, dynamics simulation should be conducted with various factors, such as pressure and temperature.

- Polymer-coated graphite or silicon should be tested to investigate the performance of the battery to validate whether the mechanical stability of its interface can be achieved.
- The effects of various electrolyte additives on the surface of the cathode should be reevaluated, especially at elevated temperatures. A comparative study of different cathode materials with electrolyte additives would be useful to provide a better understanding of the mechanisms that underlie the interactions between the additives and the cathode materials.